AWARD NUMBER: W81XWH-17-1-0542

TITLE: Molecular Cross-Talk: Bone Metastatic Prostate Cancer and Nociceptive Neurons

PRINCIPAL INVESTIGATOR: Christopher Peters, Ph.D.

CONTRACTING ORGANIZATION: Wake Forest University Health Sciences

REPORT DATE: JANUARY 2022

TYPE OF REPORT: Final report

PREPARED FOR: U.S. Army Medical Research and Materiel Command
Fort Detrick, Maryland 21702-5012

DISTRIBUTION STATEMENT: Approved for Public Release;
Distribution Unlimited

The views, opinions and/or findings contained in this report are those of the author(s) and should not be construed as an official Department of the Army position, policy or decision unless so designated by other documentation.

REPORT DOCUMENTATION PAGE

Form Approved
OMB No. 0704-0188

Public reporting burden for this collection of information is estimated to average 1 hour per response, including the time for reviewing instructions, searching existing data sources, gathering and maintaining the data needed, and completing and reviewing this collection of information. Send comments regarding this burden estimate or any other aspect of this collection of information, including suggestions for reducing this burden to Department of Defense, Washington Headquarters Services, Directorate for Information Operations and Reports (0704-0188), 1215 Jefferson Davis Highway, Suite 1204, Arlington, VA 22202-4302. Respondents should be aware that notwithstanding any other provision of law, no person shall be subject to any penalty for failing to comply with a collection of information if it does not display a currently valid OMB control number. **PLEASE DO NOT RETURN YOUR FORM TO THE ABOVE ADDRESS.**

1. REPORT DATE	2. REPORT TYPE	3. DATES COVERED
JANUARY 2022	Final	30SEPT2017 - 29SEPT2021

4. TITLE AND SUBTITLE

Molecular Cross-Talk: Bone Metastatic Prostate Cancer and Nociceptive Neurons

5a. CONTRACT NUMBER

5b. GRANT NUMBER
W81XWH-17-1-0542

5c. PROGRAM ELEMENT NUMBER

6. AUTHOR(S)

Yusuke Shiozawa, MD, PhD, Christopher Peters, PhD

E-Mail: yshiozaw@wakehealth.edu, chrpeter@wakehealth.edu

5d. PROJECT NUMBER

5e. TASK NUMBER

5f. WORK UNIT NUMBER

7. PERFORMING ORGANIZATION NAME(S) AND ADDRESS(ES)

Wake Forest University Health Sciences
Medical Center Blvd.
Winston-Salem NC 27157

8. PERFORMING ORGANIZATION REPORT NUMBER

9. SPONSORING / MONITORING AGENCY NAME(S) AND ADDRESS(ES)

U.S. Army Medical Research and Materiel Command
Fort Detrick, Maryland 21702-5012

10. SPONSOR/MONITOR'S ACRONYM(S)

11. SPONSOR/MONITOR'S REPORT NUMBER(S)

12. DISTRIBUTION / AVAILABILITY STATEMENT

Approved for Public Release; Distribution Unlimited

13. SUPPLEMENTARY NOTES

14. ABSTRACT

The goal of this project is to determine the roles of angiotensin II and its receptor in prostate cancer induced bone pain and bone metastatic growth. Aim 1 will provide the framework to identify the extent to which the interaction between cancer cells and nociceptive neurons through the angiotensin II and receptor axis affects cancer-induced bone pain. Aim 2 will determine the downstream molecular mechanisms whereby angiotensin II and its receptor axis affect bone pain. Aim 3 will define how nociceptive neuron influence tumor outgrowth. We believe that the insights derived from our investigations will lead to new strategies for reducing cancer-induced bone pain and also the outgrowth of bone metastasis.

During this period, we further identified the roles of cancer-derived angiotensin II in the nerve growth in the bone metastatic setting. Additionally, we elucidated the crosstalk between prostate cancer cells and sensory neurons in vitro. We also found that global deletion of calcitonin gene-related peptide (CGRP) did not affect bone metastatic progression of prostate cancer. We generated and validated an RM1-mCherry cell line for use in future studies examining the relationship between bone cancer pain and plasticity of subpopulations of sensory neurons using several transgenic reporter mice and deep tissue clearing and light sheet and multi-photon confocal imaging techniques.

15. SUBJECT TERMS

Prostate Cancer; Bone metastasis; Disseminated tumor cells; Cancer-induced bone pain; Sensory nerves; Bone marrow microenvironment

16. SECURITY CLASSIFICATION OF:			17. LIMITATION OF ABSTRACT	18. NUMBER OF PAGES	19a. NAME OF RESPONSIBLE PERSON
a. REPORT	b. ABSTRACT	c. THIS PAGE			19b. TELEPHONE NUMBER *(include area code)*
Unclassified	Unclassified	Unclassified	Unclassified	113	USAMRMC

Table of Contents

Page

1. **Introduction……. 4**
2. **Keywords……. 5**
3. **Accomplishments……..……... 6-15**
4. **Impact……...…… 16-17**
5. **Changes/Problems...…..…… 18**
6. **Products…….……..…..……. 19-24**
7. **Participants & Other Collaborating Organizations……. 26-27**
8. **Special Reporting Requirements…… 28**
9. **Appendices…… 29-56**

1. INTRODUCTION:

Cancer-related pain, both its causes and its management, poses a tremendous challenge to patients and their caregivers. In the quest for effective cancer therapy, maintaining quality of life can be as crucial as treating the tumor. Seventy-five percent of cancer patients experience pain throughout the course of the disease, and once cancer metastasizes to the bone, the first symptom is often acute bone pain. A full 80% of patients with bone metastasis suffer from cancer-induced bone pain (**CIBP**). Current analgesic strategies for CIBP using nonsteroidal anti-inflammatory drugs (**NSAIDs**) and opioids are effective, but side effects, abuse, and addiction are serious and growing concerns associated with their use. It is therefore essential to develop therapeutic agents that can eradicate bone metastatic diseases and relieve resultant pain.

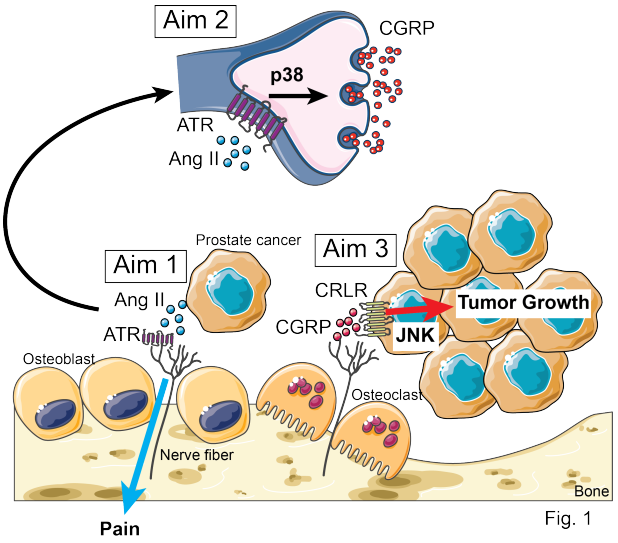

Fig. 1

Metastatic progression of disseminated tumor cells (**DTCs**) to bone may be environmentally directed by influences from the bone marrow microenvironment. Yet a full understanding of the more complex interactions that result in active bone marrow metastasis remains elusive. Our group recently discovered that early in the metastatic process, prostate cancer (**PCa**) cells target and commandeer the specific microenvironment for hematopoietic stem cells (**HSCs**), using mechanisms similar to those involved in HSC homing. Involvement of sympathetic and parasympathetic nerve fibers is crucial for both HSC maintenance and the dissemination of PCa to bone, suggesting that interactions between DTCs and nerves are at least in part responsible for controlling metastatic progression. However, the influence of sensory nerve fibers in the bone on PCa progression and metastasis has not been examined. Although it has been suggested that compression of the soft tissues or peripheral nerve fibers and interference with bone remodeling by bone tumors may be major causes of CIBP, little is known about the molecular interactions of DTCs with bone marrow nerve fibers, and how they affect CIBP.

Elucidating how these interactions influence CIBP is key. Angiotensin II (**Ang II**), a peptide that regulates blood pressure, is also involved in the progression of several types of cancer, including PCa. Ang II is pronociceptive in neuropathic and inflammatory pain models, and elicits sprouting of nociceptive neurons in the skin following inflammation through the angiotensin receptor (**ATR**). In a clinical study of several chronic musculoskeletal pain conditions, a small molecule inhibitor for ATR provided significant pain relief, suggesting that the Ang II/ATR axis controls pain signaling. Our preliminary data suggest that pain-associated neuropeptides can interact directly with PCa cells to cause enhanced proliferation. Therefore, it is critical to explore whether the Ang II/ATR axis is involved in the development of CIBP, and whether pain-associated neuropeptides regulate bone metastatic progression.

We hypothesize that **disseminated PCa stimulates sensory neurons that innervate bone through the Ang II/ATR axis; these cancer-associated sensory neurons then release neuropeptides, resulting in both CIBP and metastatic progression of PCa** (see **Fig. 1**). Ang II expressed by disseminated PCa induces CIBP (Aim 1) by stimulating sensory neurons to release calcitonin gene-related peptide (**CGRP**) through the ATR/p38 pathway (Aim 2). The nerve-derived CGRP enhances the growth of DTCs via its receptor calcitonin receptor-like receptor (**CRLR**) (Aim 3).

To address our hypothesis the following aims are proposed:

Aim 1: Determine how disseminated prostate cancer is involved in development of cancer-induced bone pain.

Aim 2: Define the intracellular signaling pathways in peripheral nerves stimulated by disseminated prostate cancer.

Aim 3: Determine the influence of nociceptive neurons on (a) tumor outgrowth in the bone and (b) cancer-induced bone pain.

The proposed studies will focus on fundamental mechanisms behind the novel concept that nerves in the bone marrow microenvironment have a crucial role in PCa bone metastasis. Aim 1 will provide the framework to identify the extent to which the interaction between DTCs and nociceptive neurons affects cancer-induced bone pain. Aim 2 will determine the molecular mechanisms of cancer-induced bone pain. Aim 3 will define how DTC/nociceptive neuron interactions influence tumor outgrowth. We believe that the insights derived from our investigations will lead to new strategies for reducing cancer-induced bone pain and also the outgrowth of DTCs. By promoting understanding of how the crosstalk between nociceptive neurons and DTCs participates in cancer-induced bone pain and tumor outgrowth, this study will lay the foundation for significant improvements in care of PCa patients, allowing development of pain targeting therapies that can also minimize bone metastatic progression. If successful, our study will not only shed new light on the fundamental mechanisms of PCa bone metastasis, but will quickly provide a gateway to novel treatment strategies to lower PCa-associated deaths and suffering, as some of the agents to be tested in this study have been in clinical trials for different diseases.

2. KEYWORDS:

Prostate Cancer; Bone metastasis; Disseminated tumor cells; Cancer-induced bone pain; Sensory nerves; Bone marrow microenvironment

3. ACCOMPLISHMENTS:

What were the major goals and objectives of the project?

The goal of this project is to determine the roles of the interaction between bone metastatic prostate cancer and sensory nerves in cancer-induced bone pain and bone metastatic growth.

Task 1: Determine whether Ang II expressed by disseminated tumor cells affects cancer-induced bone pain using pharmacological interference of Ang II and ATR interactions.

Months 1-11.

- Submit documents for local IACUC review (**Months 1-3; Dr. Shiozawa, Dr. Peters**).
- Submit IACUC approval and necessary documents for ACURO review (**Months 4-6; Dr. Shiozawa**).
- Design and develop an animal model to measure the tumor growth in the marrow, bone remodeling, and pain related behavior within the same animal (**Months 7-8; Dr. Shiozawa, Dr. Peters**).
- Test the effects of Ang II/ATR axis on the tumor growth in the marrow, bone remodeling, and pain related behavior within the same animal (**Months 9-11; Dr. Shiozawa, Dr. Peters**).

Task 2: Determine the effects of disseminated tumor cells on Ang II levels in the marrow and ATR expression in the dorsal root ganglia.

Months 12-14.

- Determine the kinetic pattern of Ang II levels in the tumor inoculated marrow and ATR expression in the tumor inoculated DRG (**Months 12-14; Dr. Shiozawa**).

Task 3: Determine the effects of Ang II expressed by disseminated tumor cells on cancer-induced bone pain by manipulating the tumor-nerve microenvironment.

Months 15-19.

- Design and develop nerve-specific ATR knockdown (KD) mice with adeno-associated viral vectors (**Months 15-16; Dr. Shiozawa, Dr. Peters**).
- Test the effects of Ang II/ATR axis on the tumor growth in the marrow, bone remodeling, and pain-related behavior within the same animal (ATR KD mice) (**Months 17-19; Dr. Shiozawa, Dr. Peters**).

Task 4: Determine whether the p38 pathway influences tumor growth, skeletal remodeling, and cancer-induced bone pain.

Months 20-22.

- Test the effects of p38 inhibitor on the tumor growth in the marrow, bone remodeling, and pain related behavior within the same animal (**Months 20-22; Dr. Shiozawa, Dr. Peters**).

Task 5: Determine the molecular mechanisms whereby Ang II expressed by disseminated tumor cells activates the bone marrow sensory nerves.

Months 23-24.

- Test the effects of ATR antagonist on the expression of pp38 and CGRP in DRG, spinal cord, and bone (**Months 23-24; Dr. Shiozawa, Dr. Peters**).

Task 6: Major Task 6: Define a link between Ang II expression by disseminated tumor cells with activation of the bone marrow sensory nerves in human subjects.

Months 1-34.

- Submit documents for local IRB review (**Months 1-3; Dr. Shiozawa**).
- Submit IRB approval and necessary documents for HRPO review (**Months 4-6; Dr. Shiozawa**).
- Clinical validation of results with bone biopsy samples of confirmed prostate cancer patients (**Months 7-34; Dr. Shiozawa, Dr. Peters**)
- Co-author manuscript on the effects of Ang II/ATR axis on the tumor growth, bone remodeling, and pain related behavior (**Months 23-26; Dr. Shiozawa, Dr. Peters**).

Task 7: Determine whether CGRP released from bone marrow sensory neurons influences tumor growth, skeletal remodeling, and cancer-induced bone pain.

Months 25-29.

- Design and develop nerve-specific CGRP knockdown (KD) mice with adeno-associated viral vectors (**Months 25-26; Dr. Shiozawa, Dr. Peters**).
- Establish CRLR KD PCa cells (**Months 25-26; Dr. Shiozawa**).

- Test the effects of CGRP/CRLR axis on the tumor growth in the marrow, bone remodeling, and pain-related behavior within the same animal (CGRP KD mice) (**Months 27-29; Dr. Shiozawa, Dr. Peters**).

Task 8: Determine whether CGRP promotes bone metastases through JNK pathway.

Months 30-31.

- Test the effects of CGRP antagonist on the expression of JNK in bone metastatic tumor (**Months 30-31; Dr. Shiozawa, Dr. Peters**).

Task 9: Determine whether JNK pathway influences tumor growth, skeletal remodeling, and cancer-induced bone pain.

Months 32-34.

- Test the effects of JNK inhibitor on the tumor growth in the marrow, bone remodeling, and pain related behavior within the same animal (**Months 32-34; Dr. Shiozawa, Dr. Peters**).

- Co-author manuscript on the effects of CGRP/CRLR axis on the tumor growth, bone remodeling, and pain related behavior (**Months 25-26; Dr. Shiozawa, Dr. Peters**).

- Co-author manuscript summarizing all the results (**Months 27-29; Dr. Shiozawa, Dr. Peters**).

What was accomplished under these goals?

(2017-2018)

Bone metastatic prostate cancer (PCa) causes enriches calcitonin gene-related peptide (CGRP)-expressing sensory nerves in the marrow, and that the CGRP/calcitonin receptor-like receptor (CRLR)/p38 pathway promotes PCa bone metastasis (Dr. Shiozawa).

CGRP downregulation in sensory nerves that innervate bone using adeno-associated virus serotype rh10 (AAVrh10) (Drs. Shiozawa and Peters).

(2018-2019)

Characterization of a syngeneic mouse model of prostate cancer-induced bone pain (Drs. Shiozawa and Peters).

Cancer-derived factors stimulated the neurite outgrowth of murine sensory neurons (Dr. Shiozawa).

(2019-2020)

Characterization of a syngeneic mouse model of prostate cancer-induced bone pain (Drs. Shiozawa and Peters).

Development of methods for deep tissue clearing and 3D light sheet imaging to investigate in more detail interactions between cancer cells, tumor associated macrophage and populations of nerve fibers within the bone microenvironment (Dr. Peters)

Prostate cancer produces angiotensin II (Ang II) from angiotensinogen (AGT) by Angiotensin converting enzyme (ACE) and secretes Ang II (Dr. Shiozawa).

No cost extension on this award (Drs. Shiozawa and Peters).

(2020-2021)

Angiotensin II (Ang II) induces nerve sprouting, and angiotensinogen (AGT) in prostate cancer cells is involved in the prostate cancer proliferation (Dr. Shiozawa).

During the previous period, we revealed that PCa cells produce and secrete Ang II from AGT. During this award period, we further attempted to determine the roles of Ang II derived from PCa cells in the induction of cancer-induced bone pain, which is one of our hypotheses. To test this hypothesis, we first addressed whether Ang II can induce sensory nerve sprouting, which is one of the mechanisms of pain induction. When we treated mouse primary sensory neuron cells with Ang II *in vitro*, greater neurite outgrowth of these sensory neuron cells was induced, compared to either vehicle or nerve growth f actor (NGF), although it did not reach significance (**Fig. 1A&B**). While Ang II induced neurite outgrowth, Ang II failed to enhance pain-associated neuropeptides calcitonin gene-related peptide (CGRP) and substance P (**Fig. 1C&D**). These data suggest that although Ang II induces neurite outgrowth, it may not be a sole inducer of cancer-induced bone pain. Therefore, out next attempt would be to determine whether Ang II can induce further neurite outgrowth of sensory neurons and enhance the production of pain-associated neuropeptides when co-treated with other factors, known to induce pain behaviros.

Next, to investigate whether Ang II derived from PCa causes cancer-induced bone pain by stimulating sensory neurons. We knocked down AGT in PCa cells by shRNA. Surprisingly, the downregulation of AGT in PCa reduced the proliferation of PCa (**Fig. 2A&B**). We are currently investigating the mechanisms of this phenomena, and planning on treating murine primary neuron cells with conditioned medium of control PCa vs. AGT-downregulated PCa cells.

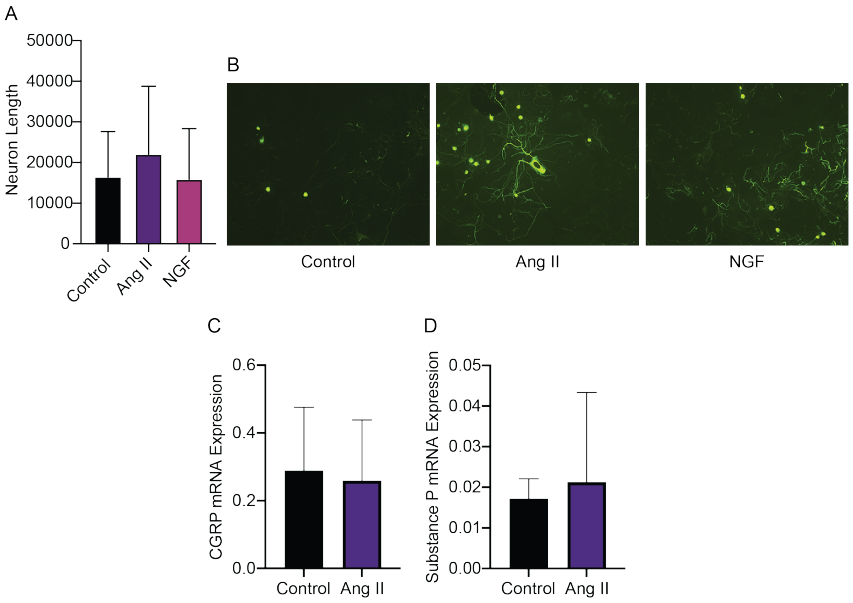

Fig. 1: Angiotensin II (Ang II) induces nerve sprouting.

(**A**) Murine primary sensory neuron cells were treated either with control, Ang II or NGF for 48h. (**B**) Representative images of sensory nerve sprouting. 20x. (**C**) CGRP and (**D**) Substance P mRNA expression of murine primary sensory neuron cells treated with either control or Ang II, using GAPDH as reference gene.

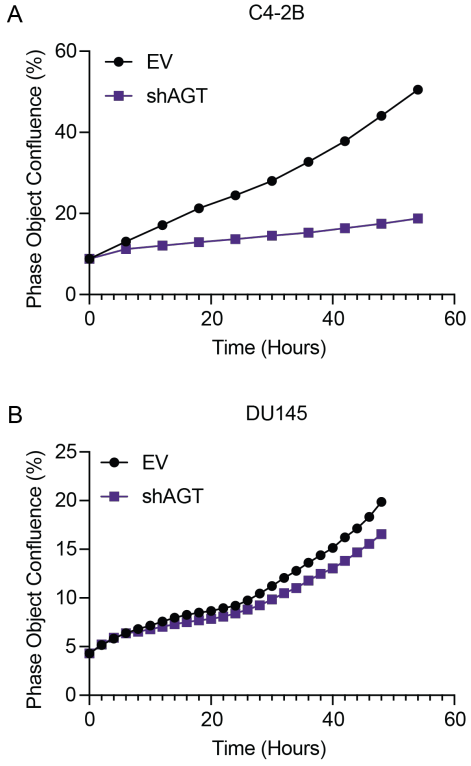

Fig. 2: Angiotensinogen (AGT) in prostate cancer cells is involved in the prostate cancer proliferation.

Incucyte cell proliferation assays were performed to compare the proliferation between prostate cancer cells ((**A**) C4-2B, (**B**) DU145) transfected with empty vector (EV) and shRNA targeting AGT.

While prostate cancer cells induce neurite outgrowth of sensory neuron, sensory neurons enhance prostate cancer proliferation (Dr. Shiozawa).

During the previous period, we developed and characterized a syngeneic mouse model of PCa-induced bone pain using RM-1 cell lines. Since having syngeneic mouse model is advantage for allowing studies in immunocompetent animals which better reflect the normal bone microenvironment, during this award period, we further attempted to expand our capacity in this area. To do so, we first determined prostate cancer cell lines which can induce nerve sprouting of sensory neurons. Interestingly, most of the murine prostate cancer cell lines could induce neurite outgrowth of both pan-sensory nerve markers β-tubulin and NF200 expressing neurons, while B16-F10 melanoma cell line, known to be less painful line, failed to induce neurite outgrowth of these cells (**Fig. 3A-D**). Currently, we are testing whether these prostate cancer cell lines can grow within the bones, and induce bone remodeling and cancer-induced bone pain. While testing the effects of the bone metastatic prostate cancer on sensory nerves in bone, we also investigated the effects of sensory nerves on prostate cancer growth. Intriguingly, when prostate cancer cells were treated with conditioned medium obtained from murine primary sensory neuron cells, the proliferation of prostate cancer cells were enhanced (**Fig. 4**). These findings suggest that there is the crosstalk between bone metastatic prostate cancer and sensory neurons to induce disease progression as well as cancer-induced bone pain. Future studies using syngeneic mouse models that we are currently developing will help better understanding of sensory neuron/cancer interactions that drive prostate cancer-induced bone pain and disease progression.

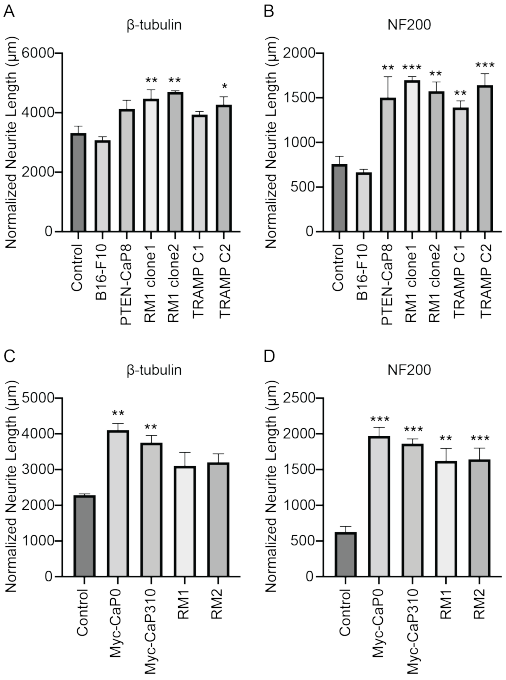

Fig. 3: Prostate cancer cells induce neurite outgrowth of sensory neuron.

Murine primary sensory neuron cells were treated either with control conditioned media (Control) or conditioned media from several different cancer cell lines for 48h. Thereafter, never fibers and cells were stained with pan-sensory neuron markers b-tubulin (**A, C**) or NF200 (**B, D**). The neurite length was normalized with cell numbers. Mean ± SEM. $^{**}p \leq 0.01$, $^{***}p \leq 0.001$ vs. Control CM treatment (one-way ANOVA, Dunnett's multiple comparisons).

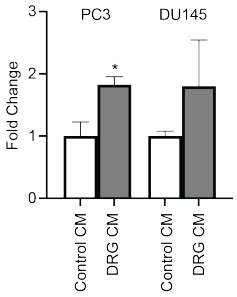

Fig. 4: Sensory neurons enhance prostate cancer proliferation.

Prostate cancer cells (PC3 and DU145) and murine primary sensory neuron cells were co-cultured on the Bidi-co-culture plate, which allows wells to exchange medium, for 48h. Thereafter, numbers of cancer cells were measured with crystal violet staining method. Growth medium was used as control. Mean ± SEM. $^{*}p \leq 0.05$vs. Control CM treatment (Student's *t*-test).

Global deletion of CGRP failed to affect disease progression (Drs. Shiozawa and Peters).

During the previous period, we demonstrated that CGRP expressed by sensory nerves is involved in the prostate cancer bone metastatic progression. During this award period, we further attempted to dissect the roles of CGRP in prostate cancer bone metastatic progression using systemic CGRP KO mice. Briefly, male homozygous CGRP KO mice were inoculated into the femur with murine RM-1 prostate cancer cells ($1x10^3$ cells/5μL). Heterozygous CGRP KO mice were used as control. Prior to injection, the RM-1 cells were transfected with luciferase reporters in order to visualize *in vivo* tumor growth longitudinally by bioluminescence image (BLI). Unexpectedly, global deletion of CGRP filed to change in both bone remodeling and disease progression (**Fig. 5A&B**), suggesting that sensory neuron-specific deletion of CGRP or sensory neuron CGRP-targeting therapy is necessary to mitigate prostate cancer bone metastatic progression. Further studies will be clearly warranted.

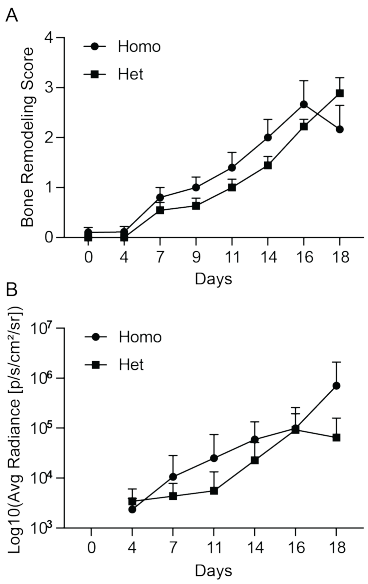

Fig. 5: Global deletion of CGRP failed to affect disease progression.

Murine prostate cancer RM-1 cells were implanted directly into femurs of homozygous CGRP KO mice (Homo) or Heterozygous CGRP KO mice (Het). (**A**) X-ray analyses were performed measure bone remodeling. The X-ray images were provided to a blinded observer to perform longitudinal scoring using the following scale for assessing degree of osteolysis (0 = Bones with no lesions; 1 = Bones with one to three small pits of radiolucent lesions; 2 = Bones with three to six small pits of radiolucent lesions; 3 = Bones with obvious loss of medullary bone and erosion of cortical bone; 4 = Bones with full thickness unicortical bone loss; and 5 = Bones with full thickness bicortical bone loss and displaced skeletal fracture). (**B**) bioluminescence image was performed to measure tumor growth. (n=10: Homo, n=11: Het).

Development of methods for deep tissue clearing and 3D light sheet imaging to investigate in more detail interactions between cancer cells, tumor associated macrophage and populations of nerve fibers within the bone microenvironment (Dr. Peters)

To further characterize the relationship between immune cells, nerve fibers and PCa cells in tumor bearing mice, we sought to evaluate several methods for clearing and light sheet imaging of decalcified mouse bones and joints. We used a modified PEGASOS and BoneClear protocols of intact bone/joints from CGRP-GFP reporter mice that expresses GFP in both unmyelinated and myelinated CGRP containing peptidergic sensory neurons (**Fig. 6**).

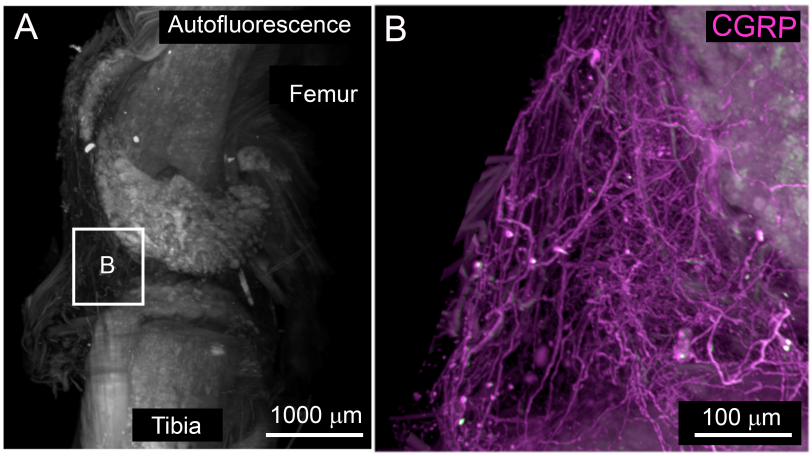

Fig. 6: Intact whole mouse knee joint imaged using light sheet microscopy displaying autofluorescence (white) to reveal structural details in CGRP-GFP reporter mouse. B. High power light sheet maximum intensity projection image of infrapatellar fat pad region in knee joint following tissue immunohistochemistry with antibodies against GFP to label peptidergic sensory neurons (CGRP, colorized purple for contrast).

In future studies, we will use CGRP-GFP reporter mice and an RM1-mCherry transduced PCa cells (**Fig. 7**) to examine the distribution and plasticity of CGRP positive sensory neurons at various time points after tumor inoculation in the mouse femur. We will also use these approaches to examine the time course of dissemination and migration of PCa cells to the bone after intracardiac injections.

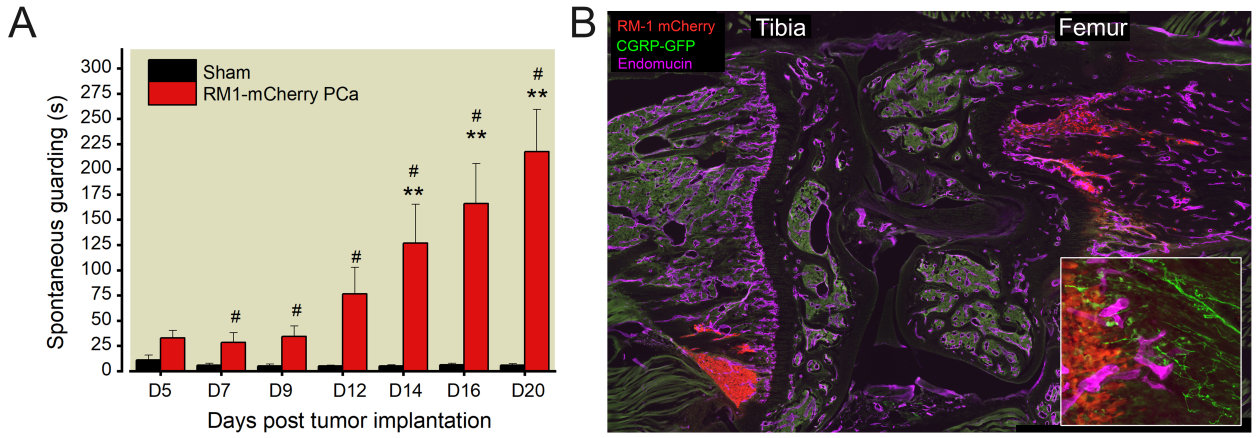

Fig. 7: (**A**) Intrafemoral injection of RM1-mCherry prostate cancer cells induces a progressive increase in spontaneous guarding in the ipsilateral limb of tumor bearing (n=9) compared to sham operated mice (n=11). Two-way RM ANOVA with Bonferreni contrasts ** $p < 0.05$ vs. D7, # $p < 0.05$ vs sham. (**B**) RM1-mCherry prostate cancer cells (red) home to the metaphysis of the tibia and femur following intracardiac injection in C57Bl6 mice. Sensory neurons (CGRP-GFP, green) and endothelial cells (purple) are closely associated with migrating PCa cells (inset). Confocal image of 25-micron thick coronal section of mouse knee joint including proximal tibia and distal femur.

What opportunities for training and professional development did the project provide?

(2017-2018)
Dr. Shiozawa was invited to give a seminar at Jikei University School of Medicine (Tokyo, Japan) on October 11, 2017.

Dr. Peters organized a symposium at Wake Forest University Medical School entitled "*Translational Cancer Pain Research: Bridging the Gap Between Basic Science and Clinical Application* ". The symposium consisted of presentations from 3 clinicians (Dr. Francis Walker, Dr. Glenn Lesser, Dr. Roy Strowd) who specialize in clinical research focused on interventional studies for the treatment of cancer related pain and sensory dysfunction as well as 2 preclinical researchers (Dr. Chris Peters, Dr. Mario Danelo Boada) who are conducted mechanistic research studies in rodent models of cancer pain. The keynote speaker was Dr. Patrick Dougherty from MD Anderson Cancer Center who presented a lecture entitled "Inflammation and Ectopic Spontaneous Activity: New Findings of Chemotherapy Induced Peripheral Neuropathy in Humans & Animals". This symposium came about largely as a result of the collaborative efforts driven by Dr. Shiozawa between clinicians within Wake Forest Comprehensive Cancer Center and faculty members within the Department of Anesthesiology at Wake Forest Baptist Medical Center.

(2018-2019)
Dr. Shiozawa was invited to give a talk at The U.S. Bone and Joint Initiative (USBJI) and Bone and Joint Canada (BJC) Young Investigator Initiative Workshop Spring 2019 (Rosemont, IL) on April 27, 2019.

Dr. Shiozawa was invited to give a seminar at University of North Carolina at Chapel hill, Adams School of Dentistry (Chapel hill, NC) on December 03, 2019.

Dr. Peters presented a poster at Neuroscience 2019 the Annual Society for Neuroscience Meeting in Chicago, Illinois October 19th-23, 2019.

(2019-2020)
Dr. Shiozawa serves as an Editor for HubLE Graphics Committee of The IFMRS (International Federation of Musculoskeletal Societies) HubLE.

Dr. Shiozawa presented an e-poster at American Society for Bone and Mineral Research (ASBMR) 2020 Annual Meeting, Virtual, September 11-14, 2020.

As of July 1st, 2020, Dr. Peters was promoted to an Associate Professor.

(2020-2021)

As of July 1st, 2021, Dr. Shiozawa was promoted to an Associate Professor with Tenure.

As of July 1st, 2021, Dr. Peters obtained Tenure.

How were the results disseminated to communities of interest?

There is nothing to report at this time.

What do you plan to do during the next reporting period to accomplish the goals and objectives?

Even after completing the award, we will continue to determine the roles of renin-angiotensin system in PCa-induced bone pain (Aim 1). We will also further elucidate the molecular mechanisms whereby bone metastatic PCa stimulates sensory nerves (Aim 2). In addition, we will continue to pursue studies examining the effects of sensory nerves on the progression of bone metastatic PCa (Aim 3).

4. IMPACT:

What was the impact on the development of the principal discipline(s) of the project?

(2017-2018)

We found that PCa enhances the sprouting of CGRP-expressing sensory nerves both in vitro and in vivo.

We found that PCa patients with bone metastases have high levels of CGRP in their serum, that PCa in bone metastatic sites expresses high levels of CRLR, and that CRLC expression levels in PCa is associated with their recurrent free survival.

We found that CGRP induces PCa proliferation through CRLR/p38 pathway.

We developed the technique to manipulate gene expression in sensory nerves innervating bones using an AAVrh10 virus vector.

(2018-2019)

We developed a syngeneic murine cancer-induced bone pain model which allows us to further investigate the mechanisms how bone metastatic PCa influence bone pain behaviors in an immunocompetent setting. Future studies will use this model in combination with transgenic Cre/Flpo driver mice to better understand sensory neuron tumor interactions that drive PCa induced bone pain and disease progression.

We established an *in vitro* sensory neuron culture system to further study interaction between PCa and sensory neurons.

We developed a semi-automated quantification method to measure the *in vitro* neurite outgrowth of sensory neurons.

(2019-2020)

We further characterized a syngeneic murine prostate cancer (PCa)-induced bone pain model which allows us to further elucidate the roles of the crosstalk between bone metastatic PCa and sensory neurons in both bone metastatic progression and its resultant bone pain in an immunocompetent setting.

We developed and refined methods for deep tissue clearing and 3D light sheet imaging to investigate in more detail interactions between cancer cells, immune cells and populations of nerve fibers within the bone microenvironment.

We began to identify the roles of cancer-derived angiotensin Il in the nerve growth in the bone metastatic setting.

We obtained the one-year no cost extension on this award due to the COVID-19 pandemic.

(2020-2021)

We found that Ang II enhances the sprouting of murine primary sensory nerves in vitro.

We identified murine prostate cancer cell lines which can induce nerite outgrowth of murine primary sensory nerves in vitro that will enable us to develop syngeneic mouse models of prostate cancer-induced bone pain.

We found that murine primary sensory nerves enhance the proliferation of prostate cancer cells in vitro.

We found that global deletion of CGRP did not affect bone metastatic progression of prostate cancer.

We continued to refine approaches for studying the relationship between prostate cancer cells, immune cells and sensory neurons within the bone microenvironment.

What was the impact on other disciplines?

There is nothing to report at this time.

What was the impact on technology transfer?

There is nothing to report at this time.

What was the impact on society beyond science and technology?

There is nothing to report at this time.

5. CHANGES/PROBLEMS:

Changes in approach and reasons for change

Nothing to report.

Actual or anticipated problems or delays and actions or plans to resolve them

Nothing to report.

Changes that have a significant impact on expenditures

Nothing to report.

Significant changes in use or care of human subjects, vertebrate animals, biohazards, and/or select agents

Nothing to report.

6. PRODUCTS:

Publications, conference papers, and presentations

Journal Publications

Peer reviewed journal

(2017-2018)

1. Park SH, Eber MR, Tsuzuki S, Booker ME, Sunil AG, Widner DB, Parker RA, **Peters CM**, **Shiozawa Y**. Adeno-associated virus serotype rh10 is a useful gene transfer vector for sensory nerves that innervate bone in immunodeficient mice. **Sci Rep**. 2017;7:17428. PMID: 29233995. PMCID: PMC5727257.
   Status of Publication: Published
   Acknowledgement of federal support: Yes

   - **Selected as Papers of the Week (9 Dec 2017- 15 Dec 2017) by Pain Research Forum**

(2018-2019)

2. Jones JD, Sinder BP, Paige D, Soki FN, Koh AJ, Thieleb S, **Shiozawa Y**, Hofbauer LC, Daignault S, Roca H, McCauley LK. Trabectedin reduces skeletal prostate cancer tumor size in association with effects on M2 macrophages and efferocytosis. **Neoplasia**. 2018;21:172-184. PMID: 30591422. PMCID: PMC6314218.
   Status of Publication: Published
   Acknowledgement of federal support: Yes

(2019-2020)

3. Lycan TW, Hsu F, Ahn CS, Thomas A, Walker FO, Sangueza OP, **Shiozawa Y**, Park SH, **Peters CM**, Romero-Sandoval EA, Melin SA, Sorscher S, Ansley K, Lesser GJ, Cartwright MS, Strowd RE. Neuromuscular ultrasound for taxane peripheral neuropathy in breast cancer. ***Muscle and Nerve***. 2020;61:587-594. PMID: 32052458. PMCID: In Progress.
   Status of Publication: Published
   Acknowledgement of federal support: Yes

4. Wu S-Y, Xing F, Sharma S, Wu K, Tyagi A, Liu Y, Zhao D, Deshpande RP, **Shiozawa Y**, Ahmed T, Zhang W, Chan M, Ruiz J, Lycan TW, Dothard A, Watabe K. Nicotine promotes brain metastasis by polarizing microglia and suppressing innate immune function. ***JEM***. 2020;217:e20191131. PMID: 32496556. PMCID: PMC7398164.
   Status of Publication: Published
   Acknowledgement of federal support: No

(2020-2021)

5. Eber MR, Park SH, Contino KF, Patel CM, Hsu F-C, **Shiozawa Y**. Osteoblasts derived from mouse mandible enhance tumor growth of prostate cancer more than osteoblasts derived from long bone. ***J Bone Oncology***. 2021;26:100346. PMID: 33425674. PMCID: PMC7779864.
   Status of Publication: Published
   Acknowledgement of federal support: Yes

6. Park SH, Eber MR, M. Fonseca M, Patel CM, Cunnane KA, Ding H, Hsu F-C, Peters CM, Ko M-C, Strowd RE, Wilson JA, Hsu W, Romero-Sandoval EA, **Shiozawa Y**. Usefulness of the measurement of neurite outgrowth of primary sensory neurons to study cancer-related painful complications. ***Biochem Pharmacol***. 2021;188:114520. PMID: **33741328.** PMCID: PMC8154668.
   Status of Publication: Published
   Acknowledgement of federal support: Yes

7. Widner DB, Liu C, Zhao Q, Sharp S, Eber MR, Park SH, Files DC, **Shiozawa Y**. Activated Mast Cells in Skeletal Muscle Can be a Potential Mediator for Cancer-Associated Cachexia. ***J. Cachexia Sarcopenia Muscle***. 2021;12:1079-1097. PMID: 34008339. PMCID: PMC8350201.
   Status of Publication: Published
   Acknowledgement of federal support: Yes

8. Wu K, Feng J, Lyu F, Xing F, Sharma S, Liu Y, Wu S-Y, Zhao D, Tyagi A, Deshpande RP, Pei X, Ruiz MG, Takahashi H, Tsuzuki S, Kimura T, Mo Y-Y, **Shiozawa Y**, Singh R, Watabe K. Exosomal miR-19a and IBSP cooperate to induce osteolytic bone metastasis of estrogen receptor-positive breast cancer. ***Nat Commun***. 2021;12:5196 PMID: 34465793. PMCID: PMC8408156.
   Status of Publication: Published
   Acknowledgement of federal support: No

Invited reviews

(2017-2018)

1. Park SH, Keller ET, **Shiozawa Y**. Bone marrow microenvironment as a regulator and therapeutic target for prostate cancer bone metastasis. **Calcif Tissue Int**. 2018;102:152-62. PMID: 29094177. PMCID: PMC5807175.
   Status of Publication: Published
   Acknowledgement of federal support: Yes

2. Widner DB, Files DC, Weaver KE, **Shiozawa Y**. Preclinical and clinical studies on cancer-associated cachexia. **Front Biol**. 2018;13:11-18. PMID: In Progress. PMCID: In Progress.
   Status of Publication: Published
   Acknowledgement of federal support: Yes

3. Park SH, Eber MR, Widner DB, **Shiozawa Y**. Role of the bone microenvironment in the development of painful complications of skeletal metastases. **Cancers (Basel)**. 2018;10:141. PMID: 29747461. PMCID: PMC5977114.
   Status of Publication: Published

Acknowledgement of federal support: Yes

- **Selected as Featured Paper**

4. Widner DB, Park SH, Eber MR, **Shiozawa Y**. Interactions between disseminated tumor cells and bone marrow stromal cells regulate tumor dormancy. **Curr Osteoporos Rep**. 2018;16:596-602. PMID: 30128835. PMCID: In Progress.
   Status of Publication: Published
   Acknowledgement of federal support: Yes

(2018-2019)

Nothing to report.

(2019-2020)

Nothing to report.

(2020-2021)

5. Patel CM, Wadas TJ, **Shiozawa Y**. Progress in Targeted Alpha-Particle-Emitting Radiopharmaceuticals as Treatments for Prostate Cancer Patients with Bone Metastases. ***Molecules***. 2021; In Press. PMID: In Progress. PMCID: PMC8070008.
   Status of Publication: Published
   Acknowledgement of federal support: Yes

- **Selected by the editors as the cover of the 2021; Volume 26 (Issue 8) (https://www.mdpi.com/1420-3049/26/8)**

Book

(2017-2018)

1. Park SH, Eber MR, **Shiozawa Y**. (2018) Tumor inoculation mouse models of prostate cancer bone metastasis. In Idris A (Ed.), *Bone Research Protocols - 3rd Edition.* In Press. London: Springer Nature.
   Status of Publication: Accepted
   Acknowledgement of federal support: Yes

2. Park SH, Eber MR, Taichman RS, **Shiozawa Y**. (2018) Determining Competitive Potential of Bone Metastatic Cancer Cells in the Murine Hematopoietic Stem Cell Niche. In Turksen K (Ed.), *Stem cells and Niche - 2nd Edition: Methods and Protocols*, Methods in Molecular Biology. In Press. New York: Humana Press. Methods Mol Biol. In Press. PMID: 30099699. PMCID: In Progress.
   Status of Publication: Published

Acknowledgement of federal support: Yes

(2018-2019)

3. Park SH, **Shiozawa Y**. (2019) Genomic mutation as a potential driver of the development of bone-related cancers. In Zaidi M (Ed.), *Encyclopedia of Bone Biology*. In Press. Elsevier.
   Status of Publication: In Press
   Acknowledgement of federal support: Yes

4. **Shiozawa Y**. (2019) The roles of bone marrow-resident cells as a microenvironment for bone metastasis. In Birbrair A (Ed.), *Tumor Microenvironments in Different Organs – Part A*. In Press. Switzerland: Springer Nature.
   Status of Publication: In Press
   Acknowledgement of federal support: Yes

(2019-2020)

5. Eber MR, Jimenez-Andrade JM, **Peters CM**, **Shiozawa Y**. (2020) A method of bone-metastatic tumor progression assessment in mice using longitudinal radiography. In Deep G (Ed.), *Cancer Biomarkers: Methods and Protocols*, Methods in Molecular Biology, In Press. New York: Humana Press. Methods Mol Biol. In Press. PMID: In Progress. PMCID: N/A.
   Status of Publication: In Press
   Acknowledgement of federal support: Yes

(2020-2021)

Nothing to report.

Presentation

(2017-2018)

1. Williams SN, Eber MR, Tsuzuki S, Park SH, **Shiozawa Y**. Does histamine influence the osteoblastic activities that help regulate the progression of bone metastatic prostate cancer? The 2017 Annual Biomedical Research Conference for Minority Students (ABRCMS), Phoenix, AZ, USA, November 1-4, 2017. Poster.

(2018-2019)

2. Lycan T, Thomas A, Hsu FC, Cartwright MS, Walker FO, Ahn C, Sangueza OP, **Shiozawa Y**, Park SH, **Peters CM**, Melin SA, Avery TP, Sorscher S, Lesser GJ, Strowd RE. Neuromuscular ultrasound for assessment of peripheral neuropathy in breast cancer patients receiving taxane therapy. J Clin Oncol 36, 2018 (suppl; abstr e22083). 2018 American Society Of Clinical Oncology (ASCO) Annual Meeting, Chicago, IL, USA, June 1-5, 2018. Poster.

3. Strowd RE, Lycan T, Thomas A, Hsu FC, Ahn C, Sangueza O, **Shiozawa Y**, Park SH, **Peters CM**, EA Romero-Sandoval, Melin SA, Sorscher S, Lesser GJ, Walker FO, Cartwright MS. Neuromuscular ultrasound for the non-invasive assessment of breast cancer patients with peripheral neuropathy from taxanes. The American Academy of Neurology 71st Annual Meeting, Philadelphia, PA, USA, May 4-10, 2019. Poster.

4. Tsuzuki S, Park S, Eber M, Widner B, Kamata Y, Kimura T, Bianchi-Frias D, Coleman I, Nelson P, Hsu F-C, **Peters C**, **Shiozawa Y**. A pain-related neuropeptide calcitonin gene-related peptide promotes bone metastatic progression of prostate cancer through p38. American Society for Bone and Mineral Research (ASBMR) 2019 Annual Meeting, Orland, FL, USA, September 20-23, 2019. Poster.

5. Park S, Eber M, Tsuzuki S, Cain R, Widner B, Kamata Y, Kimura T, Bianchi-Frias D, Coleman I, Nelson P, Hsu F-C, **Peters C**, **Shiozawa Y**. The role of the SCF/c-kit pathway in cancer-induced bone pain. American Society for Bone and Mineral Research (ASBMR) 2019 Annual Meeting, Orland, FL, USA, September 20-23, 2019. Poster.
   - **Selected as a Plenary Poster**

6. Cain R, Park SH, Eber M, Martin TJ, Parker R, Jimenez-Andrade JM, **Shiozawa Y**, **Peters C**. Characterization of a syngeneic mouse model of prostate cancer induced bone pain. Neuroscience 2019, Chicago, IL, USA, October 19-23, 2019. Poster.

   (2019-2020)

7. Ding H, Kiguchi N, Park SH, Kishioka S, **Shiozawa Y**, **Peters C**, Ko M-C. Functional roles of neuromedin B and gastrin-releasing peptide in regulating itch and pain in the spinal cord of primates. **FASEB J**. 2030;34 (S1):03569. Experimental Biology 2020 (Cancelled, but abstract was published).

8. Eber M, Park S, Hsu F-C, **Shiozawa Y**. Osteoblasts Derived from Mouse Mandible Enhance Tumor Growth of Prostate Cancer More Than Osteoblasts Derived from Long Bone. The Cancer and Bone Society (CABS) / American Society for Bone and Mineral Research (ASBMR) Pre- Meeting, The Seed and Soil: Therapeutic Targets for Cancer in Bone, Virtual, September 9-10, 2020. e-Poster.

9. Eber M, Park S, Hsu F-C, **Shiozawa Y**. Osteoblasts Derived from Mouse Mandible Enhance Tumor Growth of Prostate Cancer More Than Osteoblasts Derived from Long Bone. American Society for Bone and Mineral Research (ASBMR) 2020 Annual Meeting, Virtual, September 11-14, 2020. e-Poster.

10. Widner DB, Eber M, Park S, **Shiozawa Y**. Skeletal Muscle Resident Mast Cells as a Potential Novel Biomarker for Cancer-Associated Cachexia. Cancer Cachexia 2020, Virtual, September 10-11, 2020. e-Poster.

(2020-2021)

Nothing to report.

Website(s) or other Internet site(s)

Nothing to report.

Technologies or techniques

Nothing to report.

Inventions, patent applications, and/or licenses

Nothing to report.

Other products

Nothing to report.

7. PARTICIPANTS & OTHER COLLABORATING ORGANIZATIONS

What individuals have worked on the project?

Name: Yusuke Shiozawa
Project Role: PI, W81XWH-17-1-0541
Researcher Identifier (e.g. ORCID ID): orcid.org/0000-0001-9814-9230
Nearest person month worked: 3
Contribution to Project: Dr. Shiozawa is an Assistant Professor in the Department of Cancer Biology. He has extensive experience in the study of prostate cancer bone metastasis, and will provide oversight of the entire program including development and implementation of all policies, procedures, and processes. In this role, Dr. Shiozawa will be responsible for the completion of the project and for ensuring that systems are in place to guarantee institutional compliance with US laws, including biosafety and animal research guidelines, data collection and analyses, and facilities. Dr. Shiozawa will supervise other personnel on the project to ensure timely and effective studies.
Funding Support: Department of Defense, TEVA Pharmaceuticals, National Cancer Institute

Name: Christopher Peters
Project Role: Partnering PI, W81XWH-17-1-0542
Researcher Identifier (e.g. ORCID ID):
Nearest person month worked: 1.8
Contribution to Project: Dr. Peters is an Assistant Professor in the Department of Anesthesiology. Dr. Peters' research interests are in central and peripheral mechanisms of pain chronicity including postsurgical, bone cancer and chemotherapy induced pain and neuropathy. Dr. Peters will be responsible for supervising and training personnel in evoked and non-evoked bone cancer pain behavioral assays. As part of Aims 1 and 3, Dr. Peters will assist with *in vivo* validation of a viral vector approach for sensory neuron selective knockdown of ATR and CGRP. He will also assist with histological and immunohistochemical analysis of skeletal tissue as part of Aims 1-3. Dr. Peters has over 15 years of experience working with preclinical models of skeletal pain including rat and mouse models of bone cancer. He has extensive experience with the behavioral analysis, immunohistochemistry, biochemical analysis and fluorescent, brightfield, and confocal microscopic imaging required for this project. He will meet with Dr. Shiozawa on a weekly basis to discuss progress on projects related to this Partnering PI Prostate Cancer Research Idea Development Award.
Funding Support: National Institutes of Health, Department of Defense

Name: Fang-Chi Hsu
Project Role: Co-Investigator, W81XWH-17-1-0541
Researcher Identifier (e.g. ORCID ID):
Nearest person month worked: 0.6
Contribution to Project: Dr. Hsu is a Professor in the Department of Biostatistical Sciences. She will work closely with Dr. Shiozawa and the team to analyze the results of the project.
Funding Support: National Institutes of Health, Department of Defense

Name: Christopher Thomas
Project Role: Co-Investigator, W81XWH-17-1-0541
Researcher Identifier (e.g. ORCID ID):
Nearest person month worked: 0.12

Contribution to Project: Dr. Thomas is an Associate Professor in the Department of Hematology/Oncology. On this project, he will assist Dr. Shiozawa's laboratory in tissue procurement, experimental design, and scientific strategy.
Funding Support: Department of Defense

Name: Debra Diz
Project Role: Co-Investigator, W81XWH-17-1-0541
Researcher Identifier (e.g. ORCID ID):
Nearest person month worked: 0.6
Contribution to Project: Dr. Diz is the Co-Director of the Cardiovascular Sciences Center and Professor, Department of General Surgery. Her research focuses on cardiovascular neuroscience and neuropharmacology related to the effects of angiotensin II on neuropeptide and release of other transmitters in the context of the renin-angiotensin-system in aging and metabolic regulation. On this project, she will assist Dr. Shiozawa's laboratory in radio binding assay.
Funding Support: National Institutes of Health, Department of Defense

Name: Mark Chappell
Project Role: Co-Investigator, W81XWH-17-1-0541
Researcher Identifier (e.g. ORCID ID):
Nearest person month worked: 0.6
Contribution to Project: Dr. Chappell is a Professor in the Department of General Surgery and member of the Cardiovascular Sciences Center. He is an expert in the assessment of the renin-angiotensin-system (RAS) components and is interested in the RAS in hypertension, diabetes, fetal programming and women's health issues. On this project, he will assist Dr. Shiozawa's laboratory in radioimmnunoassay.
Funding Support: National Institutes of Health, Department of Defense

Name: Thomas Jeff Martin
Project Role: Co-Investigator, W81XWH-17-1-0542
Researcher Identifier (e.g. ORCID ID):
Nearest person month worked: 0.6
Contribution to Project: Dr. Martin is a Professor in the Department of Anesthesiology and Physiology & Pharmacology. Dr. Martin's research interests are on mechanisms of opioid abuse particularly in the setting of chronic pain. He has been instrumental in the development of operant based behavioral assays to monitor the effects of persistent pain on complex animal behaviors. Dr. Martin will assist with training, implementation and analysis of running wheel assays to assess progressive disability in mice inoculated with bone cancer as part of studies outlined in Aims 1-3.
Funding Support: National Institutes of Health, Department of Defense

Name: Juan Miguel Jimenez-Andrade
Project Role: Visiting scholar, W81XWH-17-1-0542
Researcher Identifier (e.g. ORCID ID):
Nearest person month worked: 3
Contribution to Project: Dr. Jimenez-Andrade is a Professor in the Autonomous University of Tamaulipas in Reynosa, Mexico. Dr. Jimenez-Andrade's laboratory research is focused on mechanisms of skeletal pain and osteoporosis. He assumed responsibility for performing microCT imaging and analysis as part of experiments in Aims 1-3. The subaward initially established with Ted Bateman at UNC was transferred to Dr. Jimenez-

Andrade's institution effective September 2019. Additionally, he will assist with immunohistochemical analysis of decalcified bone sections as part of studies under this proposal.
Funding Support: Department of Defense, National Institutes of Health, UC MEXUS-CONACYT

Has there been a change in the other active support of the PD/PI(s) or senior/key personnel since the last reporting period?

Nothing to report.

What other organizations have been involved as partners?

The Autonomous University of Tamaulipas at Reynosa Mexico

8. SPECIAL REPORTING REQUIREMENTS:

QUAD CHARTS.

9. APPENDICES:

The original copies of manuscript are attached.

Molecular crosstalk: bone metastatic prostate cancer and nociceptive neurons

PC160455, PC160455P1

W81XWH-17-1-0541, W81XWH-17-1-0542

PI: Yusuke Shiozawa, Christopher Peters **Org: Wake Forest University Health Sciences** **Award Amount:** $500,001 (Shiozawa) $496,403 (Peters)

Study/Product Aim(s)

- **Aim 1: Determine how disseminated prostate cancer is involved in development of cancer-induced bone pain.**
- **Aim 2: Define the intracellular signaling pathways in peripheral nerves stimulated by disseminated prostate cancer.**
- **Aim 3: Determine the influence of nociceptive neurons on (a) tumor outgrowth in the bone and (b) cancer-induced bone pain.**

Approach

The goal of this project is to determine the roles of the interaction between bone metastatic prostate cancer and sensory nerves in cancer-induced bone pain and bone metastatic growth using our innovative mouse models that enable us to measure cancer bone pain, tumor growth, and bone dynamics within the same animals. In addition, using biopsy samples from patients, we will verify the results from the animal experiments.

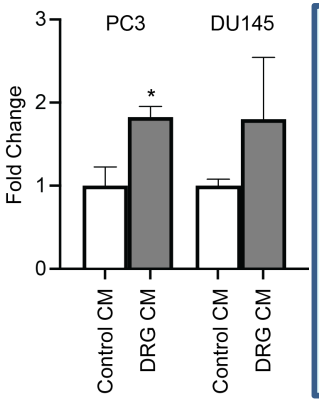

Sensory neurons enhance prostate cancer proliferation.
Prostate cancer cells (PC3 and DU145) and murine primary sensory neuron cells were co-cultured on the Bidi-co-culture plate, which allows wells to exchange medium, for 48h. Thereafter, numbers of cancer cells were measured with crystal violet staining method. Growth medium was used as control. Mean ± SEM. $^{*}p \leq 0.05$vs. Control CM treatment (Student's *t*-test).

- We found that murine primary sensory nerves enhance the proliferation of prostate cancer cells in vitro.

Timeline and Cost

Activities CY	17	18	19	20
Aim 1 (Animal Studies)				
Aim 2 (Animal Studies)				
Aim 2 (Bone sample analyses)				
Aim 3 (Animal Studies)				
Estimated Budget ($K)	**$100**	**$325**	**$325**	**$246**

Updated: 10/29/2021

Goals/Milestones (Example)

CY17 Goal – Team development

☑ Set up and organize the monthly meeting

CY18 Goals – Animal studies

☑ Develop the technique to manipulate gene in nerves with vector

☑ Determine the roles of nerves in cancer progression

CY19 Goal – Bone biopsy sample analyses/Animal studies

☑ Develop the system to assess bone biopsy samples

☑ Determine the roles of nerves in cancer progression

☑ Determine the roles of cancer in cancer-induced bone pain

CY20 Goal – Bone biopsy sample analyses/Animal studies

☑ Determine the roles of cancer in cancer-induced bone pain

☑ Assess the nerve/cancer interaction in bone biopsy samples

Comments/Challenges/Issues/Concerns

None

Budget Expenditure to Date

Projected Expenditure: $996K

Actual Expenditure: $996K

Journal of Bone Oncology 26 (2021) 100346

Contents lists available at ScienceDirect

Journal of Bone Oncology

journal homepage: www.elsevier.com/locate/jbo

Osteoblasts derived from mouse mandible enhance tumor growth of prostate cancer more than osteoblasts derived from long bone

Matthew R. Eber [a], Sun H. Park [a], Kelly F. Contino [a], Chirayu M. Patel [a], Fang-Chi Hsu [b], Yusuke Shiozawa [a,*]

[a] Department of Cancer Biology and Wake Forest Baptist Comprehensive Cancer Center, Wake Forest University Health Sciences, Winston-Salem, NC 27157, USA
[b] Department of Biostatistics and Data Science and Wake Forest Baptist Comprehensive Cancer Center, Wake Forest University Health Sciences, Winston-Salem, NC 27157, USA

ARTICLE INFO

Article history:
Received 6 May 2020
Revised 12 December 2020
Accepted 14 December 2020

Keywords:
Prostate cancer
Osteoblasts
Mandible osteoblasts
Hind limb osteoblasts
Bone metastasis
Tumor cell proliferation

ABSTRACT

Prostate cancer (PCa) metastasizes to bone, where the bone marrow microenvironment controls disease progression. However, the cellular interactions that result in active bone marrow metastases are poorly understood. A better understanding of these interactions is critical to success in the pursuit of effective treatments for this life ending disease. Anecdotally, we observe that after intracardiac injection of PCa cells, one of the greatest tools to investigate the mechanisms of bone-metastatic disease, animals frequently present with mandible metastasis before hind limb metastasis. Therefore, in this study, we investigated whether the bone cells derived from the mouse mandible influence PCa progression differently than those from the hind limb. Interestingly, we found that osteoblasts harvested from mouse mandibles grew faster, expressed more vascular endothelial growth factor (VEGF), increased vascularity and formed more bone, and stimulated faster growth of PCa cells when cultured together than osteoblasts harvested from mouse hind limbs. Additionally, these findings were confirmed *in vivo* when mouse mandible osteoblasts were co-implanted into mice with PCa cells. Importantly, the enhancement of PCa growth mediated by mandible osteoblasts was not shown to be due to their differentiation or proliferation activities, but may be partly due to increased vascularization and expression of VEGF.
© 2020 The Author(s). Published by Elsevier GmbH. This is an open access article under the CC BY-NC-ND license (http://creativecommons.org/licenses/by-nc-nd/4.0/).

1. Introduction

Prostate cancer (PCa) is deadly when it metastasizes to bone, often years after a patient is cured of the primary disease. These metastases are believed to originate from disseminated tumor cells (DTCs) shed from the primary tumor that made their way to the bone marrow and became dormant. Once in the bone marrow, progression of dormant DTCs in the bone is directed by influences from the bone marrow microenvironment. Still, a full understanding of the more complex interactions that result in active bone marrow metastases remains elusive. Our group recently discovered that early in the metastatic process, PCa cells target and commandeer the hematopoietic stem cell (HSC) specific marrow microenvironment, or HSC niche, using mechanisms similar to those involved in HSC homing to bone [1]. Osteoblasts are a major component of the HSC niche and have been shown to participate in the regulation of HSC homing and quiescence (or dormancy) [2–5]. Interestingly, DTCs also utilize osteoblasts to establish early colonization within the marrow [1,6]. Thereafter, the DTCs lie dormant within the osteoblastic niche until they begin to proliferate again, controlled by mechanisms still poorly understood, and eventually develop into full-blown metastases [7].

A tool frequently used to investigate the mechanisms of metastasis is the intracardiac injection mouse model. After a small volume of cancer cells is inoculated into the left ventricle of the mouse heart, the circulatory system becomes flooded with cancer cells that eventually colonize organs of preference, such as bone. As expected, this model consistently results in long bone metastases, including lesions in the femur and tibia. However, mandible metastases are also frequently observed in this model [8]. This appears to be a phenomenon unique to this model, as metastasis to the human mandible is uncommon for solid tumors known to metastasize to the bone, such as PCa [9]. Anecdotally, using this model we have found that sometimes the only site of metastasis is the mandible, and that in animals with multiple bone metastatic lesions, many demonstrate faster growth in the mandible than those in the hind limbs of the same animal (unpublished observations). These findings raise the question whether the bone marrow microenvironment of the mandible stimulates the growth of DTCs more than that of the hind limbs. One difference between bone cells derived from mandible and long bones that has been documented is their proliferative and differentiation potential. Indeed,

* Corresponding author at: Department of Cancer Biology, Wake Forest University Health Sciences, Medical Center Blvd., Winston-Salem, NC 27157-1082, USA.
E-mail address: yshiozaw@wakehealth.edu (Y. Shiozawa).

https://doi.org/10.1016/j.jbo.2020.100346
2212-1374/© 2020 The Author(s). Published by Elsevier GmbH.
This is an open access article under the CC BY-NC-ND license (http://creativecommons.org/licenses/by-nc-nd/4.0/).

osteoblasts derived from rat mandible bone marrow grew faster and formed more bone *in vivo* than those differentiated from long bone marrow [10]. The same effects were seen in human tissue cultures of mandible and iliac marrow derived osteoblasts [11]. Interestingly, it has recently been revealed that different subpopulations of osteoblasts contribute differently to bone metastatic progression [12]. Therefore, we hypothesized that osteoblasts harvested from mouse mandible bones would enhance the growth of PCa cells when they interact with each other, more than those harvested from hind limb bones.

In this study, we found that osteoblasts harvested from mouse mandible bones grew faster than those harvested from hind limb bones, similar to the reports of osteoblasts derived from rat and human tissues. Additionally, osteoblasts harvested from mouse mandibles expressed higher levels of vascular endothelial growth factor (VEGF). Moreover, when these osteoblasts were co-cultured with PCa cells, osteoblasts harvested from mouse mandibles significantly increased the growth of PCa cells compared to osteoblasts harvested from hind limbs. Most importantly, these findings were confirmed *in vivo*, and immunofluorescent staining of pathological specimens revealed that vascularity of mandible osteoblast implants was greater than hind limb osteoblast implants.

2. Materials and methods

2.1. Cell culture

Human PCa cell line PC-3 [American Type Culture Collection (ATCC), Manassas, VA, Cat #: CRL-1435] and DU145 cells (ATCC, Cat #: HTB-81) were transformed to stably express green fluorescent protein (GFP) and firefly luciferase (PC3-GFP-luc, and DU145-GFP-luc) by transduction with a lentivirus (Lenti-GF1-CMV-VSVG) generated by the University of Michigan Vector Core. The transduced cells were sorted for GFP positive cells at the Wake Forest Baptist Comprehensive Cancer Center Flow Cytometry Shared Resource using an Astrios EQ (Beckman Coulter, Pasadena, CA), expanded and frozen at low passage (<10). The growth media for PC-3 and DU145 was RPMI 1640 (Gibco, Gaithersburg, MD, Cat #: 11875093) supplemented with 10% FBS (Sigma-Aldrich, St. Louis, MO, Cat #: F2442), 1% Penicillin-Streptomycin (Gibco, Cat #: 15140122), and 1% L-Glutamine (Gibco, Cat #: 25030081). Murine calvarial pre-osteoblast cell line MC3T3-E1 Subclone 4 (ATCC, Cat #: CRL-2593) were cultured with MEMα without nucleosides (Gibco, Cat #: 12561056) supplemented with 10% FBS, 1% Penicillin-Streptomycin, and 1% L-Glutamine. Before supplementation, this formulation of MEMα already contains 50 mg/L Ascorbic Acid, and therefore no additional Ascorbic Acid was required. Cells were incubated at 37°C, 5% CO_2, and 100% humidity and were routinely passaged when no more than 80% confluent.

2.2. Animal care and use certification

All animal studies were approved by the Institutional Animal Care and Use Committee (Protocol A18-036) at Wake Forest University Health Sciences.

2.3. Intracardiac PCa inoculation and imaging of tumor growth

DU145-GFP-Luc (1 x 10^6 cells/100 μL of PBS) cells were injected into immunocompromised Athymic Nude mice (Charles River Laboratories, Wilmington, MA, Cat #: 490) by left ventricular intracardiac injection, as previously described [13]. To monitor cancer growth, luciferase signal was followed at least once a week for 10 weeks using the IVIS Lumina Series III system and Living Image software (Xenogen, Alameda, CA).

2.4. Primary murine osteoblast culture

Hind limbs and mandibles were dissected from 5-week old male C57BL6/J mice (The Jackson Laboratory, Bar Harbor, ME, Cat #: 000664). Epiphyses from the femurs and tibias were cut and the marrow was removed by centrifugation, as previously described [14]. Briefly, an 18g hole was bored into the bottom of a 0.6 mL microcentrifuge tube with a needle, and then the tube was placed in a 1.7 mL microcentrifuge tube. The diaphyses of the bones were placed in the smaller tube, and the apparatus was then centrifuged at max speed for 30 sec. Afterward, the bone fragments remained in the upper 0.6 mL tube, and the marrow was pelleted in the bottom 1.7 mL tube. The empty diaphyses were placed into a 10 cm dish in HBSS, no calcium, no magnesium, no phenol red (Gibco, Cat #: 14175095) supplemented with 1% Penicillin-Streptomycin and minced into smaller pieces using a scalpel. The molars, incisors and dental pulp of the mandibles were removed and the remaining pieces (ascending ramus containing the coronoid, condylar and angular processes) were placed into a 10 cm dish in HBSS supplemented with 1% Penicillin-Streptomycin and minced into smaller pieces using a scalpel. After forceful washing to remove all marrow, a 10 min Trypsin-EDTA digestion was performed on the bone and mandible pieces at 37°C. Complete MEMα [MEMα without nucleosides supplemented with 10% FBS, 1% Penicillin-Streptomycin, 1% L-Glutamine, and 10nM dexamethasone (Sigma-Aldrich, Cat #: D4902) [15]] was then added to the explant cultures and the mature bone cells were allowed to migrate out of the bone and mandible pieces and expand for two weeks. In some cases, the cells were grown in bone mineralization medium (BMM) to induce further osteoblastic differentiation and mineral deposition: this media is complete MEMα supplemented with 0.5mM L-Ascorbic acid (Sigma, Cat #: A5960), 2mM β-Glycerophosphate disodium salt hydrate (Sigma-Aldrich, Cat #: G9422), and 10mM HEPES (Thermo Fisher Scientific, Hampton, NH, Cat #: BP299). The control media for BMM is complete MEMα supplemented with 10mM HEPES (vehicle).

2.5. MTT assay

Cells were seeded at a density of 4 x 10^3 cells/100 μL complete MEMα into each well of a 96-well plate and incubated for 1, 3, and 5 days. To measure relative cell numbers, 500 μg/mL MTT (Tocris Bioscience, Minneapolis, MN, Cat #: 5224) was added to each well and incubated for 4 h. The reaction was halted, and the formazan precipitate was dissolved by the addition of an equal volume of 10% SDS in 0.01 M HCl (10 g/100 mL). The plate was incubated at 37°C, 5% CO2, and 100% humidity overnight and read on a plate reader at 560 nm with a background measurement at 650 nm.

2.6. In vitro mineralization assay

Cells were seeded at a density of 1 x 10^5 cells/250 μL complete MEMα into each well of a 24-well plate and incubated for 24 h. The complete MEMα was then replaced with 500 μL fresh complete MEMα and the plate was incubated for 48 h. The media was replaced with vehicle or BMM and incubated for 72 h. This process was continued every other day for a total of 14 days from first treatment. Half of the wells were harvested for mRNA. The remaining wells were stained with Alizarin Red S (ARS) to quantify total mineralization. Briefly, cells were fixed with 10% neutral buffered formalin for 5 min at room temperature and then stained with 2% ARS (Sigma-Aldrich, Cat #: A5533-25G) at pH 4.1 in water (2 g/100 mL) for 30 min at room temperature. Excess stain was

washed out in running tap water until the water ran clear. Representative images were captured on an EVOS inverted microscope (Thermo Fisher Scientific). Stain from each wells was quantified after lysing entire contents as described elsewhere using an acetic acid extraction method and plate reader absorbance at 405 nm [16].

2.7. Real Time qPCR

Confluent and multilayered osteoblastic cells were lysed, and RNA was harvested using the RNeasy Plus Mini Kit (Qiagen, Germantown, MD, Cat#: 74134). The RNA concentrations were determined and subsequently normalized between samples prior to cDNA generation using Invitrogen SuperScript II Reverse Transcriptase (Invitrogen, Carlsbad, CA, Cat#: 18064022). Real time qPCR was performed using TaqMan Gene Expression Master Mix (Applied Biosystems, Foster City, CA Cat#: 4369016) and Taqman Gene Expression Assays [Applied Biosystems, Cat#: 4331182, Assay IDs: Mm03413826_mH (*Bglap*: Osteocalcin, OCN), Mm00436767_m1 (*Spp1*: Osteopontin, OPN), Mm00437306_m1 (*Vegfa*: vascular endothelial growth factor, VEGF), Mm00441906_m1 (*Tnfsf11*: RANKL), Mm00435454_m1 (*Tnfrsf11b*: Osteoprotegrin, OPG), Hs00921372_m1 (*TNFRSF1*: RANK), Hs02786624_g1 (*GAPDH*), and Mm99999915_g1 (*Gapdh*)] on the Bio-Rad CFX Connect instrument (Hercules, CA). Data is presented as relative gene expression using the delta-delta Ct method, with *Gapdh* used as the reference gene.

2.8. Co-culture assay

Primary cells, or MC3T3-E1 cells, were seeded at a density of 2 x 10^4 cells/100 μL complete MEMα into each well of a 96-well plate and incubated for 24 h. In some cases, cells were growth arrested for 2.5 h with 10 μg/mL mitomycin-C (Sigma-Aldrich, Cat #: 10107409001). Thereafter, cancer cells were seeded on top of the bone cells or by themselves in new 96-well plates, at a density of 2 x 10^3 cells/100 μL complete MEMα. Plates were incubated for 48 h and the media replaced with vehicle or BMM, and incubated for 1, 3, and 5 days, with media replacement at each time point. To monitor cancer growth in real time, luciferase signal was checked before each media replacement using the IVIS system, after addition of 200μg/mL D-Luciferin (PerkinElmer, Waltham, MA, Cat #:122799) and 10 min incubation at 37°C.

2.9. Ossicle implantation

1×10^5 DU145-GFP-luc and/or 1 x 10^6 primary cells [mandible osteoblasts (MaOBs) or hind limb osteoblasts (HLOBs)] were suspended in 10 μL BMM in individual microcentrifuge tubes (inoculum tube) and stored on ice until implantation. Under sterile conditions, absorbable gelatin sponges (Ethicon, Somerville, NJ, Cat #: 1973) were cut into small cubes (~5 mm^3) and placed in a petri dish containing BMM on ice until implantation. Mice were anesthetized, backs shaved if necessary, and the surgical site was prepared using betadine. Blunt tipped scissors were used to create a small incision (~1cm) in the dorsal skin parallel to the spine, and the scissors were used to create subcutaneous pouches on both sides of the incision. Using fine tipped forceps, a sponge piece was removed from the petri dish, excess liquid was blotted using sterile gauze, and then seeded by placing it in the bottom of an inoculum tube and allowing it to absorb the entire inoculum. The seeded sponge was then implanted into one of the subcutaneous pouches. Each animal received an implant seeded with HLOBs in one pouch and an implant with MaOBs in the opposite pouch. The incision was closed with surgical staples, which were removed after 7 days. Animals implanted with tumor seeded cells were athymic nude mice and animals implanted with only primary cells were C57BL6/J (male, 5 weeks old). In order to monitor cancer growth in co-culture seeded ossicles *in vivo*, luciferase signal was followed at least once a week for 20 weeks using the IVIS system, whereas primary cell only seeded ossicles were grown for 7 weeks *in vivo*.

2.10. Tissue processing

After euthanasia, the implants were dissected and placed in 10% neutral buffered formalin for 24 h at 4°C under agitation. They were then radiographed using the MultiFocus 10x15 Digital Radiography System (Faxitron Bioptics, Tucson, AZ). Radiographs were analyzed using ImageJ software (NIH, Bethesda, MD) for densitometry. Briefly, tissue was outlined using the freehand tool and Max Gray values were determined for each implant. Next, the implants were placed in cassettes and decalcified for 14 days in 10% ethylenediaminetetraacetic acid (EDTA), with fresh solutions replaced on day 7. The tissues were then cryopreserved in 30% sucrose for 48 h. They were halved with a razor blade and one half of each tissue was arranged in plastic molds containing optimal cutting temperature (OCT) media and frozen on dry ice. Using a cryostat, 10 and 20 μm sections were made and stored at -80°C. The other tissue halves were processed for paraffin embedding and sectioned on a microtome at 5 μm sections. Hematoxylin and Eosin (H&E) staining was performed on sections, as well as immunohistochemistry (IHC) for Ki67 (Abcam, Cambridge, MA, Cat#: ab16667), and immunofluorescence (IF) for Osteocalcin (Takara Bio USA, Mountain View, CA, Cat#: M173), Pan-cytokeratin (Novus Biologicals, Centennial, CO, Cat #: NB600-579SS), Endomucin (Santa Cruz Biotechnology, Dallas, TX, Cat#: sc-65496), VEGF (Santa Cruz Biotechnology, Cat#: sc-7269), and CD31 (R&D Systems, Minneapolis, MN, Cat #: AF3628) as previously described [17]. Antigen retrieval was performed using Biogenex DeCal Retrieval Solution (Biogenex, San Ramon, CA, Cat#: HK089-5K) before incubating with the primary antibody at a concentration of 1:500 overnight at 4°C. Sections were then labeled with secondary rabbit antibody (Biogenex, Cat#: HK336-5R), Vectastain Elite ABC HRP kit (Vector, Burlingame, CA, Cat#: PK-6100) and DAB Peroxidase (HRP) Substrate Kit (Vector, Cat#: SK-4100). Slides were mounted in permanent mounting media and scanned on a NanoZoomer slide scanner (Hamamatsu, Japan) at 40x magnification. Quantitative analysis was performed using Visiopharm software (Westminster, CO) and an APP designed to automatically count DAB and hematoxylin alone positive nuclei, as well as determine tissue section area on the entire slide.

2.11. Statistical analysis

Metastatic tumor growth was measured by bioluminescent imaging (BLI), and radiance values were log transformed in order to satisfy the conditional normality assumption. The mean and standard error of the mean (SEM) of log transformed radiance values were calculated by time and location of metastatic lesions (mandible vs. hind limb). For exploratory purposes, comparisons of log transformed radiance values between locations at each time point were performed using the paired Student's t-tests. Mean differences in log transformed radiance between locations were also estimated using the mixed effects model with time, location, and interaction between time and location included in the model. The advantage of using this model was that all data were analyzed simultaneously, resulting in more efficient estimates. The hypothesis test for location effect at each time point was performed using a contrast. The nested (location within each mouse) random intercepts were used to take into account the correlated structure (e.g., repeated measures over time; measures at different locations in

the same mouse). Sub-analysis of the same data was performed to compare metastasis-free survivals, as measured with a 75% signal cut off. Event time was defined as the time from the beginning of the study to the initial endpoint ($\geq$ the 75th percentile of log transformed radiance) and censoring time as the time from the beginning of the study to the last assessment or death. The Kaplan-Meier survival curves for the initial endpoint by location were plotted. The comparison between the two survival curves were performed using the Cox proportional hazards model with robust sandwich estimates to take into account the correlated structure (e.g., different locations in the same mouse). The same statistical approaches were applied to analyses of tumors co-cultured with primary cells (MaOBs or HLOBs).

The distributions for the other outcome measures such as gene expression and OD were confirmed to be normal. The means and SEM of the outcome measures were calculated by tissue origin (mandible vs. hind limb) and by treatment (vehicle vs. BMM), and comparisons of the outcome measures were performed using the unpaired Student's t-test. The means and standard errors of the tissue section areas and of MaOB or HLOB ossicles were calculated and compared using the paired Student's t-test.

The comparison of log transformed average radiance between the combination of primary cells (MaOBs vs. HLOBs) and treatment (vehicle vs. BMM) at each time point was performed using the analysis of variance (ANOVA) for exploratory purpose. Mean differences in log transformed radiance between primary cells and treatments at each time point were also estimated using the mixed effects model with time, location, treatment, and two-way and three-way interactions included in the model. If higher order interactions were not statistically significant, they were removed from the model. For PC3 co-culture analyses, the interaction between primary cells and time as well as the interaction between treatment and time were included in the model. For DU145 co-culture analyses, only the interaction between primary cells and time was included in the model. The random intercept was used to handle repeated measurements over time. The hypothesis tests for primary cell effect and BMM effect at each time point were performed using contrasts. All the analyses were performed using the GraphPad Prism statistical program (GraphPad Software, San Diego, CA) and the SAS software (SAS Inc, Cary, NC) with significance at $P \leq 0.05$.

3. Results

3.1. Intracardiac injection results in lesions in the mandibles before the hind limbs.

Since we have anecdotally found that mandible metastases occur faster than hind limb metastases in mice following intracardiac injection of PCa cells, we sought to examine more detailed metastatic patterns and tumor growth capacities of PCa cells in the intracardiac model. To do so, human PCa cell line DU145-GFP-luc cells were inoculated intracardially into immunocompromised athymic nude mice. When the bioluminescent imaging (BLI) signals of nude mice inoculated with DU145-GFP-luc were followed, detectable tumors in the mandibles were significantly brighter, and therefore larger in size than those in the hindlimbs at day 29, but over time signals at both sites became similar (Fig. 1A&B). Curiously, the BLI signals of the mandibles actually begin to decrease after day 29, which might be explained by tumor necrosis or hypoxic environments associated with fast-growing tumors [18]. Sub-analysis of the same data was performed to compare metastasis-free survivals, as measured with a 75% signal cut off, and the onset of metastasis in the mandible appeared to occur sooner than the hindlimb, although not statistically significant (Fig. 1C).

3.2. Cells derived from mandible and hind limb bone explants have osteoblastic characteristics.

To dissect out the differences between cells in the mandibles and hind limbs, we decided to compare the functions of osteoblasts from these two areas, since proliferation of PCa is known to be regulated in part by osteoblasts [19–21]. After cleared of soft tissue and bone marrow, bone pieces obtained from the mandibles and hind limbs (femurs and tibias) of adult C57BL6/J mice were minced (Fig. 2A) and cultured in media containing dexamethasone (10nM) to differentiate any remaining cells into osteoblasts [15]. After two weeks of culture, cells derived from the bone explants were assessed of their osteoblastic characteristics. Both cultures expressed relatively high levels of the osteoblastic markers Osteocalcin and Osteopontin (Fig. 2B&C). Basal expression of Osteocalcin and Osteopontin were both lower in the mandible cell cultures than the hind limb cultures, but the presence of both markers in vehicle-treated cells revealed that the cultured bone explant cells are mostly differentiated even without the use of differentiation supplements, unlike traditional bone marrow stromal cell culture preps (Fig. 2B&C). After treatment with known osteoblastic differentiation supplements L-Ascorbic acid and β-Glycerophosphate, the levels of these markers were significantly increased in both explant cultures, however cultures of mandible cells responded to L-Ascorbic acid and β-Glycerophosphate to a greater degree than cultures of hind limb cells (Fig. 2B&C). As vascular endothelial growth factor (VEGF) derived from osteoblasts, encoded by the mouse gene *Vegfa*, has been shown to be involved in osteoblast differentiation and mineralization [22], and VEGF is implicated in PCa migration to bone and growth through induction of angiogenesis [23], we tested whether *Vegfa* expression was increased in mandible cultures. Basal expression of *Vegfa* was higher in cultures of mandible cells than those of hind limb cells and was not significantly changed in response to L-Ascorbic acid and β-Glycerophosphate supplementation in either mandible or hind limb cultures (Fig. 2D). To further test osteoblastic functional capabilities, the mineralization potentials of these cells were evaluated using Alizarin Red S (ARS) staining. Both cells derived from mandible and hind limb explants were able to mineralize, as evidenced by ARS staining (Fig. 3A&B). Interestingly, cells from mandible explants showed more mineralization than cells from hind limb explants, regardless of L-Ascorbic acid and β-Glycerophosphate supplementation (Fig. 3B). We attribute this observation to the previous finding that differentiation supplements were not required for osteoblast marker expression in our bone explant cultures (Fig. 2B&C), and therefore, not required for mineralization either. Altogether, this suggests that the cells derived from mandible and hind limb bone explants have osteoblastic characteristics. Therefore, from here on, the cells derived from mandible and hind limb bone explants will be referred to as mandible osteoblasts (MaOBs) and hind limb osteoblasts (HLOBs), respectively.

3.3. Mandible osteoblasts form more bone than hind limb osteoblasts in vivo

To further confirm the osteoblastic characteristics of MaOBs and HLOBs, these cells were implanted together with gelatin scaffolds (ossicles) subcutaneously into C57BL6/J mice, and the ossicles were allowed to grow *in vivo* for 7 weeks. Radiographs of the resulting ossicles revealed that the MaOB seeded ossicles had more mineralization than HLOB seeded ossicles (Fig. 4A&B). The ossicles were decalcified and cryosectioned in order to perform immunofluores-

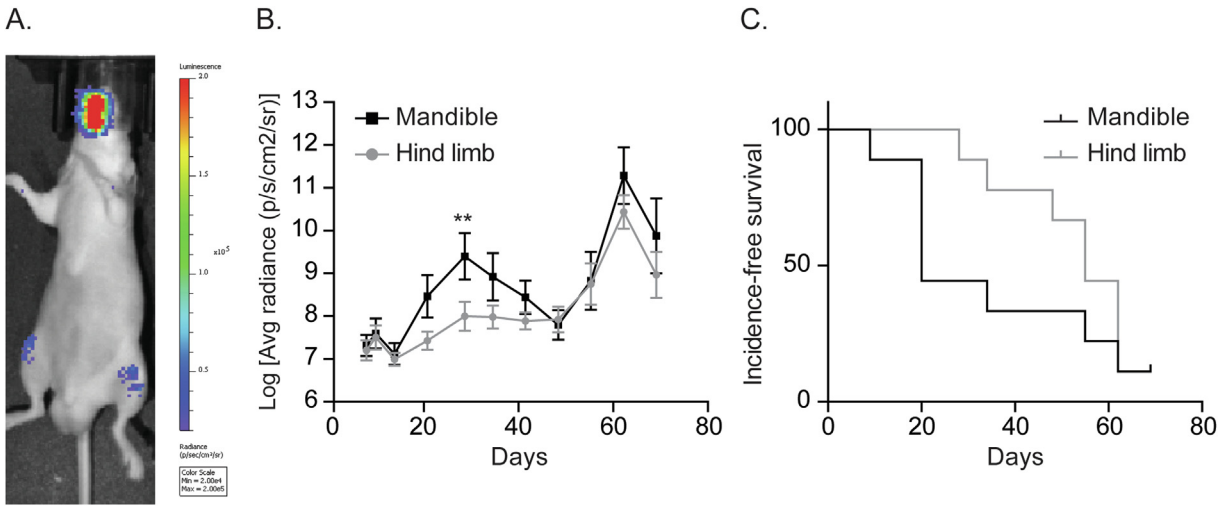

Fig. 1. Metastasis to mandible occurs first after intracardiac injection of PCa cells. Five-week old male nude mice were injected intracardially with 1 × 106 DU145-GFP-luc cells (n=8) and observed with bioluminescent imaging (BLI) for 10 weeks. (A) Representative image of a mouse at day 29 demonstrating brighter signal in the mandible than the hindlimbs. (B) All collected longitudinal BLI data after log transformation. Results displayed as Mean ± SEM. Mixed effects model. $^{**}p \leq 0.01$. (C) A 75% cut-off was employed to examine metastasis-free survival (mandible vs. hind limb). Cox proportional hazards model with robust sandwich estimates.

cence for Osteocalcin, hematoxylin and eosin (H&E) staining, and immunohistochemistry for Ki67 (Fig. 4C-E). In order to test whether the cells contained in the ossicles were still osteoblasts, immunofluorescence was performed on the cryosections for Osteocalcin. It is clear that the cells located near and on bone nodules in the ossicles remained Osteocalcin positive, and substantial Osteocalcin appeared to be deposited within the bone itself (Fig. 4C). H&E staining confirmed what was seen by radiograph, as evidenced by increased frequency of woven bone nodules in the MaOB seeded ossicles (Fig. 4D). Visiopharm software was used to automatically quantify tissue section area, and Ki67 positive and negative nuclei. MaOB seeded ossicles were no larger in area than HLOB ossicles (Fig. 4F), but contained a significantly greater number of total and proliferating cells, as evidenced by Ki67 nuclear positivity (Fig. 4G&H).

A possible explanation for the increased proliferation of MaOB cells *in vivo* could be increased vascularity of the MaOB ossicles due to higher levels of VEGF. Interestingly, we did observe greater immunostaining for the endothelial cell markers Endomucin and CD31 in the tissue surrounding and within the implants seeded with MaOBs, when compared to those seeded with HLOBs (Fig. 5A). Still, vascularity of all the implants appeared somewhat scarce and could explain why relative levels of bone formation in the implants appeared lower than other models which use bone marrow stromal cells as the inoculum for ossicle models of bone formation [15]. We also performed immunofluorescence for VEGF using ossicle cryosections as we found differential expression of *Vegfa* in our cell cultures *in vitro* (Fig. 2D). Strangely, we did not see VEGF staining in Osteocalcin positive MaOBs within the implants. However, we did detect VEGF near Osteocalcin positive MaOBs (Fig. 5B), but not HLOBs (data not shown). These results suggest that MaOBs seeded in ossicles may secrete VEGF to the tissues surrounding the implant.

3.4. Mandible osteoblasts support prostate cancer growth more than hind limb osteoblasts in vitro and in vivo

Our next attempt was then to determine whether there are differential effects between MaOBs and HLOBs on PCa growth. To address this question, human PCa cell lines PC3-GFP-luc and DU145-GFP-luc cells were seeded on top of MaOB or HLOB cells. After 3-5 days of co-culture, more PCa cells were observed on MaOBs than HLOBs using BLI (Fig. 6A&B). However, L-Ascorbic acid and β-Glycerophosphate supplement failed to induce further tumor proliferation (Fig. 6A&B), suggesting that osteoblastic mineralization was not the major cause of greater PCa proliferation mediated by MaOBs. Then, the changes in the relative amounts of viable cells during *in vitro* culture between MaOBs and HLOBs were compared. As previously reported in rat and human bones [10,11], the cultures containing MaOBs had more viable cells compared to those containing HLOBs (Fig. 6C), suggesting that MaOBs grew significantly faster than HLOBs. However, when mitomycin-C growth arrested MC3T3-E1 cells were cocultured using the same methods, PCa cells actually grew faster on top of growth arrested osteoblasts (Fig. 6D&E). These data suggest that the differences between PCa growth in culture with MaOBs vs. HLOBs are not likely due to baseline differences in mineralization or proliferation.

Next, DU145-GFP-luc cells were co-implanted with either MaOB or HLOB ossicles subcutaneously into athymic nude mice. Similar to what was seen *in vitro*, the growth of DU145-GFP-luc cells co-implanted with MaOB ossicles, as evidenced by significantly brighter BLI signals on the last five measurements, appeared to be greater than those co-implanted with HLOB ossicles (Fig. 7A&B). These results were significantly different despite the fact that one mouse had a much smaller MaOB co-implant tumor than the other four mice (Fig. 8A). With such a limited group size, this tumor cannot be considered an outlier, but it is the reason why the differences observed in the longitudinal data also seem limited (Fig. 7A&B). Sub-analysis of the same data was performed to compare incidence-free survivals, as measured with a 75% signal cut off, and tumors in the MaOB ossicles occurred significantly sooner than in the HLOB ossicles (Fig. 7C). These differences were consistent with *ex vivo* BLI analyses performed on the dissected tumors which again showed significantly brighter signal in the MaOB ossicles (Fig. 7D). As before, radiographs revealed that the MaOB seeded ossicles had more calcification than HLOB seeded ossicles (Fig. 8A&B). In order to test the composition of the cells contained in the co-implanted ossicles, immunofluorescence for pan-cytokeratin was performed on the cryosections of decalcified ossicles. Clearly, the implants with both MaOBs and HLOBs at 20 weeks contained PCa tumor cells (Fig. 8C). H&E staining and immunohistochemistry for Ki67 were also performed on the co-implanted ossicles to further determine their morphology and cell proliferation statues (Fig. 8D&E). Visiopharm software was used to auto-

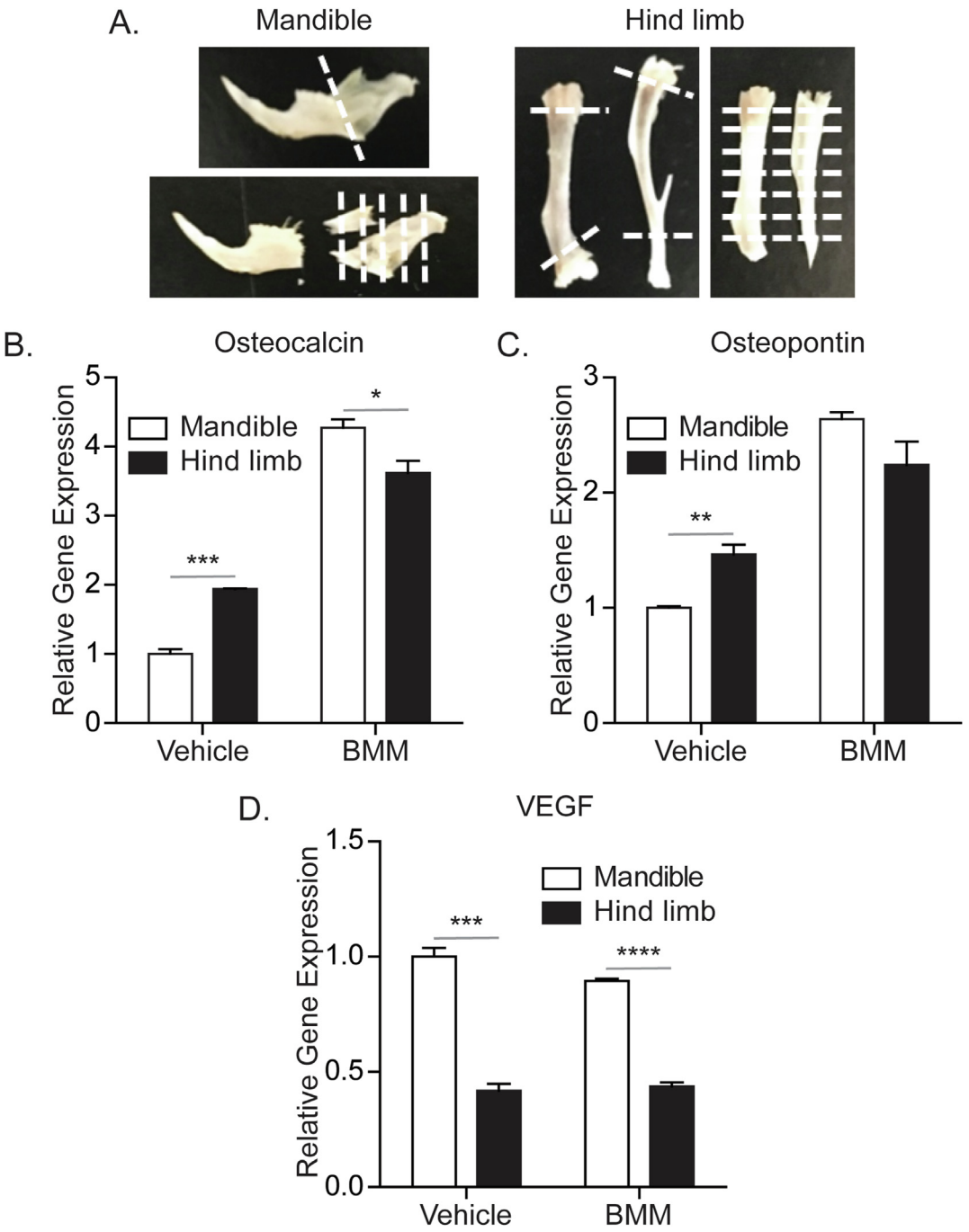

Fig. 2. Cells harvested from mandible and hind limb bones express osteoblast markers. Five-week old male C57BL6/J mice were euthanized, and mandibles and hind limbs were harvested. Mandible and hind limb cells were cultured with bone mineralization medium (BMM) (0.5mM L-Ascorbic acid, 2mM β-Glycerophosphate disodium salt hydrate, and 10mM HEPES) or vehicle (10mM HEPES) for 10 days. (A) Schematic of bone culture preparation: molars, incisors and dental pulp of the mandibles were removed and discarded; epiphyses from the femurs and tibias were cut and the marrow was removed by centrifugation; remaining pieces of the mandibles and femurs/tibias were minced into smaller pieces, digested with trypsin, and cultured and expanded for two weeks before experiments. (B) Relative gene expression of Osteocalcin (Bglap), normalized to vehicle treated mandible cell cultures. (C) Relative gene expression of Osteopontin (Spp1), normalized to vehicle treated mandible cell cultures. (D) Relative gene expression of vascular endothelial growth factor (VEGF), normalized to vehicle treated mandible cell cultures. Gapdh was used as reference gene. Delta-delta Ct method. Results displayed as Mean ± SEM. Unpaired Student's *t*-test. $^{*}p \leq 0.05$, $^{**}p \leq 0.01$, $^{***}p \leq 0.001$, $^{***}p \leq 0.0001$.

matically quantify tissue section area, and Ki67 positive and negative nuclei. MaOB seeded ossicles appeared larger in area than HLOB ossicles, although not quite significant (Fig. 8F), but contained a significantly greater number of total and proliferating cells, as evidenced by Ki67 nuclear positivity (Fig. 8G&H).

4. Discussion

In this study, we first demonstrated that in the intracardiac model of metastatic PCa, mandible bone lesions often occur before hind limb bone lesions, which is anecdotally well-recognized. We

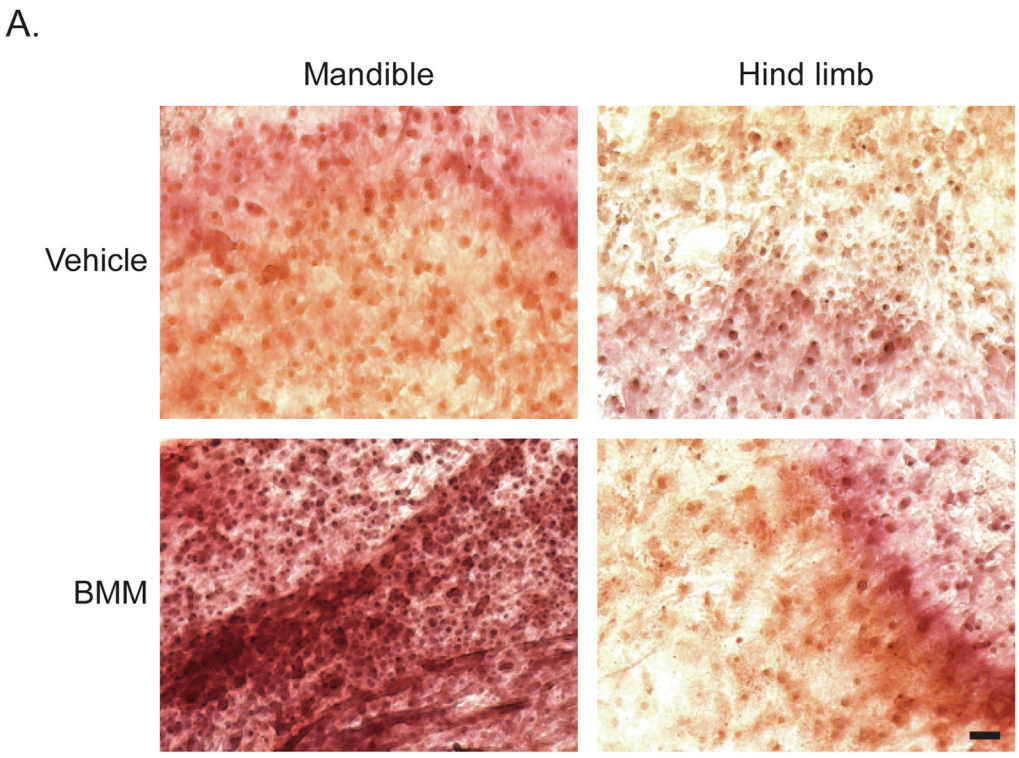

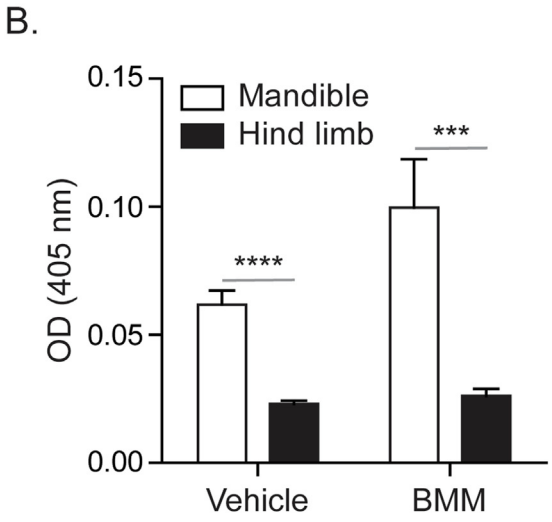

Fig. 3. Cells harvested from mandibles mineralize more than those from hind limbs. Mandible and hind limb cells were cultured with bone mineralization medium (BMM) (0.5mM L-Ascorbic acid, 2mM β-Glycerophosphate disodium salt hydrate, and 10mM HEPES) or vehicle (10mM HEPES) for 14 days. Cells were stained with 2% Alizarin Red S. (A) Representative Alizarin Red S image. Magnification 10x. Bar = 50 μm. (B) Residual stain from whole plates were extracted with acetic acid and read at 405 nm on a plate reader. Results displayed as Mean ± SEM. Unpaired Student's *t*-test. $^{***}p \leq 0.001$, $^{****}p \leq 0.0001$.

showed that cells derived from both the mandible and hind limb bones of mice have osteoblastic properties, and that MaOBs have a higher potential for osteoblastic differentiation than HLOBs both *in vitro* and *in vivo*. Interestingly, when PCa cells were co-cultured with these osteoblasts, PCa cells grew significantly faster in co-culture with MaOBs compared to HLOBs. Consistently, PCa cells co-implanted with MaOBs into animals grew faster and larger tumors than those co-implanted with HLOBs. Altogether, the data suggest that these differences may not be due to differences in mineralization status, as L-Ascorbic acid and β-Glycerophosphate supplementation failed to increase PCa growth *in vitro*, nor differences in osteoblast proliferation, as mitomycin-C growth arrest of osteoblasts actually increased PCa growth *in vitro*. However, the observations that MaOBs vascularize more *in vivo* and express significantly higher levels of *Vegfa in vitro* may be clues to a possible mechanism, although careful mechanistic studies must be performed in order to investigate this further.

The idea that there are different subpopulations of osteoblasts that exhibit different functions in the bone microenvironment has been discussed. For example, while mature osteoblasts form mineral deposits by differentiating osteocytes in healthy bone during homeostasis [24], immature osteoblasts are involved in the

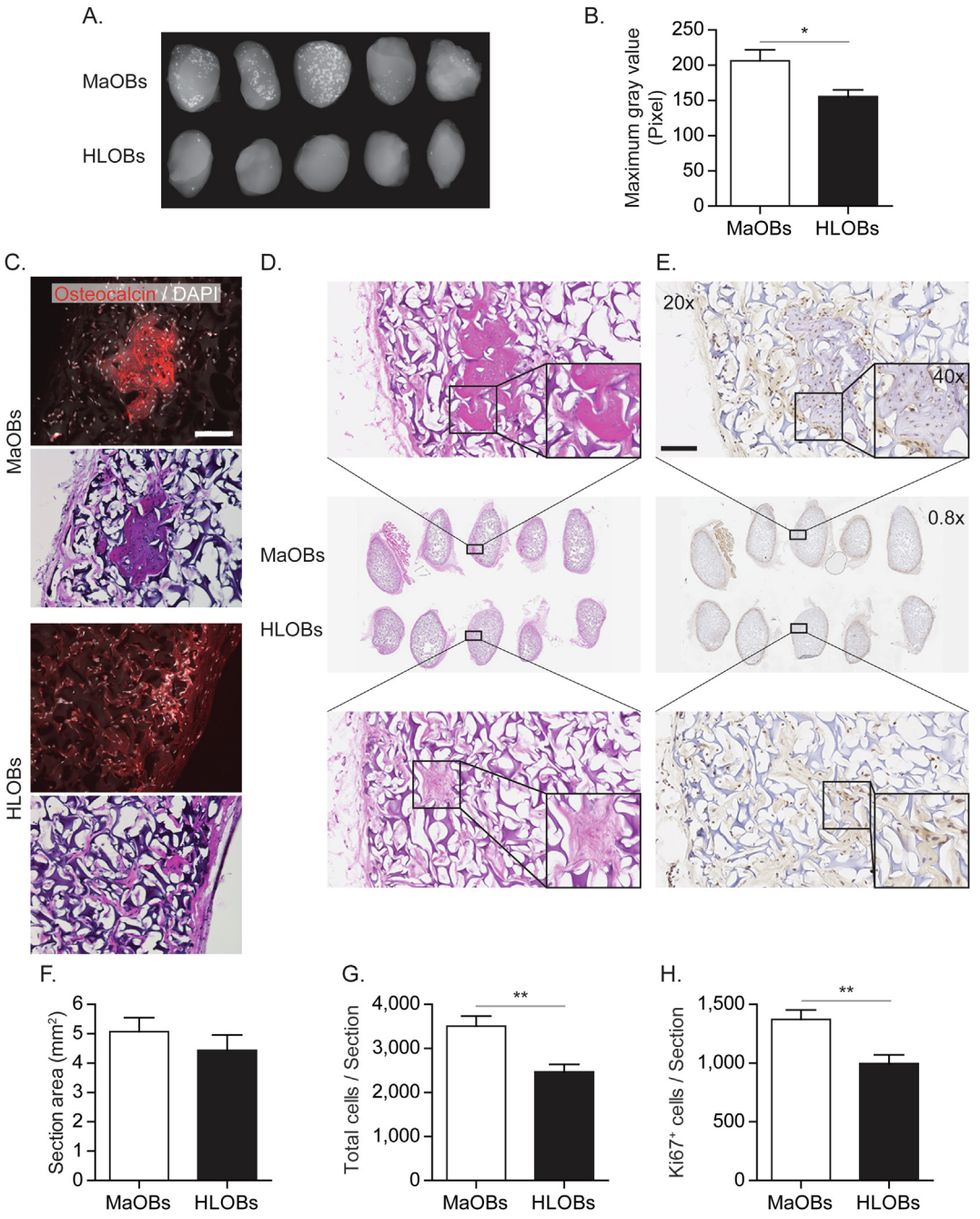

Fig. 4. Cells harvested from mandibles are more proliferative and form more bone than from hind limbs. 1×10^6 primary cells (MaOBs or HLOBs) were seeded onto absorbable gelatin sponges and implanted into subcutaneous pouches of 5-week old male C57BL6/J mice (n=5) and grown for 7 weeks *in vivo*. (A) After euthanasia, implants were dissected, fixed, and radiographed. (B) Densitometry quantification using ImageJ of (A). (C) Representative osteocalcin immunofluorescence and H&E image of (A). DAPI was used for nuclear staining. Magnification 20x. Bar = 100 μm. (D) Representative H&E image of (A). Bar = 100 μm. (E) Representative Ki67 immunohistochemical image of (A). Bar = 100 μm. (F-H) Automated quantification using Visiopharm software of (F) tissue section area, (G) total cells per tissue section, and (H) Ki67 nuclear positive cells per tissue section. Results displayed as Mean ± SEM. Paired Student's *t*-test. $^{*}p \leq 0.05$, $^{**}p \leq 0.01$.

process of bone resorption by activating osteoclasts through the production of receptor activator of NF-κB ligand (RANKL) [25,26]. In fact, when we tested relative gene expression of RANKL, we found that MaOBs express higher levels than HLOBs (1.00 ± 0.023 vs 0.097 ± 0.021), although they also expressed higher levels of osteoprotegerin (1.00 ± 0.12 vs 0.29 ± 0.014). Osteoprotegerin is a molecule that binds RANKL, inhibiting its ability to activate its receptor RANK on osteoclasts [27]. Similarly, intercellular adhesion molecule (ICAM)-1 positive osteoblasts, which are in G0/G1 phase of the cell cycle arrest, contributed more to osteoclastogenesis than bone formation, by interacting with monocytes [28]. This phenomenon is also known in the process of hematopoiesis. It has been demonstrated that the activated leukocyte cell adhesion molecule (ALCAM) positive/Sca-1 negative immature osteoblasts are responsible for maintenance of long-term reconstitution activity of HSCs [29]. On the other hand, it has been suggested that the major function of mature osteoblasts is to control the maintenance of lymphoid progenitors, but not hematopoietic stem cells or myeloerythroid progenitors [30]. Moreover, it has been recently revealed that specific subpopulations of osteoblasts influence bone

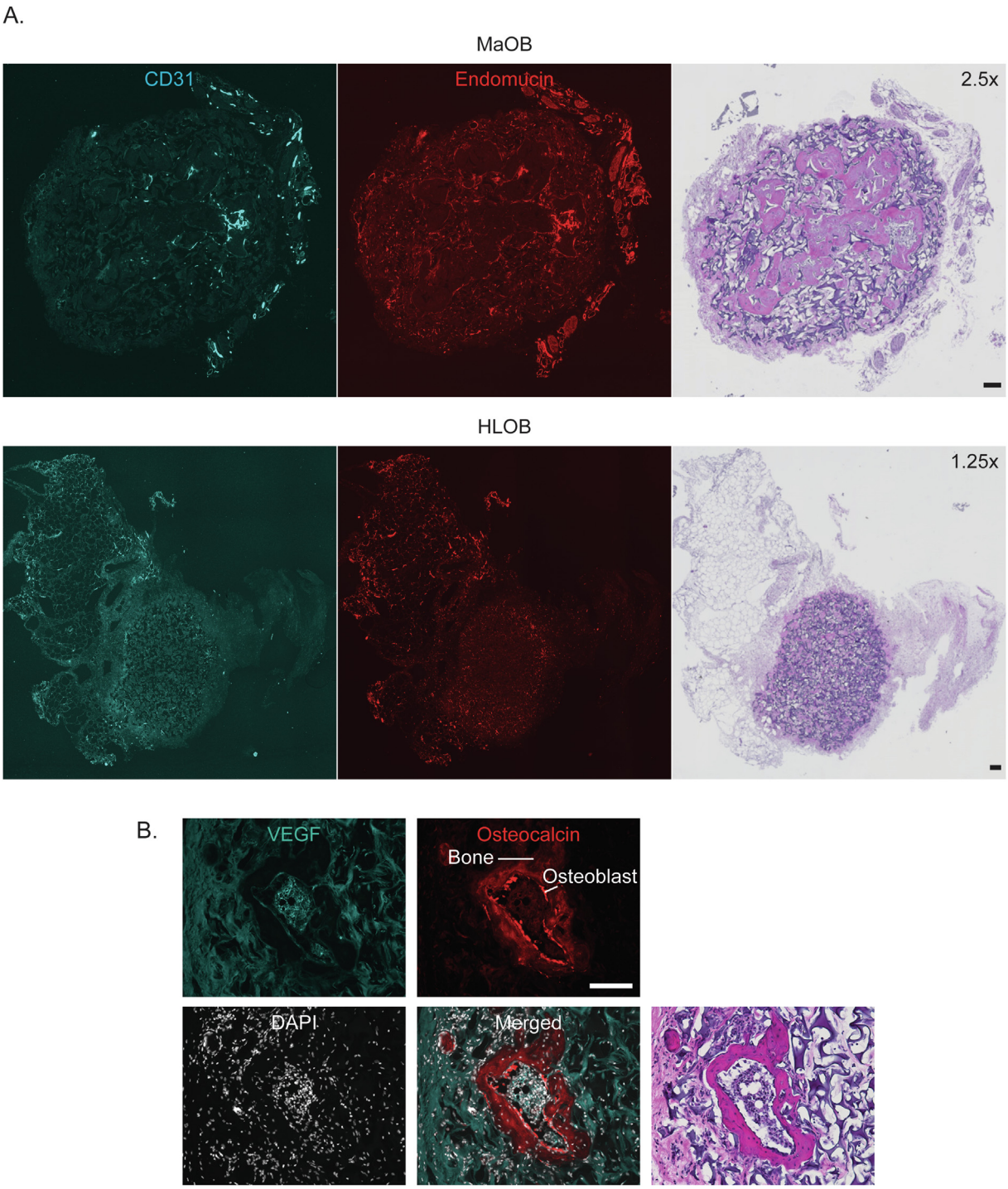

Fig. 5. Ossicle vascularity is mainly localized to tissue surrounding implant. Immunofluorescence was performed on cryosections from Fig. 4 to assess ossicle vascularity. (A) Representative CD31 and Endomucin staining, and H&E image. DAPI was used for nuclear staining. Magnification 10×. Bar = 100 μm. (B) Representative vascular endothelial growth factor (VEGF) and Osteocalcin immunofluorescence, and H&E image. DAPI was used for nuclear staining. Magnification 20×. Bar = 100 μm.

metastatic progression in the tumor microenvironment. Osteoblast progenitors, but not differentiated or mature osteoblasts, were shown to promote breast cancer cell migration through the release of hepatocyte growth factor (HGF), suggesting that the immature osteoblasts are involved in the early steps of the bone seeding process [31]. When osteoblasts interact with breast cancer cells, they are transformed into OPN positive/interleukin (IL)-6 negative/α-smooth muscle actin (SMA) negative osteoblasts [12]. When these cancer-associated osteoblasts were co-cultured with breast cancer cells, the growth of breast cancer cells was significantly suppressed and the expression of the cell cycle arrest marker p21 was activated [12].

To investigate the specific effect of osteoblasts on bone metastatic growth of PCa, we took a simplified approach, by focusing solely on the osteoblast component of the bone-metastatic tumor microenvironment. This is an obvious limitation of this study, as there are many cell types other than osteoblasts that exist in the marrow, and these cells are also known to contribute to tumor

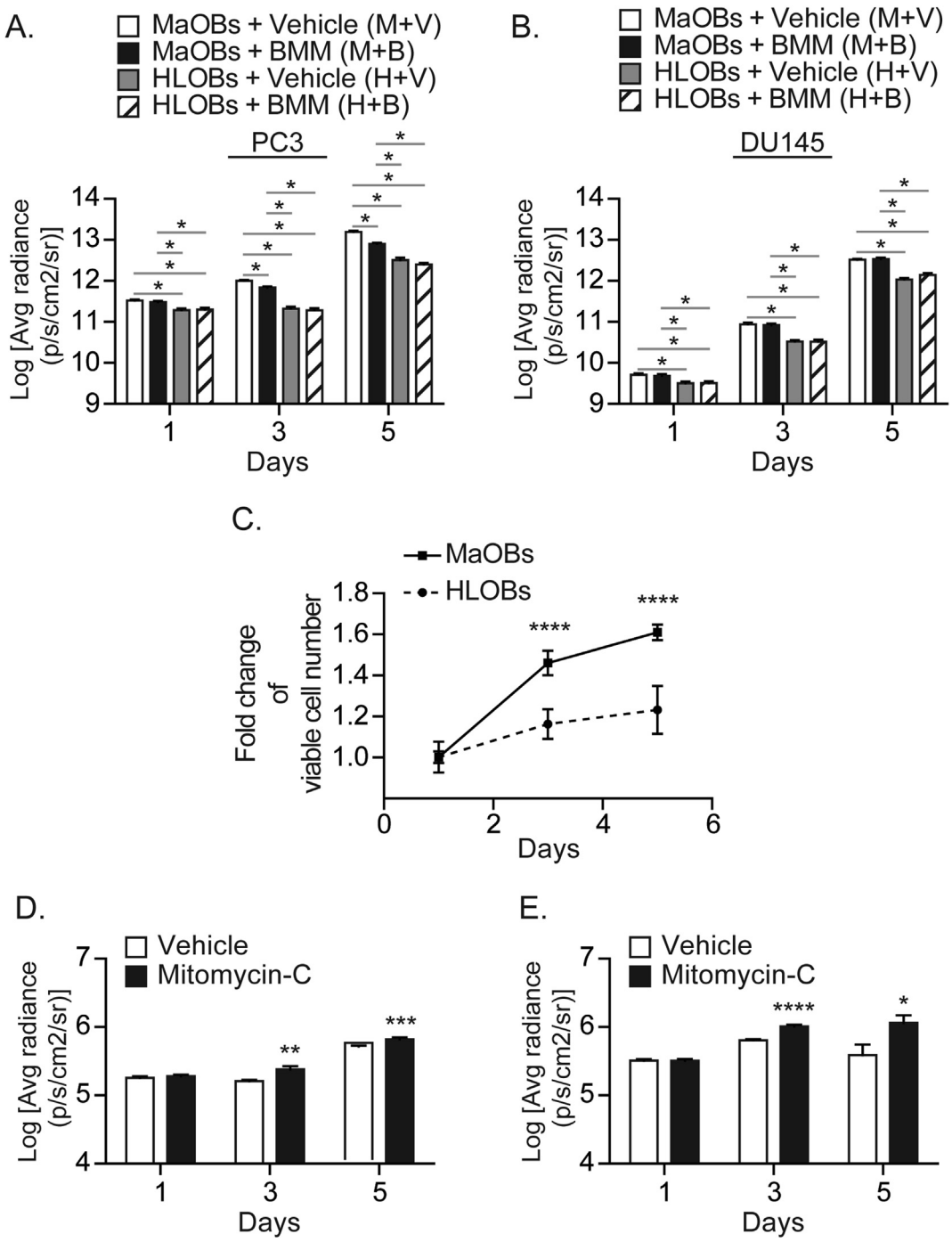

Fig. 6. PCa cells grow faster on osteoblasts harvested from mandibles than osteoblasts from hind limbs. (A) PC3-GFP-luc and (B) DU145-GFP-luc human prostate cancer cells were seeded on top of the primary cells (MaOBs or HLOBs) at a 1:10 ratio. Co-cultures were treated with bone mineralization medium (BMM) (0.5mM L-Ascorbic acid, 2mM β-Glycerophosphate disodium salt hydrate, and 10mM HEPES) or vehicle (10mM HEPES) for 5 days. Bioluminescent imaging (BLI) was measured at day 1, 3, and 5. Two-way ANOVA with Tukey's Studentized Range (HSD) Test for multiple comparisons. (C) MaOBs and HLOBs were seeded in multi-well plates and analyzed for cell proliferation after 1, 3, and 5 days of culture by MTT assay. Proliferation displayed as fold change normalized to day 1. Mixed effects models. (D) PC3-GFP-luc and (E) DU145-GFP-luc human prostate cancer cells were seeded on top of the MC3T3-E1 cells at a 1:10 ratio. To induce cell growth arrest, the MC3T3-E1 cells were pre-treated with vehicle or 10 μg/mL mitomycin-C for 2.5 h prior to co-culture. BLI was measured at day 1, 3, and 5. Paired Student's *t*-test. Results displayed as Mean ± SEM. $^{*}p \leq 0.05$, $^{**}p \leq 0.01$, $^{***}p \leq 0.00$, $^{****}p \leq 0.0001$.

growth, homeostasis, or dormancy [32]. Although further study is clearly needed, this may be part of the reason why osteoblasts failed to express VEGF during differentiation within the ossicles. Additionally, osteoblasts are not the only cells responsible for general bone health. We believe this is a major reason that we did not observe as robust bone formation as others have reported in their ossicle models of bone marrow stromal cell or mesenchymal stem cell implantation [10,11]. We believe that in the absence of other stromal cells, the VEGF and other growth factors such as RANKL released by osteoblasts are less effective at promoting angiogenesis and general bone health in an implant model. For instance, osteoblast-derived VEGF has been shown to promote bone formation in a paracrine fashion (which might explain why MaOB ossicles formed more bone than HLOB ossicles in this study), but was

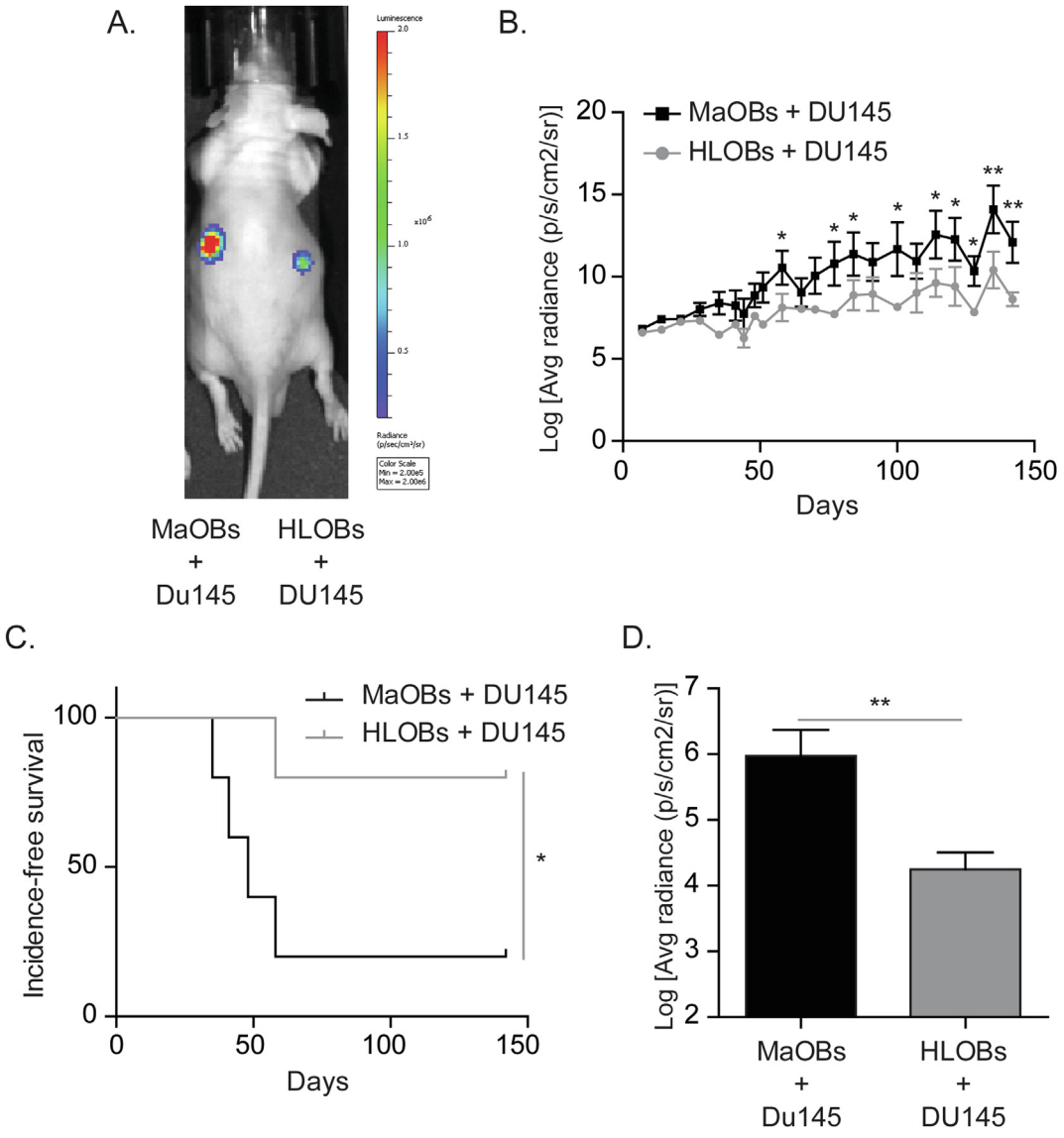

Fig. 7. PCa cells grow faster *in vivo* co-implanted with mandible bone cells. 1×10^6 primary cells (MaOBs or HLOBs) were seeded onto absorbable gelatin sponges and co-implanted into subcutaneous pouches of 5-week old male athymic nude mice (n=5) with 1×10^5 DU145-GFP-luc cells and grown for 20 weeks *in vivo*. (A) Representative bioluminescent imaging (BLI) at 20 weeks. (B) All collected longitudinal BLI data after log transformation. Results displayed as Mean ± SEM. Mixed effects model. (C) 75% cut-off was employed to examine incidence-free survival (MaOBs vs. HLOBs). Cox proportional hazards model with robust sandwich estimates. (D) After euthanasia, tumors were dissected and *ex vivo* BLI performed. Results displayed as Mean ± SEM. Paired Student's *t*-test. $^{*}p \leq 0.05$, $^{**}p \leq 0.01$.

also shown to recruit endothelial cells, macrophages, and promote osteoclastogenesis [22]. Further studies to reveal the effects of not only osteoblasts, but also the stroma, endothelium, nerves, osteocytes, osteoclasts, immune cells, and hematopoietic and mesenchymal stem cells on bone and tumor physiology are clearly warranted. The strength of our study is in the *in vivo* co-implant model, which demonstrated that MaOBs contributed to faster tumor cell proliferation than HLOBs. Although the mechanisms behind these differences remain uncertain, the observation that MaOBs promoted greater vascularization *in vivo* could serve as a foundation for further studies. Another finding deserving of future studies was the increased gene expression of RANKL and OPG in MaOBs, as we were also able to detect RANK gene expression in DU145 cells (32.2 ± 1.2 mean cycle threshold; and GAPDH: 26.3 ± 1.1 mean cycle threshold). This finding may help to inform future investigations into mouse mandible tumor frequency, as the question regarding possible differences in tissue seeding and tumor cell anchorage following intracardiac injection remains, and RANKL has previously been implicated in the bone-metastatic process [33]. Altogether, we believe that these culture methods will be valuable tools in further investigating the mechanisms of tumor cell proliferation in the bone and discovering new interventions to manipulate osteoblast proliferation, activity, or growth factor signaling, which may improve the susceptibility of PCa cells to existing cytotoxic treatments, including chemotherapies.

The findings of this study can be interpreted through the lens of existing treatments used to treat bone metastatic PCa. Current established treatments for bone metastases mainly target bone remodeling, specifically resorption, but these have only had modest success so far, namely denosumab (a human monoclonal antibody against RANKL) and bisphosphonates, which suppress osteoclast activity. Osteoclasts promote bone resorption, creating sufficient space for osteolytic bone tumors to expand and grow [34]. Denosumab and bisphosphonates antagonize bone resorption and as such were hypothesized to slow tumor growth. However, both treatments ultimately fail to improve overall survival

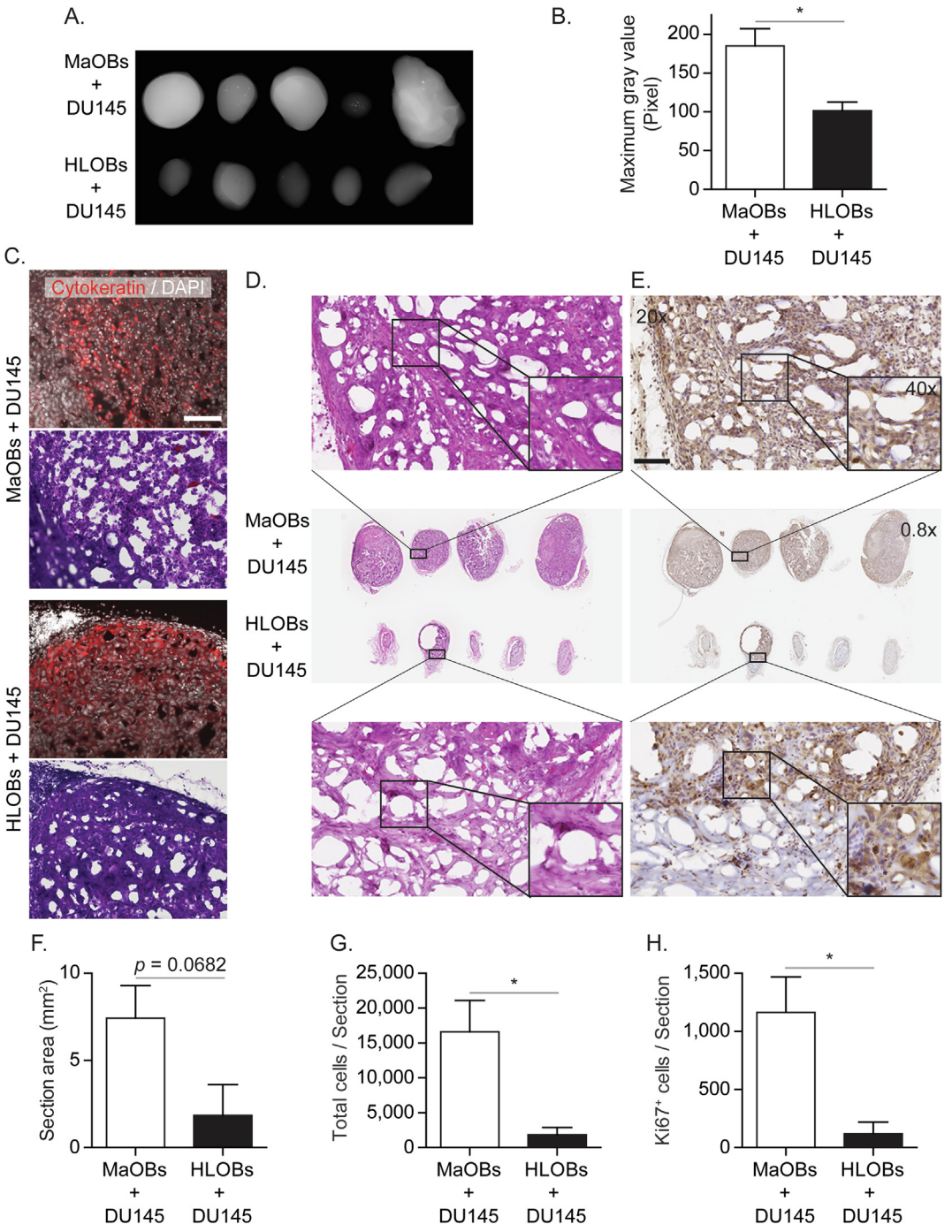

Fig. 8. Tumors from PCa/mandible bone cell co-cultures are more proliferative. (A) After euthanasia, tumors from Fig. 6 were dissected, fixed, and radiographed. (B) Densitometry quantification using ImageJ of (A). (C) Representative Pan-cytokeratin immunofluorescence and H&E image of (A). Magnification 20x. Bar = 100 μm. (D) Representative H&E image of (A). Bar = 100 μm. (E) Representative Ki67 immunohistochemical image of (A). Bar = 100 μm. (F-H) Automated quantification using Visiopharm software of (F) tissue section area, (G) total cells per tissue section, and (H) Ki67 nuclear positive cells per tissue section. Results displayed as Mean ± SE. Paired Student's *t*-test. $^{*}p \leq 0.05$.

[35,36]. On the other hand, radium-223 (Ra^{223}), which forms complexes with hydroxyapatite in bone [37–39], can extend overall survival in PCa patients with bone metastases [40], but only by a few months (mean = 3 months). A variety of combinations of therapies [e.g. docetaxel, second generation androgen depravation therapies (ADTs) such as abiraterone, enzalutamide, or others] have been shown to extend overall survival of metastatic PCa patients [41]. However, when choosing an effective combination strategy for PCa bone metastases, it may be best to avoid ADTs since they are known to negatively affect bone health [42,43]. Indeed, a recent trial of the combination of abiraterone and Ra^{223} in patients with bone-metastatic PCa not only failed to improve skeletal event-free survival, but it also increased the frequency of bone fractures compared with placebo [44]. Alternatively, the idea of inducing bone formation by enhancing osteoblastic activity as a treatment for bone metastatic disease has recently been appreciated [45,46], as inactive/immature osteoblasts can reduce PCa susceptibility to chemotherapy [47,48]. However, the results of this

study suggest that inducing osteoblastic differentiation may not be the best strategy for treating progressive bone metastatic tumors, as BMM treatments failed to increase PCa growth in co-culture models. A popular strategy to treat many cancers has been to use drugs that inhibit angiogenesis, but this strategy has been somewhat unsuccessful in the treatment of bone-metastatic PCa [49,50]. This may be in part because these inhibitors mainly target the receptor for VEGF, but not VEGF itself. Here, we see that high *Vegfa* expressing, fast growing, and bone forming MaOBs induced more tumor growth *in vivo* than HLOBs, which expressed less *Vegfa in vitro*, are slower growing, and form less bone *in vivo*. More studies are clearly necessary to elucidate whether osteoblast-derived VEGF, or other angiogenic factors, is required for the faster tumor growth observed in the mandibles of intracardially-injected mice, whether osteoblast-derived VEGF can be targeted to treat bone metastatic disease, and ultimately whether these findings correspond with bone metastatic PCa in humans. We believe that the models described here are valuable tools to aid in this research.

Author contributions

Matthew R. Eber and Yusuke Shiozawa wrote the manuscript with input from all authors. Matthew R. Eber and Yusuke Shiozawa designed study and contributed to data interpretation. Matthew R. Eber, Sun H. Park, Kelly F. Contino, and Chirayu M. Patel performed *in vitro* and *in vivo* experiments. Fang-Chi Hsu performed statistical analyses. Yusuke Shiozawa supervised the study. All authors reviewed and approved the final manuscript.

CRediT authorship contribution statement

Matthew R. Eber: Conceptualization, Data curation, Investigation, Methodology, Writing - original draft, Writing - review & editing. **Sun H. Park:** Data curation, Investigation, Methodology, Writing - review & editing. **Kelly F. Contino:** Data curation, Investigation, Writing - review & editing. **Chirayu M. Patel:** Data curation, Investigation, Writing - review & editing. **Fang-Chi Hsu:** Formal analysis, Methodology, Software, Writing - review & editing. **Yusuke Shiozawa:** Conceptualization, Funding acquisition, Methodology, Project administration, Resources, Supervision, Writing - original draft, Writing - review & editing.

Declaration of Competing Interest

Yusuke Shiozawa has received research funding from TEVA Pharmaceuticals, but not relevant to this study. The remaining authors declare that they have no known competing financial interests or personal relationships that could have appeared to influence the work reported in this paper.

Acknowledgements

This work is directly supported by the National Cancer Institute (R01-CA238888, Y.S.; R44-CA203184, Y.S.), the Department of Defense (W81XWH-14-1-0403, Y.S.; W81XWH-17-1-0541, Y.S.; W81XWH-19-1-0045, Y.S.), METAvivor (METAvivor Research Award, Y.S.), and the Wake Forest Baptist Comprehensive Cancer Center Internal Pilot Funding (Y.S.). This work is also supported by the National Cancer Institute's Cancer Center Support Grant award number P30-CA012197 issued to the Wake Forest Baptist Comprehensive Cancer Center. The authors wish to acknowledge the support of the Wake Forest Baptist Comprehensive Cancer Center Cell Engineering Shared Resource and Flow Cytometry Shared Resource, supported by the National Cancer Institute's Cancer Center Support Grant award number P30-CA012197. The content is solely the responsibility of the authors and does not necessarily represent the official views of the National Cancer Institute.

References

[1] Y. Shiozawa, E.A. Pedersen, A.M. Havens, Y. Jung, A. Mishra, J. Joseph, J.K. Kim, L. R. Patel, C. Ying, A.M. Ziegler, M.J. Pienta, J. Song, J. Wang, R.D. Loberg, P.H. Krebsbach, K.J. Pienta, R.S. Taichman, Human prostate cancer metastases target the hematopoietic stem cell niche to establish footholds in mouse bone marrow, J. Clin. Invest. 121 (4) (2011) 1298–1312.
[2] Y. Shiozawa, R.S. Taichman, Getting blood from bone: an emerging understanding of the role that osteoblasts play in regulating hematopoietic stem cells within their niche, Exp. Hematol. 40 (9) (2012) 685–694.
[3] L.M. Calvi, G.B. Adams, K.W. Weibrecht, J.M. Weber, D.P. Olson, M.C. Knight, R. P. Martin, E. Schipani, P. Divieti, F.R. Bringhurst, L.A. Milner, H.M. Kronenberg, D.T. Scadden, Osteoblastic cells regulate the haematopoietic stem cell niche, Nature 425 (6960) (2003) 841–846.
[4] F. Arai, A. Hirao, M. Ohmura, H. Sato, S. Matsuoka, K. Takubo, K. Ito, G.Y. Koh, T. Suda, Tie2/angiopoietin-1 signaling regulates hematopoietic stem cell quiescence in the bone marrow niche, Cell 118 (2) (2004) 149–161.
[5] J. Zhang, C. Niu, L. Ye, H. Huang, X. He, W.G. Tong, J. Ross, J. Haug, T. Johnson, J. Q. Feng, S. Harris, L.M. Wiedemann, Y. Mishina, L. Li, Identification of the haematopoietic stem cell niche and control of the niche size, Nature 425 (6960) (2003) 836–841.
[6] H. Wang, C. Yu, X. Gao, T. Welte, A.M. Muscarella, L. Tian, H. Zhao, Z. Zhao, S. Du, J. Tao, B. Lee, T.F. Westbrook, S.T. Wong, X. Jin, J.M. Rosen, C.K. Osborne, X. H. Zhang, The osteogenic niche promotes early-stage bone colonization of disseminated breast cancer cells, Cancer Cell 27 (2) (2015) 193–210.
[7] Y. Shiozawa, J.E. Berry, M.R. Eber, Y. Jung, K. Yumoto, F.C. Cackowski, H.J. Yoon, P. Parsana, R. Mehra, J. Wang, S. McGee, E. Lee, S. Nagrath, K.J. Pienta, R.S. Taichman, The marrow niche controls the cancer stem cell phenotype of disseminated prostate cancer, Oncotarget 7 (27) (2016) 41217–41232.
[8] F. Arguello, R.B. Baggs, C.N. Frantz, A murine model of experimental metastasis to bone and bone marrow, Cancer Res. 48 (23) (1988) 6876–6881.
[9] Y.T. Qiu, C. Yang, M.J. Chen, W.L. Qiu, Metastatic spread to the mandibular condyle as initial clinical presentation: radiographic diagnosis and surgical experience, J. Oral Maxillofac. Surg. 71 (4) (2013) 809–820.
[10] T.L. Aghaloo, T. Chaichanasakul, O. Bezouglaia, B. Kang, R. Franco, S.M. Dry, E. Atti, S. Tetradis, Osteogenic potential of mandibular vs. long-bone marrow stromal cells, J. Dent. Res. 89 (11) (2010) 1293–1298.
[11] S.O. Akintoye, T. Lam, S. Shi, J. Brahim, M.T. Collins, P.G. Robey, Skeletal site-specific characterization of orofacial and iliac crest human bone marrow stromal cells in same individuals, Bone 38 (6) (2006) 758–768.
[12] A.D. Kolb, A.B. Shupp, D. Mukhopadhyay, F.C. Marini, K.M. Bussard, Osteoblasts are "educated" by crosstalk with metastatic breast cancer cells in the bone tumor microenvironment, Breast Cancer Res. 21 (1) (2019) 31.
[13] S.H. Park, M.R. Eber, Y. Shiozawa, Models of Prostate Cancer Bone Metastasis, Methods Mol. Biol. 2019 (1914) 295–308.
[14] S.R. Amend K.C. Valkenburg K.J. Pienta Murine Hind Limb Long Bone Dissection and Bone Marrow Isolation J. Vis. Exp. (110) (2016).
[15] G.J. Pettway, L.K. McCauley, Ossicle and vossicle implant model systems, Methods Mol. Biol. 455 (2008) 101–110.
[16] C.A. Gregory, W.G. Gunn, A. Peister, D.J. Prockop, An Alizarin red-based assay of mineralization by adherent cells in culture: comparison with cetylpyridinium chloride extraction, Anal. Biochem. 329 (1) (2004) 77–84.
[17] S.H. Park, M.R. Eber, S. Tsuzuki, M.E. Booker, A.G. Sunil, D.B. Widner, R.A. Parker, C.M. Peters, Y. Shiozawa, Adeno-associated virus serotype rh10 is a useful gene transfer vector for sensory nerves that innervate bone in immunodeficient mice, Sci. Rep. 7 (1) (2017) 17428.
[18] A.A. Khalil, M.J. Jameson, W.C. Broaddus, P.S. Lin, S.M. Dever, S.E. Golding, E. Rosenberg, K. Valerie, T.D. Chung, The Influence of Hypoxia and pH on Bioluminescence Imaging of Luciferase-Transfected Tumor Cells and Xenografts, Int. J. Mol. Imaging 2013 (2013) 287697.
[19] L.Y. Yu-Lee, Y.C. Lee, J. Pan, S.C. Lin, T. Pan, G. Yu, D.H. Hawke, B.F. Pan, S.H. Lin, Bone secreted factors induce cellular quiescence in prostate cancer cells, Sci. Rep. 9 (1) (2019) 18635.
[20] L.Y. Yu-Lee, G. Yu, Y.C. Lee, S.C. Lin, J. Pan, T. Pan, K.J. Yu, B. Liu, C.J. Creighton, J. Rodriguez-Canales, P.A. Villalobos, E. Wistuba II, F. de Nadal, G.E. Posas, S.H.L. Gallick, Osteoblast-Secreted Factors Mediate Dormancy of Metastatic Prostate Cancer in the Bone via Activation of the TGFbetaRIII-p38MAPK-pS249/T252RB Pathway, Cancer Res. 78 (11) (2018) 2911–2924.
[21] Y. Shiozawa, E.A. Pedersen, L.R. Patel, A.M. Ziegler, A.M. Havens, Y. Jung, J. Wang, S. Zalucha, R.D. Loberg, K.J. Pienta, R.S. Taichman, GAS6/AXL axis regulates prostate cancer invasion, proliferation, and survival in the bone marrow niche, Neoplasia 12 (2) (2010) 116–127.
[22] K. Hu, B.R. Olsen, Osteoblast-derived VEGF regulates osteoblast differentiation and bone formation during bone repair, J. Clin. Invest. 126 (2) (2016) 509–526.
[23] E. Roberts, D.A. Cossigny, G.M. Quan, The role of vascular endothelial growth factor in metastatic prostate cancer to the skeleton, Prostate Cancer 2013 (2013) 418340.
[24] N. Sawa, H. Fujimoto, Y. Sawa, J. Yamashita, Alternating Differentiation and Dedifferentiation between Mature Osteoblasts and Osteocytes, Sci. Rep. 9 (1) (2019) 13842.
[25] H. Li, X. Jiang, J. Delaney, T. Franceschetti, I. Bilic-Curcic, J. Kalinovsky, J.A. Lorenzo, D. Grcevic, D.W. Rowe, I. Kalajzic, Immature osteoblast lineage cells

increase osteoclastogenesis in osteogenesis imperfecta murine, Am. J. Pathol. 176 (5) (2010) 2405–2413.
[26] G.P. Thomas, S.U. Baker, J.A. Eisman, E.M. Gardiner, Changing RANKL/OPG mRNA expression in differentiating murine primary osteoblasts, J. Endocrinol. 170 (2) (2001) 451–460.
[27] B.F. Boyce, L. Xing, Biology of RANK, RANKL, and osteoprotegerin, Arthritis Res Ther 9 (Suppl 1) (2007) S1.
[28] Y. Tanaka, A. Maruo, K. Fujii, M. Nomi, T. Nakamura, S. Eto, Y. Minami, Intercellular adhesion molecule 1 discriminates functionally different populations of human osteoblasts: characteristic involvement of cell cycle regulators, J. Bone Miner. Res. 15 (10) (2000) 1912–1923.
[29] Y. Nakamura, F. Arai, H. Iwasaki, K. Hosokawa, I. Kobayashi, Y. Gomei, Y. Matsumoto, H. Yoshihara, T. Suda, Isolation and characterization of endosteal niche cell populations that regulate hematopoietic stem cells, Blood 116 (9) (2010) 1422–1432.
[30] L. Ding, S.J. Morrison, Haematopoietic stem cells and early lymphoid progenitors occupy distinct bone marrow niches, Nature 495 (7440) (2013) 231–235.
[31] S. Vallet, M.H. Bashari, F.J. Fan, S. Malvestiti, A. Schneeweiss, P. Wuchter, D. Jager, K. Podar, Pre-Osteoblasts Stimulate Migration of Breast Cancer Cells via the HGF/MET Pathway, PLoS ONE 11 (3) (2016) e0150507.
[32] Y. Shiozawa, M.R. Eber, J.E. Berry, R.S. Taichman, Bone marrow as a metastatic niche for disseminated tumor cells from solid tumors, Bonekey Rep. 4 (2015) 689.
[33] T. Asano, K. Okamoto, Y. Nakai, M. Tsutsumi, R. Muro, A. Suematsu, K. Hashimoto, T. Okamura, S. Ehata, T. Nitta, H. Takayanagi, Soluble RANKL is physiologically dispensable but accelerates tumour metastasis to bone, Nat. Metab. 1 (9) (2019) 868–875.
[34] A. Maurizi, N. Rucci, The Osteoclast in Bone Metastasis: Player and Target, Cancers (Basel) 10 (7) (2018).
[35] A.T. Stopeck, A. Lipton, J.J. Body, G.G. Steger, K. Tonkin, R.H. de Boer, M. Lichinitser, Y. Fujiwara, D.A. Yardley, M. Viniegra, M. Fan, Q. Jiang, R. Dansey, S. Jun, A. Braun, Denosumab compared with zoledronic acid for the treatment of bone metastases in patients with advanced breast cancer: a randomized, double-blind study, J. Clin. Oncol. 28 (35) (2010) 5132–5139.
[36] K. Fizazi, M. Carducci, M. Smith, R. Damiao, J. Brown, L. Karsh, P. Milecki, N. Shore, M. Rader, H. Wang, Q. Jiang, S. Tadros, R. Dansey, C. Goessl, Denosumab versus zoledronic acid for treatment of bone metastases in men with castration-resistant prostate cancer: a randomised, double-blind study, Lancet 377 (9768) (2011) 813–822.
[37] S.K. Badrising, V. van der Noort, P. Hamberg, J.L. Coenen, M.J. Aarts, I.M. van Oort, A.J. van den Eertwegh, M. Los, H.P. van den Berg, H. Gelderblom, S. Vrijaldenhoven, E.D. Kerver, T. van Voorthuizen, I.J. de Jong, J.B. Haanen, A.M. Bergman, Enzalutamide as a Fourth- or Fifth-Line Treatment Option for Metastatic Castration-Resistant Prostate Cancer, Oncology 91 (5) (2016) 267–273.
[38] F. Vignani, V. Bertaglia, C. Buttigliero, M. Tucci, G.V. Scagliotti, M. Di Maio, Skeletal metastases and impact of anticancer and bone-targeted agents in patients with castration-resistant prostate cancer, Cancer Treat. Rev. 44 (2016) 61–73.
[39] D.S. Abou, D. Ulmert, M. Doucet, R.F. Hobbs, R.C. Riddle, D.L. Thorek, Whole-Body and Microenvironmental Localization of Radium-223 in Naive and Mouse Models of Prostate Cancer Metastasis, J. Natl Cancer Inst. 108 (5) (2016).
[40] C. Parker, S. Nilsson, D. Heinrich, S.I. Helle, J.M. O'Sullivan, S.D. Fossa, A. Chodacki, P. Wiechno, J. Logue, M. Seke, A. Widmark, D.C. Johannessen, P. Hoskin, D. Bottomley, N.D. James, A. Solberg, I. Syndikus, J. Kliment, S. Wedel, S. Boehmer, M. Dall'Oglio, L. Franzen, R. Coleman, N.J. Vogelzang, C.G. O'Bryan-Tear, K. Staudacher, J. Garcia-Vargas, M. Shan, O.S. Bruland, O. Sartor, A. Investigators, Alpha emitter radium-223 and survival in metastatic prostate cancer, N. Engl. J. Med. 369 (3) (2013) 213–223.
[41] G. Gravis, Systemic treatment for metastatic prostate cancer, Asian J. Urol. 6 (2) (2019) 162–168.
[42] C.E. Lee, W.D. Leslie, P. Czaykowski, J. Gingerich, M. Geirnaert, Y.K. Lau, A comprehensive bone-health management approach for men with prostate cancer receiving androgen deprivation therapy, Curr. Oncol. 18 (4) (2011) e163–e172.
[43] D.K. Kim, J.Y. Lee, K.J. Kim, N. Hong, J.W. Kim, Y.S. Hah, K.C. Koo, J.H. Kim, K.S. Cho, Effect of Androgen-Deprivation Therapy on Bone Mineral Density in Patients with Prostate Cancer: A Systematic Review and Meta-Analysis, J. Clin. Med. 8 (1) (2019).
[44] M. Smith, C. Parker, F. Saad, K. Miller, B. Tombal, Q.S. Ng, M. Boegemann, V. Matveev, J.M. Piulats, L.E. Zucca, O. Karyakin, G. Kimura, N. Matsubara, W.C. Nahas, F. Nole, E. Rosenbaum, A. Heidenreich, Y. Kakehi, A. Zhang, H. Krissel, M. Teufel, J. Shen, V. Wagner, C. Higano, Addition of radium-223 to abiraterone acetate and prednisone or prednisolone in patients with castration-resistant prostate cancer and bone metastases (ERA 223): a randomised, double-blind, placebo-controlled, phase 3 trial, Lancet Oncol. 20 (3) (2019) 408–419.
[45] E. Hesse, S. Schroder, D. Brandt, J. Pamperin, H. Saito, H. Taipaleenmaki, Sclerostin inhibition alleviates breast cancer-induced bone metastases and muscle weakness, JCI Insight 5 (2019).
[46] D. Toscani, M. Bolzoni, M. Ferretti, C. Palumbo, N. Giuliani, Role of Osteocytes in Myeloma Bone Disease: Anti-sclerostin Antibody as New Therapeutic Strategy, Front. Immunol. 9 (2018) 2467.
[47] H. Zheng, Y. Bae, S. Kasimir-Bauer, R. Tang, J. Chen, G. Ren, M. Yuan, M. Esposito, W. Li, Y. Wei, M. Shen, L. Zhang, N. Tupitsyn, K. Pantel, C. King, J. Sun, J. Moriguchi, H.T. Jun, A. Coxon, B. Lee, Y. Kang, Therapeutic Antibody Targeting Tumor- and Osteoblastic Niche-Derived Jagged1 Sensitizes Bone Metastasis to Chemotherapy, Cancer Cell 32(6) (2017) 731-747 e6.
[48] N. Sethi, X. Dai, C.G. Winter, Y. Kang, Tumor-derived JAGGED1 promotes osteolytic bone metastasis of breast cancer by engaging notch signaling in bone cells, Cancer Cell 19 (2) (2011) 192–205.
[49] A. Spreafico, K.N. Chi, S.S. Sridhar, D.C. Smith, M.A. Carducci, P. Kavsak, T.S. Wong, L. Wang, S.P. Ivy, S.D. Mukherjee, C.K. Kollmannsberger, M.A. Sukhai, N. Takebe, S. Kamel-Reid, L.L. Siu, S.J. Hotte, A randomized phase II study of cediranib alone versus cediranib in combination with dasatinib in docetaxel resistant, castration resistant prostate cancer patients, Invest. New Drugs 32 (5) (2014) 1005–1016.
[50] E. Heath, L. Heilbrun, H. Mannuel, G. Liu, P. Lara, J.P. Monk, T. Flaig, A. Zurita, P. Mack, U. Vaishampayan, P. Stella, D. Smith, S. Bolton, A. Hussain, A. Al-Janadi, D. Silbiger, M. Usman, S.P. Ivy, Phase II, Multicenter, Randomized Trial of Docetaxel plus Prednisone with or Without Cediranib in Men with Chemotherapy-Naive Metastatic Castrate-Resistant Prostate Cancer, Oncologist 24 (9) (2019) 1149–e807.

Biochemical Pharmacology 188 (2021) 114520

Contents lists available at ScienceDirect

Biochemical Pharmacology

journal homepage: www.elsevier.com/locate/biochempharm

Usefulness of the measurement of neurite outgrowth of primary sensory neurons to study cancer-related painful complications

Sun H. Park [a], Matthew R. Eber [a], Miriam M. Fonseca [b], Chirayu M. Patel [a], Katharine A. Cunnane [b], Huiping Ding [c], Fang-Chi Hsu [d], Christopher M. Peters [b], Mei-Chuan Ko [c], Roy E. Strowd [e], John A. Wilson [f], Wesley Hsu [f], E. Alfonso Romero-Sandoval [b], Yusuke Shiozawa [a,*]

[a] Department of Cancer Biology and Wake Forest Baptist Comprehensive Cancer Center, Wake Forest University Health Sciences, Winston-Salem, NC 27157, USA
[b] Department of Anesthesiology, Wake Forest University Health Sciences, Winston-Salem, NC 27157, USA
[c] Department of Physiology and Pharmacology, Wake Forest University Health Sciences, Winston-Salem, NC 27157, USA
[d] Department of Biostatistics and Data Science and Wake Forest Baptist Comprehensive Cancer Center, Wake Forest University Health Sciences, Winston-Salem, NC 27157, USA
[e] Department of Neurology and Wake Forest Baptist Comprehensive Cancer Center, Wake Forest University Health Sciences, Winston-Salem, NC 27157, USA
[f] Department of Neurosurgery, Wake Forest University Health Sciences, Winston-Salem, NC 27157, USA

ARTICLE INFO

Keywords:
Dorsal root ganglia
Nerve sprouting
Cancer-derived condition medium
Chemotherapeutic agent
Semi-automated quantification of neurite outgrowth

ABSTRACT

Abnormal outgrowth of sensory nerves is one of the important contributors to pain associated with cancer and its treatments. Primary neuronal cultures derived from dorsal root ganglia (DRG) have been widely used to study pain-associated signal transduction and electrical activity of sensory nerves. However, there are only a few studies using primary DRG neuronal culture to investigate neurite outgrowth alterations due to underlying cancer-related factors and chemotherapeutic agents. In this study, primary DRG sensory neurons derived from mouse, non-human primate, and human were established in serum and growth factor-free conditions. A bovine serum albumin gradient centrifugation method improved the separation of sensory neurons from satellite cells. The purified DRG neurons were able to maintain their heterogeneous subpopulations, and displayed an increase in neurite growth when exposed to cancer-derived conditioned medium, while they showed a reduction in neurite length when treated with a neurotoxic chemotherapeutic agent. Additionally, a semi-automated quantification method was developed to measure neurite length in an accurate and time-efficient manner. Finally, these exogenous factors altered the gene expression patterns of murine primary sensory neurons, which are related to nerve growth, and neuro-inflammatory pain and nociceptor development. Together, the primary DRG neuronal culture in combination with a semi-automated quantification method can be a useful tool for further understanding the impact of exogenous factors on the growth of sensory nerve fibers and gene expression changes in sensory neurons.

1. Introduction

Recent evidence suggests that crosstalk between the peripheral nervous system and cancer plays an important role in both cancer development and cancer-associated pain [1–3]. In head and neck cancer, tumors innervated by peripheral nerves are known to be more aggressive than those with less innervation [4]. Recent studies using mouse models have revealed that the sympathetic nervous system regulates prostate cancer tumorigenesis and bone metastasis [5], and that denervation can even attenuate tumorigenesis and metastasis in several types of cancer [5–8]. Moreover, it has been indicated that cancer-associated pain may be a negative indicator of survival in cancer patients [9], suggesting that sensory nerves influence disease progression in patients with poor prognoses. This accumulating evidence indicates that the peripheral nervous system within the tumor microenvironment may enhance disease progression.

Conversely, cancer cells are also known to affect neuronal activities. Cancer often causes pain by interacting with sensory nerves. Especially,

* Corresponding author.
E-mail address: yshiozaw@wakehealth.edu (Y. Shiozawa).

https://doi.org/10.1016/j.bcp.2021.114520
Received 14 December 2020; Received in revised form 8 March 2021; Accepted 10 March 2021
Available online 17 March 2021
0006-2952/© 2021 Elsevier Inc. All rights reserved.

when cancer cells metastasize to the bone, patients experience bone pain, referred to as cancer-induced bone pain (CIBP). Bone is richly innervated by sensory nerves [10], and it has been suggested that the acidic environment surrounding cancer, or factors, such as growth factors, cytokines, or chemokines, secreted by cancer cells can all stimulate receptors on sensory nerves to induce CIBP [11–14]. Additionally, recent studies have also demonstrated that sensory nerve outgrowth (or sprouting) is one of the potential mechanisms of CIBP [15–19]. A neurotrophic factor nerve growth factor (NGF) is known to be involved in the regulation of survival and growth of neurons [20]. NGF derived from osteosarcoma cells stimulated neuroma-like formation in the periosteum of cancer-inoculated mouse bones, resulting in CIBP [19]. When an NGF antagonist was administered to cancer-bearing mice, CIBP as well as the accompanying nerve sprouting were attenuated [19]. Consistently, abnormal sensory nerve sprouting also causes pain behaviors in other chronic pain conditions [10,21–23].

Not only nerve growth, but also nerve damage is associated with the induction of chronic pain conditions. Chemotherapy-induced peripheral neuropathy (CIPN) is a consequence of the neurotoxic effects of chemotherapy agents [24–26]. Indeed, paclitaxel reduced the density of intraepidermal nerve fibers in hind paw skin and produced pain-related behaviors in rodents [26,27].

These findings suggest (i) that nerves and cancer interact very closely with one another and (ii) abnormal plasticity or remodeling of sensory neurons may contribute to cancer-induced pain. Therefore, it is crucial to understand how nerve growth is regulated in the context of cancer and its treatments. In pursuit of this goal, animal studies are often used to investigate the systemic effects of disease states and therapies on peripheral nerves, but they are not always suitable to study local interactions. For that reason, various *in vitro* neuronal culture systems have been developed to understand the mechanisms of neurite outgrowth. The mouse pheochromocytoma cell line PC12, which is known to form neurite-like structures in response to NGF [28], has been previously used to assess the effects of cancer-derived factors on neurite outgrowth. Conditioned medium (CM) derived from pancreatic cancer cells [29] or head and neck cancer-derived exosomes [30] were shown to enhance neurite sprouting of PC12 cells. Cell lines are easy to maintain and handle but may not fully recapitulate the phenotype of sensory neurons. Moreover, only few neuronal cell lines which extend neurites are currently available. The use of primary culture of dorsal root ganglia (DRG) neurons may overcome this hurdle. To date primary DRG culture has mainly been used to investigate physiological alterations in neuronal activity [31] and to a lesser degree neurite outgrowth.

In the current study, we established methods for reliable *in vitro* primary cultures of sensory neurons derived from mouse, non-human primate, and human DRGs. Additionally, we found that these primary DRG neuronal cultures were suitable to study the neurite length alterations and changes in gene expression associated with nerve growth, and neuro-inflammatory pain and nociceptor development, mediated by CM obtained from cancer cells or paclitaxel-induced neurotoxicity. We also developed a semi-automated method for the measurement of neurite outgrowth, resulting in the reduction of overall analysis time.

2. Materials and methods

All methods were carried out in accordance with relevant guidelines and regulations. All human studies and all animal studies followed the Declaration of Helsinki and the Institutional Animal Care and Use Committee Guidelines, respectively.

2.1. Human subjects research certification

All human studies are approved by the Institutional Review Board (IRB #00056846) at Wake Forest University Health Sciences. Informed consent was obtained from all subjects involved in the current study.

2.2. Animal care and use certification

All animal studies are approved by the Institutional Animal Care and Use Committee (Protocol A18-026 for mouse and Protocol A18-161 for non-human primate) at Wake Forest University Health Sciences.

2.3. Murine DRG isolation and primary neuronal culture establishment

Primary DRG neuronal culture was prepared, according to previously published protocols [32,33] with modifications. Nine-twelve lumbar DRGs (L2-L4) of male C57BL/6 mice (8–12 weeks of age, Jackson Laboratory, Bar Harbor, ME) were dissected and directly placed into a 15 mL conical tube, containing 14 mL of ice-cold 1 × Hanks' balanced salt solution (HBSS) without Mg^{++}/Ca^{++} (Thermo Fisher Scientific, Gibco, Waltham, MA). Isolated DRGs were enzymatically digested in 3 mL of papain solution [30 U/mL papain (Worthington Biochemical Corp., Lakewood, NJ), 0.1% saturated NaHCO3 solution (Sigma-Aldrich, St. Louis, MO), 0.3 mg/mL L-Cys (Sigma-Aldrich) in HBSS without Mg^{++}/Ca^{++})] for 30 min at 37℃ with 5% CO_2, and then incubated in 3 mL of collagenase type II (CLS2)/dispase type II (Dispase II) solution [4 mg/mL CLS2 (Worthington Biochemical Corp.) and 4.7 mg/mL dispase (Sigma-Aldrich) in HBSS without Mg^{++}/Ca^{++}] for 30 min at 37℃ with 5% CO_2. The DRGs were mixed gently every 10 mins. The resulting DRGs were centrifuged at 200 × g for 2 min and washed with HBSS without Mg^{++}/Ca^{++}. The pellet was transferred to a 15 mL conical tube, containing 500 μL of neuronal growth (NG) medium [Neurobasal-A (Thermo Fisher Scientific, Gibco), 1% N2 (Thermo Fisher Scientific), 2% B-27 (Thermo Fisher Scientific), 2 mM L-glutamine (Thermo Fisher Scientific), 1% penicillin–streptomycin (Thermo Fisher Scientific), and 0.4% glucose (Sigma-Aldrich)]. The DRGs were triturated 15–20 times using p1000 and then p200 pipette tips and filtered through a stainless mesh sieve (40 μm, Thermo Fisher Scientific) to obtain single-cell suspensions and remove undigested tissue debris. After bovine serum albumin (BSA) purification [3.5% (W/V) BSA solution] (see below), 500–1,000 cells of DRGs in 30 μL of warm NG medium were seeded onto the center of 12 mm round coverslips (MatTek Corp., Ashland, MA), precoated with Poly-D-lysine (50 ug/mL, overnight at 4℃, Thermo Fisher Scientific, Corning) and laminin (20 μg/mL, 1 h at 37℃, Thermo Fisher Scientific, Corning), in 24-well plate. After 1–2 h, 1 mL of warm NG medium was gently added to the sides of wells and the cells were maintained at 37℃ with 5% CO_2.

2.4. BSA purification

After trituration and filtration, single-cell suspensions from DRGs were centrifuged through 3.5% (W/V) BSA solution (Thermo Fisher Scientific) (5 mL of BSA solution: 1mL of HBSS without Mg^{++}/Ca^{++}; 1 mL of cell suspension in a 15 mL conical tube) at 14 × g for 20 min at room temperature (RT) to separate sensory neurons (in pellet) from satellite cells and debris (in BSA layer).

2.5. Non-human primate DRG isolation and primary neuronal culture establishment

Non-human primate primary neuronal culture was prepared similarly as described in the murine primary neuronal culture with minor modifications. DRGs (T12 and L1) of a healthy 8-year old female Rhesus macaque (Worldwide Primates, Inc., Miami, FL) were dissected and directly placed in a 15 mL conical tube containing 14 mL of ice-cold HBSS without Mg^{++}/Ca^{++} and transferred to the laboratory for further procedures. Isolated DRGs were cleaned up by removing non-nervous tissues and nerve root under the laminar flow hood using sterile blade, scissors, and forceps, and cut into small pieces achieved at approximately 1–3 mm side length of a cubical volume in ice-cold HBSS without Mg^{++}/Ca^{++} and transferred to a 15 mL conical tube containing papain solution. DRGs were enzymatically digested in 6 mL of papain

solution for 1 h at 37℃ with 5% CO_2 and then incubated in 6 mL of CLS2/Dispase II solution for 1 h at 37℃ with 5% CO_2. During the digestion, DRGs were triturated 10–15 times using p1000 tips every 20 min and filtered through a stainless mesh sieve (100 μm, Thermo Fisher Scientific) to obtain single-cell suspensions and remove undigested tissue debris. After BSA purification [3.5% (W/V) BSA solution], 600 cells of DRGs in 30 μL of warm NG medium were seeded onto the center of 12 mm round coverslips, pre-coated with Poly-D-lysine and laminin, in 24-well plate. After 1–2 h, 1 mL of warm NG medium was gently added to the sides of wells and the cells were maintained at 37℃ with 5% CO_2.

2.6. Human DRG isolation and primary neuronal culture establishment

Human primary neuronal culture was prepared similarly as the non-human primate neuronal culture with minor modifications, according to previously published studies [34–38]. DRG (T10) of a male patient (41 years old age) were dissected during a T10 corpectomy for correction of kyphotic deformity secondary to discitis/osteomyelitis and directly placed in a 15 mL conical tube containing 14 mL of ice-cold HBSS without Mg^{++}/Ca^{++} and transferred to the laboratory for the further procedures. Isolated DRGs were cleaned up by removing non-nervous tissues and nerve root under the laminar flow hood using sterile blade, scissors, and forceps, and at approximately 1–3 mm side length of a cubical volume in ice-cold HBSS without Mg^{++}/Ca^{++} and transferred to a 15 mL conical tube containing papain solution. DRGs were enzymatically digested in 9 mL of papain solution for 1 h at 37℃ with 5% CO_2 and then incubated in 9 mL of CLS2/Dispase II solution for 1.5 h at 37℃ with 5% CO_2. During the digestion, DRGs were triturated 10–15 times using p1000 tips every 20 min and filtered through a stainless mesh sieve (100 μm) to obtain single-cell suspensions and remove undigested tissue debris. After BSA purification [3.5% (W/V) BSA solution, DRGs in 30 μL of warm NG medium were seeded onto the center of 12 mm round coverslips, pre-coated with Poly-D-lysine and laminin, in 24-well plate. After 1–2 h, 1 mL of warm NG medium was gently added to the sides of wells and the cells were maintained at 37℃ with 5% CO_2.

2.7. Cancer cell or normal prostate epithelial cell derived conditioned medium generation

To collect the conditioned medium (CM) from cancer cells, 5×10^5 cells of a human breast cancer cell line established from a pleural effusion, MDA-MB-231 [American Type Culture Collection (ATCC), Manassas, VA], a human prostate cancer cell line established from bone metastasis, PC-3 (ATCC), a human lung adenocarcinoma cell line established from lung carcinomatous tissue, A549 (ATCC), or a murine lung carcinoma cell line established from a primary tumor nodule from the Lewis lung carcinoma model, LL/2 (ATCC) were seeded onto a 10 cm dish with 10 mL of growth medium. These cancer cell lines were chosen since they have been shown to grow in the bone and/or can induce CIBP [39–42]. The passage number for all cell lines used was less than 25 passages. MDA-MB-231 and LL/2 cells were cultured in Dulbecco's modified eagle medium (DMEM) (Thermo Fisher Scientific, Gibco) containing 10% fetal bovine serum (FBS, Thermo Fisher Scientific, Gibco), 1% penicillin–streptomycin and glutamine (PSG) (Thermo Fisher Scientific, Gibco), while PC-3 and A549 cells were cultured in Roswell park memorial institute (RPMI) 1640 medium (Thermo Fisher Scientific, Gibco) containing 10% FBS and 1% PSG. At 24 h, the growth medium was removed and replaced with 10 mL of serum free DMEM or RPMI 1640 medium (Thermo Fisher Scientific, Gibco) containing 1% PSG. For the control medium, 10 mL of serum free DMEM or RPMI medium were added to a 10 cm dish without adding any cancer cells. To collect the CM from non-cancer cells, 5×10^5 cells of a human normal epithelial prostate cell line, PWR-1E (ATCC) were seeded onto a 10 cm dish with 10 mL of Keratinocyte-serum free medium (K-SFM) containing human recombinant EGF (5 ng/mL) and bovine pituitary extract (0.05 mg/mL) provided with the K-SFM kit (Thermo Fisher Scientific, Gibco). The passage number for all cell lines used was less than 25 passages. At 24 h, the growth medium was removed and replaced with 10 mL of K-SFM without any supplements. For the control medium, 10 mL of K-SFM were added to a 10 cm dish without adding any cells. After 24 h of incubation at 37℃ with 5% CO_2, the CM were collected and filtered through a 0.2 μm syringe filter (Thermo Fisher Scientific) to remove any cell debris. Additionally, cancer-derived CM were concentrated to 4 × using an Amicon Ultra-15 centrifugal filter tube (MilliporeSigma, Burlington, MA, NMWL10K) performed at 4,000 × g for 20 min at RT. The CM was stored at 4℃ until use.

2.8. Neurite outgrowth assay

After 48 h (murine and non-human primate) or 72 h (human) of primary DRG neuronal culture establishment (the time required to achieve 20–30% nerve fiber occupancy on the slide based on Fig. 3**A**), half (500 μL) of medium was replaced with 500 μL of either control, normal epithelial cell-derived CM, or cancer-derived CM, and then the cells were incubated another 48–72 h (the time required to achieve 70–80% nerve fiber occupancy on the slide based on Fig. 3**A**). In some cases, the cells were treated with 500 μL of NG medium containing either dimethyl sulfoxide (DMSO) control or paclitaxel (Sigma-Aldrich) for 24 h. At the termination of the experiments, the cells were fixed in 500 μL of 4% paraformaldehyde (PFA) for 10 min at RT, and immediately subjected to immunofluorescence or stored in 1 × D-PBS at 4℃ until use.

2.9. Immunofluorescence assay

Fixed cells were blocked with immunofluorescence (IF) buffer [1x D-PBS supplemented with 5% Normal Donkey serum (Jackson ImmunoResearch, West Grove, PA) and 0.03% Triton X-100 (Sigma-Aldrich) for 1 h at RT and incubated with primary antibodies overnight at 4 °C in IF buffer. Primary antibodies used: mouse anti-β-III tubulin antibody (1:1,000, Biolegend, San Diego, CA, cat #: 801201); chicken anti-200kD neurofilament (NF200) antibody (1:3,000, Neuromics, Cambridge, MA, cat #: ab134459); rabbit anti-protein gene product 9.5 (PGP9.5) antibody (1:1,000; Cederlane, Rosemont, IL, cat #: 14730–1-AP); rabbit anti-calcitonin gene-related peptide (CGRP) antibody (1: 5,000, Sigma-Aldrich, cat #: C8198); biotinylated isolectin B4 (IB4) antibody (1: 2,500, Sigma-Aldrich, cat #: L2140); rabbit anti-S100 antibody (1: 1,000, Abcam, Cambridge, UK, cat #: ab868); or goat anti-glial fibrillary acidic protein (GFAP) antibody (1: 200, Santa Cruz, Dallas, TX, cat #: sc-6170). Thereafter, the cells were incubated with secondary antibodies for 2 h at RT in IF buffer. The specific choices of secondary antibodies were made based on primary antibodies used. Secondary antibodies used: anti-rabbit cyanine 3 (CY3) (1:700, Jackson ImmunoResearch, cat #: 711–165-152); anti-chicken CY2 (1:600, Jackson ImmunoResearch, cat #: 703–225-155); anti-streptavidin CY5 (1:500, Jackson ImmunoResearch, cat #: 016–170-084); anti-goat CY5 (1:500, Jackson ImmunoResearch, cat #: 705–175-147); or anti-mouse CY2 (1:600, Jackson ImmunoResearch, cat #: 715–225-150). After washing 5 times with 1x D-PBS, the cells were mounted with ProLong Gold antifade mountant with DAPI (Thermo Fisher Scientific).

2.10. Imaging and quantification of immunofluorescence

For each group, 2–3 coverslips were quantified, and 6–10 images were taken from each coverslip using a Nikon Eclipse Ni fluorescent microscope system (Nikon, Tokyo, Japan). Images were saved in nd2 or tiff files for further analysis using Visiopharm (Hørsholm, Denmark) or Image J (NIH, Bethesda, Maryland) software, respectively.

2.11. Image J analysis

Neuron J, a plugin for Image J software was used to manually analyze nerve density, as previously described [43,44]. Briefly, images

were opened in Image J (https://imagej.net/Fiji/Downloads) and converted to 8-bit, which were then individually opened in Neuron J plugin. Thereafter, total neurite lengths of neuronal markers NF200 or β-III tubulin positive neurites per each image were traced and normalized with the numbers of neurons, which were counted using a multi-point tool of Image J.

2.12. Visiopharm image analysis

An algorithm (called an "APP") was created in the Visiopharm software, which uses digital masks and associated labels to automatically detect and count the somas of NF200 positive neurons, as well as detect and measure total NF200 positive neurite length. In some cases, PGP9.5, β-III tubulin, or activating transcription factor 3 (ATF3) were used as markers instead of NF200 for neurite length or soma quantification. The APP was designed to exploit the observations that somas are usually brighter in fluorescence intensity than neurites, and neurites are long, thin structures whereas somas are round and larger in diameter. This APP uses thresholds, which were set manually according to the set of images to be analyzed, as sets of images can vary in fluorescence intensity between experiments due to staining and microscope setting differences. The APP includes post-processing for cleaning up the classification (i.e. small object removal, skeletonization, erosion, dilation, etc.) and the calculation of the variable included in our measurements.

2.13. Real time qPCR

After murine primary DRG neuron cultures were treated with (i) either control or cancer-derived CM (48 h), or (ii) either DMSO or paclitaxel (10 μM) (24 h), cells were lysed in 350 μL RLT-β-ME buffer. RNA was extracted using the RNeasy plus micro kit (Qiagen, Germantown, MD) and cDNA was generated using Invitrogen SuperScript II Reverse Transcriptase (Invitrogen, Carlsbad, CA). Real time PCR (qPCR) was performed using Taqman gene expression master mix (Applied Biosystems, Foster City, CA) and Taqman gene expression assays on the Bio-Rad CFX Connect instrument (Hercules, CA). Taqman gene expression assays used: growth associated protein 43 (GAP43) (Mm00500404_m1), NF200 (Mm01191456_m1), CGRP (Mm00801463_g1), Substance P (Mm01166996_m1), Bradykinin (Mm04207315_s1), tumor necrosis factor-α (TNF-α) (Mm00443258_m1), suppressor of cytokine signaling 3 (SOCS3) (Mm00545913_s1), immunoglobulin superfamily containing leucine rich repeat 2 (ISLR2) (Mm00623260_s1), and GAPDH (Mm99999915_g1). For interleukin-6 (IL-6), cDNAs were amplified by qPCR using SsoAdvanced Universal SYBR green supermix (Bio-rad laboratories, Hercules, CA). Primers used: mouse IL-6 Forward: 5′-TTCCTACCCCAATTTCCAAT-3′ and Reverse: 5′-CCTTCTGTGACTCCAGCTTATC-3′ (Integrated DNA Technologies, Newark, NJ). Data is presented using the delta-delta Ct method, with GAPDH used as the reference gene.

2.14. Statistical analysis

Numerical data are expressed as mean ± the standard error of the mean (SEM). Statistical analysis was performed by unpaired two-tailed Student's *t* test or one-way ANOVA with Tukey's multiple comparisons, using the GraphPad Prism statistical program (GraphPad Software, San Diego, CA) with significance at $p \leq 0.05$. The chi-square goodness-of-fit test was used to test whether the distribution of the three soma size groups (0–599 μm^2, 600–1,199 μm^2, and 1,200–1,300 μm^2) of one species was the same as that of the other species.

3. Results

3.1. Murine DRGs can survive, and sensory neurons can grow neurites even in serum-free condition

To establish a primary 2D DRG neuron culture, L2-4 DRGs were collected from C57BL/6 mice and dissociated into single cell suspension by enzymatic digestion. The resulting DRGs were plated onto Poly-D-lysine/laminin-coated coverslips and cultured in neuronal growth medium. Unlike other studies [45–48], DRGs were maintained in the condition that serums and nerve-related growth factors (e.g. NGFs, GDNFs) were withdrawn to avoid their effects on the survival of neurons and neurite outgrowth. As shown in Fig. 1**A**, cells obtained from DRGs, including sensory neurons and satellite cells, could maintain viability for at least 15 days in serum and growth factor-free conditions. Although approximately 90% of sensory neurons extended neurites, it was very difficult to observe under the light microscope since two cell types overlapped with each other. To visualize sensory neurons, DRGs were stained with DAPI and three different neuronal markers: 200kD neurofilament (NF200) (all myelinated A-fibers); calcitonin gene-related peptide (CGRP) (peptidergic myelinated thin Aδ-fibers and unmyelinated C-fibers) and Substance P (peptidergic unmyelinated C-fibers). Sensory neurons expressed these markers, whereas satellite cells failed to do so (Fig. 1 **B**).

3.2. Murine DRG sensory neurons were purified using a BSA gradient centrifugation

It has been demonstrated that, in the peripheral nervous system, satellite cells are involved in the regulation of survival and axonal growth of neurons [49,50]. Since one of our main purposes of establishment of primary DRG neuronal culture is to investigate the direct effects of exogenous factors on the neurite outgrowth of sensory neurons or neurite toxicity, our next attempt was to separate sensory neurons from satellite cells. To do so, density gradient centrifugation was performed using 3.5% BSA solution. After purification, sensory neurons were enriched in the pellet fraction, while satellite cells were concentrated in the BSA layer. When cells in the pellet fraction were plated, the numbers of satellite cells (S100 positive) were reduced, compared to those before purification (Fig. 2**A**). To further confirm the quality of purification, both cells in the pellet fraction and the BSA layer were plated. As expected, cells in the pellet fraction could extend neurites, while cells in the BSA layer failed to do so (Fig. 2**B**).

Afterwards, the neurite outgrowth of neuronal cells in the pellet fraction were followed over time. The nerve fiber occupancy on the slides increased in a time dependent manner (10% nerve fiber occupancy at 24 h, 20–30% nerve fiber occupancy at 48 h, 50–60% nerve fiber occupancy at 72 h, and 70–80% nerve fiber occupancy at 96 h) (Fig. 3**A**). Neuronal cells in the pellet fraction were also segregated into three groups based on soma size (Fig. 3**B**). The size of soma was divided into small ($\leq$599 μm^2), medium (600–1,199 μm^2) and large (1,200–1,300 μm^2), which has been used for *in vivo* characterization of rodent DRGs [51–55]. The majority of murine sensory neuron somas were smaller than 599 μm^2 (Fig. 3**B**). Additionally, cells were stained with NF200, CGRP, and isolectin B4 (IB4) (non-peptidergic unmyelinated C-fibers) to further characterize the subpopulation of the DRG neurons. Interestingly, NF200 positive neurons always co-localized with CGRP positive neurons, but not IB4 positive neurons (Fig. 3**C**). Additionally, some CGRP positive neurons overlapped with IB4 positive neurons (Fig. 3**C**). Moreover, small size neurons consisted of NF200 negative/CGRP negative/IB4 positive neurons; medium size neurons consisted of NF200 negative/CGRP positive/IB4 positive, NF200 negative/CGRP positive/IB4 negative, or NF200 positive/CGRP positive/IB4 negative neurons; and large size neurons consisted of NF200 positive/CGRP positive/IB4 negative neurons (Fig. 3**C**).

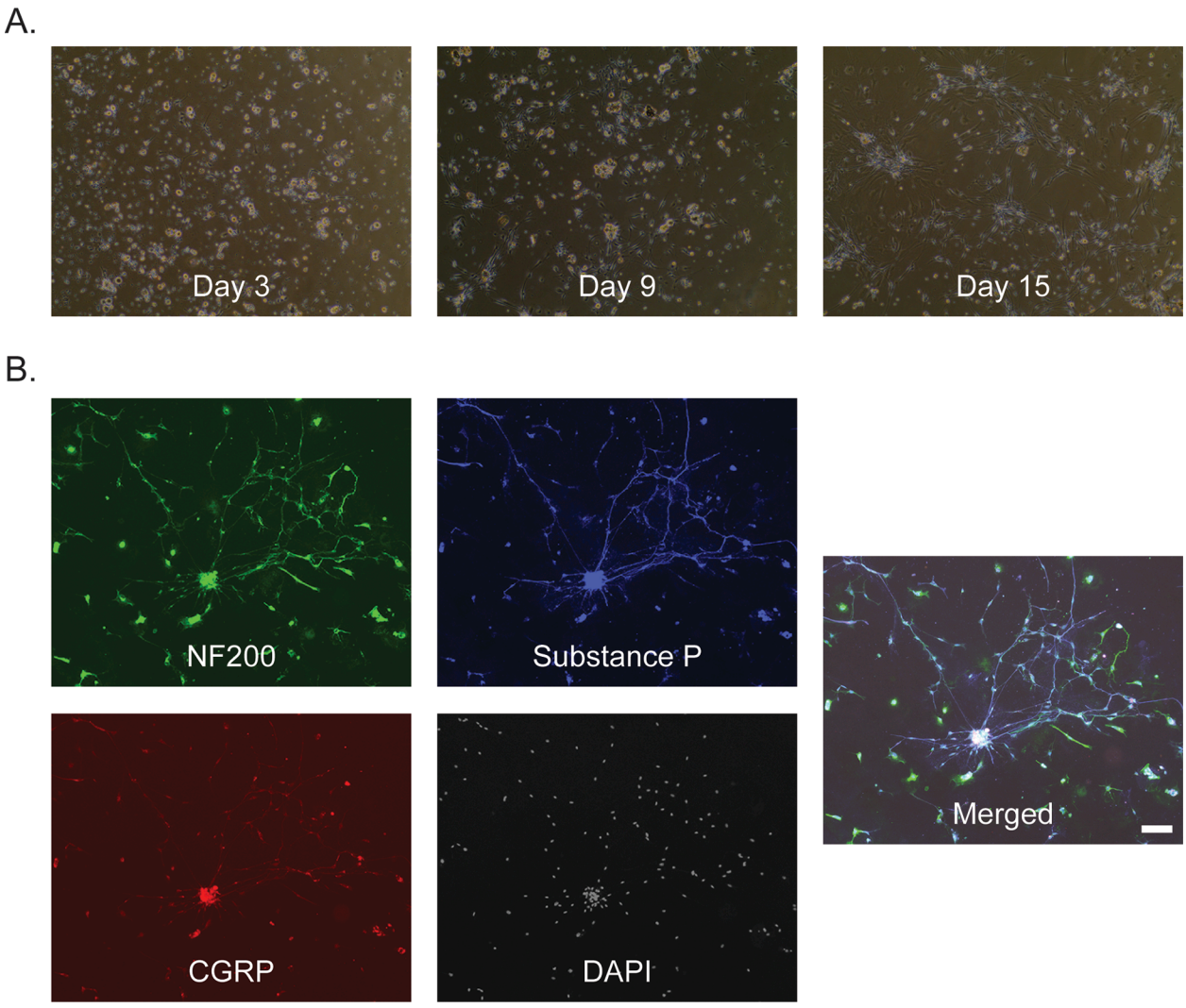

Fig. 1. Establishment of a murine primary 2D DRG neuron culture. (**A**) Representative bright field images of murine primary DRG culture (9-12x lumbar DRGs (L2-L4) from 8 to 12-week-old male C57BL/6 mice) seeded onto Poly-D-lysine/laminin coated coverslips at Day 3, 9, and 15. Magnification 4×. (**B**) Representative immunofluorescence images of (A) at Day 15. Sensory neurons were stained with antibodies against 200 kD neurofilament (NF200) (green) (all myelinated A-fibers), calcitonin gene-related peptide (CGRP) (red) (peptidergic myelinated thin Aδ-fibers and unmyelinated C-fibers), and Substance P (blue) (peptidergic unmyelinated C-fibers). DAPI (gray) is used for nuclear staining. Magnification 10×. Bar = 100 μm. (For interpretation of the references to colour in this figure legend, the reader is referred to the web version of this article.)

3.3. Cancer-derived factors stimulated the neurite outgrowth of murine sensory neurons, whereas a chemotherapeutic agent reduced.

Next, to test whether the growth of sensory neurons can be manipulated *in vitro* by exogenous factors, which again is our main purpose of the establishment of primary sensory neuron cultures, murine primary sensory neurons were treated with either cancer-derived CM or paclitaxel. We chose cancer-derived CM treatments since it is known to (i) enhance neurite sprouting [29,30] and (ii) induce pain behaviors in rodents when delivered with an intraplantar injection [56]. When sensory neurons were exposed to CM derived from human breast cancer cell line MDA-MB-231 cells, human prostate cancer cell line PC3 cells, human lung cancer cell line A549 cells, or murine lung cancer cell line LL/2 cells, the sprouting of sensory neurons significantly increased, compared to those exposed to control CM (Fig. 4**A&B**). However, CM derived from normal prostate epithelial cells did not affect the growth of sensory nerves (Fig. 4**C**). Interestingly, we observed more nerve sprouting in sensory neurons treated with CM derived from lung cancer cell lines (A549 and LL/2). This finding might be consistent with orthopedic surgeons' anecdotal evidence that bone metastasis from lung cancer are more painful than those from other cancer types (e.g. prostate cancer and breast cancer) (personal communications), although further studies to confirm this observation are clearly warranted. On the other hand, when sensory neurons were treated with paclitaxel, the growth of sensory nerve fibers was reduced in a dose dependent manner (Fig. 4**D&E**). Mouse sensory neurons were treated with 10 μM paclitaxel, since this dose is close to a physiological-dose [57].

For quantification of neurite outgrowth, we used a commercially available image analysis software, Visiopharm to automatically measure a total neurite length and Image J to count the numbers of the soma in each coverslip. Then, a total neurite length was normalized with soma count. To validate whether an automated method can accurately be used to measure neurite outgrowth, we first created a novel algorithm (called an "APP") using Visiopharm that enabled us to detect the somas and measure the length of their neurites based on structural differences and fluorescence intensity, respectively (Fig. 5**A**). Then, values obtained automatically (Visiopharm) were compared to those obtained manually (Image J). As shown in Fig. 5**B**, total neurite lengths obtained using these two different methods were highly correlated ($r^2 = 0.8975$). However, soma counts were not as highly correlated as total neurite lengths ($r^2 =$

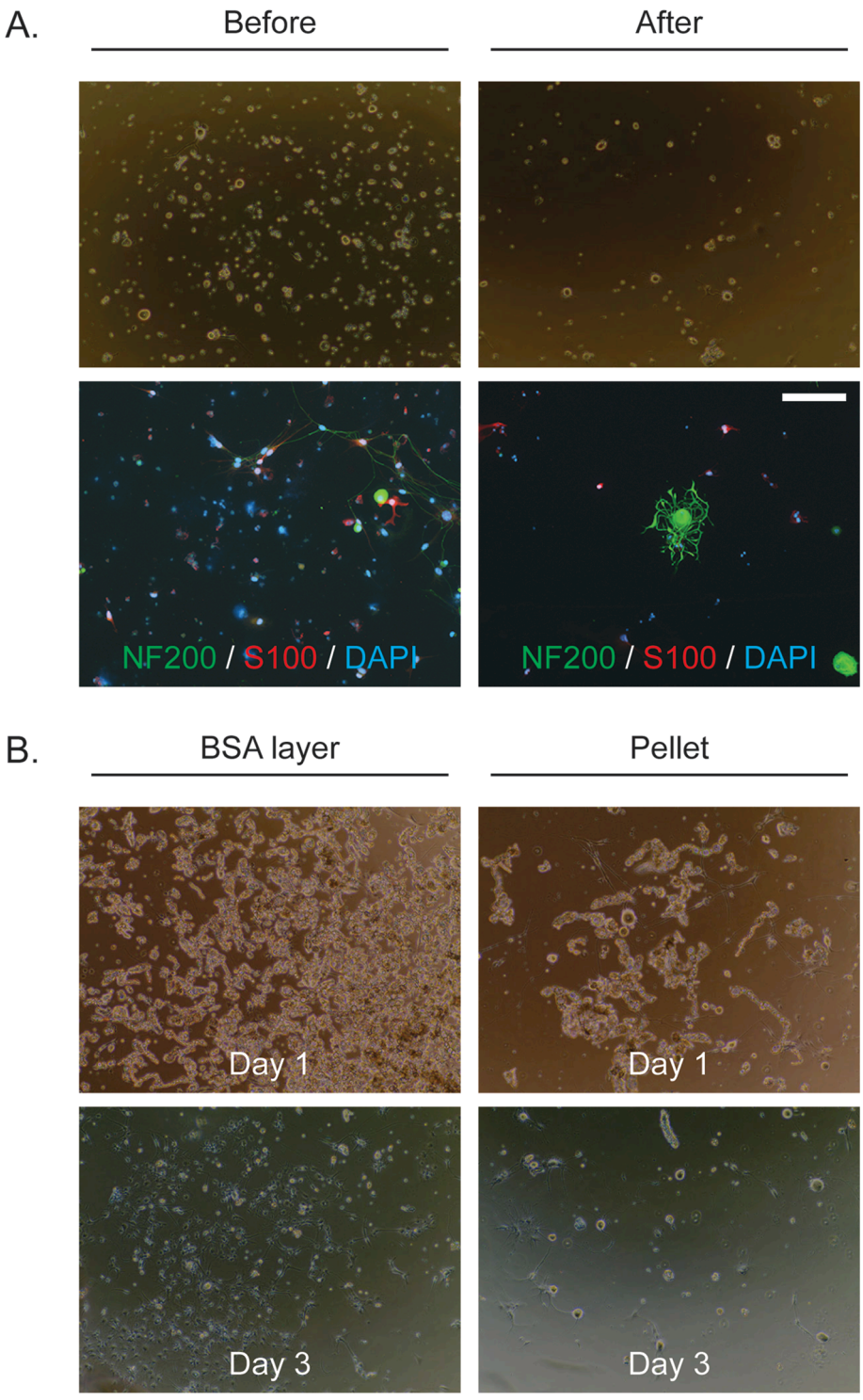

Fig.2. Purification of murine primary DRG sensory neurons using a BSA gradient centrifugation. (**A**) DRG cells were seeded onto Poly-D-lysine/laminin coated coverslips before or after a BSA gradient centrifugation [3.5% (W/V) BSA solution]. Representative bright field images of murine DRGs before and after a BSA gradient centrifugation (top panels). Magnification 4×. Representative immunofluorescence images murine DRGs before and after BSA centrifugation (bottom panels). Sensory neurons were stained with antibodies against 200kD neurofilament (NF200) (green), and satellite cells were stained with antibodies against S100b (red), DAPI (blue) is used for nuclear staining. Magnification 20×. Bar = 100 μm. (**B**) After a BSA gradient centrifugation, cells obtained from the pellet fraction (pellet) and BSA layer were seeded onto Poly-D-lysine/laminin coated coverslips. Representative bright field images of cells from the pellet fraction and BSA layer at Day 1 (top panels) and 3 (bottom panels). Magnification 4×. (For interpretation of the references to colour in this figure legend, the reader is referred to the web version of this article.)

0.1561) (Fig. 5**C**). This might in part be due to the difficulty to segregate the cluster of the somas into a single soma. These studies demonstrated the following: (i) the total neurite length obtained using an automated method were similar to that obtained manually; (ii) a manual counting method provided more accurate information regarding the numbers of soma than an automated method; and (iii) counting somas manually was not as time consuming as measuring neurite length. Therefore, we chose the quantification strategy described above.

3.4. The impact of cancer-derived factors and a chemotherapeutic agent on the expression of genes, associated with nerve growth and neuro-inflammatory pain, in murine sensory neurons

Next, to determine whether the alterations of sensory neuron length mediated by exogenous factors are associated with pain, gene expression analyses were performed by qPCR on murine primary sensory neurons treated with either cancer-derived CM or paclitaxel. In this case, we chose CM derived from A549 cells (A549 CM), since the greatest enhancement of murine primary sensory neuron sprouting was observed

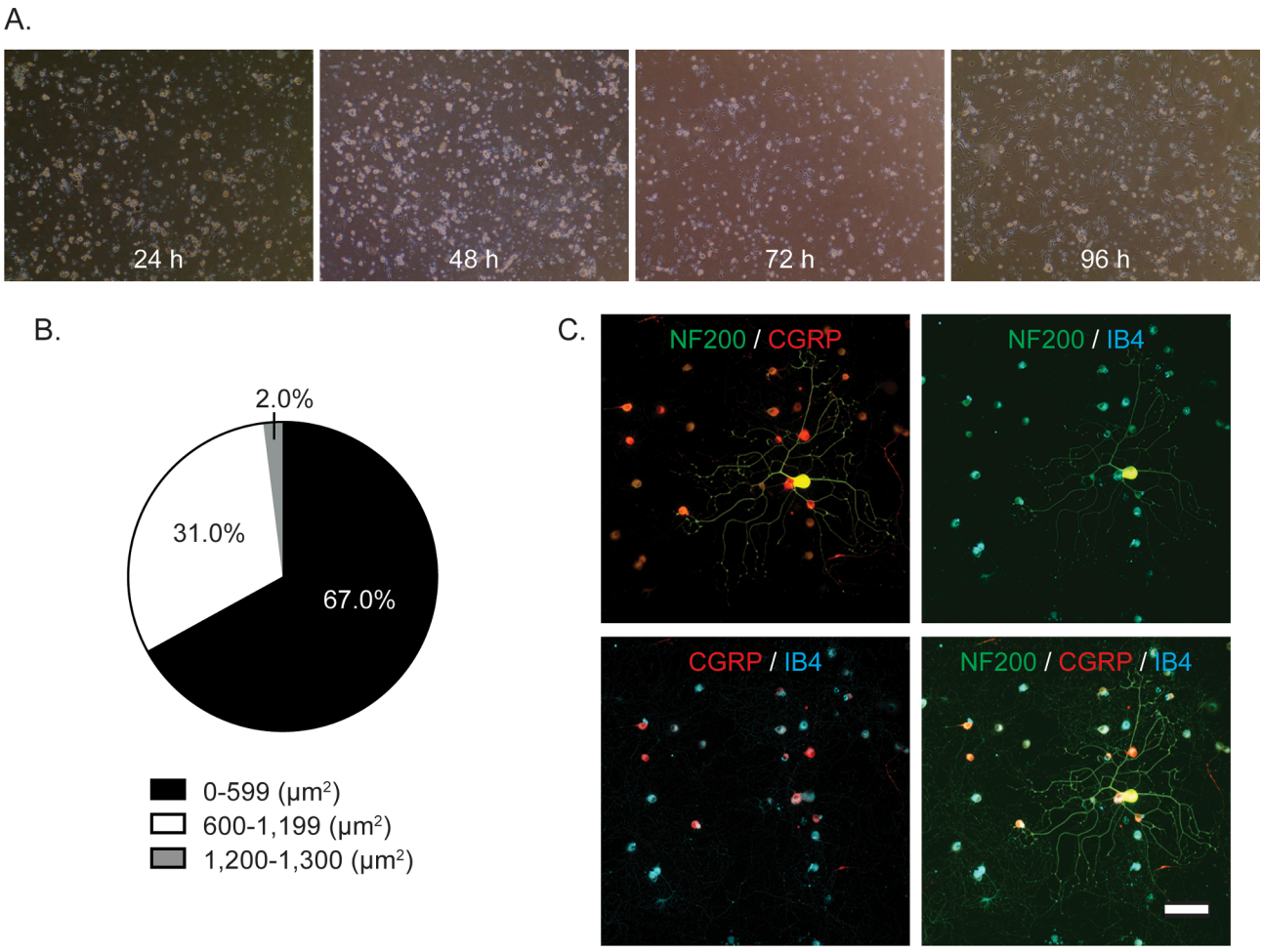

Fig. 3. Characterization of murine primary DRG sensory neurons. (**A**) Representative bright field images of murine primary DRG culture (9-12x lumbar DRGs (L2-L4) from 8 to 12-week-old male C57BL/6 mice) after a BSA gradient centrifugation [3.5% (W/V) BSA solution] seeded onto Poly-D-lysine/laminin coated coverslips at 24, 48, 72, and 96 h. Magnification 4x. (**B**) Quantification analysis of the cell size distribution of murine primary DRG sensory neurons (n = 467). Areas of soma (μm^2) of cells from (A) were measured using image J software. (**C**) Representative immunofluorescence images of murine primary DRG sensory neurons after a BSA gradient centrifugation. Sensory neurons were stained with antibodies against 200kD neurofilament (NF200) (Green) (all myelinated A-fibers), calcitonin gene-related peptide (CGRP) (red) (peptidergic myelinated thin Aδ-fibers and unmyelinated C-fibers), and isolectin B4 (IB4) (light blue) (non-peptidergic unmyelinated C-fibers). Magnification 10×. Bar = 100 μm. (For interpretation of the references to colour in this figure legend, the reader is referred to the web version of this article.)

when treated with A549 CM (Fig. 4**A**). To determine whether our observations in the neurite length changes mediated by exogenous factors correlate to gene expression patterns, the levels of growth associated protein 43 (GAP43), a nerve growth marker [58], and NF200 gene expression in A549 CM or paclitaxel-treated murine primary sensory neurons were measured. Consistent with our findings in the neurite length changes, A549 CM significantly increased GAP43 expression, while paclitaxel exerted opposite effects (Fig. 6**A**). A similar trend was observed in changes in NF200 gene expression patterns as those of GAP43, although it did not reach statistical significance (Fig. 6**B**). Then, gene expression levels of pain-related molecules, including neuropeptides (CGRP, Substance P, Bradykinin) and cytokines involved in pathological pain conditions [tumor necrosis factor-α (TNF-α), interleukin-6 (IL-6)] [59,60] were measured to determine the association between nerve growth and pain. Interestingly, patterns of gene expression changes were different depending on the treatments used. Neither A549 CM nor paclitaxel affected CGRP expression levels (Fig. 6**C**), while A549 CM significantly decreased Substance P expression levels (Fig. 6**D**), and both A549 CM and paclitaxel significantly increased Bradykinin expression levels in murine primary sensory neuron (Fig. 6**E**). Paclitaxel significantly increased TNF-α expression levels (Fig. 6**D**), whereas A549 CM significantly decreased IL-6 expression levels (Fig. 6**G**). Additionally, the gene expression levels of suppressor of cytokine signaling 3 (SOCS3) and immunoglobulin superfamily containing leucine rich repeat 2 (ISLR2), which were significantly increased in DRGs derived from patients with neuropathic pain, compared to those derived from patients without pain [36], were measured. SOCS3 and ISLR2 are known to be involved in development of cancer-related pain [61] and nociceptive sensory neuron development [62], respectively. In these cases, A549 CM significantly impacted on the gene expression of SOCS3 (increased, Fig. 6**H**) and ISLR2 (decreased, Fig. 6**I**), while paclitaxel failed to do so.

3.5. Sensory neurons obtained from non-human primate and human DRGs act similar to those of mice.

To enhance translational potential, non-human primate primary DRG sensory neuron culture was established using similar methods to establish murine primary sensory neuron culture. Consistent with murine culture, the BSA purification method could largely reduce satellite cell population, and about 90% of the viable neurons grew neurite in serum and growth factor-free conditions (Fig. 7**A**). Additionally, the majority of non-human primate sensory neuron somas were between 600 μm^2 to 1,199 μm^2 (Fig. 7**B**). Furthermore, non-human primate sensory neurons responded to cancer-derived CM (Fig. 7**C&D**) and paclitaxel treatment (Fig. 7**E&F**), similar to murine sensory neurons.

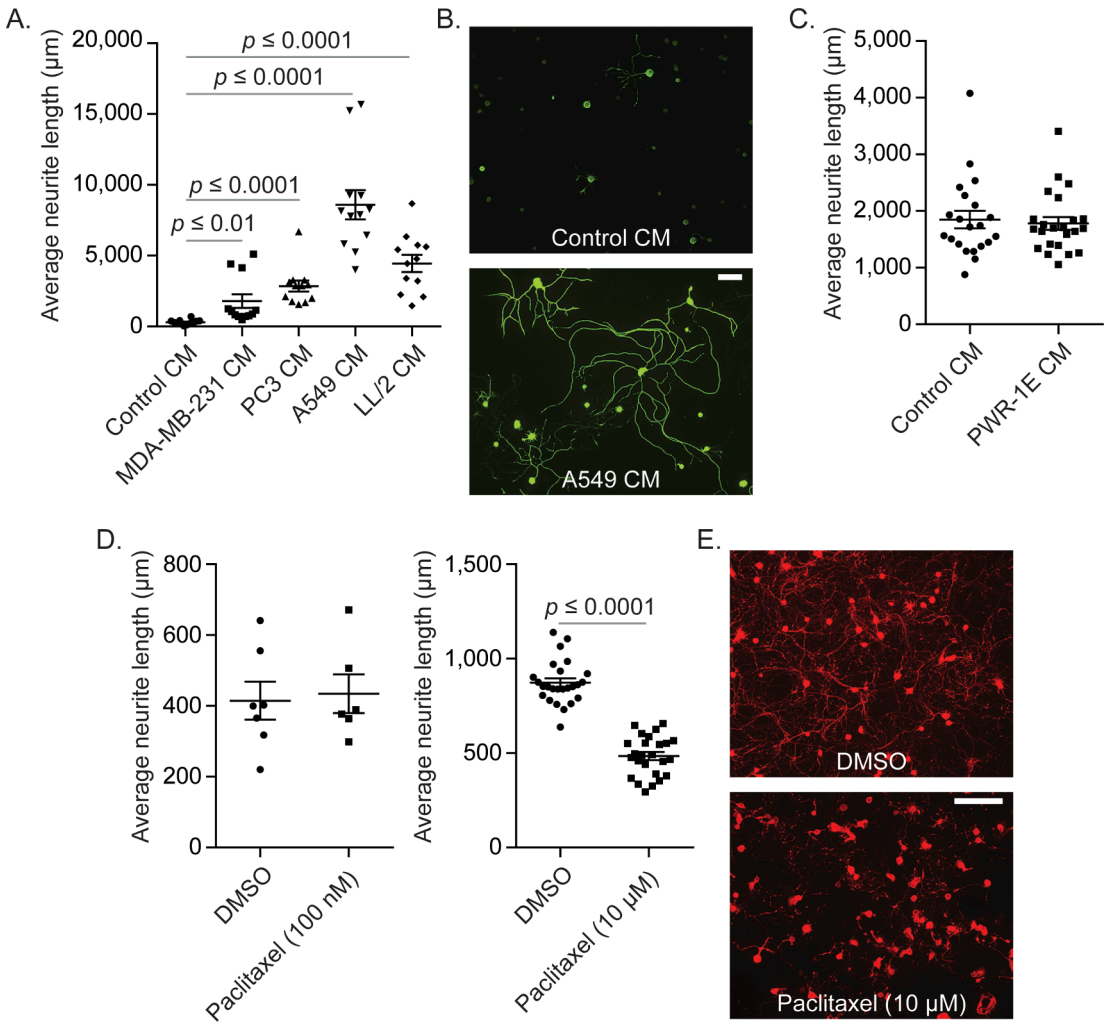

Fig. 4. Manipulation of the sprouting of murine primary DRG sensory neurons by exogenous factors. (**A**) Murine primary DRG sensory neurons were treated with either control medium (Control CM) or conditioned medium (CM, 0% serum) derived from human breast cancer cell line MDA-MB-231 cells (MDA-MB-231 CM), human prostate cancer cell line PC3 cells (PC3 CM), human lung cancer cell line A549 cells (A549 CM), or murine lung cancer cell line LL/2 cells (LL/2 CM) for 48 h. Sensory neurons were stained with antibodies against 200kD neurofilament (NF200). Quantification of the average of the total neurite length. Mean ± SEM. Student's *t*-test, significance at $p \leq 0.05$. The figure is a representative of two independent experiments, and 6 random images from each coverslip (n = 2) were analyzed in a blind manner. (**B**) Representative immunofluorescence images of murine primary DRG sensory neurons treated with either control or human lung cancer cell line A549 CM. Magnification 10×. Bar = 100 μm. (**C**) Murine primary DRG sensory neurons were treated with either control medium (Control CM) or CM derived from human normal prostate epithelial cell line PWR-1E cells (PWR-1E CM) for 48 h. Sensory neurons were stained with antibodies against NF200. Quantification of the average of the total neurite length. Mean ± SEM. Student's *t*-test. The figure is a representative of one independent experiment, and 7–8 random images from each coverslip (n = 3) were analyzed in a blind manner. (**D**) Murine primary DRG sensory neurons treated with either DMSO or paclitaxel (100 nM, 10 μM) for 24 h. Sensory neurons were stained with antibodies against PGP9.5. Quantification of the average of the total neurite length. Mean ± SEM. Student's *t*-test, significance at $p \leq 0.05$. Experiment was performed once, and 8–10 random images from each coverslip (n = 3) were analyzed in a blind manner. (**E**) Representative immunofluorescence images of murine primary DRG sensory neurons treated with either DMSO or paclitaxel (10 μM) for 24 h. Magnification 10×. Bar = 100 μm.

Non-human primate and human sensory neurons were treated with 1 μM paclitaxel, since a concentration of 10 μM used for mouse sensory neurons was too toxic to them (Data not shown).

Primary sensory neuron culture of human DRGs was also established. Consistent with murine and non-human primate culture, the BSA purification method could reduce satellite cell population, and about 93% of the viable neurons grew neurite in serum and growth factor-free conditions (Fig. 8**A**), and the majority of the soma size was smaller than 599 μm^2 (Fig. 8**B**). Since sensory neurons from three different species showed different size distributions of cell population, we sought to determine whether there are any similarities in the soma size distribution among murine, non-human primate, and human sensory neurons. Interestingly, the chi-square goodness-of-fit test showed that the distributions of the soma size were different among the three species (all *p*-values from pairwise comparisons less than 0.0001). Additionally, when neurons were treated with cancer-derived CM, the lengths of neurite were significantly longer than those treated with control CM (Fig. 8**C&D**). On the other hand, when neurons were treated with paclitaxel, the growth of neurite was significantly reduced compare to the neurons treated with vehicle (Fig. 8**E&F**).

4. Discussion

In this study, we demonstrated four important findings: (1) primary DRG sensory neuron cultures can be derived from mouse, non-human primate, and human tissues and cultured in serum and growth factor-free conditions, (2) a BSA gradient centrifugation method is useful to separate sensory neurons from satellite cells, (3) DRG sensory neurons maintain their heterogeneous subpopulations, and (4) the length of nerve fibers and gene expression pattern, associated with nerve growth,

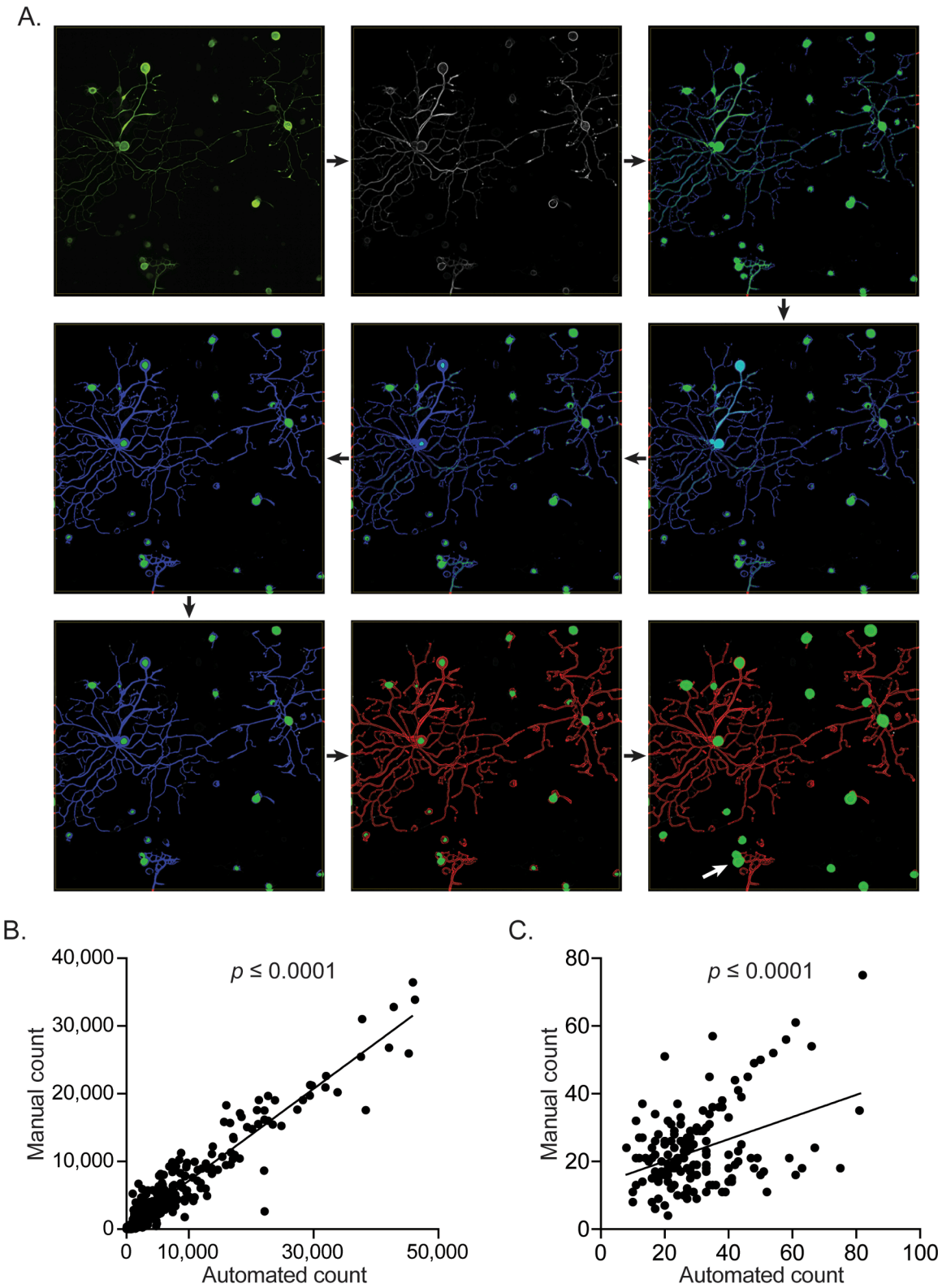

Fig. 5. Quantification of total neurite length by automated imaging analysis. (**A**) Representative images of the image-processing steps performed in the Visiopharm APP used for automated neurite length quantification and soma count, starting from the original fluorescent image of 200kD neurofilament (NF200) stained mouse DRG neurons (top left) to the final quantified image (bottom right) with relevant masks for neurite length (red) and soma count (green). Black arrow: direction of processing steps. White arrow: two neurons inaccurately counted as one. (**B**) 316 images of murine primary DRG sensory neurons stained with antibodies against NF200 were analyzed using the Visiopharm APP and by manual tracing using ImageJ software and values for total neurite length were plotted (μm): Linear regression analyses, significance at $p \leq 0.05$. (**C**) 164 images of murine primary DRG sensory neurons stained with antibodies against NF200 were analyzed using the Visiopharm APP and by manual counting using ImageJ software and values for total soma numbers were plotted (counts): Linear regression analyses, significance at $p \leq 0.05$. (For interpretation of the references to colour in this figure legend, the reader is referred to the web version of this article.)

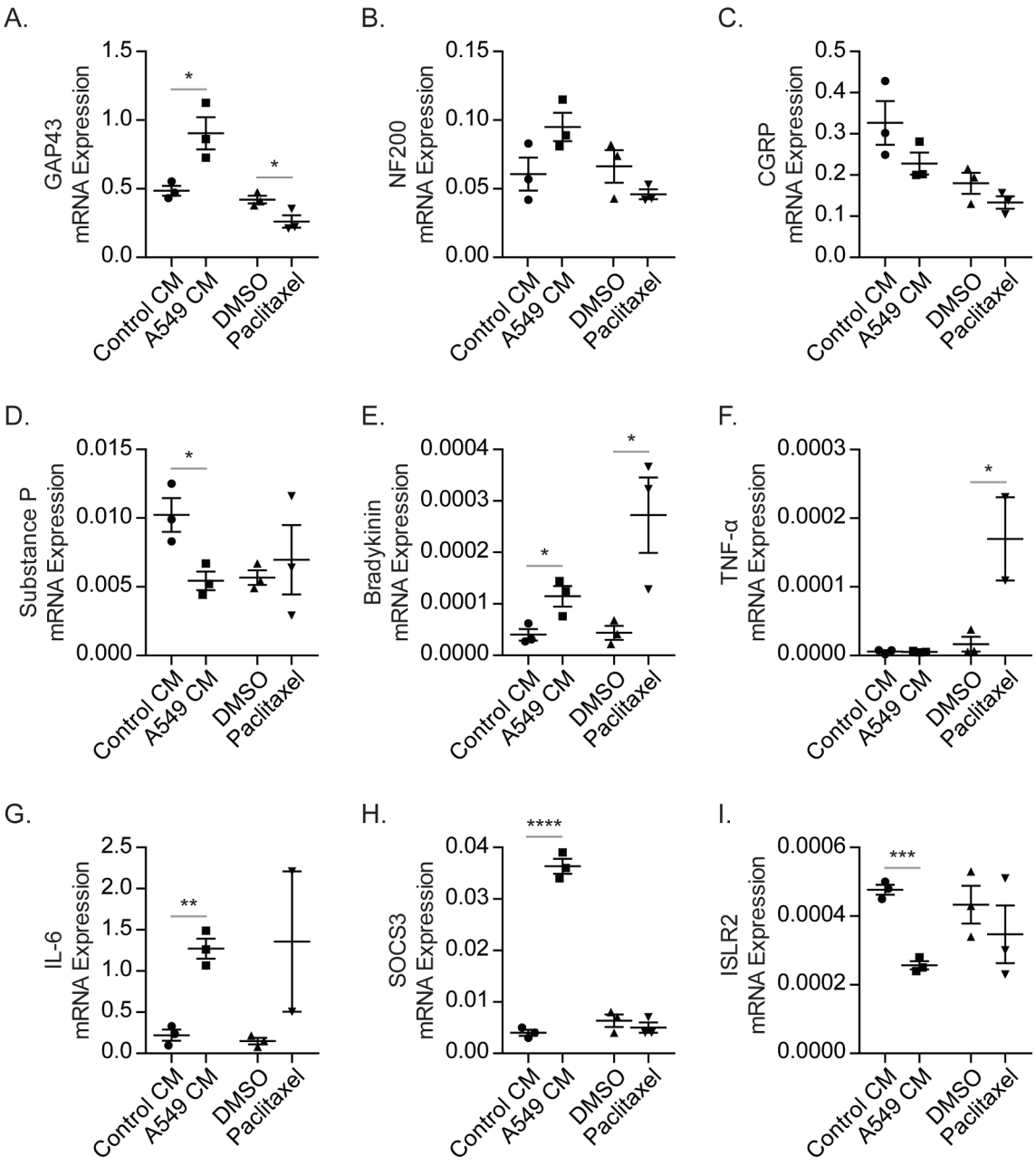

Fig. 6. Changes in expression of genes associated with nerve growth and pain in murine primary DRG sensory neurons by exogenous factors. Murine primary DRG sensory neuron cells were treated with control medium (Control CM) or human lung cancer cell line A549 cell-derived conditioned medium (A549 CM) for 48 h, and DMSO or paclitaxel (10 μM) for 24 h. Expression of (**A**) GAP43 and (**B**) NF200, which are genes associated with nerve growth. Expression of (**C**) CGRP, (**D**) Substance P, (**E**) Bradykinin, (**F**) TNF-α, (**G**) IL-6, (**H**) SOCS3, and (**I**) ISLR2, which are genes associated with neuro-inflammatory pain and nociceptor development. GAPDH was used reference gene. Delta-delta Ct method. Results were displayed as Mean ± SEM. Student's *t*-test. $^{*}p \leq 0.05$, $^{**}p \leq 0.01$, $^{***}p \leq 0.001$, $^{****}p \leq 0.0001$. GAP43: growth associated protein 43; NF200: 200kD neurofilament; CGRP: calcitonin gene-related peptide; TNF-α: tumor necrosis factor-α; IL-6: interleukin-6; SOCS3: suppressor of cytokine signaling 3; ISLR2: immunoglobulin superfamily containing leucine rich repeat 2.

and neuro-inflammatory pain and nociceptor development, of sensory neurons were altered by responding to exogenous factors, such as cancer-derived CM and reduced by responding to a chemotherapeutic agent. We developed a semi-automated quantification method which allowed us to analyze the neurite growth in an accurate and time-efficient manner. Together, these findings suggest that a semi-automated measurement of the neurite growth, along with gene expression analyses, of primary DRG sensory neurons can be a useful *in vitro* tool to study the impact of exogenous factors on the growth of sensory neurons. The schematic workflow of the primary DRG sensory neuron culture preparation and analyses, is described in Fig. 9.

Animal models have been widely used to study pathological mechanisms underlying human diseases and to test therapeutic strategies. Although *in vivo* studies are useful for addressing large-scale biological questions, *in vitro* methods are better suited for exploring micro-level mechanisms. In this study, using primary neuronal cultures, we demonstrated that (i) cancer-derived CM induced the sprouting of nerve fibers and (ii) the chemotherapeutic agent, paclitaxel inhibited the neurite outgrowth. One of the most important aspects of our studies is that the structural changes observed in our *in vitro* setting recapitulate pathological conditions observed in *in vivo* rodent models. For example, the inoculation of cancer cells into the bone of rodents resulted in increased neurite density around the bone, which is associated with CIBP behaviors [17,18]. Similarly, the systemic administration of

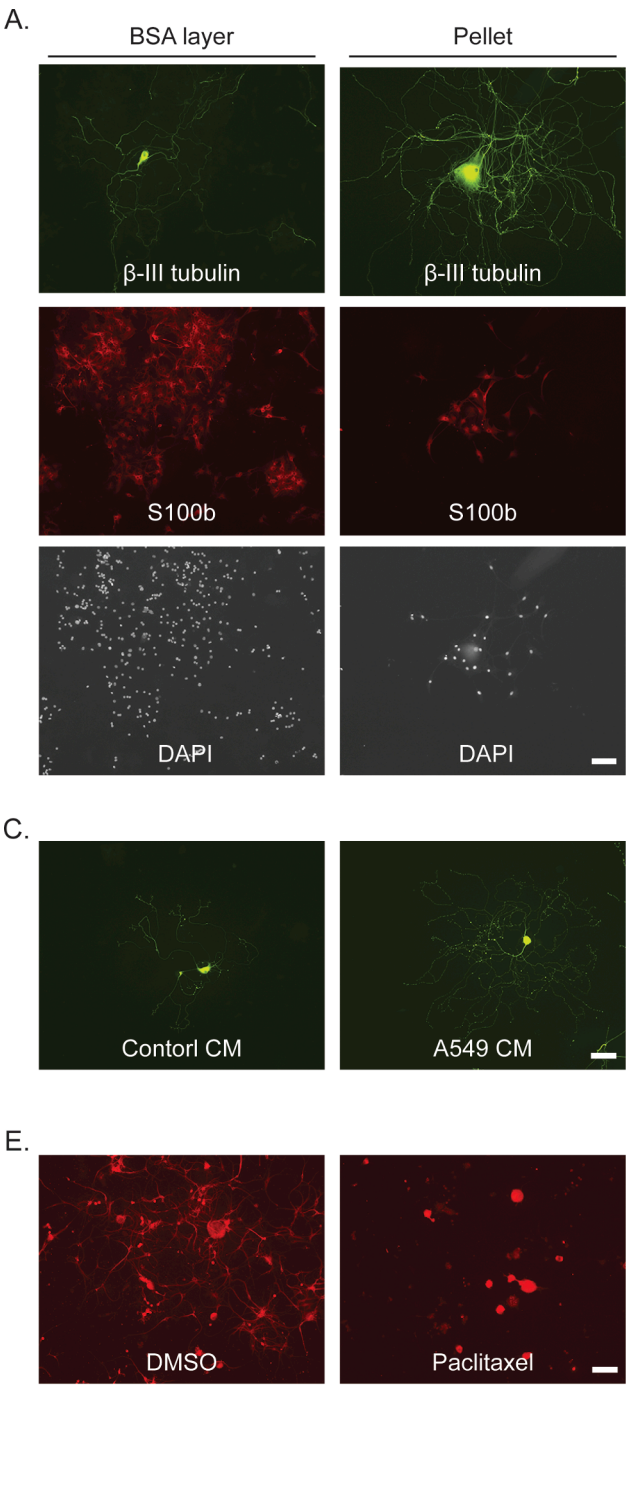

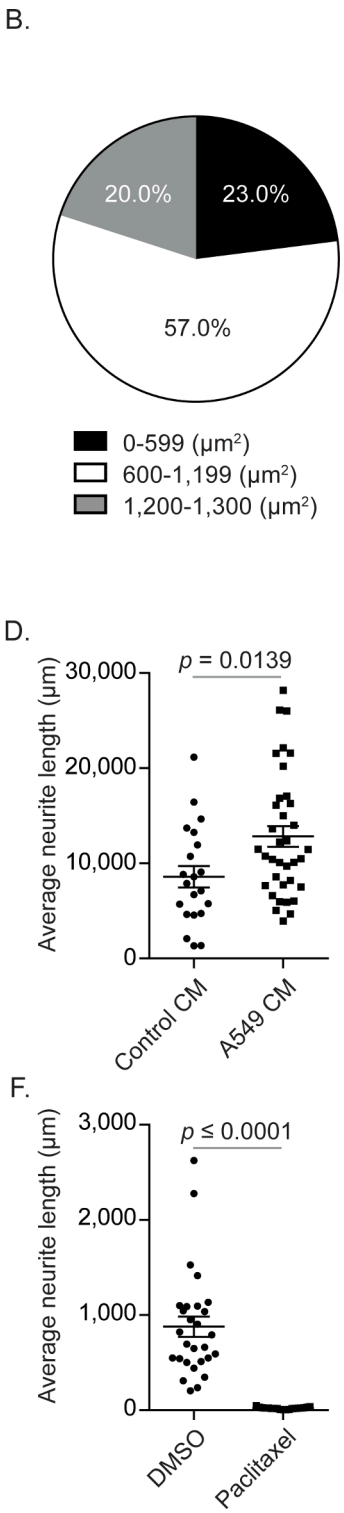

Fig. 7. Establishment of a non-human primate primary DRG sensory neuron culture. (**A**) Representative immunofluorescence images non-human primate DRGs (T12 and L1 of a healthy 8-year old female Rhesus macaque) before and after BSA centrifugation [3.5% (W/V) BSA solution]. Sensory neurons were stained with antibodies against β-III tubulin (green), and satellite cells were stained with antibodies against S100b (red), DAPI (gray) is used for nuclear staining. Magnification 10×. Bar = 100 μm. (**B**) Quantification analysis of the cell size distribution of non-human primate primary DRG sensory neurons (n = 309). Areas of soma (μm^2) of cells from (A) were measured using image J software. (**C**) Representative immunofluorescence images of non-human primate primary DRG sensory neurons treated with either control medium (Control CM) or human lung cancer cell line A549 cell-derived conditioned medium (A549 CM) (0% serum) for 72 h. Sensory neurons were stained with antibodies against β-III tubulin. Magnification 10×. Bar = 100 μm. (**D**) Quantification of the average of the total neurite length per image of (C): Mean ± SEM. Student's *t*-test, significance at $p \leq 0.05$. The figure is a representative of two independent experiments, and 8–12 random images from each coverslip (n = 3) were analyzed in a blind manner. (**E**) Representative immunofluorescence images of non-human primate primary DRG sensory neurons treated with either DMSO or paclitaxel (1 μM) for 24 h. Sensory neurons were stained with antibodies against PGP9.5. Magnification 10x. Bar = 100 μm. (**F**) Quantification of the average of the total neurite length per image of (E): Mean ± SEM. Student's *t*-test, significance at $p \leq 0.05$. Experiment was performed once, and 8–12 random images from each coverslip (n = 3) were analyzed in a blind manner. (For interpretation of the references to colour in this figure legend, the reader is referred to the web version of this article.)

paclitaxel to rodents led to a reduction of intraepidermal neuronal fiber density in the skin, which is a hall mark of CIPN [26,27]. Our *in vitro* primary DRG sensory culture manipulations were in line with these *in vivo* structural changes in peripheral sensory neurons. Thus, *in vitro* primary DRG sensory neuron culture system established in this study is an alternative tool to study the impact of soluble factors and/or direct cell–cell interactions on the architectural remodeling of sensory neurons.

Even though the use of rodent *in vivo* and *in vitro* models is essential for the advancement of science, the results of pre-clinical studies do not always translate to the human condition. In fact, a recent meta-analysis of 2,000 scientific studies using animal models revealed that more than half of these studies (~60%) either could not be replicated or failed to move forward to clinical trials [63]. To overcome this hurdle, studies using human tissues are receiving growing attention. Therefore, an additional salient finding of our studies is the reproducibility of pathologic neurite outgrowth following cancer-derived CM and paclitaxel-induced neurotoxicity in non-human primate and human primary

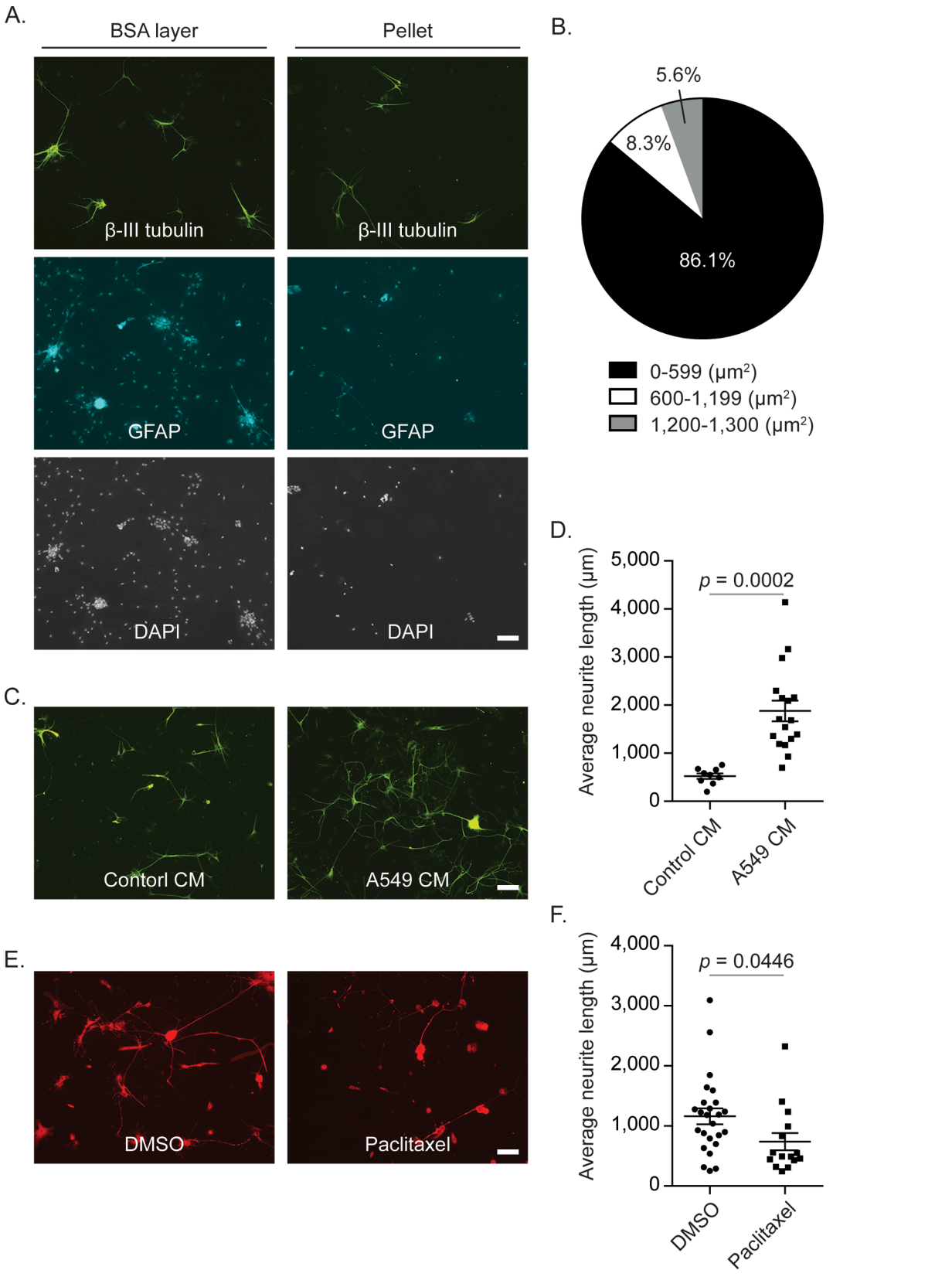

(caption on next page)

Fig. 8. Establishment of a human primary DRG sensory neuron culture. (**A**) Representative immunofluorescence images human primary DRGs (T10 of a 41-year-oldmale patient with discitis/osteomyelitis) before and after BSA centrifugation [3.5% (W/V) BSA solution]. Sensory neurons were stained with antibodies against β-III tubulin (green), and satellite cells were stained with antibodies against glial fibrillary acidic protein (GFAP) (blue), DAPI (gray) is used for nuclear staining. Magnification 10x. Bar = 100 μm. (**B**) Quantification analysis of the cell size distribution of human primary DRG sensory neurons (n = 72). Areas of soma (μm^2) of cells from (A) were measured using image J software. (**C**) Representative immunofluorescence images of human primary DRG sensory neurons treated with either control medium (Control CM) or human lung cancer cell line A549 cell-derived conditioned medium (A549 CM) (0% serum) for 72 h. Sensory neurons were stained with antibodies against β-III tubulin. Magnification 10x. Bar = 100 μm. (**D**) Quantification of the average of the total neurite length per image of (C): Mean ± SEM. Student's *t*-test, significance at $p \leq 0.05$. The figure is a representative of two independent experiments, and 8–13 random images from each coverslip (n = 2) were analyzed in a blind manner. (**E**) Representative immunofluorescence images of human primary DRG sensory neurons treated with either DMSO or paclitaxel (1 μM) for 24 h. Sensory neurons were stained with antibodies against PGP9.5. Magnification 10x. Bar = 100 μm. (**F**) Quantification of the average of the total neurite length per image of (E): Mean ± SEM. Student's *t*-test, significance at $p \leq 0.05$. Experiment was performed once, and 8–10 random images from each coverslip (n = 2) were analyzed in a blind manner. (For interpretation of the references to colour in this figure legend, the reader is referred to the web version of this article.)

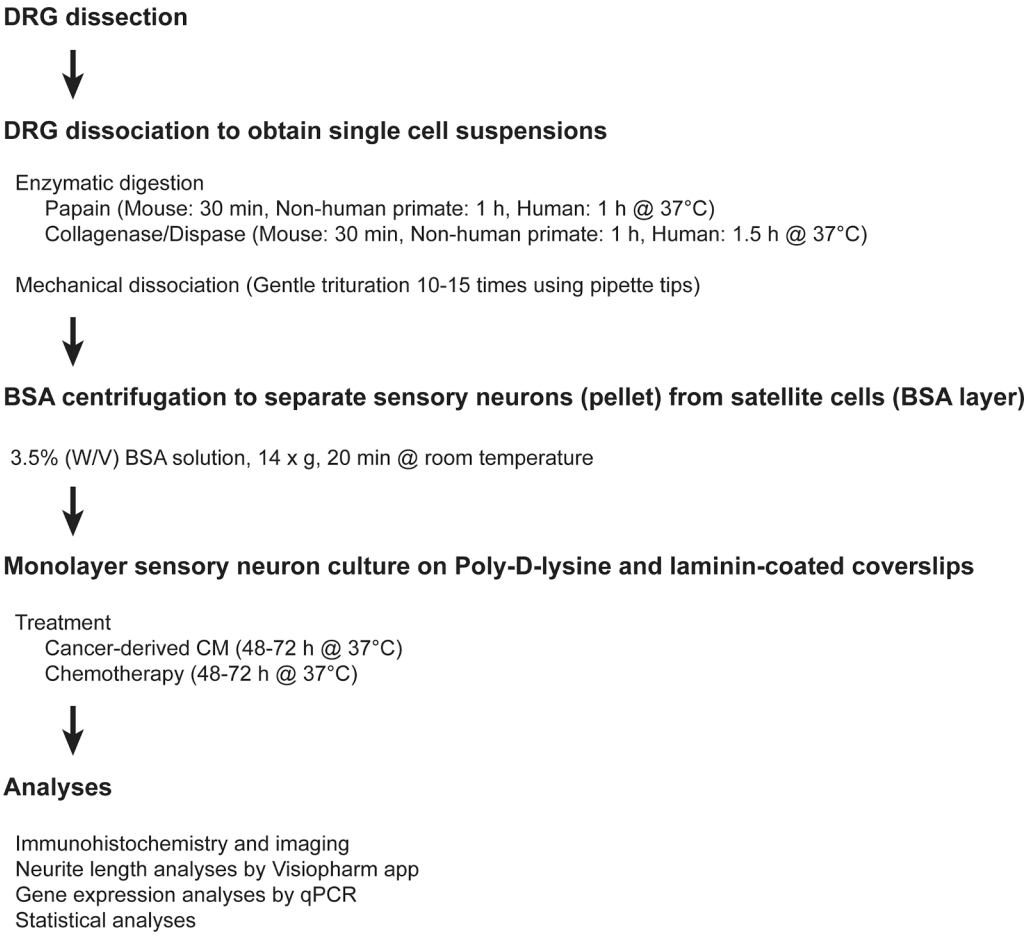

Fig. 9. The schematic workflow of the primary DRG sensory neuron culture preparation and analyses. Dorsal root ganglia of mice, non-human primate, or human, were dissociated by enzymatic digestion and mechanical dissociation to obtain single cell suspensions. Then, the resulting cells were segregated into sensory neurons and satellite cells using a BSA gradient centrifugation. Thereafter, sensory neurons were plated onto Poly-D-lysine and laminin-coated coverslips to establish monolayer culture. In some cases, sensory neurons were exposed to exogenous factors, such as cancer-derived conditioned medium (CM) or chemotherapeutic agents, and then changes in nerve fiber length and gene expression were analyzed by immunohistochemical analyses and qPCR, respectively.

neuronal cultures, similar to murine neuronal cultures. Our findings also indicate that our approach with rodent sensory neurons provides an alternative to the use of non-human primate or human primary sensory neuron samples so that these precious resources can be used specifically for translational assessments after more thorough characterization with mouse neuron cells. We also recognized that the use of non-human primate or human primary sensory neurons is not trivial and requires a great deal of resources to obtain fresh DRGs. In fact, one of the major challenges that we faced in the course of our studies was the coordination of multiple departments and laboratories. However, these constraints become minor when there is solid coordination and commitment among different departments and laboratories, and a frequent communication and engagement between physicians and basic scientists.

Our study also uncovered that our approach has some limitations. For example, although successful, the numbers of sensory neurons recovered from human DRG were relatively lower than those from mice and non-human primate, which limited the number of conditions performed in each experiment. This may be in part due to the difficulty in the digestion step of human DRGs. Human DRGs contains more connective tissues, including fibroblasts, blood vessels, and base membrane, than murine and non-human primate DRGs [64]. Consistent with this notion, during preparation of culture, the large number of fibroblasts were observed in human DRG, while few or no fibroblasts were seen in murine and non-human primate DRGs. Since thick connective tissues surrounding neurons may interfere with enzymatic reaction, it is crucial to cut the human DRGs into small pieces prior to the digestion step. Another potential limitation is the fact that the most abundant population of neurons in human DRG was small neurons in contrast to murine and non-human primate DRGs. Although the result is in line with previous findings [65,66], this suggests that our approach might not be ideal for studies targeting medium or large size of human sensory neurons. However, it is important to note that the cell size characterization method used in this study might not translate into non-human primate and/or human sensory neurons. Not only cell size differences, but also

there may be differences in responses to exogenous factors among DRGs derived from these species at a molecular and functional levels, although the effects of cancer-derived CM and paclitaxel treatments on nerve growth were consistent in all species. Indeed, nicotine evoked currents as well as nicotinic receptor expression patterns are significantly different between human and rodent DRGs [34]. Therefore, further subpopulation, molecular, and functional characterizations of murine, non-human primate, and human DRGs are clearly warranted.

Once logistic and technical optimization issues were overcome, we found that the image analysis of neurite length represents a challenge due to the lack of reliable methods to accurately measure the length of nerve fiber, and perhaps this is the reason why very few studies include this outcome. We found that manual measurement is accurate when performed by the same experimenter using a blinded method, but at the same time it is extremely time consuming and experimenter biases might reduce its reproducibility. These challenges prompted us to develop a method of image analysis aimed to reduce potential experimenter biases and increase efficiency in analysis time. In this study, we successfully developed a semi-automated method using the Visiopharm platform for the measurement of neurite length. The highly correlated values between this method and the manual approach using Image J demonstrate that our unbiased approach using the Visiopharm interface is accurate enough to consistently detect neurite length. One of the limitations of our approach however is the lack of tight correlation between automatically and manually generated soma counts. This might be attributed to the use of only one marker for two different cellular structures; i.e. NF200 staining was used to detect both soma count and neurite length. We uncovered that this approach does not allow the algorithm (APP) to differentiate a cluster of multiple neurons from individual neurons, something that the human eye could discern or infer. This limitation could be overcome by using different markers for neuronal soma (or nucleus) from neurites. Thus, the APP in this study was designed to maximize the accuracy of its neurite length measurements at the expense of accurate soma counts, since manually counting somas is significantly easier than manually tracing neurites. We are currently working to develop soma quantification APPs using nuclear stains for future studies capable of generating counts that are highly correlated with manual methods.

Although the importance of nerves for cancer progression has been appreciated [1], there are no treatments yet available which target the nerve-cancer interaction (e.g. cancer-induced nerve sprouting). In addition, chemotherapy is still the gold standard for cancer treatments and results in CIPN in many patients due to drug neurotoxicity. It is, therefore, critical to understand the interactions between cancer and/or chemotherapeutic agents, and sensory nerves, as well as how these interactions affect the progression of these painful complications, so that safer and more effective treatments can be developed. Although further electrophysiological analyses, phenotypical analyses, and chemical neural stimulation (e.g. capsaicin or KCL) on neuronal cell bodies might strengthen our findings, the measurement of neurite length and gene expression changes mediated by exogenous factors (e.g. cancer-derived factors, chemotherapeutic agents) can be a useful tool to elucidate the causes and mechanisms of these painful symptoms. For example, it has been suggested that nerve-related growth factors [29] or exosomes [30,56] derived from cancer cells induce cancer-related pain by stimulating neurite outgrowth [15–19], and that axonal damage mediated by chemotherapeutic agents through mitochondrial dysfunction in nerve cells and oxidative stress on nerve cells are responsible for CIPN symptoms [67]. We believe that our developed approaches could be used to reveal these underlying mechanisms. Moreover, the use of higher species' neuronal tissues in tandem with the development of an accurate and time-efficient methodology to measure neurite length under different pathological conditions will enhance clinical translational of our discovery. For success of this approach, a well-coordinated multidisciplinary team between physicians and basic scientists, which we began to establish, is clearly essential.

Author contributions

S.H.P., M.R.E., and Y.S. wrote the manuscript with input from all authors. S.H.P., M.R.E., C.M.P., M.C.K., R.S., W.H., E.A.R-S., and Y.S. designed study and contributed to data interpretation. S.H.P., M.M.F., H. D., and C.M.P. performed animal surgeries. M.C.K. provided monkey DRG. J.A.W. and W.H. provided human DRG. S.H.P. and M.M.F. established DRG culture. S.H.P., M.R.E., M.M.F., K.A.C., and C.M.P. performed immunohistochemistry and quantification analyses. F.H. performed statistical analyses. C.M.P., M.C.K., R.S., W.H., E.A.R-S., and Y.S. supervised the study. All authors reviewed and approved the final manuscript.

Declaration of Competing Interest

Y.S. has received research funding from TEVA Pharmaceuticals, but not relevant to this study. No conflict of interest exists for remaining authors.

Acknowledgements

This work is directly supported by the National Cancer Institute (R01-CA238888, Y.S.; R44-CA203184, Y.S.; and R21-CA248106, R.S. and E.A.R-S.), Department of Defense (W81XWH-17-1-0541, Y.S.; W81XWH-19-1-0045, Y.S.; and W81XWH-17-1-0542, C.M.P.), METAvivor (METAvivor Research Award, Y.S.), and the Wake Forest Baptist Comprehensive Cancer Center Internal Pilot Funding (Y.S.). This work is also supported by the National Cancer Institute's Cancer Center Support Grant award number P30-CA012197 issued to the Wake Forest Baptist Comprehensive Cancer Center. The authors wish to acknowledge the support of the Wake Forest Baptist Comprehensive Cancer Center Cell Engineering Shared Resource and Flow Cytometry Shared Resource, supported by the National Cancer Institute's Cancer Center Support Grant award number P30-CA012197. The content is solely the responsibility of the authors and does not necessarily represent the official views of the National Cancer Institute and Department of Defense.

References

[1] B. Boilly, S. Faulkner, P. Jobling, H. Hondermarck, Nerve dependence: from regeneration to cancer, Cancer Cell 31 (3) (2017) 342–354.
[2] S. Faulkner, P. Jobling, B. March, C.C. Jiang, H. Hondermarck, Tumor neurobiology and the war of nerves in cancer, Cancer Discov 9 (6) (2019) 702–710.
[3] N. Kuol, L. Stojanovska, V. Apostolopoulos, K. Nurgali, Role of the nervous system in cancer metastasis, J. Exp. Clin. Cancer Res. 37 (1) (2018) 5.
[4] J.J. Fagan, B. Collins, L. Barnes, F. D'Amico, E.N. Myers, J.T. Johnson, Perineural invasion in squamous cell carcinoma of the head and neck, Arch. Otolaryngol. Head Neck Surg. 124 (6) (1998) 637–640.
[5] C. Magnon, S.J. Hall, J. Lin, X. Xue, L. Gerber, S.J. Freedland, P.S. Frenette, Autonomic nerve development contributes to prostate cancer progression, Science 341 (6142) (2013) 1236361.
[6] Y. Hayakawa, K. Sakitani, M. Konishi, S. Asfaha, R. Niikura, H. Tomita, B.W. Renz, Y. Tailor, M. Macchini, M. Middelhoff, Z. Jiang, T. Tanaka, Z.A. Dubeykovskaya, W. Kim, X. Chen, A.M. Urbanska, K. Nagar, C.B. Westphalen, M. Quante, C.S. Lin, M.D. Gershon, A. Hara, C.M. Zhao, D. Chen, D.L. Worthley, K. Koike, T.C. Wang, Nerve growth factor promotes gastric tumorigenesis through aberrant cholinergic signaling, Cancer Cell 31 (1) (2017) 21–34.
[7] C.M. Zhao, Y. Hayakawa, Y. Kodama, S. Muthupalani, C.B. Westphalen, G. T. Andersen, A. Flatberg, H. Johannessen, R.A. Friedman, B.W. Renz, A.K. Sandvik, V. Beisvag, H. Tomita, A. Hara, M. Quante, Z. Li, M.D. Gershon, K. Kaneko, J. G. Fox, T.C. Wang, D. Chen, Denervation suppresses gastric tumorigenesis, Sci. Transl. Med. 6 (250) (2014) 250ra115.
[8] J.L. Saloman, K.M. Albers, D. Li, D.J. Hartman, H.C. Crawford, E.A. Muha, A. D. Rhim, B.M. Davis, Ablation of sensory neurons in a genetic model of pancreatic ductal adenocarcinoma slows initiation and progression of cancer, Proc Natl Acad Sci U S A 113 (11) (2016) 3078–3083.
[9] C. Parker, S. Nilsson, D. Heinrich, S.I. Helle, J.M. O'Sullivan, S.D. Fossa, A. Chodacki, P. Wiechno, J. Logue, M. Seke, A. Widmark, D.C. Johannessen, P. Hoskin, D. Bottomley, N.D. James, A. Solberg, I. Syndikus, J. Kliment, S. Wedel, S. Boehmer, M. Dall'Oglio, L. Franzen, R. Coleman, N.J. Vogelzang, C.G. O'Bryan-Tear, K. Staudacher, J. Garcia-Vargas, M. Shan, O.S. Bruland, O. Sartor, A. Investigators, Alpha emitter radium-223 and survival in metastatic prostate cancer, N. Engl. J. Med. 369 (3) (2013) 213–223.

[10] P.W. Mantyh, The neurobiology of skeletal pain, Eur. J. Neurosci. 39 (3) (2014) 508–519.
[11] P.W. Mantyh, D.R. Clohisy, M. Koltzenburg, S.P. Hunt, Molecular mechanisms of cancer pain, Nat. Rev. Cancer 2 (3) (2002) 201–209.
[12] A.N. Lozano-Ondoua, A.M. Symons-Liguori, T.W. Vanderah, Cancer-induced bone pain: Mechanisms and models, Neurosci Lett 557 Pt A (2013) 52–59.
[13] J.R. Ghilardi, H. Rohrich, T.H. Lindsay, M.A. Sevcik, M.J. Schwei, K. Kubota, K. G. Halvorson, J. Poblete, S.R. Chaplan, A.E. Dubin, N.I. Carruthers, D. Swanson, M. Kuskowski, C.M. Flores, D. Julius, P.W. Mantyh, Selective blockade of the capsaicin receptor TRPV1 attenuates bone cancer pain, J. Neurosci. 25 (12) (2005) 3126–3131.
[14] T. Yoneda, K. Hata, M. Nakanishi, M. Nagae, T. Nagayama, H. Wakabayashi, T. Nishisho, T. Sakurai, T. Hiraga, Involvement of acidic microenvironment in the pathophysiology of cancer-associated bone pain, Bone 48 (1) (2011) 100–105.
[15] K.G. Halvorson, K. Kubota, M.A. Sevcik, T.H. Lindsay, J.E. Sotillo, J.R. Ghilardi, T. J. Rosol, L. Boustany, D.L. Shelton, P.W. Mantyh, A blocking antibody to nerve growth factor attenuates skeletal pain induced by prostate tumor cells growing in bone, Cancer Res. 65 (20) (2005) 9426–9435.
[16] A.P. Bloom, J.M. Jimenez-Andrade, R.N. Taylor, G. Castaneda-Corral, M. J. Kaczmarska, K.T. Freeman, K.A. Coughlin, J.R. Ghilardi, M.A. Kuskowski, P. W. Mantyh, Breast cancer-induced bone remodeling, skeletal pain, and sprouting of sensory nerve fibers, J. Pain 12 (6) (2011) 698–711.
[17] J.R. Ghilardi, K.T. Freeman, J.M. Jimenez-Andrade, W.G. Mantyh, A.P. Bloom, M. A. Kuskowski, P.W. Mantyh, Administration of a tropomyosin receptor kinase inhibitor attenuates sarcoma-induced nerve sprouting, neuroma formation and bone cancer pain, Mol Pain 6 (2010) 87.
[18] J.M. Jimenez-Andrade, A.P. Bloom, J.I. Stake, W.G. Mantyh, R.N. Taylor, K. T. Freeman, J.R. Ghilardi, M.A. Kuskowski, P.W. Mantyh, Pathological sprouting of adult nociceptors in chronic prostate cancer-induced bone pain, J. Neurosci. 30 (44) (2010) 14649–14656.
[19] W.G. Mantyh, J.M. Jimenez-Andrade, J.I. Stake, A.P. Bloom, M.J. Kaczmarska, R. N. Taylor, K.T. Freeman, J.R. Ghilardi, M.A. Kuskowski, P.W. Mantyh, Blockade of nerve sprouting and neuroma formation markedly attenuates the development of late stage cancer pain, Neuroscience 171 (2) (2010) 588–598.
[20] T.J. Price, M.D. Louria, D. Candelario-Soto, G.O. Dussor, N.A. Jeske, A. M. Patwardhan, A. Diogenes, A.A. Trott, K.M. Hargreaves, C.M. Flores, Treatment of trigeminal ganglion neurons in vitro with NGF, GDNF or BDNF: effects on neuronal survival, neurochemical properties and TRPV1-mediated neuropeptide secretion, BMC Neurosci 6 (2005) 4.
[21] D. Hong, M.R. Byers, R.J. Oswald, Dexamethasone treatment reduces sensory neuropeptides and nerve sprouting reactions in injured teeth, Pain 55 (2) (1993) 171–181.
[22] J.R. Ghilardi, K.T. Freeman, J.M. Jimenez-Andrade, K.A. Coughlin, M. J. Kaczmarska, G. Castaneda-Corral, A.P. Bloom, M.A. Kuskowski, P.W. Mantyh, Neuroplasticity of sensory and sympathetic nerve fibers in a mouse model of a painful arthritic joint, Arthritis Rheum. 64 (7) (2012) 2223–2232.
[23] S.R. Chartier, M.L. Thompson, G. Longo, M.N. Fealk, L.A. Majuta, P.W. Mantyh, Exuberant sprouting of sensory and sympathetic nerve fibers in nonhealed bone fractures and the generation and maintenance of chronic skeletal pain, Pain 155 (11) (2014) 2323–2336.
[24] W.H. Xiao, G.J. Bennett, Chemotherapy-evoked neuropathic pain: Abnormal spontaneous discharge in A-fiber and C-fiber primary afferent neurons and its suppression by acetyl-L-carnitine, Pain 135 (3) (2008) 262–270.
[25] J.P. Cata, H.R. Weng, A.W. Burton, H. Villareal, S. Giralt, P.M. Dougherty, Quantitative sensory findings in patients with bortezomib-induced pain, J. Pain 8 (4) (2007) 296–306.
[26] C. Siau, W. Xiao, G.J. Bennett, Paclitaxel- and vincristine-evoked painful peripheral neuropathies: loss of epidermal innervation and activation of Langerhans cells, Exp. Neurol. 201 (2) (2006) 507–514.
[27] G. Lauria, R. Lombardi, M. Borgna, P. Penza, R. Bianchi, C. Savino, A. Canta, G. Nicolini, P. Marmiroli, G. Cavaletti, Intraepidermal nerve fiber density in rat foot pad: neuropathologic-neurophysiologic correlation, J. Peripher. Nerv. Syst. 10 (2) (2005) 202–208.
[28] K.P. Das, T.M. Freudenrich, W.R. Mundy, Assessment of PC12 cell differentiation and neurite growth: a comparison of morphological and neurochemical measures, Neurotoxicol. Teratol. 26 (3) (2004) 397–406.
[29] A.A. Bapat, R.M. Munoz, D.D. Von Hoff, H. Han, Blocking Nerve Growth Factor Signaling Reduces the Neural Invasion Potential of Pancreatic Cancer Cells, PLoS ONE 11 (10) (2016), e0165586.
[30] M. Madeo, P.L. Colbert, D.W. Vermeer, C.T. Lucido, J.T. Cain, E.G. Vichaya, A. J. Grossberg, D. Muirhead, A.P. Rickel, Z. Hong, J. Zhao, J.M. Weimer, W. C. Spanos, J.H. Lee, R. Dantzer, P.D. Vermeer, Cancer exosomes induce tumor innervation, Nat. Commun. 9 (1) (2018) 4284.
[31] W. Chang, T. Berta, Y.H. Kim, S. Lee, S.Y. Lee, R.R. Ji, Expression and role of voltage-gated sodium channels in human dorsal root ganglion neurons with special focus on Nav1.7, species differences, and regulation by paclitaxel, Neurosci. Bull. 34 (1) (2018) 4–12.
[32] S.A. Malin, B.M. Davis, D.C. Molliver, Production of dissociated sensory neuron cultures and considerations for their use in studying neuronal function and plasticity, Nat. Protoc. 2 (1) (2007) 152–160.
[33] R. Liu, G. Lin, H. Xu, An efficient method for dorsal root ganglia neurons purification with a one-time anti-mitotic reagent treatment, PLoS ONE 8 (4) (2013), e60558.
[34] X. Zhang, J.E. Hartung, R.L. Friedman, H.R. Koerber, I. Belfer, M.S. Gold, Nicotine evoked currents in human primary sensory neurons, J. Pain 20 (7) (2019) 810–818.
[35] Y. Li, C.E. Tatsui, L.D. Rhines, R.Y. North, D.S. Harrison, R.M. Cassidy, C. A. Johansson, A.K. Kosturakis, D.D. Edwards, H. Zhang, P.M. Dougherty, Dorsal root ganglion neurons become hyperexcitable and increase expression of voltage-gated T-type calcium channels (Cav3.2) in paclitaxel-induced peripheral neuropathy, Pain 158 (3) (2017) 417–429.
[36] R.Y. North, Y. Li, P. Ray, L.D. Rhines, C.E. Tatsui, G. Rao, C.A. Johansson, H. Zhang, Y.H. Kim, B. Zhang, G. Dussor, T.H. Kim, T.J. Price, P.M. Dougherty, Electrophysiological and transcriptomic correlates of neuropathic pain in human dorsal root ganglion neurons, Brain 142 (5) (2019) 1215–1226.
[37] M.V. Valtcheva, B.A. Copits, S. Davidson, T.D. Sheahan, M.Y. Pullen, J.G. McCall, K. Dikranian, R.W.t. Gereau, Surgical extraction of human dorsal root ganglia from organ donors and preparation of primary sensory neuron cultures, Nat. Protoc. 11 (10) (2016) 1877–1888.
[38] S. Davidson, J.P. Golden, B.A. Copits, P.R. Ray, S.K. Vogt, M.V. Valtcheva, R. E. Schmidt, A. Ghetti, T.J. Price, R.W.T. Gereau, Group II mGluRs suppress hyperexcitability in mouse and human nociceptors, Pain 157 (9) (2016) 2081–2088.
[39] P. Yao, Y. Ding, Z. Han, Y. Mu, T. Hong, Y. Zhu, H. Li, Suppression of asparaginyl endopeptidase attenuates breast cancer-induced bone pain through inhibition of neurotrophin receptors, Mol. Pain 13 (2017), 1744806917708127.
[40] T. Yoneda, P.J. Williams, T. Hiraga, M. Niewolna, R. Nishimura, A bone-seeking clone exhibits different biological properties from the MDA-MB-231 parental human breast cancer cells and a brain-seeking clone in vivo and in vitro, J. Bone Miner. Res. 16 (8) (2001) 1486–1495.
[41] H. Wakabayashi, S. Wakisaka, T. Hiraga, K. Hata, R. Nishimura, M. Tominaga, T. Yoneda, Decreased sensory nerve excitation and bone pain associated with mouse Lewis lung cancer in TRPV1-deficient mice, J. Bone Miner. Metab. 36 (3) (2018) 274–285.
[42] T.T. Wu, R.A. Sikes, Q. Cui, G.N. Thalmann, C. Kao, C.F. Murphy, H. Yang, H. E. Zhau, G. Balian, L.W. Chung, Establishing human prostate cancer cell xenografts in bone: induction of osteoblastic reaction by prostate-specific antigen-producing tumors in athymic and SCID/bg mice using LNCaP and lineage-derived metastatic sublines, Int. J. Cancer 77 (6) (1998) 887–894.
[43] J. Popko, A. Fernandes, D. Brites, L.M. Lanier, Automated analysis of NeuronJ tracing data, Cytometry A 75 (4) (2009) 371–376.
[44] P. Cottrell, S. Ahmed, C. James, J. Hodson, P.J. McDonnell, S. Rauz, G.P. Williams, Neuron J is a rapid and reliable open source tool for evaluating corneal nerve density in herpes simplex keratitis, Invest. Ophthalmol. Vis. Sci. 55 (11) (2014) 7312–7320.
[45] P.B. Tran, R.E. Miller, S. Ishihara, R.J. Miller, A.M. Malfait, Spinal microglial activation in a murine surgical model of knee osteoarthritis, Osteoarthritis Cartilage 25 (5) (2017) 718–726.
[46] S. Katzenell, J.R. Cabrera, B.J. North, D.A. Leib, Isolation, purification, and culture of primary murine sensory neurons, Methods Mol. Biol. 1656 (2017) 229–251.
[47] T. Dong, S. Li, W. Liu, M. Yan, J. Yu, X. Deng, A new method for primary culture of mouse dorsal root ganglion neurons, bioRxiv (2018) 466110.
[48] M. Au Fornaro, H. Au Sharthiya, V. Au Tiwari, Adult mouse DRG explant and dissociated cell models to investigate neuroplasticity and responses to environmental insults including viral infection, JoVE 133 (2018) e56757.
[49] K.R. Jessen, Glial cells, Int. J. Biochem. Cell Biol. 36 (10) (2004) 1861–1867.
[50] R.D. Fields, B. Stevens-Graham, New insights into neuron-glia communication, Science 298 (5593) (2002) 556–562.
[51] X. Zhao, Z. Tang, H. Zhang, F.E. Atianjoh, J.Y. Zhao, L. Liang, W. Wang, X. Guan, S. C. Kao, V. Tiwari, Y.J. Gao, P.N. Hoffman, H. Cui, M. Li, X. Dong, Y.X. Tao, A long noncoding RNA contributes to neuropathic pain by silencing Kcna2 in primary afferent neurons, Nat. Neurosci. 16 (8) (2013) 1024–1031.
[52] J.E. Roa-Coria, J.B. Pineda-Farias, P. Barragan-Iglesias, G.N. Quinonez-Bastidas, A. Zuniga-Romero, J.C. Huerta-Cruz, J.G. Reyes-Garcia, F.J. Flores-Murrieta, V. Granados-Soto, H.I. Rocha-Gonzalez, Possible involvement of peripheral TRP channels in the hydrogen sulfide-induced hyperalgesia in diabetic rats, BMC Neurosci 20 (1) (2019) 1.
[53] Q. Mao, J. Yuan, X. Ming, S. Wu, L. Chen, A. Bekker, T. Yang, Y.X. Tao, Role of dorsal root ganglion K2p1.1 in peripheral nerve injury-induced neuropathic pain, Mol. Pain 13 (2017), 1744806917701135.
[54] C. Lyu, G.W. Lyu, A. Martinez, T.S. Shi, Effect of nerve injury on the number of dorsal root ganglion neurons and autotomy behavior in adult Bax-deficient mice, J Pain Res 10 (2017) 2079–2087.
[55] M. Malet, P.R. Brumovsky, VGLUTs and Glutamate Synthesis-Focus on DRG Neurons and Pain, Biomolecules 5 (4) (2015) 3416–3437.
[56] A. Bhattacharya, M.N. Janal, R. Veeramachaneni, I. Dolgalev, Z. Dubeykovskaya, N.H. Tu, H. Kim, S. Zhang, A.K. Wu, M. Hagiwara, A.R. Kerr, M.D. DeLacure, B. L. Schmidt, D.G. Albertson, Oncogenes overexpressed in metastatic oral cancers from patients with pain: potential pain mediators released in exosomes, Sci. Rep. 10 (1) (2020) 14724.
[57] F.A. Fitzpatrick, R. Wheeler, The immunopharmacology of paclitaxel (Taxol), docetaxel (Taxotere), and related agents, Int. Immunopharmacol. 3 (13–14) (2003) 1699–1714.
[58] A.B. Oestreicher, P.N. De Graan, W.H. Gispen, J. Verhaagen, L.H. Schrama, B-50, the growth associated protein-43: modulation of cell morphology and communication in the nervous system, Prog. Neurobiol. 53 (6) (1997) 627–686.
[59] L. Leung, C.M. Cahill, TNF-alpha and neuropathic pain–a review, J Neuroinflammation 7 (2010) 27.
[60] J. Gonzalez-Lopez, F. Macias-Garcia, J. Larino-Noia, J.E. Dominguez-Munoz, Theoretical approach to local infusion of antibiotics for infected pancreatic necrosis, Pancreatology 16 (5) (2016) 719–725.

[61] J. Wei, M. Li, D. Wang, H. Zhu, X. Kong, S. Wang, Y.L. Zhou, Z. Ju, G.Y. Xu, G. Q. Jiang, Overexpression of suppressor of cytokine signaling 3 in dorsal root ganglion attenuates cancer-induced pain in rats, Mol. Pain 13 (2017), 1744806916688901.
[62] K. Mandai, T. Guo, C. St Hillaire, J.S. Meabon, K.C. Kanning, M. Bothwell, D. D. Ginty, LIG family receptor tyrosine kinase-associated proteins modulate growth factor signals during neural development, Neuron 63 (5) (2009) 614–627.
[63] N. Tageja, Bridging the translation gap - new hopes, new challenges, Fundam. Clin. Pharmacol. 25 (2) (2011) 163–171.
[64] R.V. Haberberger, C. Barry, N. Dominguez, D. Matusica, Human dorsal root ganglia, Front. Cell. Neurosci. 13 (271) (2019).
[65] S. Davidson, B.A. Copits, J. Zhang, G. Page, A. Ghetti, R.W. Gereau, Human sensory neurons: Membrane properties and sensitization by inflammatory mediators, Pain 155 (9) (2014) 1861–1870.
[66] U. Anand, M. Sinisi, M. Fox, A. MacQuillan, T. Quick, Y. Korchev, C. Bountra, T. McCarthy, P. Anand, Mycolactone-mediated neurite degeneration and functional effects in cultured human and rat DRG neurons: Mechanisms underlying hypoalgesia in Buruli ulcer, Mol. Pain 12 (2016).
[67] Y. Han, M.T. Smith, Pathobiology of cancer chemotherapy-induced peripheral neuropathy (CIPN), Front. Pharmacol. 4 (2013) 156.

ORIGINAL ARTICLE

Journal of Cachexia, Sarcopenia and Muscle (2021)
Published online in Wiley Online Library (wileyonlinelibrary.com) **DOI:** 10.1002/jcsm.12714

Activated mast cells in skeletal muscle can be a potential mediator for cancer-associated cachexia

D. Brooke Widner[1], Chun Liu[2], Qingxia Zhao[1], Sarah Sharp[1,3], Matthew R. Eber[1], Sun H. Park[1], D. Clark Files[2] & Yusuke Shiozawa[1]*

[1]*Department of Cancer Biology and Comprehensive Cancer Center, Wake Forest University Health Sciences, Winston-Salem, NC, USA;* [2]*Internal Medicine-Sections in Pulmonary and Critical Care Medicine and Geriatrics and the Critical Illness Injury and Recovery Research Center, Wake Forest University Health Sciences, Winston-Salem, NC, USA;* [3]*Department of Biology, Wake Forest University, Winston-Salem, NC, USA*

Abstract

Background Eighty per cent of United States advanced cancer patients faces a worsened prognosis due to cancer-associated cachexia. Inflammation is one driver of muscle atrophy in cachexia, and skeletal muscle-resident immune cells could be a source of inflammation. This study explores the efficacy of cancer activated skeletal muscle-resident mast cells as a biomarker and mediator of cachexia.

Methods Individual gene markers for immune cells were assessed in a publicly available colon carcinoma cohort of normal ($n = 3$), moderate cachexia ($n = 3$), and severe cachexia ($n = 4$) mice. Lewis lung carcinoma (LL/2) cells induced cachexia in C57BL/6 mice, and a combination of toluidine blue staining, immunofluorescence, quantitative polymerase chain reaction, and western blots measured innate immune cell expression in hind limb muscles. *In vitro* measurements included C2C12 myotube diameter before and after treatment with media from primary murine mast cells activated with LL/2 conditioned media. To assess translational potential in human samples, innate immune cell signatures were assessed for correlation with skeletal muscle atrophy and apoptosis, dietary excess, and cachexia signatures in normal skeletal muscle tissue. Gene set enrichment analysis was performed with innate immune cell signatures in publicly available cohorts for upper gastrointestinal (GI) cancer and pancreatic ductal adenocarcinoma (PDAC) patients (accession: GSE34111 and GSE130563, respectively).

Results Individual innate immunity genes (TPSAB1 and CD68) showed significant increases in severe cachexia (weight loss $> 15\%$) mice in a C26 cohort (GSE24112). Induction of cachexia in C57BL/6 mice with LL/2 subcutaneous injection significantly increased the number of activated skeletal muscle-resident degranulating mast cells. Murine mast cells activated with LL/2 conditioned media decreased C2C12 myotube diameter ($P \leq 0.05$). Normal human skeletal muscle showed significant positive correlations between innate immune cell signatures and muscle apoptosis and atrophy, dietary excess, and cachexia signatures. The mast cell signature was up-regulated (positive normalized enrichment score and false discovery rate ≤ 0.1) in upper GI cachectic patients ($n = 12$) compared with control ($n = 6$), as well as in cachectic PDAC patients ($n = 17$) compared with control patients ($n = 16$).

Conclusions Activated skeletal muscle-resident mast cells are enriched in cachectic muscles, suggesting skeletal-muscle resident mast cells may serve as a biomarker and mediator for cachexia development to improve patient diagnosis and prognosis.

Keywords Cancer-associated cachexia; Mast cells; Degranulation; Innate immunity; Skeletal muscle

Received: 15 September 2020; Revised: 14 April 2021; Accepted: 19 April 2021
**Correspondence to: Yusuke Shiozawa, Wake Forest University Health Sciences, Medical Center Blvd, Winston-Salem, NC 27157-1082, USA. Phone: 336-716-8743, Fax: 336-716-0255, Email: yshiozaw@wakehealth.edu*

© 2021 The Authors. Journal of Cachexia, Sarcopenia and Muscle published by John Wiley & Sons Ltd on behalf of Society on Sarcopenia, Cachexia and Wasting Disorders
This is an open access article under the terms of the Creative Commons Attribution-NonCommercial-NoDerivs License, which permits use and distribution in any medium, provided the original work is properly cited, the use is non-commercial and no modifications or adaptations are made.

Introduction

In general, 50% of all collective cancer patients, and 80% of all advanced cancer patients, in the United States will experience rapid weight loss of 5% or more of their total body weight within a 6 month timeframe. This condition is clinically designated as cancer-associated cachexia[1,2] and is concomitant with both a reduced quality of life and an overall worsened prognosis.[1,3] Indeed, one-third of all cancer-related deaths are now being attributed to cancer-associated cachexia, due to cachexia-driven systemic organ failure.[1,4] Historically, the strategy for caring for cachexia patients has been to focus on treating the cancer. Unfortunately, cancer treatments are inherently more difficult in cachectic patients who are often unable to undergo major surgeries and full chemotherapy treatments.[3,4] Patients in the final stage of cachexia, no longer respond to any form of cancer treatment, and weight loss continues to progress in spite of increased nutrient intake or supplementation.[2] As a result, treatment plans for these patients are primarily palliative in nature.[2,5] To date, there are no standard approved therapeutic options for cancer-associated cachexia.

Cancer-associated cachexia is an incredibly complex and variable metabolic syndrome, making both treatment and early identification of at-risk patients a challenge.[6,7] A general consensus in the field is that the condition's characteristic skeletal muscle mass loss is due to a combination of increased protein degradation and decreased protein synthesis. This imbalance between degradation and synthesis is thought to largely be driven by inflammatory factors, such as tumour-necrosis factor-α and interleukin 6 (IL-6).[1,3,5,6,8–10] However, the usefulness of these circulating cytokines as biomarkers for the development of cachexia has been met with variable levels of success.[5,6] Additionally, while specific inflammatory cytokine inhibitors have been tested in therapeutic studies for cancer-associated cachexia, these studies have been largely ineffective in part due to targeting only individual cytokines.[6,11,12] One strategy for overcoming this obstacle to treatment, is to examine common sources of these inflammatory cytokines, such as cells from the adaptive or innate immune system. One potential cell type fitting this description is the mast cells.[13]

Mast cells are granulocytes most commonly known for their role in allergies. They circulate throughout the body in their progenitor form, and then upon differentiation move to reside in tissues as a long-lived sentinel cell of the innate immune system. Upon activation through a stimulus, mast cells will degranulate and release inflammatory mediators, including histamine, cytokines, and proteases into the surrounding area, rapidly triggering an inflammatory response and attracting additional immune cells to the area.[13,14] Following this initial release of inflammatory factors, mast cells will then proceed to generate additional inflammatory mediators through *de novo* synthesis, increasing inflammation over time. Furthermore, differentiated mature mast cells reside naturally in the connective tissue, between individual skeletal muscle fibres, making them an immediate source of inflammation in muscle tissue. Notably, mast cells have been previously implicated in the inflammatory myopathy, polymyositis,[15] as well as in the genetic disorder Duchenne muscular dystrophy,[16] but have not been looked at in depth for their role in cancer-associated cachexia. Examining the presence and activation of resident skeletal muscle mast cells in cachectic samples is necessary to ascertain the usability of mast cells as a biomarker for cachexia development, as well as present a potential new therapeutic target for the treatment or prevention of cancer-associated cachexia.

In this paper, a combination of *in vivo*, *in vitro*, and bioinformatics techniques were used to assess the presence of immune cells in cachectic muscle tissue. A mouse colon carcinoma cachexia cohort showed changes in genes associated with innate immune cell genes, but not adaptive immune cell genes.[17–19] The Lewis lung carcinoma (LL/2) model showed an increase in degranulating skeletal muscle-resident mast cells in cachectic mice compared with their non-cancer controls, while there was no significant change in the number of macrophages and neutrophils. Subsequently, murine mast cells were activated to degranulate through secreted factors from the LL/2 cells, and the activated mast cells decreased fibre size of murine C2C12 myotube cultures. Finally, human cohorts showed increased expression of mast cell activation signature in cachectic patients, as well as correlations with muscle apoptosis and atrophy signatures with the mast cell signature in normal muscle tissues.[18–30]

Materials and methods

Cell culture

The murine mastocytoma P815, lung carcinoma LL/2, and myoblast C2C12 cell lines were purchased from the American Type Culture Collection (ATCC, Manassas, VA). Cells lines were cultured in Dulbecco's Modified Eagle's Medium (DMEM) (Gibco, Waltham, MA), supplemented with 10% (*V*/V) foetal bovine serum (Gibco), 1% (V/V) penicillin and streptomycin (Gibco), and 1% (V/V) L-glutamine (Gibco), and all plates were maintained at 37°C with 5% CO_2.

Cachectic mouse model

Male C57BL/6 J mice (Jax Stock #00064) were purchased from Jackson Laboratories (Bar Harbour, ME). Mice were housed with ad libitum access to food and water. All experiments abided by the Institutional Animal Care and Use Committee (IACUC) guidelines of Wake Forest University Health Sciences

DOI: 10.1002/jcsm.12714

(Protocol A18-026). Male 5-month-old mice were inoculated with either 2.0 × 10^6 LL/2 cells in 100 μL of DMEM or 100 μL of serum-free DMEM through subcutaneous injection into the right flank. Tumour volume was tracked using a calliper, starting 10 days after injection of the tumour cells. Daily body mass was recorded for each mouse. The average daily food intake per mouse was calculated based on the average food consumed per each cage of five mice. At the time of harvest, tumour mass and tumour-free body mass were measured, following excision of the tumour.

Force transducer assays for muscle function

An *in vivo* force transducer (Aurora Scientific, Aurora, ON, Canada) was used for force frequency and time to fatigue measurements.[31] Electrodes stimulated plantarflexion of the right hind limb. The maximum contractile force [the highest elicited force following excitation with a range of increasing electrical stimulation frequencies (e.g. 20, 40, 60, 80, 100, 125, 150, 200, 250, and 300 Hz) every 2 min with a force transducer] was recorded. Time to muscle fatigue (the time it takes for the maximum force generated to decrease by 50% in response to repeated electrode stimulation at 60 Hz) was also recorded, following 5 min of rest.

Excised muscle measurements and immunostaining

The excised muscle mass of the soleus (SOL), extensor digitorum longus (EDL), tibialis anterior (TA), and gastrocnemius (GA) muscles were measured at harvest. Muscles were snap-frozen in liquid nitrogen for cryosectioning and immunostaining. Transverse sections were made using a Leica CM3050 S cryostat (Leica Biosystems, Wetzlar, Germany) to prepare 20 μm of thick sections on slides for immunofluorescence or immunohistochemistry staining. All microscopy quantifications were performed using three sections per muscle per mouse.

Muscle wasting was assessed using a wheat germ agglutinin Alexa Fluor 488 conjugate (Invitrogen, Waltham, MA, cat #: W11261) to measure muscle fibre cross-sectional area of the transverse sections. Images were taken at 10× magnification to cover 80–100% of muscle tissue (one image per section for EDL and SOL tissues, three images per section for GA and TA tissues). Cross-sectional area quantification was performed using ImageJ (National Institutes of Health, Bethesda, MD).

In some cases, muscle sections were stained with toluidine blue (Sigma-Aldrich, St. Louis, MO, cat #: T3620), CD68 (Abcam, Cambridge, MA, cat #: 125212), and neutrophil elastase (NE) (Abcam, cat #: 68672) primary antibodies, and Cy-3 conjugated-AffiniPure Donkey Anti Rabbit IgG secondary antibody (Jackson ImmunoResearch Laboratories, West Grove, PA, cat #: 711-165-152), according to the manufacturer's instructions. The number of total and degranulating mast cells encompassed in the skeletal muscle endomysium and perimysium were quantified using 40× images. Images were coded and randomized to allow for blinded quantification without knowledge of the cachexia status of the mice. Muscle sections stained for CD68 and NE underwent citrate buffer antigen retrieval, as previously described.[32] The total number of CD68 and NE positive staining were quantified using 20× images and ImageJ to set a minimum staining intensity threshold for positive staining.

Quantitative polymerase chain reaction of muscle ubiquitin ligases and immune cell genes

Excised muscles were homogenized with a pestle and lysed using a Direct-Zol Mini Prep lysis kit (Zymo Research, Irvine, CA) according to the manufacturer's instructions. The GA and TA tissues from each mouse were lysed individually. The EDL and SOL tissues were pooled within groups and lysed. cDNA was prepared from the lysed samples, and quantitative polymerase chain reaction was run using tripartite motif containing 63 (TRIM63) (Mm01185221_m1), F-box protein 32 (FBXO32) (Mm00499523_m1), tryptase alpha/beta 1 (TPSAB1) (Mm00491950_m1), tryptase beta 2 (TPSB2) (Mm00487645_m1), CD68 (Mm03047343_m1), and neutrophil elastase gene (ELANE) (Mm00469310_m1) target primers, with GAPDH (Mm99999915_g1) as a housekeeping gene (TaqMan Applied Biosystems, Waltham, MA). Relative gene expression was calculated using the $2^{-\Delta\Delta CT}$ values.

Western blots

Excised muscles were homogenized with a pestle and lysed for protein in RIPA Lysis and Extraction buffer (Fisher Scientific) with EDTA-free protease inhibitor cocktail (Sigma-Aldrich). All muscles were lysed individually. Likewise, differentiated C2C12 myotubes were lysed following a 24 h incubation with the indicated conditioned media. Western blots were run using antibodies for tryptase (Abcam, cat #: ab151757), Mas-related gene X2 (MrgX2) (1:1000, Novus Biological, Littleton, CO, cat #: NB110-75035), CD68 (1:1,000, Abcam, cat #: ab125212), myeloperoxidase (MPO) (1:1000, Abcam, cat #: ab208670), muscle-specific RING finger-1 (MuRF1) (1:1000, Santa Cruz Biotechnology, Dallas, TX, cat #: sc-398608), muscle atrophy F-box (MAFbx) (1:1000, Santa Cruz Biotechnology, cat #: sc-166806), and fast myosin skeletal heavy chain (MyHC) (1:1,000, Abcam, cat #: ab91506). GAPDH (1:5000, Cell Signalling Technology, Danvers, MA, cat #: 2118) was used as the loading control.

DOI: 10.1002/jcsm.12714

Expression of target proteins was normalized based on GAPDH expression using ImageJ.

LL/2 conditioned media collection

LL/2 cells were plated in 10 cm dishes at a concentration of 10×10^5 cells/mL in serum-free DMEM for 24 h. Conditioned media (CM) was concentrated using a 10 kDa cut-off Ultra Centrifugal Filter Unit (Millipore Sigma, Burlington, MA).

Measuring lysosome-associated membrane protein 2 (LAMP2) expression with flow cytometry

Lysosome-associated membrane protein 2 (LAMP2) expression was measured, as previously described.[33] Briefly, P815 cells were washed and resuspended in HEPES Buffer with 5% (V/V) bovine serum albumin. Cells were treated with either HEPES buffer, concentrated LL/2 CM, or concentrated DMEM (control CM) for 10 min. The reaction was stopped, cells were labelled with LAMP2 antibody (BioLegend, San Diego, CA, cat #: 108505), and analysed by flow cytometry with a BD Accuri C6 Analyser flow cytometer (BD Biosciences, San Jose, CA). Assay was repeated three times.

Primary bone marrow-derived mast cells culture

Primary bone marrow-derived mast cells (BMMCs) were established *in vitro*, as previously described.[34] Briefly, excised femurs and tibias from 6-week-old male C57BL/6 mice were flushed with Roswell Park Memorial Institute 1640 media (Gibco) supplemented with 10% (V/V) foetal bovine serum (Gibco), 1% (V/V) penicillin and streptomycin (Gibco), 1% (V/V) L-glutamine (Gibco), 1% HEPES buffer (Fisher Scientific, Waltham, MA), and 50 μM 2-mercaptoethanol (Fisher Scientific). Resulting cells were cultured in complete mast cell media containing recombinant murine IL-3 (PeproTech Cranbury, NJ, cat #: 213-13) to promote mast cell maturation for 4 weeks and were used within 6 weeks. The purity of the mature population was confirmed using a BD Accuri C6 Analyser flow cytometer (BD Biosciences) following a 30 min incubation with antibodies for both c-Kit-allophycocyanin (APC) (Biolegend, cat #: 105812) and IgER-fluorescein isothiocyanate (eBioscience, San Diego, CA, cat #: 11-5898-82). Mast cells are double positive for c-Kit and IgER.[34]

Interleukin 6 release of activated mast cells

Bone marrow-derived mast cells were cytokine starved overnight without IL-3 prior to plating. BMMCs were plated in a 24 well plate at a concentration of 5×10^5 cells/mL. Cells were treated with either concentrated LL/2 or control CM for 24 h. The concentration of IL-6 in the CM was measured in triplicate using an ELISA kit (R&D Systems, Minneapolis, MN) according to the manufacturer's protocol.

C2C12 myotube diameter measurement

Changes in differentiated C2C12 myotube diameter in the presence of conditioned media or fresh growth media was measured using basic microscopy and quantitative software (ImageJ), as previously described.[35] Briefly, 90% confluent C2C12 cells were incubated with media containing 2% (V/V) horse serum (Gibco) to promote formation of myotubes. Media was changed every 48 h for 7 days. After 7 days of incubation, the myotubes were treated with 10 μM cytosine arabinoside hydrochloride (Sigma-Aldrich, cat #: C6645) for 3 days to remove remaining myoblasts.[35] Myotubes were treated with fresh growth media (Control CM), LL/2 CM, BMMC CM, or LL/2-pre-activated BMMC CM. Myotube cultures were photographed prior to treatment and 24 h following treatment. Average myotube diameter for each well was calculated using five random fields of view at 40× magnification captured with an EVOS XL Core Cell Imaging System (Invitrogen). For each field the diameter of five myotubes was calculated using 10 random points along the myotube. Images were coded to allow for blinded quantification without knowledge of the treatment conditions of the wells. Data were normalized according to average myotube diameter of the control wells.

Bioinformatics

The Gene Expression Omnibus was used to access genomics data available for murine C26 cachexia model (GSE24112), and human upper gastrointestinal (GI) cancer (GSE34111) or pancreatic ductal adenocarcinoma (GSE130563) cohorts.[17–21,30] Molecular signatures for immune cell activation were obtained from the Molecular Signatures Database (MSigDB, accessed in 2019) and were contributed by the Gene Ontology Consortium.[22–26] Molecular signatures for dietary excess (reflecting heightened energy expenditure) and cachexia were also obtained from MSigDB (accessed in 2021) and were contributed by the Gene Ontology Consortium and The Jackson Laboratory Human Phenotype Ontology Group, respectively.[36]

Signatures used are listed below:

GO_MAST_CELL_MEDIATED_IMMUNITY
GO_NEUTROPHIL_ACTIVATION_INVOLVED_IN_IMMUNE_RESPONSE
GO_MACROPHAGE_ACTIVATION_INVOLVED_IN_IMMUNE_RESPONSE
GO_POSITIVE_REGULATION_OF_MUSCLE_CELL_APOPTOTIC_PROCESS

DOI: 10.1002/jcsm.12714

GO_MUSCLE_ATROPHY
ADAPTIVE_IMMUNE_RESPONSE (GO:0002250)
INNATE_IMMUNE_RESPONSE (GO:0045087)
GO_RESPONSE_TO_DIETARY_EXCESS (GO:0002021)
HP_CACHEXIA (HP:0004326)

Gene Set Enrichment Analysis (v4.0.3) was used to measure enrichment of these signatures within the human cohorts to examine enrichment in cachectic patients.[24,27] The Gene Expression Profiling Interactive Analysis (GEPIA) was used to access correlation between the innate immune cell signatures and muscle atrophy or apoptosis signatures listed above in normal muscle tissue from the Genotype-Tissue Expression project as linked on the GEPIA2 website.[28,29] Correlation analysis was expressed using the Spearman correlation.

Statistical analyses

Numerical data are expressed as mean ± standard error of the mean (SEM). Statistical analysis was performed using the GraphPad Prism statistical program (GraphPad Software, San Diego, CA) with significance at $P \leq 0.05$. An unpaired Student's *t*-test or one-way analysis of variance (ANOVA) with Tukey's or Bonferroni's post-test was used to compare single measurements between groups where indicated. A two-way ANOVA was used to compare between groups with multiple or repeated measurements.

Results

Increased expression of innate immune cell genes in a cachexia model

To address whether muscle-resident immune cells, including mast cells, are involved in the pathogenesis of cancer-associated cachexia, first the association between the cancer-associated cachexia condition and expression of genes commonly associated with cells from the innate and adaptive immune system was assessed (*Figure* 1A & B). To do so, a publicly available cohort was used, which examined array-based gene expression profiling of quadriceps muscles from CD2F1 mice bearing murine C26 colon carcinoma cells (accession: GSE24112).[17] In this study, mice were divided into normal control, moderate cachexia (10% loss of baseline body mass), and severe cachexia (15% loss of body mass). There was no significant difference in the examined genes from the adaptive immune system (*Figure* 1A). However, there was a significant difference in the tryptase alpha/beta 1 (TPSAB1) and Cluster of Differentiation 68 (CD68) genes from the innate immune system (*Figure* 1B). TPSAB1 and tryptase beta 2 (TPSB2) are commonly associated with mast cells.[37] CD68 is commonly used as a macrophage marker.[38] Closer inspection of each of the genes showed significantly increased expression of TPSAB1 in the muscle of cachectic mice compared with the corresponding normal control mice (*Figure* 1C), and there was also an observed trend toward increased TPSB2 expression in early cachectic mice compared with control (*Figure* 1D). Additionally, CD68 expression was significantly increased in the severe cachexia mice compared with normal control mice (*Figure* 1E). Collectively, these data suggest the innate immune cells, such as mast cells and macrophages, are accumulated in the skeletal muscles derived from mice with cancer-associated cachexia.

Subcutaneous LL/2 injection induces cachexia in vivo

The LL/2 subcutaneous injection model is one of the most well-established murine cancer-associated cachexia models currently in use to induce loss of muscle mass and function.[39–41] Therefore, LL/2 cells were inoculated subcutaneously into C57BL/6 mice to establish cancer-associated cachexia. The tumour-free body mass of the LL/2-bearing mice at the time of harvest was significantly lower than corresponding sham mice (*Figure* 2A). However, there was no significant difference in daily food intake between the groups, indicating that a change in diet is not responsible for the weight loss (*Figure* 2B). There was a trend toward higher percentage loss of body mass correlating with increased tumour size (*Figure* 2C). To assess if loss of muscle mass specifically was contributing to this loss in body mass, the primarily fast twitch fibre EDL, predominantly slow twitch fibre SOL, and mixed fibre type GA and TA muscles were excised and weighed.[40,42] In this case, to further assess correlations between the reduction of body weight and the reduction of muscle weight, LL/2-bearing mice were stratified further into mice losing less than 10% [LL/2 (<10%)] and 10% or greater [LL/2 (≥10%)] of their baseline (pre-inoculation) body mass. Significant decreases in individual excised muscle mass of the TA (*Figure* 2D) and GA muscles (*Figure* 2E) in LL/2 (≥10%) mice were observed compared with sham, indicative of muscle wasting. There were slight trends toward decreased mass in the EDL (*Figure* 2F) and SOL muscles (*Figure* 2G), although this did not reach statistical significance. Furthermore, muscle function was examined using an *in vivo* force transducer system to measure force frequency following electrode stimulated plantarflexion.[31] There was a significant decrease in force frequency in measurements taken in LL/2 (≥10%) mice compared with sham in measurements taken just prior to harvest (*Figure* 2H), and a trend toward decreased time to muscle fatigue (*Figure* 2I).

A

Gene	ILMN ID#	Adaptive Immunity	Summary P Value
CD19	2975994	B Cells	0.3594
CD3D	2697415	T Cells	0.4321
CD3G	2722784	T Cells	0.6233
CD8	2664929	Cytotoxic T Cells	0.9938
CD4	1249663	Helper T Cells	1.0000

B

Gene	ILMN ID#	Innate Immunity	Summary P Value
TPSAB1	2705860	Mast Cells, Basophils	0.0018
CD68	2689785	Macrophages, Monocytes	0.0167
TPSB2	3161036	Mast Cells	0.0557
CD14	2742075	Macrophages, Neutrophils	0.1907
CD86	1217041	Antigen Presenting Cells	0.2026
CD123	2916571	Basophils, GMPs	0.3110
Ly6G	2697910	Neutrophils, Monocytes	0.3314
CD80	2877958	Antigen Presenting Cells	0.5797
NK1.1	2952650	NK Cells	0.5799

GMPs: Granulocyte-Monocyte Progenitor Cells

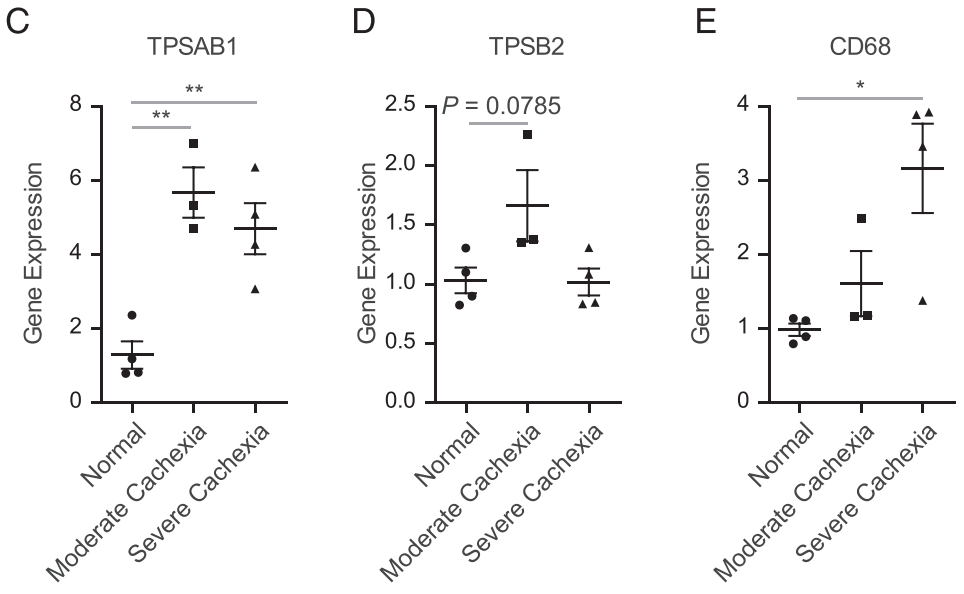

Figure 1 Increased expression of innate immune cell genes in cachectic mice skeletal muscle. (*A*) Expression of adaptive immunity-related genes in quadriceps muscles of C26 colon carcinoma-bearing mice [GSE24112, normal (n = 4), moderate cachexia (n = 3), and severe cachexia (n = 4)]. (*B*) Expression of innate immunity-related genes. Detailed analyses of (*C*) tryptase alpha/beta 1 (TPSAB1), (*D*) tryptase beta 2 (TPSB2), and (*E*) CD68 gene expression from (B). Mean ± SEM. $^{*}P \leq 0.05$, $^{**}P \leq 0.01$ (one-way ANOVA, Tukey's multiple comparisons test).

Individual muscle fibres from each of the excised muscle tissues were visualized using Wheat Germ Agglutinin to further analyse changes in muscle fibre sizes (*Figure* 3A). Quantification of the distribution of fibre sizes within each muscle showed a significant shift toward a higher frequency of small muscle fibres in the TA (*Figure* 3B) and

DOI: 10.1002/jcsm.12714

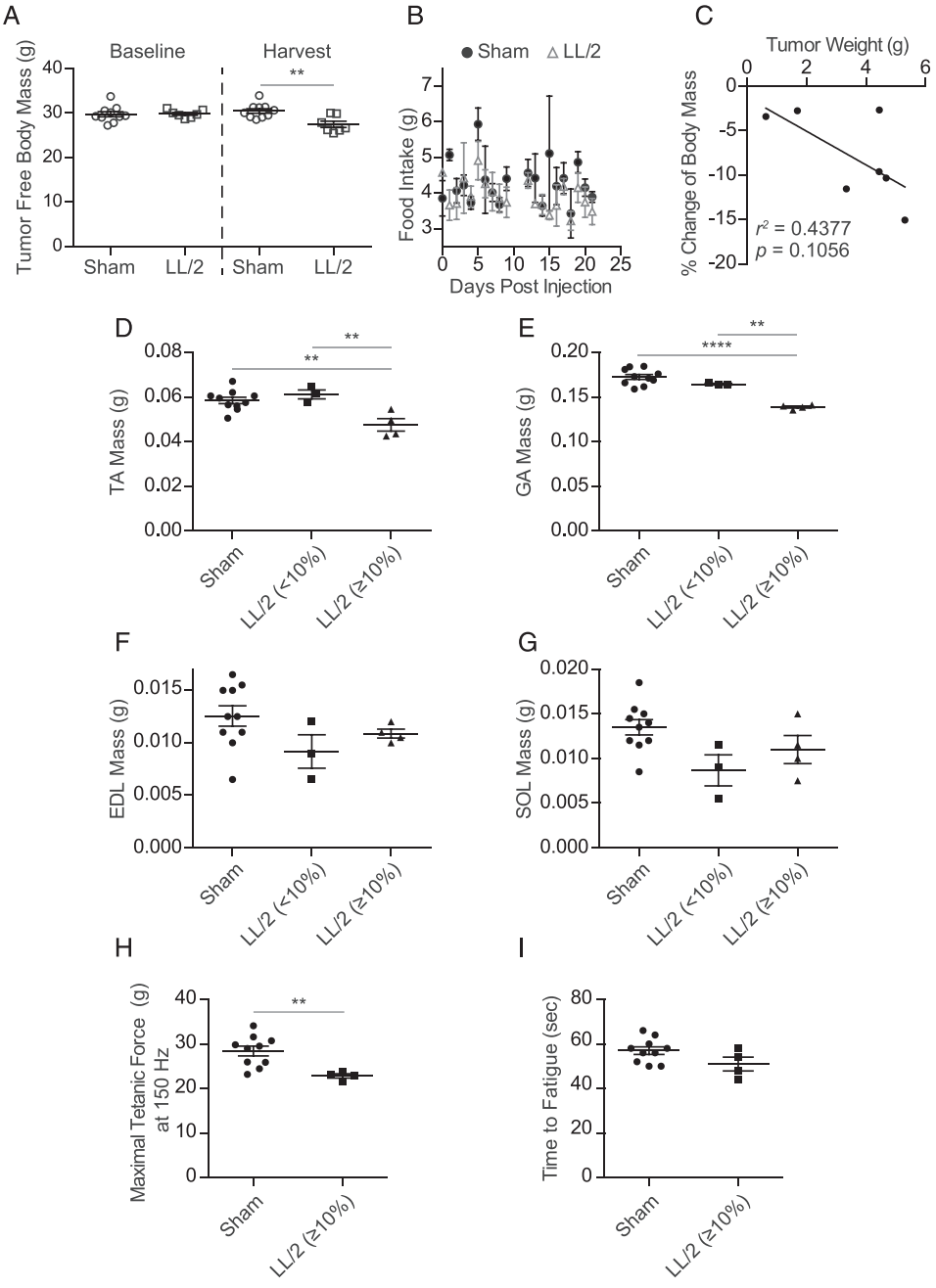

Figure 2 Murine model of LL/2 induced cachexia. Murine lung cancer LL/2 cells or cell culture medium without cells (sham) were inoculated into C57BL/6 mice subcutaneously (sham n = 10, LL/2 n = 7). Body weight, food intake, tumour growth, and muscle function were assessed after 3 weeks. (*A*) Tumour free body mass of LL/2 and sham-bearing mice at baseline and termination of experiment. (*B*) Longitudinal measurement of daily food intake of LL/2 and sham-bearing mice. (*C*) Correlative comparison of excised tumour mass with percentage of body mass lost. (*D–G*) Comparison of muscle mass among sham-bearing mice and LL/2 bearing mice losing <10% or ≥10% baseline body mass at termination of experiment. Mean ± SEM, $^{**}P \leq 0.01$, $^{****}P \leq 0.0001$ vs. sham-injected group (one-way ANOVA, Bonferroni's multiple comparisons test). (*H, I*) Hind limb muscle function [(H) maximal tetanic force and (I) time to fatigue] was measured by force transduction at termination of experiment. Mean ± SEM, $^{**}P \leq 0.01$ vs. sham-injected group (Student's *t*-test).

GA (*Figure* 3C) in LL/2 (≥10%) mice, compared with the sham control. A similar trend was seen in the EDL muscle, although this did not reach statistical significance (*Figure* 3D). However, the SOL tissue did not show a significant change in fibre size distribution (*Figure* 3E). This is potentially due to fast-twitch muscle fibres being predominantly affected in cancer cachexia.[43] Interestingly, mRNA expression of the muscle protein specific E3 ubiquitin ligases

DOI: 10.1002/jcsm.12714

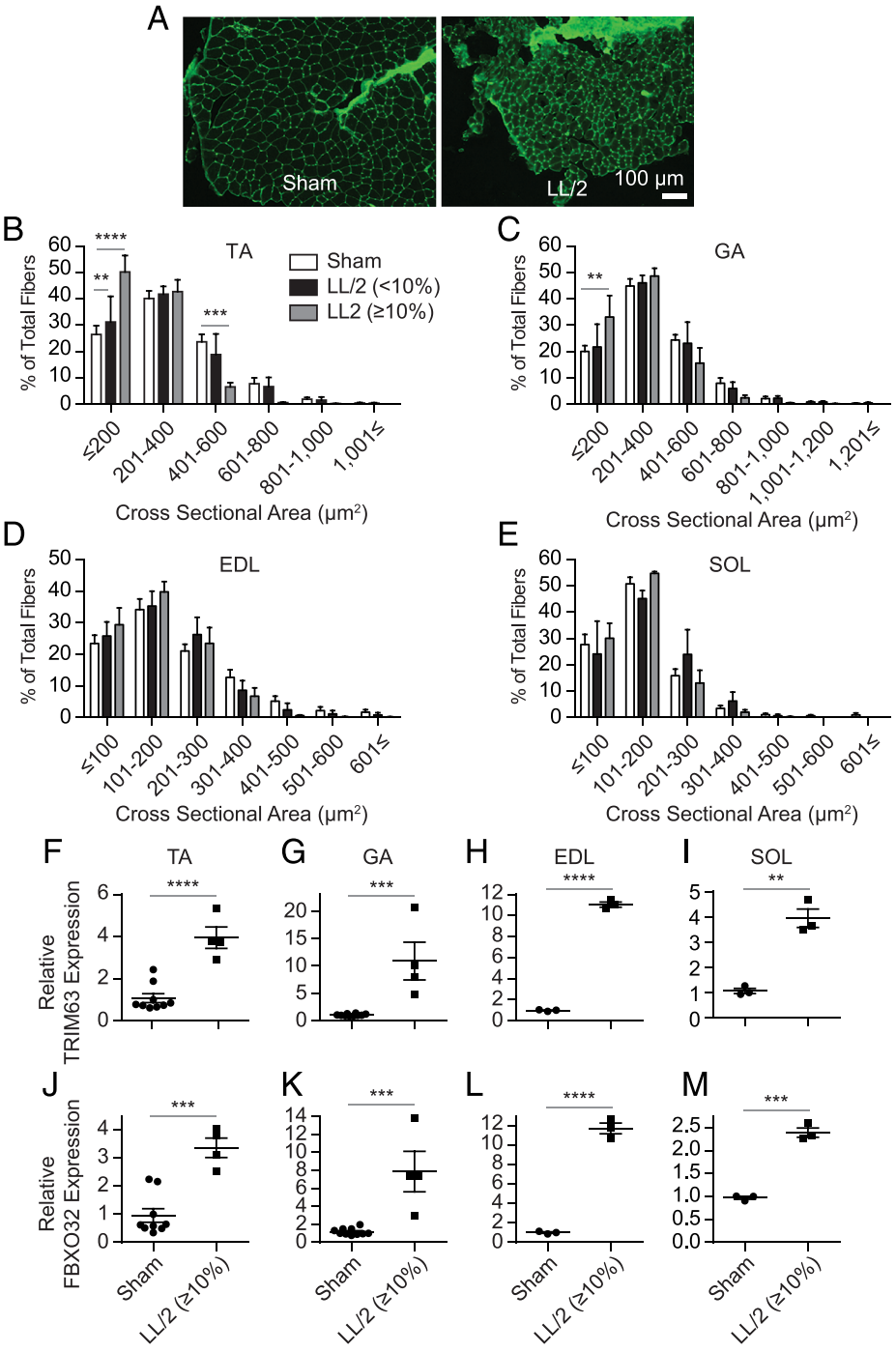

Figure 3 Cachexia shifts muscle fibre size distribution and increases cachexia-related genes in *in vivo* murine model. Analysis of muscle fibre cross-sectional area and cachexia-related gene expression in muscles obtained from animals in *Figure*2. (*A*) Representative images of wheat germ agglutinin (WGA) stained TA muscles. ×10. Bar = 100 µm. (*B–E*) Quantification of muscle fibre cross-sectional area percent distribution. Mean ± SEM, $^{**}P \leq 0.01$, $^{***}P \leq 0.001$, $^{****}P \leq 0.0001$ vs. sham-injected group (two-way ANOVA, Tukey's multiple comparisons test). (*F–I*) tripartite motif containing 63 (TRIM63) and (*J–M*) F-box protein 32 (FBXO32) mRNA expression of muscles. Mean ± SEM. $^{**}P \leq 0.01$, $^{***}P \leq 0.001$, $^{****}P \leq 0.0001$ vs. sham-injected group (Student's *t*-test).

tripartite motif containing 63 (TRIM63) and F-box protein 32 (FBXO32), which have previously been shown to be up-regulated in cancer-associated cachexia,[44,45] were significantly increased in all of the skeletal muscles of LL/2 (≥10%) mice compared with the sham control. Together, these findings suggest mice that lost 10% or greater of their weight are representative of a cancer-associated cachexia phenotype.

DOI: 10.1002/jcsm.12714

Cachectic mice have increased degranulating skeletal muscle mast cells, but not macrophages and neutrophils

In order to assess the presence of innate immune cells in this model, skeletal muscle tissue was examined for resident mast cells, macrophages, and neutrophils within the endomysium and perimysium. The presence of mast cells within the skeletal muscle was visually confirmed using toluidine blue stain (*Figure* 4A). Mast cells naturally resided in the skeletal muscle of both sham control and LL/2-bearing mice. The total number of mast cells per muscle cross section was quantified, and there was a significant increase of the total number of mast cells in the EDL tissue of LL/2 (≥10%) mice (*Figure* 4B–E). Degranulation, or granule release, of activated mast cells was assessed using the morphology of the mast cells.

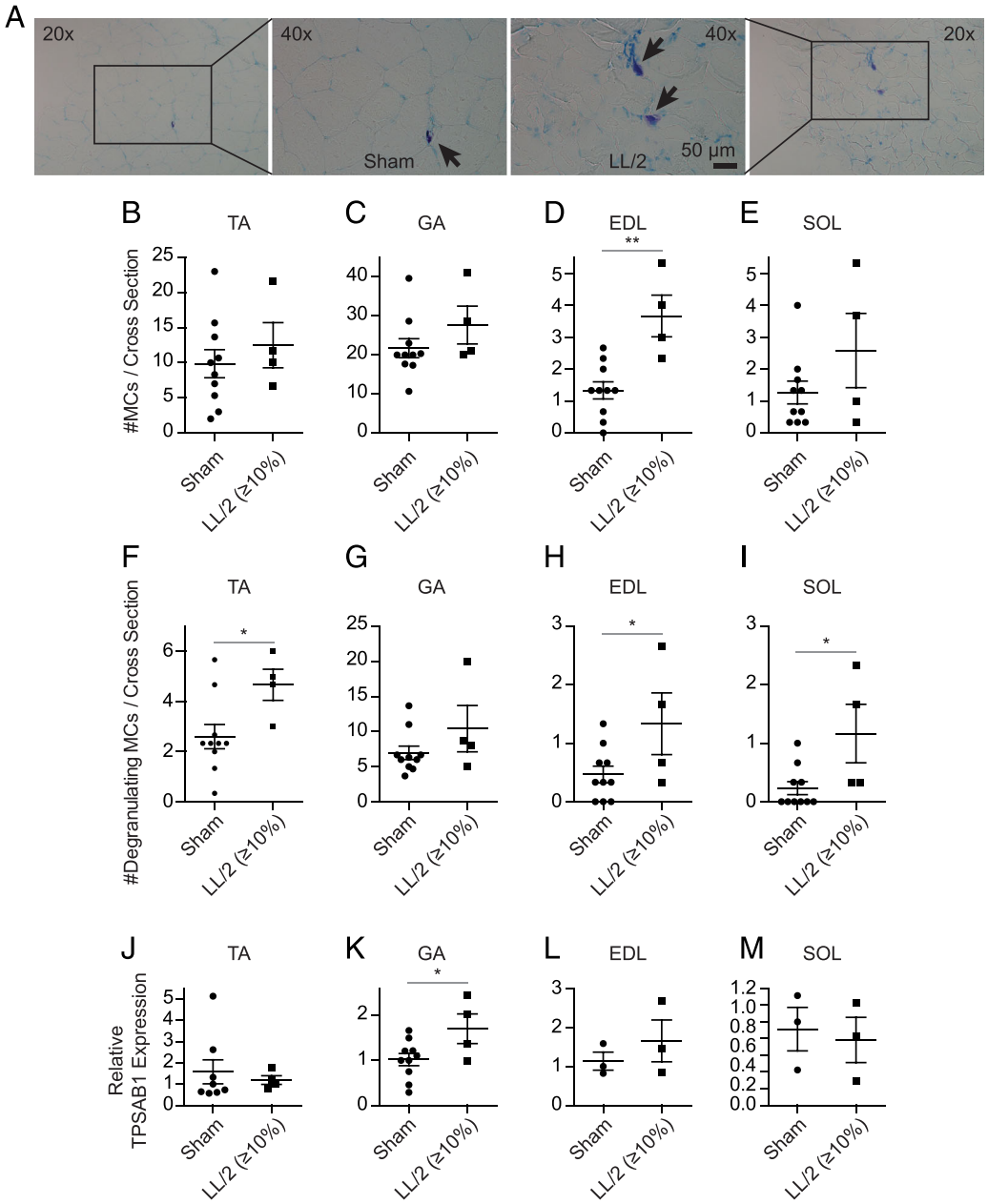

Figure 4 Degranulating skeletal muscle-resident mast cells increase in *in vivo* murine cancer-associated cachexia model. Examination of skeletal muscle-resident mast cells (MCs) in muscles obtained from animals in *Figure*2. (*A*) Representative images of toluidine blue stained TA muscle. ×20 and ×40. Bar = 25 μm. (*B–I*) Quantification of total number of muscle-resident (*B–E*) mast cells and (*F–I*) activated degranulating mast cells in hind limb skeletal muscles. (*J–M*) Relative mRNA expression of tryptase alpha/beta 1 (TPSAB1) in the muscles. Mean ± SEM, $^{*}P \leq 0.05$, $^{**}P \leq 0.01$ vs. sham-injected group (Student's *t*-test).

DOI: 10.1002/jcsm.12714

Interestingly, there was a significant increase in the number degranulating mast cells within the EDL, TA, and SOL tissue, and a trend toward increased degranulating mast cells in the GA of LL/2 (≥10%) mice, compared with the sham mice (*Figure* 4F–I). Relative TPSAB1 mRNA expression was also assessed in each of these muscle tissues (*Figure* 4J–M). Only a significant difference was observed in the GA muscle (*Figure* 4K), potentially due to the larger number of mast cells present within this larger muscle compared with the other smaller muscles measured.

CD68 (*Figure* 5A) and neutrophil elastase (NE) positive staining (*Figure* 5J) were quantified as representative markers for macrophages and neutrophils, respectively, within the skeletal muscle tissue. However, within this model, skeletal muscle-resident macrophages (*Figure* 5B–E) and neutrophils (*Figure* 5K–N) were not upregulated in the cachectic TA, GA, EDL, and SOL muscles. Relative mRNA expressions of the corresponding genes for these markers were also assessed in each muscle of interest. There was a significant increase in CD68 expression in the SOL of LL/2 (≥10%) mice (*Figure* 5I), but not in the TA, GA, and EDL muscles (*Figure* 5F–H). Relative mRNA expression of the neutrophil elastase gene (ELANE) showed no significant difference in the TA (*Figure* 5O), significantly lower levels in the EDL of LL/2 (≥10%) mice (*Figure* 5Q), and significantly higher levels in the GA and SOL muscles (*Figure* 5P & R).

Next, to examine if the gene expression changes observed in *Figures* 3–5 corresponded with changes in protein expression, Western blot assays were performed on the excised muscles. There was a significant increase in mast cell-specific protease tryptase expression in the TA of LL/2 (≥10%) mice, but not in the GA, EDL, and SOL muscles (*Figures* 6A–D & 7A). While tryptase remains a well-established component of mast cell granules, typically mast cells are heterogeneous and may or may not produce tryptase,[46] which may partially explain why degranulating mast cells from different muscles also differ in tryptase protein expression. Additionally, upon degranulation tryptase may enter the circulation, thus serum levels may be needed in future studies to fully assess changes in tryptase protein expression.[47] No change was observed in mast cell surface protein Mas-related gene X2 (MrgX2) levels in all four muscle types (*Figures* 6A–D & 7B), suggesting again that the activation status of mast cells may be changing, while the total number of mast cells remains the same. CD68 protein expression showed significantly lower levels in the TA of LL/2 (≥10%) mice (*Figures* 6A & 7C), and significantly higher levels in the GA (*Figures* 6B & 7C). There was a significant increase in MPO, an enzyme found in neutrophils, expression in the TA, EDL, and SOL of LL/2 (≥10%) mice (*Figures* 6A, C, & D & 7D), but not in the GA (*Figures* 6B & 7D**)**. Although there were significant increases of mRNA expression of the muscle protein specific E3 ubiquitin ligases TRIM63 and FBXO32 in all of the skeletal muscles of LL/2 (≥10%) mice (*Figure* 3F–M), there were no significant increases in the expression of muscle-specific RING finger-1 (MuRF1, protein for TRIM63) and muscle atrophy F-box (MAFbx, protein for FBXO32) (*Figures* 6A–D & 7E & F), suggesting that muscle degradation through the muscle protein specific E3 ubiquitin ligases may not be the sole mechanism of muscle atrophy observed in our study. Moreover, there were no significant changes in fast myosin skeletal heavy chain (MyHC), known to be decreased in cancer-related cachectic muscles,[10,48] protein expression (*Figures* 6A–D & 7G). However, some reduction of MyHC levels were observed in TA and GA muscles of LL/2-bearing mice, which show significant muscle wasting (*Figures* 2D & E & 3B & C), although this reduction did not reach statistical significance (*Figures* 6A & B & 7G). This is consistent with recent findings that MyHC may not be selectively decreased in murine cancer cachexia,[49] and that other insults (e.g. denervation) are necessary to develop MyHC loss in cancer-associated cachectic muscles.[50] Although further studies are clearly warranted, this may be one reason that we did not observe significant reduction of MyHC protein levels at the time of harvest.

Collectively, the histology data indicate an overall increase in the number of degranulating mast cells, but not $CD68^+$ and NE^+ cells in the skeletal muscle of cancer-associated cachectic mice, while western blot analysis shows some increase of tryptase, CD68, and MPO protein levels in those muscles.

Cancer cell secretome activates mast cells

To next address the ability of secreted factors from cachexia-inducing cancer cells to activate mast cells, mast cells were treated with CM from the LL/2 cell line. LL/2 CM up-regulated lysosome-associated membrane protein 2 (LAMP2) expression in the P815 mastocytoma cell line relative to control following 10 min of stimulation (*Figure* 8A). This up-regulation occurs when mast cells are activated to degranulate.[33] Primary BMMC released significantly higher levels of IL-6 in the media 24 h post-stimulation with LL/2 CM compared with IL-6 levels of BMMC or LL/2 CM alone, indicative of mast cell activation (*Figure* 8B). Differentiated C2C12 murine myotubes treated with media from LL/2-pre-activated mast cells showed significantly reduced myotube diameter at 24 h post-treatment compared with C2C12 myotubes treated with fresh growth media (Control CM), LL/2 CM, or BMMC CM (*Figure* 8C). To further determine whether the observed reduction of myotube diameter mediated by BMMC-derived CM were associated with muscle atrophy, MyHC levels in C2C12 myotubes were compared. Interestingly, similar trends were observed in changes in MyHC expression as those in myotube diameter reduction observed in *Figure* 8C, although it did not reach statistical significance (*Figure* 8D & E). This trend is also similar to MyHC level changes observed in TA and GA muscles of LL/2-bearing mice (*Figures* 6A & B & 7G) which show significant muscle

DOI: 10.1002/jcsm.12714

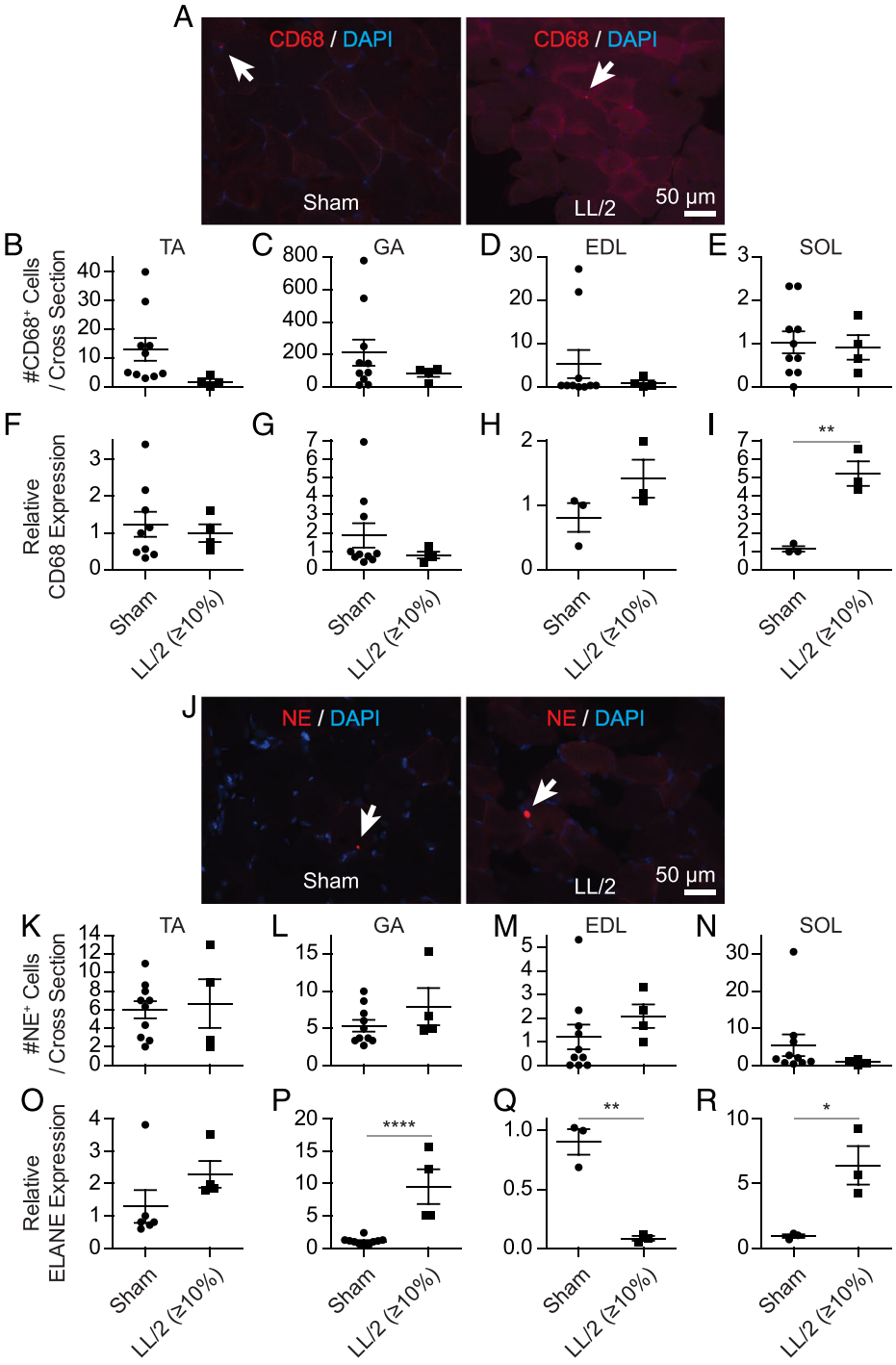

Figure 5 No change in skeletal muscle-resident macrophages and neutrophils in murine cancer-associated cachexia model. Examination of skeletal muscle-resident CD68 (macrophage marker) positive cells and neutrophil elastase (NE) (neutrophil marker) positive cells in muscles obtained from animals in *Figure*2. (*A*) Representative immunofluorescence images of CD68 and DAPI stained TA muscle. ×20. Bar = 50 μm. (*B–E*) Quantification of number of positive CD68 cells per muscle cross section. (*F–I*) Relative mRNA expression of CD68 in muscle. (*J*) Representative immunofluorescence images of NE and DAPI stained TA muscle ×20. Bar = 50 μm. (*K–N*) Quantification of number of positive NE cells per muscle cross section. (*O–R*) Relative mRNA expression of neutrophil elastase gene (ELANE) in muscle. Mean ± SEM. $^{*}P \leq 0.05$, $^{**}P \leq 0.01$, $^{****}P \leq 0.0001$ vs. sham-injected group (Student's *t*-test).

DOI: 10.1002/jcsm.12714

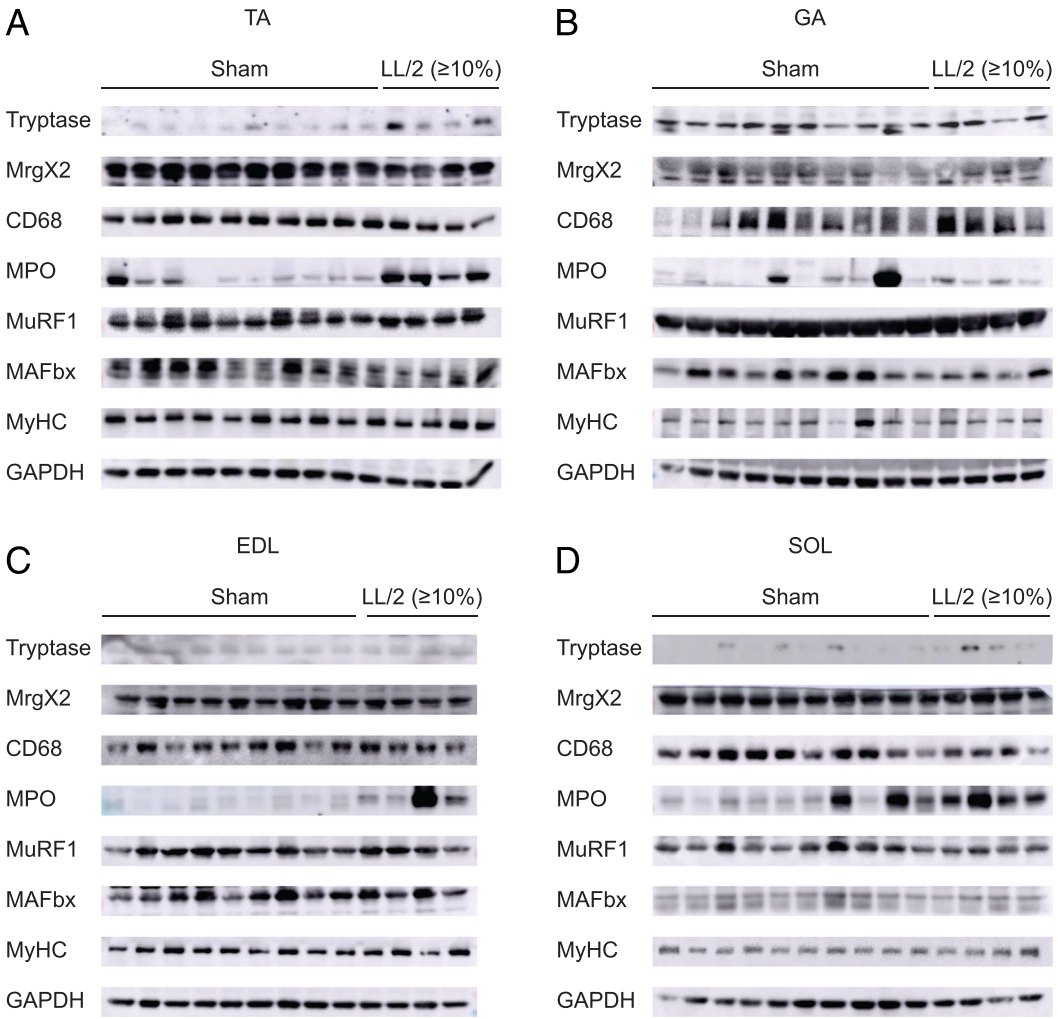

Figure 6 LL/2 altered expression of innate immune cell markers in skeletal muscles, but did not affect protein expression of muscle protein specific E3 ubiquitin ligases. Representative western blot of tryptase, Mas-related gene X2 (MrgX2), CD68, myeloperoxidase (MPO), muscle-specific RING finger-1 (MuRF1), muscle atrophy F-box (MAFbx), and fast myosin skeletal heavy chain (MyHC) on (*A*) TA, (*B*) GA, (*C*) EDL, and (*D*) SOL muscles obtained from animals in *Figure*2. GAPDH was used for loading control.

wasting (*Figures* 2D & E & 3B & C). LL/2 cells release factors into their secretome that initiate measurable levels of mast cell activation and degranulation *in vitro*. In turn, activated mast cell media has a direct effect on myotube fibre size, suggesting that cancer-activated mast cells may promote the progression of the characteristic muscle atrophy in cachexia.

Mast cell signatures up-regulated in cachectic skeletal muscle

To address the translational potential of our findings in humans and evaluate the efficaciousness of mast cells as a cachexia biomarker and mediator in humans, we first assessed the correlation between cachexia-related signatures and innate immune cell signatures in human skeletal muscle tissue. Publicly available signatures for mast cells, neutrophils, and macrophages had a significant positive correlation with both skeletal muscle atrophy (*Figure* 9A–C) and apoptosis (*Figure* 9D–F), dietary excess/increased energy expenditure (*Figure* 10A–C), and cachexia (*Figure* 10D–F) signatures in normal skeletal muscle tissue samples from the Genotype-Tissue Expression project.[22–26,28,29] To examine if these immune signatures were also enriched in cachectic muscle tissue, gene set enrichment analysis was used with publicly available human cohorts of upper GI cancer and pancreatic ductal adenocarcinoma (PDAC).[24,27] In the upper GI cancer cohort, patient quadriceps muscle biopsies were divided into normal control samples, and PreOp samples from upper GI cancer patients scheduled for tumour resection with a 7% body mass loss (accession: GSE 34111).[20] The primary criteria considered for evaluating enrichment significance were: (i) a positive normalized enrichment score (NES), (ii) a false discovery rate below 0.1, and (iii) a family-wise error rate below 0.05. Using this

DOI: 10.1002/jcsm.12714

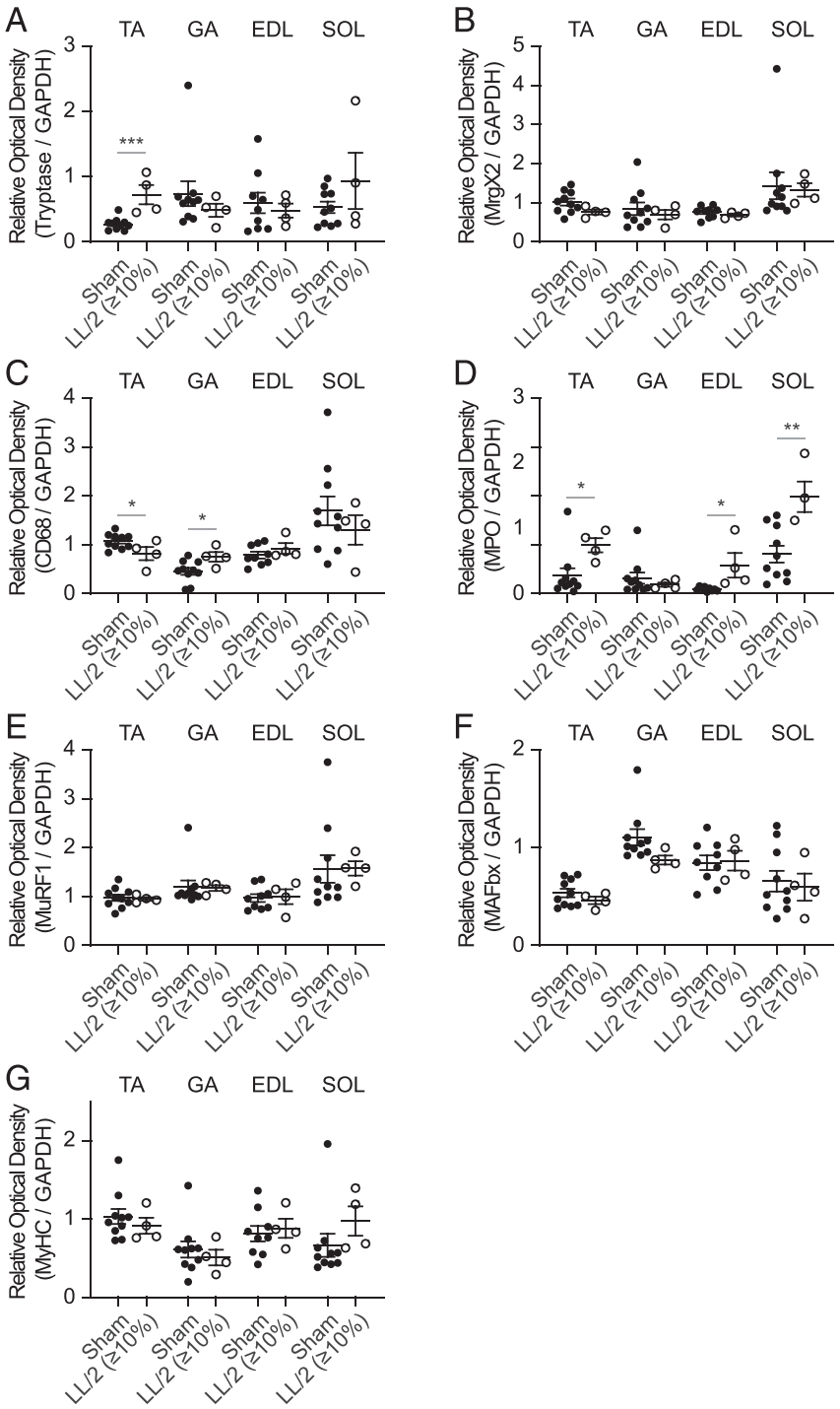

Figure 7 LL/2 altered expression of innate immune cell markers in skeletal muscles, but did not affect protein expression of muscle protein specific E3 ubiquitin ligases. Quantifications of western blots in *Figure* 6. (*A*) tryptase, (*B*) Mas-related gene X2 (MrgX2), (*C*) CD68, (*D*) myeloperoxidase (MPO), (*E*) muscle-specific RING finger-1 (MuRF1), (*F*) muscle atrophy F-box (MAFbx), and (*G*) fast myosin skeletal heavy chain (MyHC). Mean ± SEM. $^{*}P \leq 0.05$, $^{**}P \leq 0.01$, $^{***}P \leq 0.001$ vs. sham-injected group (Student's *t*-test).

criterion, there was no significant enrichment in gene signatures for adaptive immunity, macrophages, or neutrophils in the cachectic PreOp samples (*Figure* 11A, D, & E); however, there was enrichment of both the innate immunity and mast cell signatures (*Figure* 11B & C). The PDAC cohort contained rectus abdominis muscle biopsy samples from both cachectic and non-cancer bearing patients (GSE130563).[21,30] In this cohort, the greatest enrichment and lowest false discovery rate

DOI: 10.1002/jcsm.12714

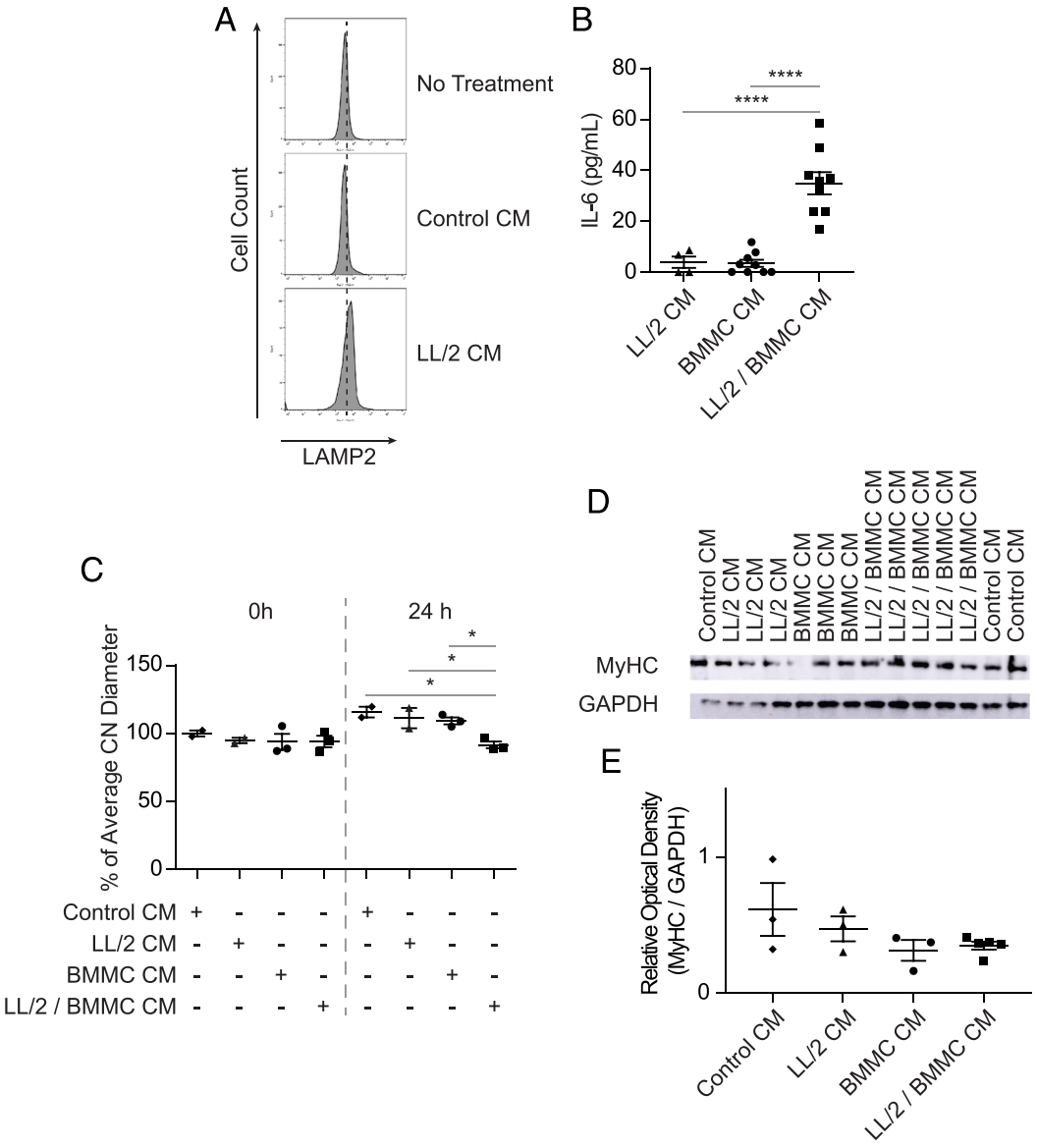

Figure 8 LL/2 activated mast cells decrease differentiated Myotube diameter. (*A*) Representative histogram of LAMP2 expression in P815 cells with no treatment, control conditioned media (CM), or LL/2 CM. (*B*) IL-6 levels at 24 h in (i) LL/2 CM, (ii) bone marrow-derived MC (BMMC) CM, and (iii) BMMC CM treated with LL/2 CM (LL/2 / BMMC CM). Mean ± SEM. $^{****}P \leq 0.0001$ (one-way ANOVA, Tukey's multiple comparisons test). (*C*) Differentiated murine C2C12 myotubes were treated with (i) control CM, (ii) LL/2 CM, (iii) BMMC CM, or (iv) LL/2/BMMC CM for 24 h. The average C2C12 myotube diameter was measured under the microscope. Mean ± SEM. $^{*}P \leq 0.05$ (one-way ANOVA, Tukey's multiple comparisons test). (*D*) Representative western blot of fast myosin skeletal heavy chain (MyHC) expression in differentiated murine C2C12 myotubes treated with (i) control CM, (ii) LL/2 CM, (iii) BMMC CM, or (iv) LL/2/BMMC CM for 24 h. (*E*) Quantification of western blot in *Figure*8D. Mean ± SEM. (one-way ANOVA, Tukey's multiple comparisons test).

was seen in the mast cell signature (*Figure* 11H), compared with the adaptive immunity, innate immunity, macrophage, and neutrophil signatures (*Figure* 11F, G, I, & J). The enrichment of this mast cell signature within muscle biopsies of cancer-associated cachectic patients from two separate cancer types suggests that skeletal-resident mast cells are enriched in the muscles of cancer-associated cachexia patients.

Discussion

This study sought to identify and assess the potential efficacy of skeletal-muscle resident immune cells as mediators and/or biomarkers for cancer-associated cachexia. Using a publicly available murine bioinformatics cohort, individual innate and adaptive immune cell genes in a murine C26 model of cachexia revealed significant changes only in innate immune

DOI: 10.1002/jcsm.12714

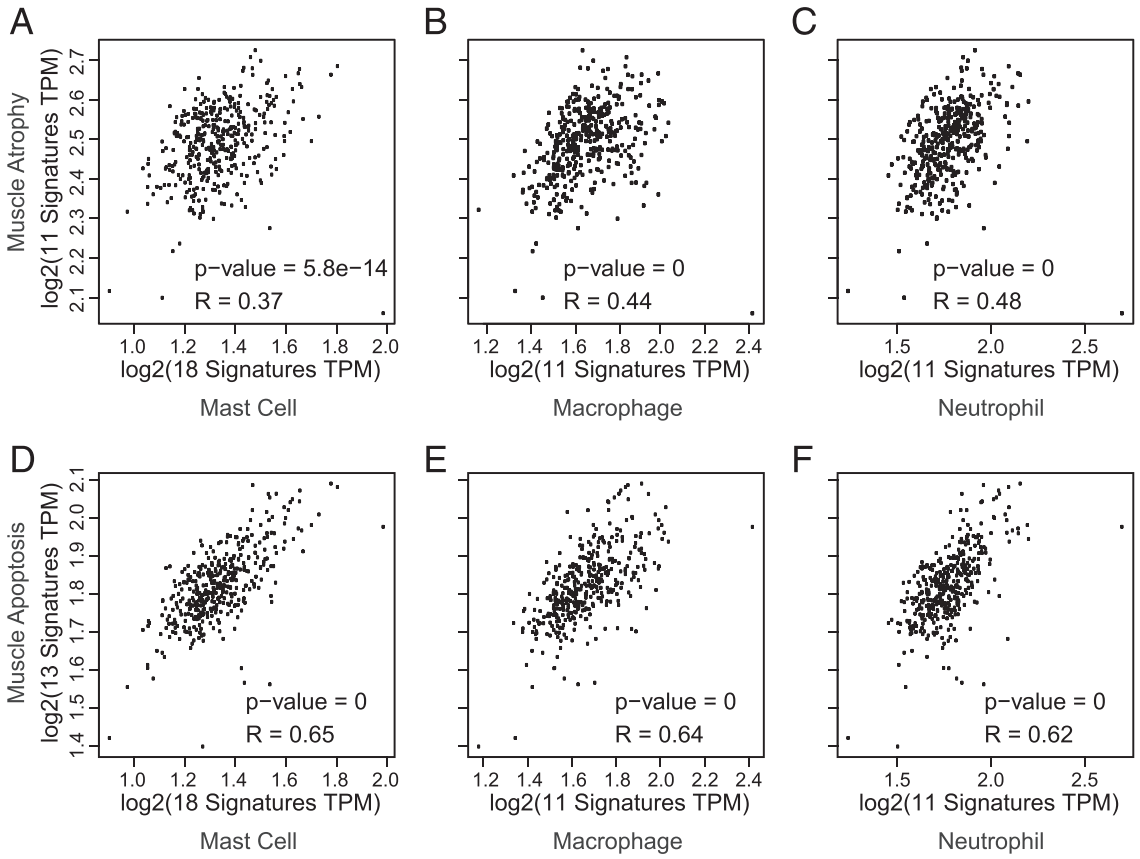

Figure 9 Innate immune cell signatures positively correlate with skeletal muscle atrophy and apoptosis signatures. Spearman's correlation of muscle atrophy gene signature and (*A*) mast cell, (*B*) macrophage, and (*C*) neutrophil gene signatures in human skeletal muscle tissue from the genotype-tissue expression (GTEx) project. Correlation of muscle apoptosis signatures and (*D*) mast cell, (*E*) macrophage, and (*F*) neutrophil gene signatures.

cell genes.[17–19] This finding prompted a focus on innate immune cells in an *in vivo* LL/2 model for cancer-associated cachexia. The development of cachexia in the immunocompetent C57BL/6 mice coincided with an increased number of activated and degranulating skeletal muscle-resident mast cells, as shown through toluidine blue staining. However, immunofluorescence staining for macrophages and neutrophils showed no significant difference in the skeletal muscle. To determine the effect of LL/2-activated degranulating mast cells on muscle cells in a controlled *in vitro* setting, C2C12 myotubes were treated with LL/2-pre-activated BMMC CM and decreased myotube diameter was observed after 24 h. With the observations from the murine bioinformatics cohort, *in vivo* LL/2 model, and *in vitro* C2C12 experiments indicating a potential role for mast cell activation in the progression of cancer-associated cachexia, publicly available human cohorts were assessed to determine the translational potential of these findings. While immune response signatures for mast cells, macrophages, and neutrophils all positively correlated with signatures for muscle apoptosis and atrophy, dietary excess, and cachexia signatures in normal skeletal muscle tissue, only the mast cell signature was enriched in both the cachectic patients of the upper GI cancer and PDAC cohorts.[18–29] These findings suggest that activated skeletal-muscle resident mast cells are enriched in the cachectic muscles. Therefore, skeletal-muscle resident mast cells may serve as a biomarker and mediator for cancer-associated cachexia.

It is well established that inflammatory factors are key in the development of cancer-associated cachexia, and the exact sources of this inflammation have remained a focus of study in the cachexia field.[1] Mast cells are one established producer of the well characterized pro-cachectic cytokine IL-6,[13] and as evidenced in our *in vivo* and *in vitro* experiments are activated directly by the cachexia-inducing LL/2 cell secretome. While little is known about the effects of skeletal muscle-resident mast cell accumulation and activation on skeletal muscle tissue in cancer-associated cachexia patients, there are multiple instances of mast cell promoted muscle atrophy occurring in other conditions. For example, elevated numbers of degranulating skeletal muscle-resident mast cells have been previously implicated in the development of the autoimmune myopathy polymyositis[15] and Duchenne muscular dystrophy.[16] Another recent study observed increased

DOI: 10.1002/jcsm.12714

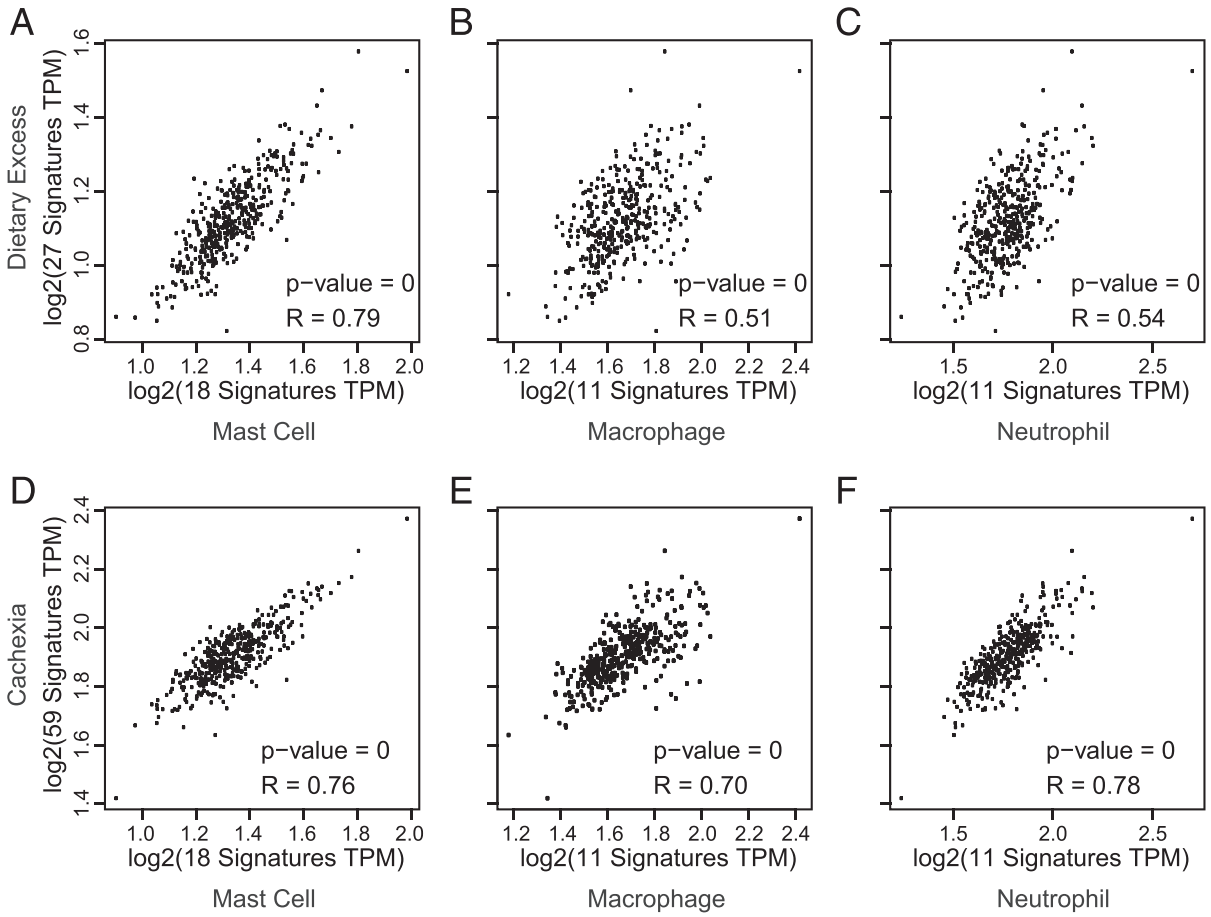

Figure 10 Innate immune cell signatures positively correlate with dietary excess and cachexia signatures. Spearman's correlation of dietary excess gene signature and (*A*) mast cell, (*B*) macrophage, and (*C*) neutrophil gene signatures in human skeletal muscle tissue from the genotype-tissue expression (GTEx) project. Correlation of cachexia signatures and (*D*) mast cell, (*E*) macrophage, and (*F*) neutrophil gene signatures.

levels of mast cells, many with a degranulating phenotype, in the quadriceps muscle of amyotrophic lateral sclerosis patients.[51] These cases establish a clear precedent of skeletal-muscle resident mast cell numbers and activation increasing in conditions resulting in skeletal muscle atrophy. Furthermore, the results from these muscle atrophy studies are mirrored in our own findings, where cancer-associated cachexia: (i) increased the number of activated degranulating skeletal muscle-resident mast cells in murine hind limb muscles and (ii) increased a mast cell mediated immunity signature in cachectic patient samples.

Although a potential key player in the characteristic inflammation observed in this condition, skeletal muscle-resident mast cells may not be the sole inducer of cancer-associated cachexia and all of its systemic effects. There may be other immune cells simultaneously at play throughout the various tissues affected in cancer-associated cachexia. For example, macrophages are upregulated in the colon of cachectic colon cancer patients.[52] However, within the skeletal muscle tissue specifically, mast cell activation was the most consistently observed innate immune cell up-regulation across the murine and patient samples (both upper GI cancer and PDAC) in this study. It is worth noting that other immune cells may also be up-regulated dependent upon the cancer type and immune cell markers used for identification. For example, $CD163^+$ macrophages, or M2 macrophages, were up-regulated in the skeletal muscle of cachectic PDAC patients in a recent study,[53] while we observed a statistically insignificant enrichment in cachectic PDAC patients and no enrichment in cachectic upper GI cancer patients using a macrophage immune response gene signature. Additionally, the C26 mouse bioinformatics cohort (GSE24112) showed an up-regulation in CD68 expression in the skeletal muscle, while our *in vivo* studies with LL/2 showed no significant increase in skeletal muscle-resident $CD68^+$ cells and only slightly increased CD68 protein in GA muscle tissues. This contradiction may be due to inherent differences in the colon carcinoma and lung cancer models or in the examined muscles (e.g. quadriceps vs. GA). Furthermore, we observed significant increases of MPO protein expression in TA, EDL,

DOI: 10.1002/jcsm.12714

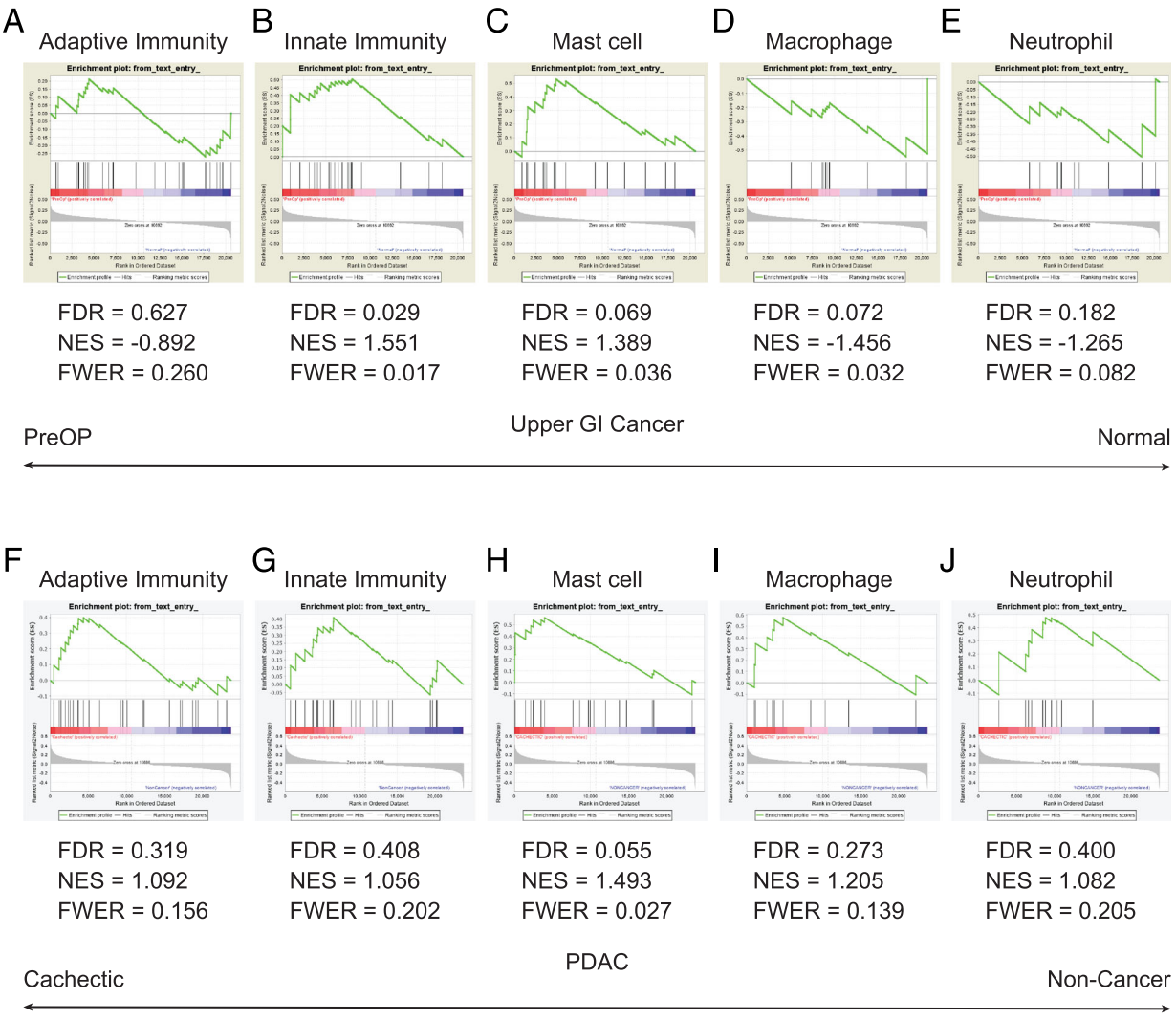

Figure 11 Enriched mast cell gene signature in muscles of cachectic upper GI cancer and PDAC patients. Gene set enrichment analyses of (*A*) adaptive immunity, (*B*) innate immunity, (*C*) mast cell, (*D*) macrophage, and (*E*) neutrophil gene signatures expressed in the quadriceps muscles obtained from upper gastrointestinal (GI) cancer patients from GSE34111 with 7% weight loss (n = 12, PreOp) and normal controls (n = 6, normal). Enrichment plots of (*F*) adaptive immunity, (*G*) innate immunity, (*H*) mast cell, (*I*) macrophage, and (*J*) neutrophil gene signatures expressed in the rectus abdominis muscles obtained from pancreatic ductal adenocarcinoma (PDAC) patients from GSE130563 with cachexia (n = 17, cachectic) or non-cancer controls (n = 16, non-cancer). FDR, false discovery rate; NES, normalized enrichment score; FWER, family-wise error rate.

and SOL muscles, while there was no change in the number of NE^+ cells in those muscles. Because MPO is known to be a potent and selective inhibitor of mast cell tryptase,[54] some compensatory mechanisms may be initiated to mitigate the impact of skeletal muscle-resident mast cells on muscle wasting, resulting in upregulation of this protein. Further studies are clearly required to determine the full efficacy and penetrance of skeletal muscle-resident mast cell activation as a biomarker and mediator for cancer-associated cachexia in patients across multiple cancer types and stages, as cachexia is a complex and variable condition.[4] For a less invasive diagnostic strategy, it would also be prudent to evaluate levels of activated mast cell released factors such as tryptase and heparin in the serum of cancer cachexia patients in future studies.[55,56] Still, the addition of skeletal muscle-resident activated mast cells as a biomarker has the potential to enhance identification of at-risk cancer patients.

Cancer-associated cachexia is a prominent problem for advanced cancer patients and is associated with both decreased quality of life and poor prognosis. More than one million cancer patients in the United States are affected by cachexia.[57] Patients with cachexia and their families pay a tremendous price physically, emotionally, and financially, attempting to cope with this condition. The financial burden of health care, including length and cost of hospitalization, is growing steadily, and all patients with cachexia face this added hardship.[58] However,

DOI: 10.1002/jcsm.12714

a consistently efficacious and approved therapeutic option for cachexia is currently lacking, making earlier diagnosis and assessment of cachexia risk all the more critical in cancer patients. Our study posits activated skeletal muscle-resident mast cells as a tool for assessing cancer patient risk for cachexia development, in order to improve cachexia diagnoses as well as patient quality of life and prognoses.

Author contributions

D.B.W. and Y.S. wrote the manuscript with input from all authors. All authors reviewed and approved the final manuscript. D.B.W., S.H.P., M.R.E., C. L., D.C.F., and Y.S. designed study and contributed to data interpretation. D.B.W. and C. L. performed animal studies. D.B.W. and S.S. performed immunohistochemistry and quantification analyses. Q.Z. performed western blot and quantification analyses. D.C.F. and Y.S. supervised the study.

Acknowledgements

We would like to thank Drs Osvaldo Delbono and Tracy Criswell (Wake Forest University Health Sciences) for the constructive discussion and technical support. This work is directly supported by the National Cancer Institute (R01-CA238888, Y.S.; R44-CA203184, Y.S.), Department of Defence (W81XWH-17-1-0541, Y.S.; W81XWH-19-1-0045, Y.S.), METAvivor (METAvivor Research Award, Y.S.), and the Wake Forest Baptist Comprehensive Cancer Center Internal Pilot Funding (Y.S.). This work is also supported by the National Cancer Institute's Cancer Center Support Grant award number P30-CA012197 issued to the Wake Forest Baptist Comprehensive Cancer Center. The authors wish to acknowledge the support of the Wake Forest Baptist Comprehensive Cancer Center Cell Engineering Shared Resource and Flow Cytometry Shared Resource, supported by the National Cancer Institute's Cancer Center Support Grant award number P30-CA012197. The content is solely the responsibility of the authors and does not necessarily represent the official views of the National Cancer Institute and Department of Defense. The authors of this manuscript certify that they comply with the ethical guidelines for authorship and publishing in the Journal of Cachexia, Sarcopenia and Muscle.[59]

Conflict of interests

Yusuke Shiozawa has received research funding from TEVA Pharmaceuticals, but not relevant to this study. No conflict of interest exists for remaining authors.

References

1. Onesti JK, Guttridge DC. Inflammation based regulation of cancer cachexia. *Biomed Res Int* 2014;**2014**:168407.
2. Fearon K, Strasser F, Anker SD, Bosaeus I, Bruera E, Fainsinger RL, et al. Definition and classification of cancer cachexia: an international consensus. *Lancet Oncol* 2011;**12**:489–495.
3. Al-Majid S, Waters H. The biological mechanisms of cancer-related skeletal muscle wasting: the role of progressive resistance exercise. *Biol Res Nurs* 2008;**10**:7–20.
4. Porporato PE. Understanding cachexia as a cancer metabolism syndrome. *Oncogenesis* 2016;**5**:e200.
5. Penet MF, Bhujwalla ZM. Cancer cachexia, recent advances, and future directions. *Cancer J* 2015;**21**:117–122.
6. Mueller TC, Bachmann J, Prokopchuk O, Friess H, Martignoni ME. Molecular pathways leading to loss of skeletal muscle mass in cancer cachexia—can findings from animal models be translated to humans? *BMC Cancer* 2016;**16**:75.
7. Ni J, Zhang L. Cancer cachexia: definition, staging, and emerging treatments. *Cancer Manag Res* 2020;**12**:5597–5605.
8. Narsale AA, Carson JA. Role of interleukin-6 in cachexia: therapeutic implications. *Curr Opin Support Palliat Care* 2014;**8**:321–327.
9. Weiss K, Mu X, Agarwal R. *Notch signaling and inflammation in a murine model of sarcoma-associated cachexia [abstract]*. Philadelphia, PA: AACR Cancer Research; 2015.
10. Acharyya S, Ladner KJ, Nelsen LL, Damrauer J, Reiser PJ, Swoap S, et al. Cancer cachexia is regulated by selective targeting of skeletal muscle gene products. *J Clin Invest* 2004;**114**:370–378.
11. Jatoi A, Dakhil SR, Nguyen PL, Sloan JA, Kugler JW, Rowland KM, et al. A placebo-controlled double blind trial of etanercept for the cancer anorexia/weight loss syndrome: results from N00C1 from the North Central Cancer Treatment Group. *Cancer* 2007;**110**:1396–1403.
12. Wu C, Fernandez SA, Criswell T, Chidiac TA, Guttridge D, Villalona-Calero M, et al. Disrupting cytokine signaling in pancreatic cancer: a phase I/II study of etanercept in combination with gemcitabine in patients with advanced disease. *Pancreas* 2013;**42**:813–818.
13. Wernersson S, Pejler G. Mast cell secretory granules: armed for battle. *Nat Rev Immunol* 2014;**14**:478–494.
14. Urb M, Sheppard DC. The role of mast cells in the defence against pathogens. *PLoS Pathog* 2012;**8**:e1002619.
15. Yokota M, Suzuki K, Tokoyoda K, Meguro K, Hosokawa J, Tanaka S, et al. Roles of mast cells in the pathogenesis of inflammatory myopathy. *Arthritis Res Ther* 2014;**16**:R72.
16. Radley HG, Grounds MD. Cromolyn administration (to block mast cell degranulation) reduces necrosis of dystrophic muscle in mdx mice. *Neurobiol Dis* 2006;**23**:387–397.
17. Bonetto A, Aydogdu T, Kunzevitzky N, Guttridge DC, Khuri S, Koniaris LG, et al. STAT3 activation in skeletal muscle links muscle wasting and the acute phase response in cancer cachexia. *PLoS One* 2011;**6**:e22538.
18. Edgar R, Domrachev M, Lash AE. Gene expression omnibus: NCBI gene expression and hybridization array data repository. *Nucleic Acids Res* 2002;**30**:207–210.
19. Barrett T, Wilhite SE, Ledoux P, Evangelista C, Kim IF, Tomashevsky M, et al. NCBI GEO: archive for functional genomics data sets—

update. *Nucleic Acids Res* 2013;**41**: D991–D995.
20. Gallagher IJ, Stephens NA, MacDonald AJ, Skipworth RJ, Husi H, Greig CA, et al. Suppression of skeletal muscle turnover in cancer cachexia: evidence from the transcriptome in sequential human muscle biopsies. *Clin Cancer Res* 2012;**18**: 2817–2827.
21. Callaway CS, Delitto AE, Patel R, Nosacka RL, D'Lugos AC, Delitto D, et al. IL-8 released from human pancreatic cancer and tumor-associated stromal cells signals through a CXCR2-ERK1/2 axis to induce muscle atrophy. *Cancers (Basel)* 2019;**11**:1863.
22. The Gene Ontology C. The gene ontology resource: 20 years and still GOing strong. *Nucleic Acids Res* 2019;**47**:D330-D8.
23. Ashburner M, Ball CA, Blake JA, Botstein D, Butler H, Cherry JM, et al. Gene ontology: tool for the unification of biology. *The Gene Ontology Consortium Nat Genet* 2000;**25**:25–29.
24. Subramanian A, Tamayo P, Mootha VK, Mukherjee S, Ebert BL, Gillette MA, et al. Gene set enrichment analysis: a knowledge-based approach for interpreting genome-wide expression profiles. *Proc Natl Acad Sci U S A* 2005;**102**:15545–15550.
25. Liberzon A, Subramanian A, Pinchback R, Thorvaldsdottir H, Tamayo P, Mesirov JP. Molecular signatures database (MSigDB) 3.0. *Bioinformatics* 2011;**27**:1739–1740.
26. Liberzon A. A description of the Molecular Signatures Database (MSigDB) Web site. *Methods Mol Biol* 2014;**1150**: 153–160.
27. Mootha VK, Lindgren CM, Eriksson KF, Subramanian A, Sihag S, Lehar J, et al. PGC-1alpha-responsive genes involved in oxidative phosphorylation are coordinately downregulated in human diabetes. *Nat Genet* 2003;**34**:267–273.
28. Consortium GT. The genotype-tissue expression (GTEx) project. *Nat Genet* 2013;**45**:580–585.
29. Tang Z, Kang B, Li C, Chen T, Zhang Z. GEPIA2: an enhanced web server for large-scale expression profiling and interactive analysis. *Nucleic Acids Res* 2019;**47**: W556–W560.
30. Judge SM, Nosacka RL, Delitto D, Gerber MH, Cameron ME, Trevino JG, et al. Skeletal muscle fibrosis in pancreatic cancer patients with respect to survival. *JNCI Cancer Spectr* 2018;**2**:pky043.
31. Files DC, D'Alessio FR, Johnston LF, Kesari P, Aggarwal NR, Garibaldi BT, et al. A critical role for muscle ring finger-1 in acute lung injury-associated skeletal muscle wasting. *Am J Respir Crit Care Med* 2012;**185**:825–834.
32. Shi SR, Chaiwun B, Young L, Cote RJ, Taylor CR. Antigen retrieval technique utilizing citrate buffer or urea solution for immunohistochemical demonstration of androgen receptor in formalin-fixed paraffin sections. *J Histochem Cytochem* 1993;**41**: 1599–1604.
33. Cruse G, Gilfillan AM, Smrz D. Flow cytometry-based monitoring of mast cell activation. *Methods Mol Biol* 2015;**1220**: 365–379.
34. Meurer SK, Neß M, Weiskirchen S, Kim P, Tag CG, Kauffmann M, et al. Isolation of mature (peritoneum-derived) mast cells and immature (bone marrow-derived) mast cell precursors from mice. *PLoS One* 2016;**11**:e0158104.
35. Menconi M, Gonnella P, Petkova V, Lecker S, Hasselgren PO. Dexamethasone and corticosterone induce similar, but not identical, muscle wasting responses in cultured L6 and C2C12 myotubes. *J Cell Biochem* 2008;**105**:353–364.
36. Kohler S, Gargano M, Matentzoglu N, Carmody LC, Lewis-Smith D, Vasilevsky NA, et al. The human phenotype ontology in 2021. *Nucleic Acids Res* 2021;**49**: D1207–D1217.
37. Payne V, Kam PC. Mast cell tryptase: a review of its physiology and clinical significance. *Anaesthesia* 2004;**59**:695–703.
38. Pelekanou V, Villarroel-Espindola F, Schalper KA, Pusztai L, Rimm DL. CD68, CD163, and matrix metalloproteinase 9 (MMP-9) co-localization in breast tumor microenvironment predicts survival differently in ER-positive and -negative cancers. *Breast Cancer Res* 2018;**20**:154.
39. Deboer MD. Animal models of anorexia and cachexia. *Expert Opin Drug Discovery* 2009;**4**:1145–1155.
40. Choi E, Carruthers K, Zhang L, Thomas N, Battaglino RA, Morse LR, et al. Concurrent muscle and bone deterioration in a murine model of cancer cachexia. *Physiol Rep* 2013;**1**:e00144.
41. Iwata Y, Suzuki N, Ohtake H, Kamauchi S, Hashimoto N, Kiyono T, et al. Cancer cachexia causes skeletal muscle damage via transient receptor potential vanilloid 2-independent mechanisms, unlike muscular dystrophy. *J Cachexia Sarcopenia Muscle* 2016;**7**:366–376.
42. Aulino P, Berardi E, Cardillo VM, Rizzuto E, Perniconi B, Ramina C, et al. Molecular, cellular and physiological characterization of the cancer cachexia-inducing C26 colon carcinoma in mouse. *BMC Cancer* 2010;**10**:363.
43. Wang Y, Pessin JE. Mechanisms for fiber-type specificity of skeletal muscle atrophy. *Curr Opin Clin Nutr Metab Care* 2013;**16**:243–250.
44. Yuan L, Han J, Meng Q, Xi Q, Zhuang Q, Jiang Y, et al. Muscle-specific E3 ubiquitin ligases are involved in muscle atrophy of cancer cachexia: an in vitro and in vivo study. *Oncol Rep* 2015;**33**: 2261–2268.
45. Li YP, Reid MB. NF-kappaB mediates the protein loss induced by TNF-alpha in differentiated skeletal muscle myotubes. *Am J Physiol Regul Integr Comp Physiol* 2000;**279**:R1165–R1170.
46. Moon TC, Befus AD, Kulka M. Mast cell mediators: their differential release and the secretory pathways involved. *Front Immunol* 2014;**5**:569.
47. Beck SC, Wilding T, Buka RJ, Baretto RL, Huissoon AP, Krishna MT. Biomarkers in human anaphylaxis: a critical appraisal of current evidence and perspectives. *Front Immunol* 2019;**10**:494.
48. Banduseela V, Ochala J, Lamberg K, Kalimo H, Larsson L. Muscle paralysis and myosin loss in a patient with cancer cachexia. *Acta Myol* 2007;**26**:136–144.
49. Cosper PF, Leinwand LA. Myosin heavy chain is not selectively decreased in murine cancer cachexia. *Int J Cancer* 2012;**130**: 2722–2727.
50. Yamada T, Ashida Y, Tatebayashi D, Abe M, Himori K. Cancer cachexia induces preferential skeletal muscle myosin loss when combined with denervation. *Front Physiol* 2020;**11**:445.
51. Trias E, King PH, Si Y, Kwon Y, Varela V, Ibarburu S, et al. Mast cells and neutrophils mediate peripheral motor pathway degeneration in ALS. *JCI Insight* 2018;**3**.
52. Costa RGF, Caro PL, de Matos-Neto EM, Lima J, Radloff K, Alves MJ, et al. Cancer cachexia induces morphological and inflammatory changes in the intestinal mucosa. *J Cachexia Sarcopenia Muscle* 2019;**10**: 1116–1127.
53. Shukla SK, Markov SD, Attri KS, Vernucci E, King RJ, Dasgupta A, et al. Macrophages potentiate STAT3 signaling in skeletal muscles and regulate pancreatic cancer cachexia. *Cancer Lett* 2020;**484**:29–39.
54. Cregar L, Elrod KC, Putnam D, Moore WR. Neutrophil myeloperoxidase is a potent and selective inhibitor of mast cell tryptase. *Arch Biochem Biophys* 1999;**366**: 125–130.
55. Molderings GJ, Brettner S, Homann J, Afrin LB. Mast cell activation disease: a concise practical guide for diagnostic workup and therapeutic options. *J Hematol Oncol* 2011;**4**:10.
56. Akin C, Valent P, Metcalfe DD. Mast cell activation syndrome: proposed diagnostic criteria. *J Allergy Clin Immunol* 2010;**126**: 1099–1104 e4.
57. Morley JE, Thomas DR, Wilson MM. Cachexia: pathophysiology and clinical relevance. *Am J Clin Nutr* 2006;**83**:735–743.
58. Arthur ST, Noone JM, Van Doren BA, Roy D, Blanchette CM. One-year prevalence, comorbidities and cost of cachexia-related inpatient admissions in the USA. *Drugs Context* 2014;**3**:212265.
59. von Haehling S, Morley JE, Coats AJS, Anker SD. Ethical guidelines for publishing in the Journal of Cachexia, Sarcopenia and Muscle: update 2019. *J Cachexia Sarcopenia Muscle* 2019;**10**:1143–1145.

nature COMMUNICATIONS

ARTICLE

https://doi.org/10.1038/s41467-021-25473-y OPEN

Exosomal miR-19a and IBSP cooperate to induce osteolytic bone metastasis of estrogen receptor-positive breast cancer

Kerui Wu[1], Jiamei Feng[1,2], Feng Lyu[1,3], Fei Xing[1], Sambad Sharma[1], Yin Liu[1], Shih-Ying Wu[1], Dan Zhao[1], Abhishek Tyagi[1], Ravindra Pramod Deshpande[1], Xinhong Pei[1,4], Marco Gabril Ruiz[1], Hiroyuki Takahashi[5], Shunsuke Tsuzuki[5], Takahiro Kimura[5], Yin-yuan Mo[6], Yusuke Shiozawa[1], Ravi Singh[1] & Kounosuke Watabe[1✉]

Bone metastasis is an incurable complication of breast cancer. In advanced stages, patients with estrogen-positive tumors experience a significantly higher incidence of bone metastasis (>87%) compared to estrogen-negative patients (<56%). To understand the mechanism of this bone-tropism of ER$^+$ tumor, and to identify liquid biopsy biomarkers for patients with high risk of bone metastasis, the secreted extracellular vesicles and cytokines from bone-tropic breast cancer cells are examined in this study. Both exosomal miR-19a and Integrin-Binding Sialoprotein (IBSP) are found to be significantly upregulated and secreted from bone-tropic ER$^+$ breast cancer cells, increasing their levels in the circulation of patients. IBSP is found to attract osteoclast cells and create an osteoclast-enriched environment in the bone, assisting the delivery of exosomal miR-19a to osteoclast to induce osteoclastogenesis. Our findings reveal a mechanism by which ER$^+$ breast cancer cells create a microenvironment favorable for colonization in the bone. These two secreted factors can also serve as effective biomarkers for ER$^+$ breast cancer to predict their risks of bone metastasis. Furthermore, our screening of a natural compound library identifies chlorogenic acid as a potent inhibitor for IBSP-receptor binding to suppress bone metastasis of ER$^+$ tumor, suggesting its preventive use for bone recurrence in ER$^+$ patients.

[1] Department of Cancer Biology, Wake Forest University School of Medicine, Winston-Salem, NC, USA. [2] Mammary Department, Shuguang Hospital Affiliated to Shanghai University of Traditional Chinese Medicine, Shanghai, China. [3] Department of Breast Surgery, Henan Provincial People's Hospital, People's Hospital of Zhengzhou University, People's Hospital of Henan University, Zhengzhou, Henan, China. [4] Department of Breast Surgery, The First Affiliated Hospital of Zhengzhou University, Zhengzhou, Henan, China. [5] Department of Pathology, Jikei University School of Medicine, Minato City, Tokyo, Japan. [6] Cancer Institute, University of Mississippi Medical Center, Jackson, MS, USA. ✉email: kwatabe@wakehealth.edu

Bone metastasis is the most predominant complication of breast cancer. More than 50% of patients have bone as the first site of distant metastases, followed by lung (17%), brain (16%), and liver (6%)[1]. Ultimately, 70% of metastatic breast cancer patients experience a distant bone relapse during the course of disease[2,3]. Bone metastasis leads to a worse prognosis in breast cancer patients, with a 16-month median survival[4], and it causes many other complications. Patients develop skeletal-related events (SREs) such as severe bone pain, pathological fracture, hypercalcemia, and infiltration of the bone marrow[5]. Crosstalk between cancer cells and bone stroma cells, including mesenchymal stem cells, osteoblast cells, and osteoclast (OC) cells, play critical roles in bone metastasis[6]. Most breast cancer patients develop osteolytic lesions, which are mainly resulted from OC-mediated bone resorption rather than physical destruction by the cancer cells[7,8]. The interaction with breast cancer cells activates OC cells, induces the bone resorption[9,10], and liberates the growth factors embedded in the bone matrix, which in turn stimulate the growth of cancer cells[11]. This process is termed "the vicious cycle of bone metastases"[12]. To impede this pathway, bisphosphonate (Zoledronic Acid) and RANKL inhibitor (Denosumab) were developed as bone-targeted therapies[13,14]. However, the use of these drugs in breast cancer patients has several limitations. As to the preventive use of bone-targeted therapies for bone metastasis, while bisphosphonate showed a moderate preventive effect in postmenopausal breast cancer patients, it did not decrease the rate of bone recurrence in premenopausal patients[15]. The significant side effects, including osteonecrosis of the jaws[16], make it an unfavorable preventive regimen. Moreover, RANKL inhibitor (Denosumab) failed to prevent bone recurrence among both premenopausal and postmenopausal patients[17]. For therapeutic use, these drugs have been proven to reduce the symptoms, but not to extend the patients' survival[18,19]. Thus, there is an urgent need for effective treatments for preventive and curative management of breast cancer bone metastasis (BCBM).

Among different subtypes of breast cancer, patients with estrogen receptors$^+$ (ER$^+$) tumors experience the most frequent bone metastases. Bone metastases account for as high as 87% of metastatic diseases among ER$^+$ breast cancer patients, while the incidence of bone metastasis is <56% among ER$^-$ breast cancer patients[20] with metastatic diseases. ER positivity is also associated with a higher rate of bone recurrence[21,22], and ER$^+$ breast cancer relapses more frequently in the bone than in other organs[23]. Although ER$^+$ breast cancer patients are regularly treated with adjuvant endocrine therapy for a long-term after surgery, cancer cells frequently develop late-onset recurrence in bone[22]. This suggests drug resistance to endocrine therapy developed in the bone-metastatic cells. The long-dormant period also deprioritizes current preventive bone-targeted therapy due to their significant side effects. Thus, it is important to identify biomarkers that can be used for predicting the risk of bone recurrence among ER$^+$ breast cancer patients. Despite the strong association between ER positivity and bone metastasis, how ER$^+$ cancer cells acquire the bone tropism remains unclear. Understanding the mechanism of such organotropism warrants major opportunities to identify specific biomarkers and preventive/therapeutic targets for ER$^+$ breast cancer bone metastasis. To survive in the bone microenvironment, breast cancer cells need to interact with bone microenvironment cells. Cell-secreted free proteins, including PTHrP, IL-1, and IL-6 were known to facilitate the communication between cancer cells and bone cells[24]. In addition to the cytokines, cancer cells are also able to interact with microenvironment cells through extracellular vesicles (EVs)[25]. These vesicles, including apoptotic bodies (ABs), microvesicles (MVs), and exosomes, encapsulate tumor-specific content, and transmit them into environmental cells and circulation. They promote tumor growth by directly transducing tumor cells[26], or affecting surrounding cells to generate metastatic niche[27–29]. As yet, no secretory factors specific to ER$^+$ breast cancer have been identified to elucidate the association between ER positivity and bone metastasis.

In the current study, to decipher the molecular mechanism by which ER$^+$ cancer preferentially metastasizes to the bone, we examined both the EVs and the free proteins secreted by ER$^+$ bone-tropic breast cancer. We found that the expression of exosomal miR-19a and IBSP is significantly upregulated in the secretion of ER$^+$ bone-tropic breast cancer cell lines, as well as in ER$^+$ breast cancer patients with bone metastases. While the miR-19a was found to be upregulated in breast cancer, its exact role in tumor progression has been poorly understood[30,31]. IBSP is a major structural protein of the bone matrix and is mainly expressed by bone cells[32]. We found that ectopic expression of both factors promoted bone metastasis in our in vivo models, suggesting both factors cooperate for ER$^+$ breast cancer bone metastasis. We also screened a natural compound library and identified chlorogenic acid (CGA) that is capable of blocking this pathway. These findings illustrate a unique pathway of how ER$^+$ breast cancer interacts with the bone microenvironment and establishes bone colonization. Furthermore, these two secretory factors would serve as prognostic markers for predicting the risk of bone metastasis in ER$^+$ breast cancer patients.

Results

Bone-metastatic ER$^+$ breast cancer cells secrete miR-19a and IBSP. Considering the importance of cell–cell communication in bone metastasis, ER$^+$ cells may shed secretory factors in the bone microenvironment to exert strong bone tropism. To test this hypothesis, we examined both EVs and proteins secreted from bone-tropic breast cancer cells. Small non-coding RNA is known to be selectively transported and enriched in EVs[33,34], suggesting its importance as a disease regulator and feasible biomarker. Thus, we compared the transcriptome profiles of miRNA in EVs isolated from MCF7BoM2, a previously reported organotropic ER$^+$ breast cancer cell line that prefers bone colonization[35], with the EVs from its parental cell line MCF7 (Fig. 1a). We made sure that the increased bone metastasis rate of the MCF7BoM2 line was not due to an alteration in the cell growth ability, as implantation of MCF7 and MCF7BoM2 into the mammary fat pads generated primary tumors with similar sizes and weights (Supplementary Fig. 1a–d). We found 157 miRNAs that were significantly upregulated in the EVs from MCF7BoM2. To validate the clinical relevance of these exosomal miRNAs, we examined whether they are secreted into the blood of ER$^+$ patients using the cohort data set of the circulating miRNA profiles from 23 ER$^+$ breast cancer patients and 22 healthy donors (Fig. 1a). Among the 157 miRNAs, three of them (miR-19a, miR-133b, and miR-576-5p) were found to be significantly upregulated in the blood of ER$^+$ breast cancer patients. Kaplan–Meier survival analyses were performed to investigate the association between these three miRNAs with metastatic events, and only miR-19a was found to be positively correlated with metastatic disease in ER$^+$ breast cancer patients (Fig. 1b). There is no difference in metastatic incidence between ER$^-$ breast cancer patients with or without elevated miR-19a expression (Fig. 1b), and both miR-133b and miR-576-5p are not significantly associated with metastasis in either ER$^+$ or ER$^-$ patients (Supplementary Fig. 2a). We also compared the ER$^+$ breast cancer tissue from bone-metastatic lesions with ER$^+$ primary breast cancer tissue from breast cancer patients without recurrence for 10 years, and with brain and lung metastatic lesions from ER$^+$ breast cancer patients with visceral metastases

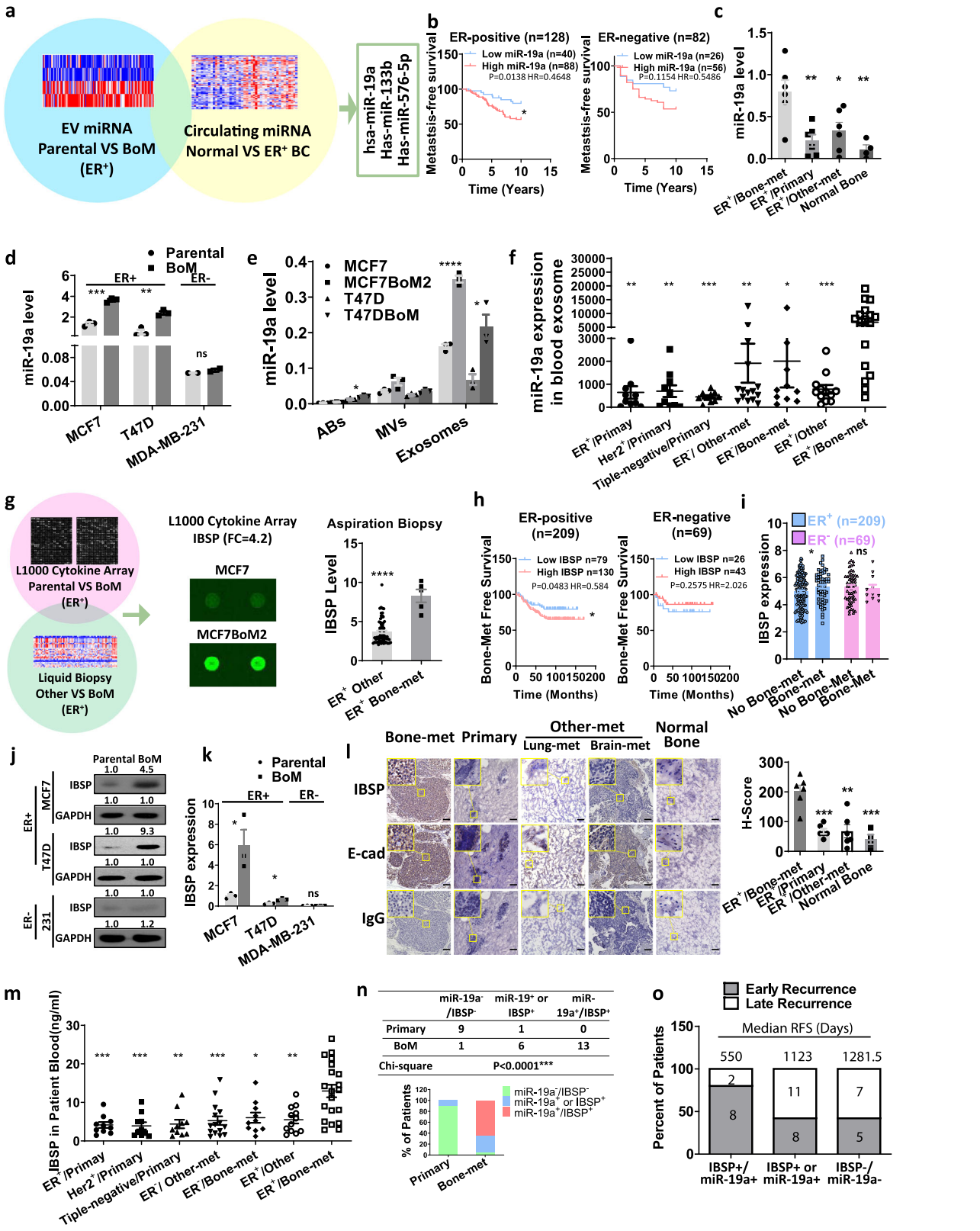

only, as well as with normal bone tissue. It was found that miR-19a is indeed only increased in bone-metastatic tissues (Fig. 1c). To validate the specificity of miR-19a associated with ER$^+$ tumor, we established another ER$^+$ bone-tropic cell line, T47DBoM. Similar to MCF7BoM2, T47DBoM generated comparable size and weight of primary tumors when implanted in the mammary fat pads. On the other hand, T47DBoM caused more aggressive bone metastases when it was implanted intravenously (Supplementary Fig. 1e–h). We examined the expression of miR-19a in ER$^+$ and ER$^-$ cancer cell lines and found that the ER$^+$ bone-tropic breast cancer cells, MCF7BoM2 and T47DBoM, have a higher endogenous expression of miR-19a compared to the parental cell lines, MCF7 and T47D (Fig. 1d). On the other hand, the expression of miR-19a did not show any difference in the bone-

Fig. 1 Bone-metastatic ER$^+$ breast cancer cells secrete miR-19a and IBSP. a EVs were prepared from the conditioned medium of bone-metastatic cell line MCF7BoM2 and the parental cell line MCF7, followed by extraction of RNA. They were then subjected to miRNA profiling by GeneAtlas miRNA Array. Using the criteria of FDR < 0.05 and Fold change > 1.3, 156 miRNAs were selected for further study. These miRNAs were then examined whether they are secreted in the blood of ER$^+$ patients using the cohort data set (GSE41922) of the circulating microRNA profiles between 23 ER$^+$ breast cancer (BC) patients and 22 healthy donors (Normal). Three miRNAs (miR-19a. miR-133b, miR-576-5p), were found to be significantly upregulated (FDR < 0.05 and logFC > 0.5) in the blood of breast cancer patients. BoM, bone metastatic. **b** Kaplan–Meier analysis of miR-19a was performed between breast cancer patients with low miR-19a and high miR-19a expression using GSE22220. **c** RNA from bone-met(metastatic) lesions ($n = 6$), primary tumors ($n = 6$), lung and brain lesions ($n = 6$) of ER$^+$ breast cancer patients, and normal bones ($n = 4$) was extracted and miR-19a expression was examined by Taqman-PCR. A two-sided student's *t*-test was performed (Primary vs Bone-met, $p = 0.0047$; Other-met vs Bone-met, $p = 0.0249$; Normal Bone vs Bone-met, $p = 0.0059$). Data are presented as mean values ± SEM. **d** The expression of miR-19a in parental cell lines (MCF7, T47D, and MDA-MB-231) and bone-tropic cell lines (MCF7BoM2, T47DBoM, and 231BoM-1833) were assayed by Taqman PCR. Two-sided student's *t*-tests were performed between parental groups and bone-metastatic (BoM) groups. $p = 0.0003$ (MCF7 vs MCF7BoM2, $n = 3$), $p = 0.0028$ (T47D vs T47DBoM, $n = 3$), $p = 0.1996$ (MDA-MB-231 vs 231BoM-1833, $n = 2$). Data are presented as mean values ± SEM. **e** The expressions of miR-19a in ABs, MVs, and exosomes from the parental cell lines (MCF7 and T47D) as well as their bone-tropic variants (MCF7BoM2 and T47DBoM) were examined by Taqman PCR. Two-sided student's *t*-tests were performed between parental groups and bone-metastatic (BoM) groups, $n = 3$ in each group. $p = 0.0408$ (ABs, T47D vs T47DBoM), $p < 0.0001$ (Exosomes, MCF7 vs MCF7BoM2), $p = 0.0167$ 0001 (Exosomes, T47D vs T47DBoM). Data are presented as mean values ± SEM. **f** Exosomes were isolated from the serum of breast cancer patients and the expression of miR-19a was compared among seven groups: (i) ER$^+$ ($n = 10$), (ii) Her2$^+$ ($n = 10$), and (iii) triple-negative ($n = 10$) breast cancer patients who were recurrence-free for 10 years, and (iv) ER$^-$ breast cancer patients with visceral metastases ($n = 15$), (v) ER$^-$ breast cancer patients with bone metastasis ($n = 10$), (vi) ER$^+$ breast cancer patients with visceral metastases ($n = 12$) and ER$^+$ breast cancer patients with bone metastasis ($n = 20$). Two-sided student's *t*-tests were performed to compare the miR-19a expression between the ER$^+$/Bone-met group with each of the other groups. $p = 0.0012$, 0.003, 0.0008, 0.0036, 0.016, and 0.0005 from left to right. Data are presented as mean values ± SEM. **g** Cytokine/growth factor profiling was performed on conditioned media from MCF7 and MCF7BoM2 using L1000 array (Raybiotech), and 49 upregulated cytokines (fold change > 3) were selected. This list was cross-examined with gene profiles of the ER$^+$ breast cancer biopsy database (GSE56493). Genes upregulated (FDR < 0.05 and fold change > 1.2) in biopsy of bone metastasis ($n = 5$) compared to other sites ($n = 75$) were selected. IBSP in conditioned media, as well as in ER$^+$ breast cancer biopsy from the bone lesion and other sites (GSE56493, $p < 0.0001$, presented as mean values ± SEM) were presented. **h** Kaplan–Meier analyses were performed for the association between IBSP expression and bone metastasis-free survival among 209 ER$^+$ breast cancer patients and 69 ER$^-$ breast cancer patients using GSE2034. **i** The IBSP expression was compared between ER$^+$ breast cancer patients with (n = 57) or without ($n = 152$) bone metastasis ($p = 0.04625$, two-sided student's *t*-test), as well as between ER$^-$ breast cancer patients with ($n = 11$) or without ($n = 58$) bone metastases ($p = 0.6944$, two-sided student's *t*-test). Data are presented as mean values ± SEM. **j** Western blot analysis for IBSP expression in MCF7 and MCF7BoM2, T47D and T47DBoM, MDA-MB-231 and 231BoM-1833. Quantification of the bands was performed using the ImageJ program and the value was normalized to that of control (left panel). **k** PCR analysis for IBSP expression was performed in MCF7 and MCF7BoM2 ($p = 0.0341$), T47D and T47DBoM ($p = 0.0120$), MDA-MB-231 and 231BoM-1833 ($p = 0.3494$), $n = 3$ in all groups. Two-sided student's *t*-tests were used in each pair of comparisons. Data are presented as mean values ± SEM. **l** IBSP was examined by IHC on bone lesions ($n = 6$), primary breast cancer tissue without recurrence for 10 years ($n = 6$), brain and lung lesions ($n = 6$) and normal bones ($n = 4$). The staining was quantified by *H*-score assessment and compared by the two-sided student's *t*-test. $p = 0.0002$ (Primary vs Bone-met); $p = 0.0014$ (Other-met vs Bone-met); $p = 0.0006$ (Normal Bone vs Bone-met). Data are presented as mean values ± SEM. E-cad (E-cadherin) was stained as the marker of breast cancer cells. Rabbit IgG was used as isotype control. Scale bar, 100 μm. **m** ELISA was performed to quantify the IBSP level in the serum of ER$^+$ ($n = 10$), Her2$^+$ (n = 10) and triple-negative ($n = 10$) breast cancer patients without recurrence for 10 years, and ER$^-$ breast cancer patients with visceral metastases ($n = 15$), ER$^-$ breast cancer patients with bone metastasis ($n = 10$), ER$^+$ breast cancer patients with visceral metastases ($n = 12$) and ER$^+$ breast cancer patients with bone metastasis ($n = 20$). Two-sided student's *t*-tests were performed to compare the miR-19a expression between the ER$^+$/Bone-met group with each of the other groups. $p = 0.0009$, 0.0009, 0.0016, 0.0010, 0.0101, and 0.0024 from left to right. Data are presented as mean values ± SEM. **n** ER$^+$ breast cancer patients with or without bone metastases were separated into three groups according to the serum levels of IBSP and exosomal miR-19a, including miR-19a low/IBSP low group (miR-19a$^-$/IBSP$^-$), miR-19a low/IBSP high or miR-19a high/IBSP low group (miR-19$^+$ or IBSP$^+$) and miR-19a high/IBSP high group (miR-19a$^+$/IBSP$^+$). The percentage in each group was calculated and plotted as the bar graph. The chi-square test was performed. **o** ER$^+$ breast cancer patients with recurrent disease were selected from TCGA. Patients with early recurrence (<1000 days) and late recurrence (≥1000 days) were separated into three groups: miR-19a low/IBSP low group (miR-19a$^-$/IBSP$^-$), miR-19a low/IBSP high or miR-19a high/IBSP low group (miR-19$^+$ or IBSP$^+$) and miR-19a high/IBSP high group (miR-19a$^+$/IBSP$^+$). The percentage of patients and the median RFS (recurrence-free survival) days in each group were calculated.

tropic triple-negative cell line derived from MDA-MB-231[36] (Fig. 1d). To examine whether free or vesicle-encapsulated miRNAs are the major source of secreted miR-19a, we treated the conditioned medium from MCF7BoM2 with RNase. The RNase treatment did not degrade the secreted miR-19a from breast cancer cells, suggesting that they are protected in the membrane vesicles (Supplementary Fig. 2b). This finding is consistent with the previous report that the majority of miRNA in serum is encapsulated by EVs[37,38]. EVs include ABs, MVs and exosomes. To further clarify the source of EV-derived miR-19a, we examined the miR-19a expression in these three components of EVs from MCF7 and T47D as well as their bone-tropic variants. After confirming the purity of the isolated vesicles by nanoparticle tracking analysis (NTA), electron microscope (EM), as well as a western blot (Supplementary Fig. 2c, d), the expression of miR-19a in these vesicles, were examined by Taqman PCR. We found that miR-19a is most highly expressed in exosomes compared to other EVs (Fig. 1e). Importantly, there is a strong upregulation of miR-19a in the exosomes from ER$^+$ bone-metastatic variants, MCF7BoM2 and T47DBoM (Fig. 1e), compared to their parental cell lines. However, ER$^-$ 231BoM showed only a negligible increase of miR-19a in the exosomes (Supplementary Fig. 2e). Next, we examined whether the increase of exosomal miR-19a can be detected in the serum of ER$^+$ breast cancer patients with bone metastases. Strikingly, ER$^+$ breast cancer patients with bone metastasis are significantly associated with higher expression of exosomal miR-19a in serum (Fig. 1f). It should be noted that the expression of exosomal miR-19a remained low in the patients with primary breast cancer with no recurrence within 10 years. We also did not observe any increase in exosomal miR-19a in the

serum of ER$^-$ breast cancer patients at advanced stages nor in ER$^+$ patients with visceral metastases but with no bone involvement (Fig. 1f). These data suggest that miR-19a is specifically upregulated in both endogenous and exosomal levels of ER$^+$ bone-tropic breast cancer cells.

We also examined secreted proteins and cytokines from ER$^+$ bone-tropic breast cancer cells. By performing L1000 cytokine array analysis, 1000 secreted proteins were examined in the conditioned medium from MCF7 and MCF7BoM2, and 49 proteins were found to be upregulated in the cell culture media from MCF7BoM2. Among these 49 proteins, IBSP was the only significantly upregulated gene in the aspiration biopsy from bone-metastatic lesions of ER$^+$ breast cancer patients, compared to the biopsy samples from other sites (Fig. 1g). IBSP is a major structural protein of the bone matrix. It is synthesized by skeletal-associated cell types as a secreted protein, and is able to bind to calcium and hydroxyapatite via its acidic amino acid clusters[39]. In breast cancer, we observed cancer cell-specific upregulation of IBSP, while the paired normal breast epithelial cells did not express IBSP (Supplementary Fig. 2f). This finding suggests a possible role of IBSP in breast cancer progression. Since many cytokines were previously reported to bind to the surface of EVs, we also looked at the membrane fractions of EVs by western blot (Supplementary Fig. 2g), but IBSP was not detected. We also performed immunostaining of IBSP and CD63 for the exosomes isolated from MCF7BoM2, and found that only CD63 but not IBSP was detected on the surface of exosomes (Supplementary Fig. 2h). Thus, we concluded that IBSP in the extracellular region is mainly in the form of free secreted protein. To further clarify the connection between IBSP and bone metastasis of ER$^+$ breast cancer, we performed Kaplan–Meier analyses among 278 breast cancer patients. IBSP was found to be positively correlated with bone metastasis only in ER$^+$ breast cancer patients, but not in ER$^-$ breast cancer patients (Fig. 1h). There is an increase in IBSP expression in the bone-metastatic group compared to the non-bone-metastatic group among ER$^+$ breast cancer patients, but not among ER$^-$ breast cancer patients (Fig. 1i). We also verified that ER$^+$ bone-metastatic cell lines have higher expression of IBSP compared to the parental cell lines. The PCR and western blot analyses confirmed the upregulation of IBSP in MCF7BoM2 and T47DBoM, but not in ER$^-$ bone-metastatic cell line 231BoM (Fig. 1j, k). When ER$^+$ breast cancer tissue from bone lesions was compared with ER$^+$ primary breast cancer tissue from patients with no recurrence within 10 years, and with brain and lung metastatic lesions from ER$^+$ breast cancer patients with visceral metastases only, as well as with normal bone tissue, IBSP was found to be significantly increased in bone-metastatic tissues (Fig. 1l). Next, we examined whether the increase of IBSP can be detected in the serum of ER$^+$ breast cancer patients with bone metastases. A significant upregulation of IBSP protein in the serum of ER$^+$ breast cancer patients with bone metastasis was detected (Fig. 1m), but not in the serum of patients with only primary breast cancer, advanced ER$^-$ breast cancer patients, or ER$^+$ breast cancer patients with visceral metastases other than bone.

Our data (Fig. 1a–m) suggest both miR-19a and IBSP are positively related to bone metastasis of ER$^+$ cancer cells. However, how they are associated with bone metastasis remains unknown. We further investigated whether miR-19a and IBSP are mutually related to bone metastasis of ER$^+$ breast cancer cells. We combined the results from Fig. 1f with Fig. 1m, and stratified the patients into three groups: both miR-19a and IBSP low, miR-19a or IBSP high, both miR-19a and IBSP high. Strikingly, ER$^+$ breast cancer patients with bone metastasis are significantly associated with higher expression of both IBSP and miR-19a. Upregulation of sole factor led to a negligible, but not significant increase of the bone-metastatic incidence, suggesting a possible cooperative role of these two factors in bone metastasis of ER$^+$ breast cancer cells (Fig. 1n). Next, we examined the expression of miR-19a and IBSP in breast cancer patients using the TCGA database. Among 41 ER$^+$ breast cancer patients with recurrence, IBSP and miR-19a could predict the recurrence risk as the majority of patients with high levels of both factors experienced earlier recurrence within 1000 days (Fig. 1o). The median recurrence-free survival (RFS) time of patients with high levels of both miR-19a and IBSP is only 550 days, while the median RFS time of patients with high expression of either miR-19a or IBSP and patients with low levels of both miR-19a/IBSP are 1123 days and 1281.5 days, respectively. These results indicate that miR-19a and IBSP are positively associated with bone metastasis, and they serve as biomarkers for a higher risk of bone metastasis when they are both upregulated in ER$^+$ breast cancers.

Both IBSP and miR-19a are essential for bone metastasis of ER$^+$ breast cancer. To test whether both miR-19a and IBSP are required for bone metastasis of ER$^+$ breast cancer cells, we ectopically expressed IBSP and miR-19a in MCF7, and established stable overexpression cell lines (Supplementary Fig. 3a–d). Ectopic expression of miR-19a did not alter the level of IBSP, and vice versa, indicating there is no regulatory network involved between IBSP and miR-19a. Neither miR-19a nor IBSP could induce any change of exosome production (Supplementary Fig. 3e), proliferation, or migration of the cells in vitro (Supplementary Fig. 3f, g). Intra-mammary fat pad injection of MCF7 with miR-19a and/or IBSP forced-expression did not induce any difference in tumor growth in vivo (Fig. 2a, b). Strikingly, ectopic expression of both miR-19a and IBSP together in MCF7 led to a significant increase in bone metastasis in the xenograft model with the intracardiac injection of cancer cells (Fig. 2c). Nonetheless, miR-19a or IBSP alone did not increase the incidence of bone metastasis. These data suggest miR-19a and IBSP promote bone metastasis through the tumor microenvironment instead of affect cancer cells directly. Since IBSP is known to regulate bone turnover by binding to integrin αVβ3 receptor on the surface of OC cells[40], we examined the bone densities of mice implanted with the breast cancer cells. We found that ectopic expression of both IBSP/miR-19a resulted in a significant decrease in bone density in the tumor lesions (Fig. 2d). We also quantified the total area of TRAP$^+$ OC surface and its percentage of total bone surface area (OC.S/BS%) in the tumor-bearing bones and found that synchronous overexpression of miR-19a and IBSP significantly increased the osteoclastogenesis (Fig. 2e). We then repeated this experiment in another ER$^+$ cell line, T47D. Both IBSP and miR-19a were ectopically introduced into T47D (Supplementary Fig. 3h, i), and stable overexpression cell lines had been established (Supplementary Fig. 3j, k) before the cells were inoculated into mouse tibia. Similar to MCF7, ectopic expression of both miR-19a and IBSP resulted in increased tumor burden in the bones (Fig. 2f), while discrete expression of miR-19a or IBSP alone did not affect the tumor growth. Bone lesions of T47D/IBSP/miR-19a presented decreased bone densities (Fig. 2g) and increased OC activities (Fig. 2h). These results indicate that miR-19a and IBSP work together to induce osteolytic bone metastasis in ER$^+$ breast cancer patients, though not directly affecting cancer cell growth or motility.

miR-19a promotes osteolytic bone metastasis. Because both miR-19a and IBSP are necessary to promote the bone metastasis of ER$^+$ breast cancer cells, we investigated how each of them contributes to the bone-tropic metastasis of cancer cells. MiR-19a,

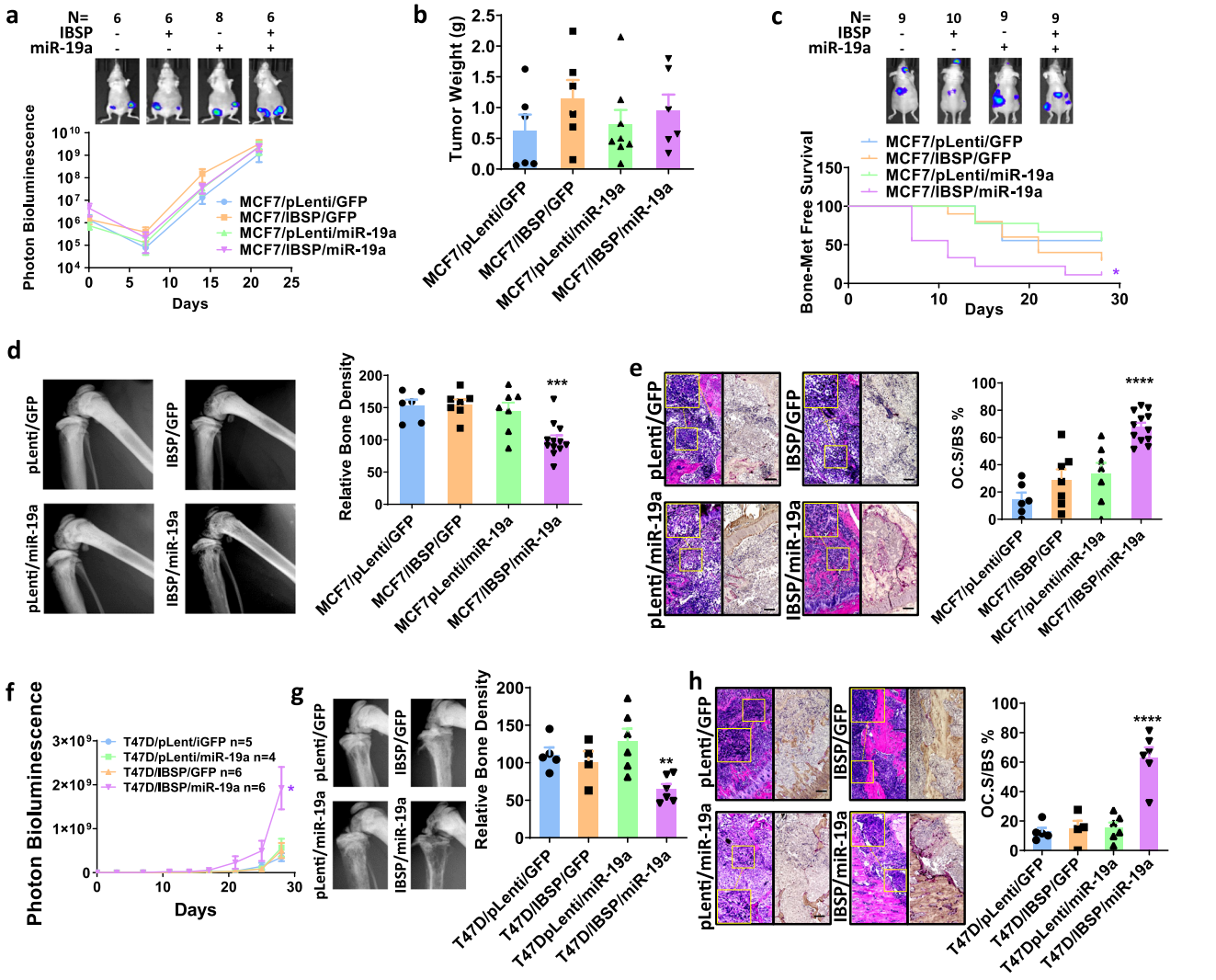

Fig. 2 Both IBSP and miR-19a are essential for bone metastasis of ER$^+$ breast cancer. a miR-19a and/or IBSP were ectopically expressed in MCF7, and they were transplanted into mammary fat pads of female nude mice. The growth of the tumor was monitored by measuring the luciferase activity by IVIS Bioimager. $p = 0.3110$ (MCF7/pLenti/GFP vs MCF7/IBSP/miR-19a; $n = 6$ vs 6), $p = 0.2649$ (MCF7/pLenti/GFP vs MCF7/IBSP/GFP; $n = 6$ vs 6), $p = 0.4739$ (MCF7/pLenti/GFP vs MCF7/pLenti/miR-19a; $n = 6$ vs 8). Data are presented as mean values ± SEM. **b** At day 21, tumors were removed from the mammary fat pad and their weights were measured. $p = 0.3971$ (MCF7/pLenti/GFP vs MCF7/IBSP/miR-19a; $n = 6$ vs 6), $p = 0.2178$ (MCF7/pLenti/GFP vs MCF7/IBSP/GFP; $n = 6$ vs 6), $p = 0.7632$ (MCF7/pLenti/GFP vs MCF7/pLenti/miR-19a; $n = 6$ vs 8). Data are presented as mean values ± SEM. **c** miR-19a and/or IBSP were ectopically expressed, and they were transplanted into female nude mice via intracardiac injection. The incidence of bone metastasis was monitored by measuring the luciferase activity by IVIS Bioimager. Log-rank (Mantel–Cox) test was performed to calculate the *p*-value. $p = 0.0105$ (MCF7/pLenti/GFP vs MCF7/IBSP/miR-19a), $p = 0.3982$ (MCF7/pLenti/GFP vs MCF7/IBSP/GFP), $p = 0.9230$ (MCF7/pLenti/GFP vs MCF7/pLenti/miR-19a). **d** The legs of mice were imaged by X-ray and the bone density was measured by ImageJ. $p = 0.0007$ (MCF7/pLenti/GFP vs MCF7/IBSP/miR-19a; $n = 6$ vs 12), $p = 0.8621$ (MCF7/pLenti/GFP vs MCF7/IBSP/GFP, $n = 6$ vs 7), $p = 0.6397$ (MCF7/pLenti/GFP vs MCF7/pLenti/miR-19a, $n = 6$ vs 7). Two-sided student's *t*-tests were performed. Data are presented as mean values ± SEM. **e** TRAP staining was performed in tumor-bearing bones from mice. The total OC surface area relative to the bone surface area was measured by ImageJ, then calculated and compared among different groups. H&E staining of the same field was shown together with the TRAP staining. Scale bar, 100 μm. $p < 0.0001$ (MCF7/pLenti/GFP vs MCF7/IBSP/miR-19a, $n = 6$ vs 12), $p = 0.1598$ (MCF7/pLenti/GFP vs MCF7/IBSP/GFP, $n = 6$ vs 7), $p = 0.0867$(MCF7/pLenti/GFP vs MCF7/pLenti/miR-19a, $n = 6$ vs 7). Two-sided student's *t*-tests were performed. Data are presented as mean values ± SEM. **f** miR-19a and/or IBSP were ectopically expressed, and they were transplanted into female nude mice via intra-tibia injection. The growth of tumor in bone was monitored by measuring the luciferase activity by IVIS Bioimager. $p = 0.0175$ (T47D/pLenti/GFP vs T47D/IBSP/miR-19a), $p = 0.4877$ (T47D/pLenti/GFP vs T47D/IBSP/GFP), $p = 0.3305$ (T47D/pLenti/GFP vs T47D/pLenti/miR-19a). Data are presented as mean values ± SEM. **g** The legs of mice were imaged by X-ray and the bone density was measured by ImageJ. $p = 0.0034$ (T47D/pLenti/GFP vs T47D/IBSP/miR-19a $n = 5$ vs 6), $p = 0.5750$ (T47D/pLenti/GFP vs T47D/IBSP/GFP, $n = 5$ vs 4), $p = 0.3809$ (T47D/pLenti/GFP vs T47D/pLenti/miR-19a, $n = 5$ vs 6). Two-sided student's *t*-tests were performed. Data are presented as mean values ± SEM. **h** TRAP staining was performed in tumor-bearing bones from the mice. The OC surface relative to the bone surface was calculated and compared among different groups. H&E staining of the same field was shown together with the TRAP staining. Scale bar, 100 μm. $p = 0.0001$ (T47D/pLenti/GFP vs T47D/IBSP/miR-19a, $n = 5$ vs 6), $p = 0.7711$ (T47D/pLenti/GFP vs T47D/IBSP/GFP, $n = 5$ vs 4), $p = 0.5701$ (T47D/pLenti/GFP vs T47D/pLenti/miR-19a, n = 5 vs 6). Two-sided student's *t*-tests were performed. Data are presented as mean values ± SEM.

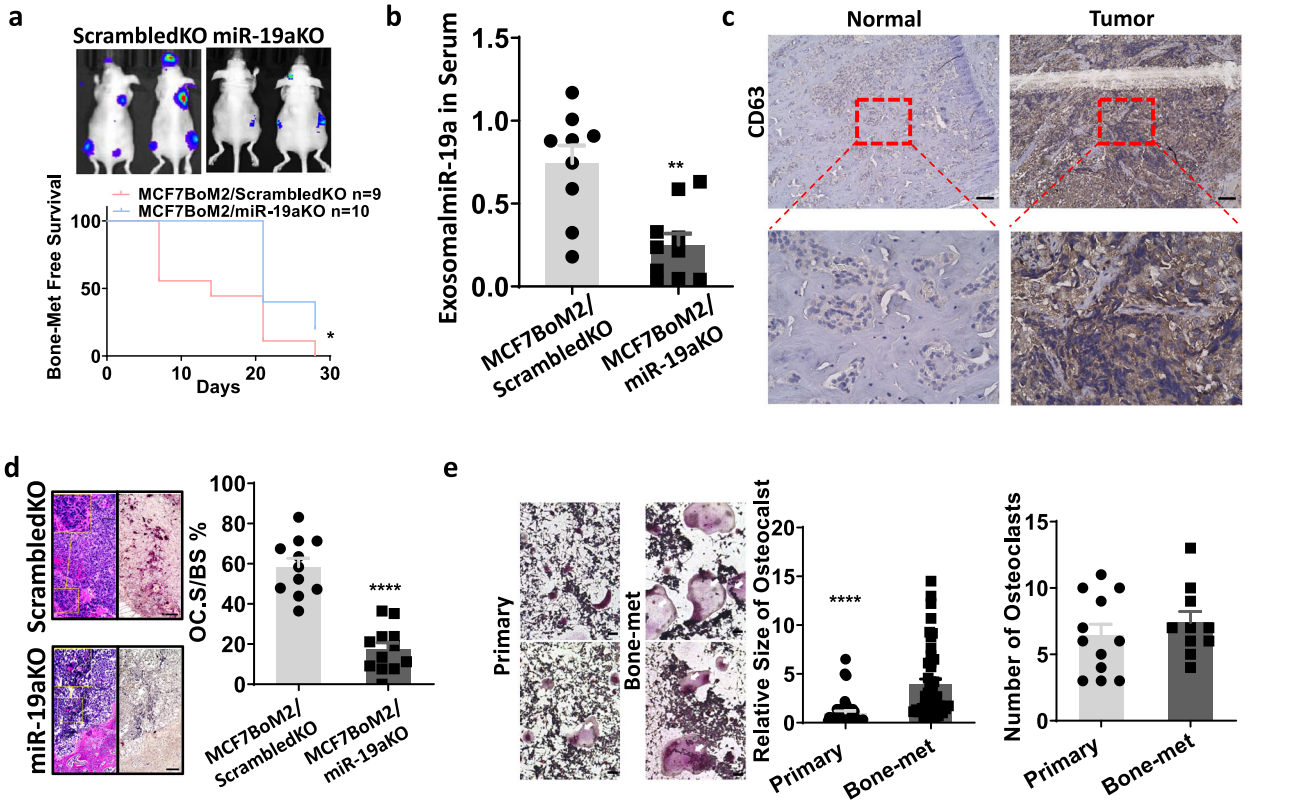

Fig. 3 miR-19a promotes osteolytic bone metastasis. a MCF7BoM2/ScrambledKO and MCF7BoM2/miR-19aKO were transplanted into female nude mice via intracardiac injection. The growth of bone metastasis was monitored by measuring the luciferase activity by IVIS Bioimager. Log-rank (Mantel–Cox) test was performed to calculate the *p*-value ($p = 0.0109$). **b** At the endpoint (day 28), mice were sacrificed and the expression of exosomal miR-19a from serum was examined by Taqman. A two-sided student's *t*-test was performed ($p = 0.0011$, $n = 9$ vs 10). Data are presented as mean values ± SEM. **c** Representative figures of the expression of exosomal marker CD63 in normal bone and tumor-bearing bone from the mice. Scale bar, 100 μm. **d** TRAP staining for osteoclast cells in tumor-bearing bones from the mice transplanted with MCF7BoM2/ScrambledKO or MCF7BoM2/miR-19aKO. OC surface relative to the bone surface was calculated and compared. H&E staining of the same field was shown together with the TRAP staining. Scale bar, 100 μm. A two-sided student's *t*-test was performed ($p = 0.00000014$, $n = 11$ vs 12). Data are presented as mean values ± SEM. **e** Exosomes from the serum of ER^+ breast cancer patients with ($n = 10$) or without ($n = 12$) bone metastasis were isolated. The harvested exosomes were incubated with mouse bone marrow-derived monocytes. After 1 week, the cells were fixed and TRAP staining was performed. The size ($p = 0.0000039$) and number ($p = 0.4254$) of differentiated OC were quantified and compared. Scale bar, 100 μm. Two-sided student's *t*-tests were performed. Data are presented as mean values ± SEM.

as a member of the OncomiR-1 family, was previously found to be upregulated in multiple malignancies[41–43]. It was also found to be expressed in breast cancer cells, although its role remains unclear[30,44]. We found both endogenous and secreted levels of miR-19a were higher in the bone-metastatic cell lines compared to the parental cell lines. However, endogenous expression of miR-19a did not affect breast cancer cells per se because the ectopic expression of miR-19a did not alter the growth or motility of cells in vitro (Supplementary Fig. 3f, g). To further clarify the role of miR-19a in bone metastasis of ER^+ breast cancer cells, we applied the CRISPR/Cas9 technology to knock out the miR-19a in MCF7BoM cells. A specific gRNA (guide RNA) was designed to target the stem-loop of miR-19a precursor so that the biogenesis of mature miR-19a was hindered. The genomic DNA cleaving ability of our gRNA targeting miR-19a was verified by the T7E1 enzyme (Supplementary Fig. 4a). Four independent clones with minimal miR-19a expression and unaltered proliferation were selected and combined to establish the stable knockout cell line (Supplementary Fig. 4b–d). When tested in vitro, we found that knockout of miR-19a did not alter the cell migration or invasion abilities (Supplementary Fig. 4e–f). However, when miR-19a knockout cells were implanted into nude mice by intracardiac injection, loss of miR-19a significantly decreased bone metastasis (Fig. 3a). These data are consistent with our previous finding that miR-19a is needed for bone-tropic metastasis of MCF7BoM2. MCF7BoM2 has a high expression of both miR-19a and IBSP. Knockout of miR-19a, but leaving IBSP alone, compromised the bone-metastatic ability of MCF7BoM2. Interestingly, when we examined the serum exosomes in the mice, we found that the knockout of miR-19a significantly decreased exosomal miR-19a in the serum (Fig. 3b). This finding suggests that serum exosome could represent the dynamic changes of breast cancer cells. These results are also in agreement with the previous finding that miR-19a could not induce the intrinsic change of cancer motility. Accordingly, we investigated whether exosomal miR-19a could promote bone metastasis by remodeling environmental cells in a paracrine manner instead of directly affecting cancer cells. The tumor lesion in the bone exhibited abundant expression of exosomal marker CD63 (Fig. 3c), implying exosome activity in the microenvironment. Since we found an aberrant osteolytic change in our previous data, we examined the OC in the bone lesions. There was a decrease of osteoclastogenesis in the tumor-bearing bones when miR-19a was knocked out from the cancer cells (Fig. 3d), indicating a possible role of exosomal miR-19a in

promoting OC cells. To verify this hypothesis, exosomes from serum of ER$^+$ breast cancer patients with or without bone metastases were isolated and incubated with primary OC precursors. Exosomes prepared from the patients with bone metastases significantly promoted OC maturation and differentiation (Fig. 3e). These results indicate that miR-19a is involved in the osteolytic bone metastasis and exosomal miR-19a could directly promote OC activity in the bone microenvironment.

Exosomal miR-19a targets PTEN/AKT pathway to promote osteoclastogenesis. To validate our hypothesis that exosomal miR-19a promotes the activity of OC cells, we first examined whether exosomes can be directly up-taken by OC cells. OC precursor RAW264.7 cells were treated with PalmGFP-labeled exosomes derived from bone-metastatic breast cancer cells. The result indicates that exosomes from MCF7BoM2 were indeed incorporated into RAW264.7 cells 24 h after the treatment (Fig. 4a). It was reported that miR-19a targeted PTEN 3′UTR[45] and that OC differentiation and their activity were regulated by NF-κB and AKT pathways[46,47], both of which were known to be inhibited by PTEN[48,49]. Thus, it is plausible that cancer cells secrete miR-19a and suppress PTEN expression in OC cells when exosomes are internalized. The decrease of PTEN leads to activation of NF-κB and AKT pathways that promote OC cells. To test this notion, we examined whether exosomal miR-19a modulates OC activity by suppressing PTEN expression, using the 3′ UTR reporter assay. We confirmed that the miR-19a-targeted sequence on PTEN is conserved between human and mouse (Supplementary Fig. 5a, b), and found that ectopic expression of miR-19a indeed targeted PTEN, while mutation of the miR-19a binding site on PTEN 3′UTR rescued the reporter activity (Fig. 4b). Furthermore, ectopic expression of miR-19a in OC precursor cells, RAW264.7, suppressed PTEN expression and induced NF-κB and AKT pathway with increased phosphorylated P65 and AKT (Fig. 4c, d). We also examined whether increased miR-19a could promote OC differentiation of RAW264.7 by performing TRAP staining. The ectopic expression of miR-19a significantly increased the number of mature OC cells and their size (Fig. 4e). Next, we tested whether direct treatment of OC precursor cells with exosomal miR-19a, instead of lentiviral overexpression, could also induce the activation of P65 and AKT pathways. Although there was no difference in the efficiency of exosome uptake (Supplementary Fig. 5c), compared to exosomes from the parental cell line, exosomes from bone-metastatic MCF7BoM2 increased miR-19a, decreased PTEN and induced AKT, and P65 activation in mouse bone marrow monocyte (mBMM), which is the primary precursor of OC (Fig. 4f, g). In addition, exosomes from MCF7BoM2 promoted the differentiation of mBMM into OC (Fig. 4h). In a bone resorption assay, mBMMs were seeded on the bone chips and incubated with exosomes from MCF7 and MCF7BoM2. Exosomes from MCF7BoM2 exhibited significantly higher competence to induce the osteolytic activities of OC cells as shown by the increased area of resorption pit (Fig. 4i). Consistent with our finding of enriched miR-19a in exosomes, only exosomes, but not MV or AB, could induce the differentiation of OC cells (Supplementary Fig. 5d). To further investigate whether miR-19a is responsible for the OC-promoting effect of the exosomes, OC cells were incubated with exosomes isolated from MCF7BoM2/ScrabmbleKO cells or MCF7BoM2/miR-19aKO cells (Fig. 4j–m and Supplementary Fig. 6a–c). When miR-19a was knockout, exosomes were unable to deliver miR-19a into OC cells and suppress PTEN expression (Fig. 4j and Supplementary Fig. 6b). We also found that exosomes prepared from bone-metastatic breast cells with miR-19a knockout could not induce P65 and AKT activation (Fig. 4k and Supplementary Fig. 6c) and reversed the OC-promoting effect (Fig. 4l, m and Supplementary Fig. 6a). Collectively, we demonstrated that bone-metastatic cells delivered miR-19a-containing exosomes to OC precursor cells and suppressed PTEN expression. Decreased PTEN induced the activation of NF-κB and AKT signaling pathways, promoting the differentiation and osteolytic activity of OC cells. This notion was also verified by examining the effect of exosomes from MCF7 and MCF7/miR-19a cell lines on OC cells. Compared to exosomes from parental MCF7 cells, exosomes from MCF7 with ectopic expression of miR-19a significantly increased the miR-19a expression and decreased PTEN expression in both recipient RAW264.7 and mBMM cells, increased OC number, and promoted the differentiation of OC in vitro (Supplementary Fig. 6d–i).

ER$^+$ breast cancer cells secrete IBSP to recruit osteoclast precursors. Next, we examined the role of IBSP in osteolytic bone metastasis induced by miR-19a. IBSP is known to act as a ligand of integrin αVβ3 receptor that is highly expressed on the surface of OC[40]. A previous study found that IBSP knockout in mice resulted in decreased OC number in bones[40]. Integrin αVβ3 is known to be associated with OC migration and adhesion[50,51], and IBSP was previously found to be a cell-secreted protein with bone matrix binding ability[52]. Therefore, we hypothesize that IBSP secreted from the bone lodging cancer cells can recruit the OC precursors to the micro-metastatic site followed by creating an OC precursor-enriched niche. Such an environment enhances the uptake of miR-19a-containing exosomes by the OC precursors in a concentration-dependent manner. In a trans-well migration assay, we found that both MCF7BoM2 and MCF7/IBSP recruited more OC precursors to abluminal chambers compared to MCF7 (Fig. 5a), which supports our hypothesis that IBSP attracts OC precursors. We then performed the knockout of IBSP using the CRISPR-Cas9 system in MCF7BoM2. To rule out the clonal effect, three clones that showed no IBSP expression and no alteration of growth ability were selected and mixed into one heterogeneous line, MCF7BoM2/IBSPKO (Fig. 5b, c and Supplementary Fig. 7a). The knockout of IBSP expression did not alter the cell migration ability of MCF7BoM2/IBSPKO (Fig. 5d). However, the bone-metastatic ability was significantly compromised by IBSP knockout in MCF7BoM2/IBSPKO cells in the xenograft mouse model (Fig. 5e). Loss of IBSP also preserved the density of tumor-bearing bones (Fig.5f). Results from TRAP staining of the tumor-bearing tibias also suggested that the IBSP knockout led to decreased osteoclastogenesis (Fig. 5g). These results strongly support our hypothesis that IBSP recruits OC cells to the tumor lesions in the bone, which is essential for the uptake of exosomes and establishment of bone metastasis of ER$^+$ breast cancer cells.

CGA blocks cooperative function of miR-19a and IBSP in ER$^+$ BCBM. We hypothesized that cooperation between exosomal miR-19a and IBSP generates the osteolytic bone microenvironment, enabling the ER$^+$ tumor growth in the bone. Therefore, we examined the changes in bone microenvironment induced by directly injecting IBSP and exosomal miR-19a prepared from MCF7BoM2 into the tibial bone of mice every two days without tumor cell injection. This treatment resulted in a significant increase in the number of OC at the treatment site (Supplementary Fig. 7b). We also found that the DiD-labeled exosomes from MCF7BoM2 were incorporated into OC cells when they were injected into the tibial bone (Supplementary Fig. 7c). These results suggest that exosomal miR-19a and IBSP cooperatively create an osteolytic bone microenvironment. We then tested whether such change could enhance the growth of primary MCF7

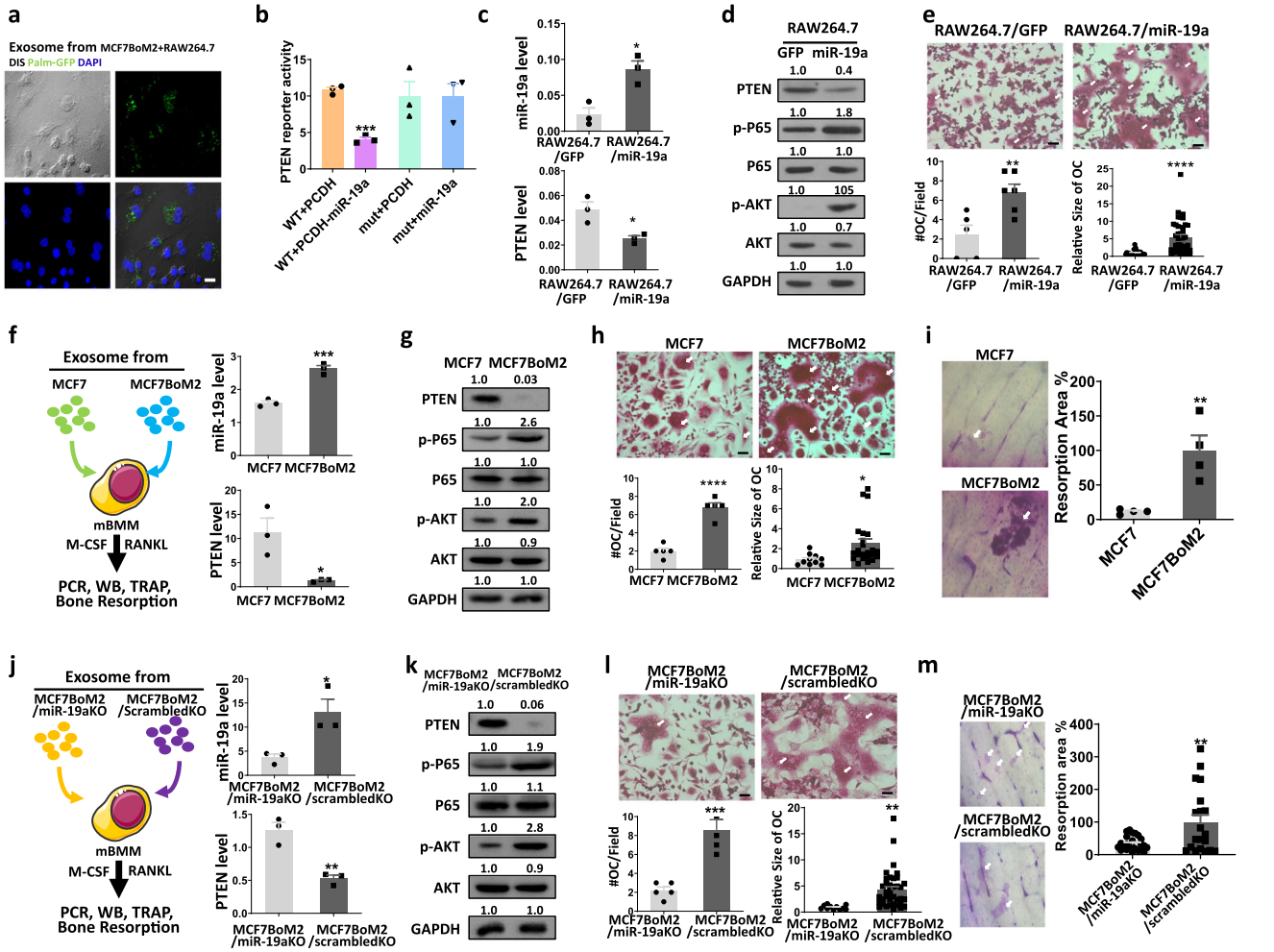

Fig. 4 Exosomal miR-19a targets PTEN/AKT pathway to promote osteoclastogenesis. a Exosomes were labeled with GFP by ectopic expression of PalmGFP in MCF7BoM2 cells. OC cells were then treated with the labeled exosomes. After 24 h, uptake of exosome by osteoclast cells was monitored by confocal microscope. Scale bar, 10 μm. **b** Luciferase reporter assay for the constructs containing wild-type PTEN 3′UTR or mutant PTEN 3′UTR was performed after transfecting the cells with the miR-19a expression vector. $p = 0.0001$ (WT + PCDH vs WT + PCDH-miR-19a, two-sided student's *t*-test). Data are presented as mean values ± SEM. **c** Taqman PCR for miR-19a expression ($p = 0.0131$, $n = 3$), and SYBR Green qPCR for PTEN expression ($p = 0.0232$, $n = 3$) in RAW264.7/GFP and RAW264.7/miR-19a were performed. Two-sided student's *t*-tests were performed. Data are presented as mean values ± SEM. **d** Western blot analysis for PTEN, phospho-NF-κB P65, total NF-κB P65, phospho-AKT and total AKT expression in RAW264.7/GFP and RAW264.7/miR-19a cell lines. The band intensity was quantified and normalized to that of control (left panels). **e** TRAP staining of RAW264.7/GFP and RAW264.7/miR-19a cells. On day 4, the number of differentiated osteoclasts ($p = 0.0080$, $n = 5$ vs 6) and the size of these cells ($p < 0.0001$, $n = 30$ vs 40) were measured. Two-sided student's *t*-tests were performed. Data are presented as mean values ± SEM. Scale bar, 100 μm. **f** Mouse BMMs were induced into OC cells with the treatment of exosomes and cytokines. Taqman PCR for miR-19a expression ($p = 0.0008$, $n = 3$) and SYBR Green qPCR for PTEN ($p = 0.0271$, $n = 3$) expression were performed for OC cells treated with exosomes from MCF7 and MCF7BoM2. Two-sided student's *t*-tests were performed. Data are presented as mean values ± SEM. **g** Western blot analysis for PTEN, phospho-NF-κB P65, total NF-κB P65, phospho-AKT and total AKT expression in mouse BMMs treated with exosomes from MCF7 and MCF7BoM2. The band intensity was quantified and normalized to that of control (left panels). **h** TRAP staining was performed for mouse BMMs treated with exosomes from MCF7 and MCF7BoM2. On day 4, the number of differentiated osteoclast ($p = 0.000036$, $n = 5$ vs 5) and their sizes ($p = 0.0323$, $n = 10$ vs 23) were measured. Two-sided student's *t*-tests were performed. Data are presented as mean values ± SEM. Scale bar, 100 μm. **i** Bone-resorbing activities of OC treated with exosomes from MCF7 and MCF7BoM2 were measured by the bone-resorption assay. BMMs were seeded on a bone chip and treated with exosomes and cytokines. Resorption pits were measured and compared ($p = 0.0070$, $n = 4$). Two-sided student's *t*-tests were performed. Data are presented as mean values ± SEM. **j** Taqman PCR for miR-19a expression ($p = 0.0291$, $n = 3$) and SYBR Green qPCR for PTEN expression ($p = 0.0047$, $n = 3$) were performed for mouse BMMs treated with exosomes from MCF7BoM2/miR-19aKO and MCF7BoM2/ScrambledKO. Two-sided student's *t*-tests were performed. Data are presented as mean values ± SEM. **k** Western blot analysis was performed for PTEN, phospho-NF-κB P65, total NF-κB P65, phospho-AKT, and total AKT expression in mouse BMMs treated with exosomes from MCF7BoM2/miR-19aKO and MCF7BoM2/ScrambledKO. The band intensity was quantified and normalized to that of control (left panels). **l** TRAP staining was performed for mouse BMMs that were treated with exosomes from MCF7BoM2/miR-19aKO and MCF7BoM2 /ScrambledKO. On day 4, the number of differentiated osteoclast cells ($p = 0.0005$, $n = 5$ vs 5) and their sizes were measured ($p = 0.0029$, $n = 11$ vs 38). Scale bar, 100 μm. Two-sided student's *t*-tests were performed. Data are presented as mean values ± SEM. **m** The bone-resorbing activity of OC was measured by the bone-resorption assay using BMMs that were treated with exosomes from MCF7BoM2/miR-19aKO and MCF7BoM2/ScrambledKO ($p = 0.0025$, $n = 24$ vs 20). Two-sided student's *t*-tests were performed. Data are presented as mean values ± SEM.

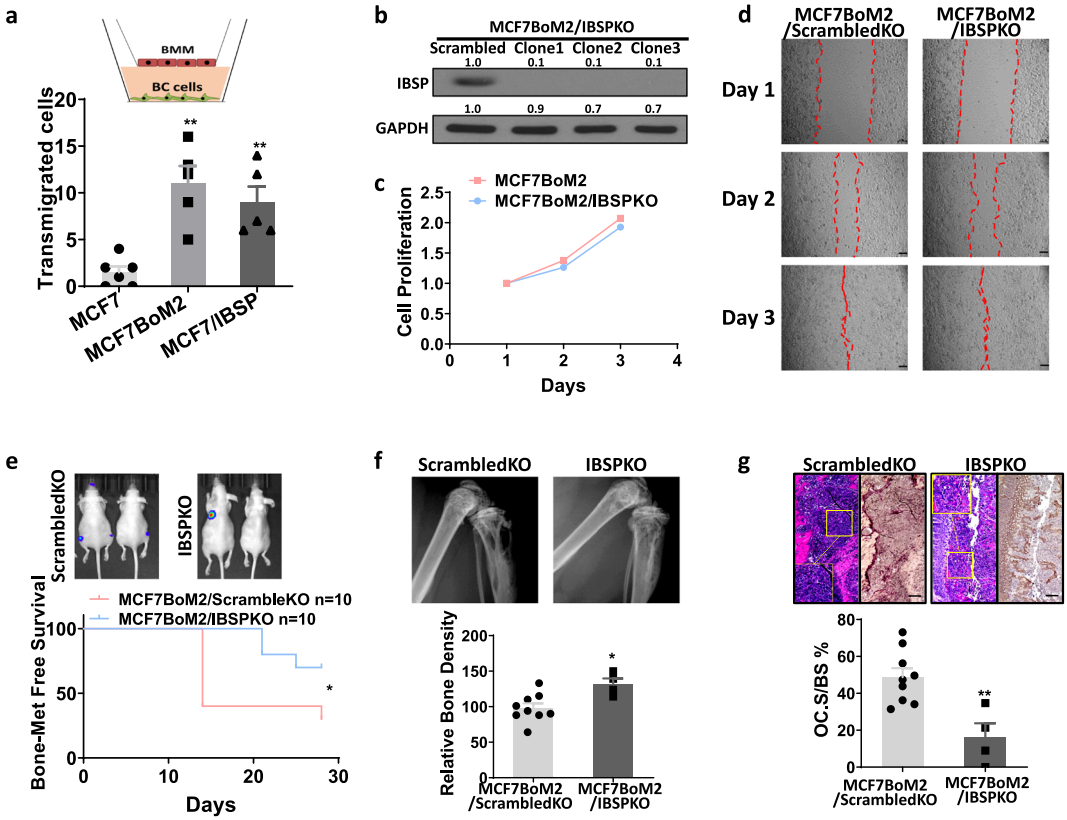

Fig. 5 ER$^+$ breast cancer cells secrete IBSP to recruit osteoclast precursors. a Trans-well migration assays were performed to measure the migration ability of BMMs towards breast cancer cells. BMMs were seeded on the luminal side and breast cancer cells (MCF7, MCF7BoM2, and MCF7/IBSP) were seeded on the abluminal chamber. Data are presented as mean values ± SEM. **b** CRISPR-Cas9 mediated knockout of IBSP in MCF7BoM2. Three knockout clones were confirmed by western blot. The band intensity was quantified and normalized to that of control (left panels). **c** The selected clones were mixed and designated as MCF7BoM2IBSPKO. Cell proliferation was measured for MCF7BoM2 and MCF7BoM2/IBSPKO by MTS assay. A two-sided student's *t*-test was performed on day 3 and $p = 0.0496$ ($n = 3$ vs 3). Data are presented as mean values ± SEM. **d** Cell migration ability of MCF7BoM2 and MCF7BoM2/IBSPKO was measured by wound-healing assay. Scale bar, 100 μm. **e** MCF7BoM2/ScrambledKO and MCF7BoM2/IBSPKO (500,000/0.1 ml PBS) were transplanted into female nude mice via intracardiac injection. The growth of bone metastasis was monitored by measuring the luciferase activity by IVIS Bioimager, and the Kaplan–Meier analysis was done for bone metastasis-free survival ($p = 0.0496$, HR = 4.101). **f** The tumor-bearing bones were imaged by X-ray, and the relative bone densities were quantified by ImageJ ($p = 0.0124$, $n = 9$ vs 4). Two-sided student's *t*-tests were performed. Data are presented as mean values ± SEM. **g** OC surface relative to the bone surface was calculated and compared after TRAP staining. H&E staining of the same field was shown together with the TRAP staining ($p = 0.0036$, $n = 9$ vs 4). Two-sided student's *t*-tests were performed. Data are presented as mean values ± SEM. Scale bar, 100 μm.

cells in the mice's tibias (Fig. 6a). MCF7 cells were transplanted into the tibial bone. At the same time, both IBSP and exosomes from MCF7BoM2 were given every two days into the tumor site. To evaluate the roles of exosomal miR-19a, exosomes from MCF7BoM2/miR-19aKO were used as a control. We found that the injection of miR-19a-containing exosomes and IBSP significantly promoted tumor growth (Fig. 6a) in the bones, which resulted in a decrease in bone density (Fig. 6b) and an increase in OC activity (Fig. 6c). These results suggest the indispensable roles of exosomal miR-19a and IBSP in bone metastasis of ER$^+$ breast cancer cells. Consistent with these results, knockout of miR-19a or IBSP from MCF7BoM2 significantly decreased the bone-metastatic ability of cancer cells, while ectopic expression of each factor alone did not rescue the effect. (Supplementary Fig. 7d, e).

Because IBSP plays a critical role in recruiting OC precursor cells and enabling the delivery of exosomal miR-19a to promote bone metastasis, targeting IBSP could be an effective preventive strategy to block the IBSP/exosome pathway, and decrease the risks of bone metastasis/recurrence. Therefore, we used a competitive binding assay to screen a natural compounds library aiming at identifying compound(s) that block the binding of IBSP with its receptor integrin αVβ3. In this assay, we layered integrin αVβ3 on the bottom of wells, followed by adding IBSP in the presence or absence of 176 natural compounds. The binding of IBSP protein to integrin αVβ3 was quantified using an enzyme-tagged antibody to measure the inhibitory effect of natural compounds. We found that Chlorogenic acid (CGA) most significantly inhibited the binding of IBSP to integrin αVβ3 (Fig. 6d). To ensure that the inhibitory ability is not a result of direct interaction between the natural compound and the enzyme tag, we repeated our screening with a different enzyme-tagged antibody (Supplementary Fig. 8a). In a chemotaxis assay, we found that CGA significantly blocked the recruitment of OC precursors (mBMM) by IBSP (Fig. 6e). On the other hand, CGA did not directly suppress the growth or migration of cancer cells (Supplementary Fig. 8b, c). These data indicate CGA is a competent inhibitor of the recruitment of OC by IBSP. Importantly, in the xenograft model, both CGA and exosome inhibitor GW4869 effectively suppressed ER$^+$ breast cancer bone metastasis (Fig. 7a), while no notable side effects were observed with the mice received CGA treatment (Supplementary Fig. 8d, e). It should be noted that the inhibitory effect of CGA on bone metastasis is not a result of its effect on tumor cell growth, because CGA did not affect the primary tumor growth

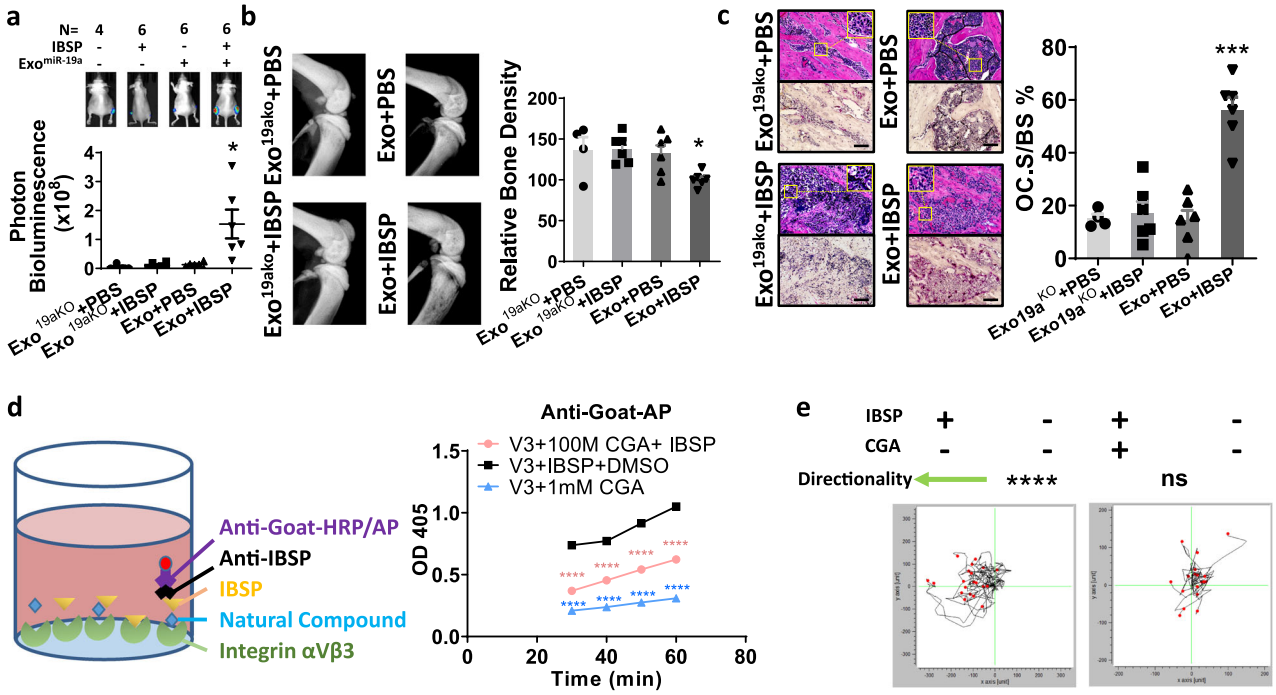

Fig. 6 IBSP and miR-19a cooperatively induce osteoclastogenesis and promote cancer cell growth in the bone. a, **b** MCF7 cells were injected into the tibias of mice. These mice also received 2 μg exosomes prepared from MCF7BoM2 and 0.5 μg recombinant IBSP injected into the tibias every 2 days. The exosomes prepared from MCF7BoM2/miR-19aKO and PBS were used as controls. After three weeks, the bioluminescence signals of tibial bones were measured. Two-sided student's t-tests were performed. $p = 0.4670$ (Exo^{19aKO} + PBS vs Exo^{19aKO} + IBSP, $n = 4$ vs 6), $p = 0.1949$ (Exo^{19aKO} + PBS vs Exo + PBS, $n = 4$ vs 6), $p = 0.0446$ (Exo^{19aKO} + PBS vs Exo + IBSP, $n = 4$ vs 6). Data are presented as mean values ± SEM (**a**). The bones were then removed and bone densities were measured by X-ray. Two-sided student's *t*-tests were performed; $p = 0.9280$ (Exo^{19aKO} + PBS vs Exo^{19aKO} + IBSP, $n = 4$ vs 6), $p = 0.9143$ (Exo^{19aKO} + PBS vs Exo + PBS, $n = 4$ vs 6), $p = 0.0257$ (Exo^{19aKO} + PBS vs Exo + IBSP, $n = 4$ vs 6) Data are presented as mean values ± SEM (**b**). **c** The removed bones were decalcified, sectioned, and examined for the amount of OC surface by TRAP staining followed by quantification using the ImageJ. Two-sided student's *t*-tests were performed; $p = 0.7224$ (Exo^{19aKO} + PBS vs Exo^{19aKO} + IBSP, $n = 4$ vs 6), $p = 0.8773$ (Exo^{19aKO} + PBS vs Exo + PBS, $n = 4$ vs 6), $p = 0.0002$ (Exo^{19aKO} + PBS vs Exo + IBSP, $n = 4$ vs 6). Data are presented as mean values ± SEM. **d** Integrin αVβ3 was seeded on the bottoms of 96-well plates. IBSP was then added to the well in the presence or absence of the library of natural compounds. The bound IBSP was measured by colorimetric substrates of alkaline phosphatase (AP). The OD 405 was compared between CGA-treated groups and the DMSO-treated group. Two-sided student's *t*-tests were performed; $p < 0.0001$ ($n = 3$) in all groups. CGA was found to most significantly inhibit the binding of IBSP to integrin αVβ3. Data are presented as mean values ± SEM. **e** The role of IBSP as a chemoattractant of osteoclast cells, and the inhibitory effect of CGA on this chemoattraction were examined by the μ-Slide Chemotaxis assay. The movement of 20 OC cells with the highest mobility was tracked and the directionality was calculated by Chemotaxis and Migration Tool. *p*-value was calculated with the Rayleigh test (left: $p = 0.0000002$, right: $p = 0.194763$).

(Supplementary Fig. 8f, h). On the other hand, CGA did not suppress the bone metastasis of 231BoM cells in our ER$^-$ breast cancer xenograft model (Supplementary Fig. 8i). These results demonstrate that CGA is a promising preventive reagent for bone metastasis of ER$^+$ breast cancer. With either CGA treatment or exosome blockade, the bone-metastatic lesions showed significantly decreased osteoclastogenesis (Fig. 7b) and increased bone density (Fig. 7c). We also confirm our findings in the T47D xenograft mouse model. When the T47D cells were implanted into mice by intracardiac injection, ectopic expression of miR-19a and IBSP significantly increased the rate of bone metastasis (Fig. 7d), decreased the bone density of the metastatic lesions (Fig. 7e), and increased the OC activities (Fig. 7f). The CGA treatment significantly decreased the rate of bone metastasis, and rescue the osteolytic changes in the bone lesions (Fig. 7d–f). Interestingly, when we generated organ culture of tumor tissues from various distant metastatic lesions in the T47D inoculated mice, we found significantly more exosomal miR-19a in the culture media of bone-metastatic lesions compared to other metastatic sites (Supplementary Fig. 8j). We also examined whether CGA was able to suppress the established bone metastasis. We first transplanted MCF7BoM2 into the tibial bone of mice. After confirming the tumor growth by measuring the bioluminescent signals, CGA or bisphosphonate-DMDP (Dichloromethylenediphosphonic acid disodium salt) was given to the mice. We found that CGA was able to suppress the cancer cell growth of established tumors in the bone more effectively compared to the control group or the bisphosphonate treatment group (Fig. 7g, h).

Discussion

ER$^+$ breast cancer patients have a considerably higher risk of bone metastasis[20,22,53–55] compared to other subtypes. In this study, we identified exosomal miR-19a and IBSP as key secreted factors from ER$^+$ bone-metastatic cells. Ectopic expression of one factor alone did not increase bone lesions in our animal models. However, upregulation of both factors together significantly promoted the tumor growth in the bone and osteoclastogenesis, indicating the cooperative roles of exosomal mIR-19a and IBSP in promoting osteolytic bone metastasis. We found that ER$^+$ cancer cells secrete IBSP as a chemoattractant for precursors of OC cells, while exosomal miR-19a enhances the osteoclastogenesis in the early metastatic site, which promotes the bone colonization of ER$^+$ breast cancer cells (Fig. 8). Importantly, in both serum and transcriptome profiles of breast cancer patients, we verified that miR-19a and IBSP are correlated with bone metastasis and recurrence

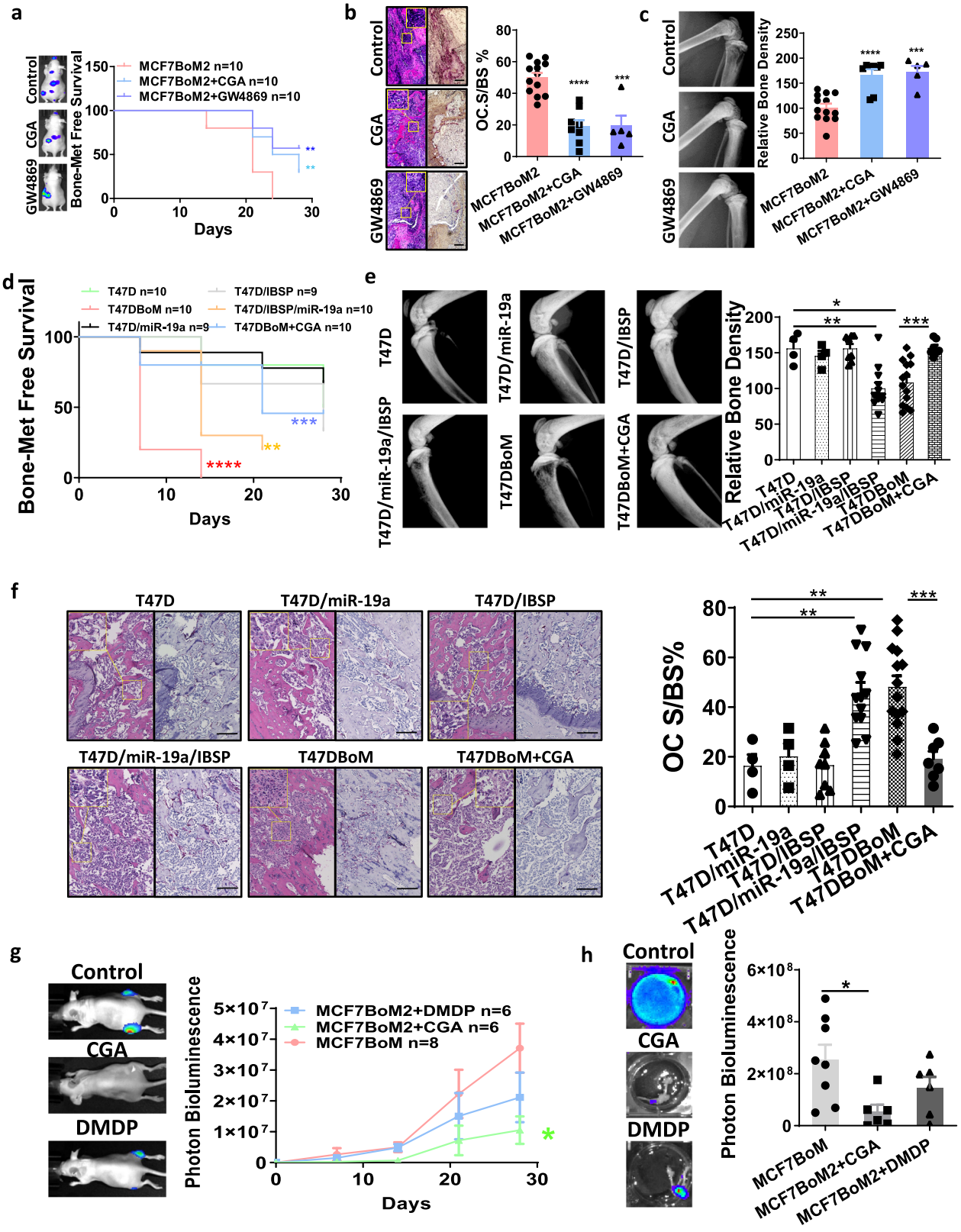

status. While the serum of advanced breast cancer patients in this study was collected during the course of treatment with tumor burden, we did not see a significant difference in the expression of exosomal miR-19a and IBSP between groups with different treatment histories (Supplementary Data 5). These data suggest the potential use of exosomal miR-19a and IBSP of serum as liquid biomarkers to stratify ER$^+$ breast cancer patients with a high risk of bone recurrence.

MiR-19a is located in the miR-17-92 cluster (oncomiR-1), which is characterized as a set of mammalian microRNA oncogenes[56]. The tumor-promoting role of miR-19a has been reported in multiple types of cancers[57–61], and it is known to

Fig. 7 CGA blocks cooperative function of miR-19a and IBSP in ER$^+$ BCBM. a The mice were treated with 2 μg exosomes prepared from MCF7BoM2 and 0.5 μg recombinant IBSP by injecting them into the tibias every two days. The exosomes from MCF7BoM2/miR-19aKO and PBS were used as controls. After two weeks, the bones were removed, and the TRAP staining of the bones was performed. The OC surface of the bone surface was quantified by ImageJ and compared by the two-sided student's *t*-test. $p = 0.0181$ (PBS + Exo^{19aKO} vs IBSP + Exo), $p = 0.2436$ (PBS + Exo^{19aKO} vs PBS + Exo), $p = 0.4594$ (PBS + Exo^{19aKO} vs IBSP + Exo^{19aKO}). $n = 5$ in all groups. **b** The ratio of OC surface relative to the bone surface was calculated after TRAP staining. $p < 0.0001$ (MCF7BoM2 vs MCF7BoM2 + CGA, $n = 13$ vs 8), $p = 0.0001$ (MCF7BoM2 vs MCF7BoM2 + GW4869, $n = 13$ vs 5). Representative H&E staining of the same field was shown (left panel) together with the TRAP staining (right panel). Scale bar, 100 μm. Two-sided student's *t*-tests were performed. Data are presented as mean values ± SEM. **c** The legs of tumor-bearing mice were imaged by X-ray, and the bone density was measured by ImageJ. Two-sided student's *t*-tests were performed. $p < 0.0001$ (MCF7BoM2 vs MCF7BoM2 + CGA, $n = 13$ vs 8), $p = 0.0002$ (MCF7BoM2 vs MCF7BoM2 + GW4869, $n = 13$ vs 5). Data are presented as mean values ± SEM. **d** T47D, T47DBoM, and T47D with ectopic expression of miR-19a or/and IBSP were intra-cardially injected into mice. One group of mice injected with T47DBoM also received CGA treatment. The growth of bone metastasis was monitored by IVIS Bioimager, and the Kaplan–Meier analysis and log-rank tests were performed for bone metastasis-free survival. $p = 0.000036$ (T47D vs T47DBoM); $p = 0.0078$ (T47D vs T47D/IBSP/miR-19a); $p = 0.0003$ (T47DBoM vs T47DBoM + CGA). **e** The legs of tumor-bearing mice were imaged by X-ray, and the bone density was measured by ImageJ. $p = 0.0027$ (T47D vs T47D/IBSP/miR-19a, $n = 4$ vs 12); $p = 0.0111$ (T47D vs T47DBoM, $n = 4$ vs 14); $p = 0.0009$ (T47DBoM vs T47DBoM + CGA, $n = 14$ vs 7). Two-sided student's *t*-tests were performed. Data are presented as mean values ± SEM. **f** The ratio of OC surface relative to the bone surface was calculated and compared after TRAP staining. H&E staining of the same field was shown (left panels) together with the TRAP staining (right panels). Scale bar, 100 μm. $p = 0.0028$ (T47D vs T47D/IBSP/miR-19a, $n = 4$ vs12); $p = 0.0023$ (T47D vs T47DBoM, $n = 4$ vs 14); $p = 0.0003$ (T47DBoM vs T47DBoM + CGA, $n = 14$ vs 7). Two-sided student's *t*-tests were performed. Data are presented as mean values ± SEM. **g** One week after intra-tibia injection of MCF7BoM2, mice were treated with CGA or DMDP. The growth of bone tumors was monitored by measuring the luciferase activity by IVIS Bioimager. Two-sided student's *t*-tests were performed. $p = 0.0215$ (MCF7BoM2 vs MCF7BoM2 + CGA, $n = 8$ vs 6), $p = 0.1920$ (MCF7BoM2 vs MCF7BoM2 + DMDP $n = 8$ vs 6). Data are presented as mean values ± SEM. **h** After 24 days, the legs were removed and the bioluminescence of each leg was quantified. Two-sided student's *t*-tests were performed. $p = 0.0144$ (MCF7BoM2 vs MCF7BoM2 + CGA, $n = 8$ vs 6), $p = 0.1747$ (MCF7BoM2 vs MCF7BoM2 + DMDP $n = 8$ vs 6). Data are presented as mean values ± SEM.

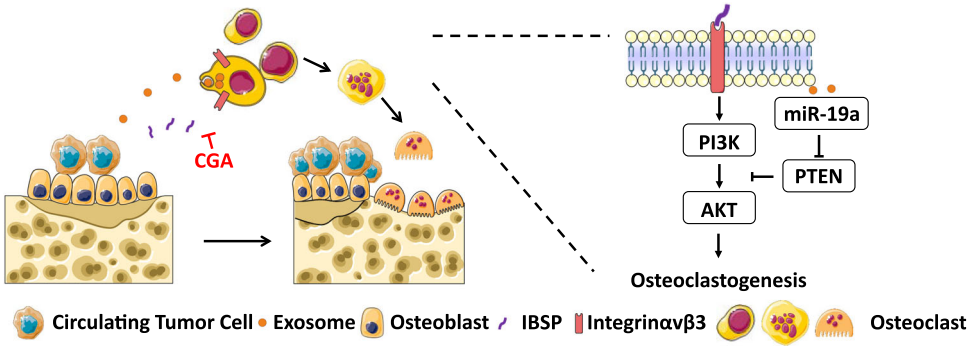

Fig. 8 Proposed mechanism of exosomal miR-19a and IBSP mediated bone metastasis in ER$^+$ breast cancer. In the early metastatic niche, ER$^+$ breast cancer cells secrete IBSP as a chemoattractant to recruit precursors of OC cells, creating an OC precursor-enriched microenvironment. OC precursors incorporate exosomes from breast cancer cells, and miR-19a is transported into OC precursors. Inside the OC precursors, miR-19a suppresses PTEN expression, activates NF-κB and AKT pathways, and promotes osteoclastogenesis. Mature OC cells induce bone resorption, liberating growth factors from the bone matrix, which further promote the growth of cancer cells.

directly target tumor suppressor PTEN[42,62,63]. It is also predicted to target ER. However, overexpression of miR-19a did not alter the level of ER in breast cancer cells[64], and the exact role of miR-19a in breast cancer is yet poorly understood. The previous study has characterized miR-19a targets in breast cancer by quantitative proteomic approach[30]. No growth-suppressive effect was found when those targets were ectopically expressed, suggesting that endogenous miR-19a does not directly alter the growth of cancer cells per se. Consistent with their finding, the results of our study revealed that modulation of miR-19a expression in breast cancer cells did not alter the growth or migration abilities in vitro. Interestingly, ectopic expression of miR-19a did not affect the expression of PTEN in the cancer cells (data not shown). A possible explanation is that miR-19a is actively sorted out of cancer cells by exosomes. Accordingly, miR-19a expression is positively correlated with osteolytic bone metastasis in vivo, strongly suggesting a role of miR-19a as a key modulator of tumor microenvironment in the process of bone metastasis of breast cancer. In the "vicious cycle of bone metastasis"[65], breast cancer cells are known to interact with host cells to generate a favorable microenvironment for cancer cell growth in the bone through direct cell–cell contact or via secreted proteins[66–68]. We found that the oncogenic role of miR-19a in ER$^+$ breast cancer is dependent on its secretory nature as exosomes. Exosomal miR-19a secreted from tumor cells are internalized into the OC precursor and induces the differentiation of OC into mature OC. OC osteoclastogenesis is one of the key steps related to the establishment of bone metastasis, and miR-19a augments this process by activating the p-AKT pathway. Therefore, this study revealed a specific role of miR-19a in ER$^+$ breast cancer bone metastasis. The nature of miR-19a encapsulated inside exosomes also makes it a promising candidate as a circulating biomarker for diagnostic and prognostic purposes[69–72].

IBSP constitutes around 12% of the non-collagenous proteins in human bone and it is synthesized by bone resident cells. Several types of cancers, including colon, breast, prostate, and lung cancers were reported to have upregulated IBSP expression[73]. In breast cancer, IBSP was also detected in cancer cells[74], and we found that IBSP is only expressed in breast cancer cells but not in normal breast tissue, making it a good candidate as a tumor-specific biomarker. Indeed, IBSP was previously reported to be associated with poor survival of breast cancer

patients[75]. Interestingly, it was also found to be positively associated with bone metastasis, but negatively associated with lung metastasis in breast cancer[75]. These observations can be well explained by our results, as we found IBSP regulates bone metastasis in ER$^+$ breast cancer. ER$^+$ breast cancer is known to have a higher incidence of bone metastasis compared to other subtypes, while they have a lower incidence of lung metastasis[55]. By classifying subtypes of breast cancer patients, we have shown the feasibility of using IBSP, together with exosomal miR-19a to predict the risk of bone metastasis in ER$^+$ patients. More importantly, we clarified a cooperative pathway between IBSP and miR-19a, that mobilizes the bone microenvironment to guide the ER$^+$ breast cancer cells to the bone and support their cell growth. However, in this study, we did not observe a regulatory effect in gene expression between miR-19a and IBSP (Supplementary Fig. 2a, b). Therefore, the increased bone metastasis is likely to be a result of the colonial selection of high miR-19a/IBSP cells that adapt well to the early metastatic niche due to the interaction with OC cells.

Currently, there is no effective and safe regimen to prevent bone recurrence in breast cancer. The present bone-targeted therapy does not improve the survival of breast cancer patients, and patients with bone metastases still rely on systemic treatment. However, patients with bone recurrence develop resistance to systemic treatment as the cancer cells acquired resistance to these drugs at an early stage. In this study, we found that CGA blocks the interaction between IBSP and OCs, inhibiting the pro-osteoclastogenesis effect of cancer-derived exosomes. CGA is abundant in the extract from plants, and it has minimum side effects for long-term preventive treatment. By using exosomal miR-19a and IBSP to predict the risk of bone metastasis, ER$^+$ breast cancer patients could benefit from this agent in preventing late-onset recurrence in the bone. CGA could also be used as a combination therapy to treat ER$^+$ breast cancer patients with bone metastasis.

Collectively, our study identified exosomal miR-19a and IBSP as mediators of cell–cell communication between breast cancer cells and OC cells, which promotes the vicious cycle of bone metastasis in ER$^+$ breast cancer. Importantly, the natural compound CGA can block this process. This study sheds light on the molecular mechanism of bone metastasis in ER$^+$ breast cancer, which warrants further investigation on the miR19a-IBSP axis for the development of an effective therapeutic strategy.

Methods

Cells and cell culture. Human breast carcinoma cell lines, MDA-MB-231, MCF7, T47D, and mouse monocyte/macrophage cell line RAW 264.7 were purchased from American Type Tissue Culture Collection (ATCC, Manassas, VA, USA). MCF7BoM2 and 231BoM-1833, the bone-metastatic derivative of breast cancer cell lines were kindly provided by Dr. Joan Massagué (Memorial Sloan-Kettering Cancer Center)[76,35]. To select bone-tropic T47DBoM, 100,000 T47D cells were injected into the left cardiac ventricle of athymic-nu/nu mice. Subsequently, bone-metastatic tumor cells were isolated from the tibias. Three rounds of selection were performed to establish the T47DBoM cell line. Luciferase-labeled cells were generated by infecting the lentivirus carrying the firefly luciferase gene. MDA-MB-231, MCF7 cells and their variants, as well as RAW264.7, were cultured in DMEM medium supplemented with 10% FBS and antibiotics. Murine bone marrow-derived monocytes and macrophages (BMMs) were generated as previously described[77]. Briefly, bone marrow cells were harvested by flushing the femurs and tibias of six to eight-week-old C57BL/6 mice (The Jackson Laboratory, Bar Harbor, ME, USA) with minimum essential medium-α (α-MEM; Invitrogen, Carlsbad, CA, USA). The cells were then washed, centrifuged, and incubated in complete α-MEM containing 10% heat-inactivated fetal bovine serum and penicillin/streptomycin for 18 h to separate the floating and adherent cells. The floating cells were collected and cultured in complete α-MEM supplemented with 50 ng/ml murine recombinant Macrophage Colony Stimulating Factor (M-CSF; Peprotech, Rocky Hill, NJ, USA). After 3 days, non-adherent cells were washed out and the adherent cells were used as BMMs.

Animal experiments. For experimental metastasis assay, cancer cells in 100 µl of PBS were injected into the left cardiac ventricle of the athymic-nu/nu mice (7–8 weeks). For intratibial implantation of cancer cells, cells with or without ectopic expression of miR-19a and IBSP were injected into the tibia at a final concentration of 100,000 cells/10 µl. To investigate the effect of miR-19a and IBSP on the primary tumor, cancer cells (1×10^6) in 50 µl PBS were mixed with Matrigel matrix (Corning, Corning, NY, USA) at 1:1 ration, and implanted into mammary fat pads of athymic-nu/nu mice. All mice received implantation of 1.7 mg estradiol continuous release pellets (Innovative Research of America). To confirm a successful injection, we immediately monitored photon flux from the whole body of the mice after injection. The growth of tumors in the bones was monitored and quantified by measuring luminescence using IVIS Xenogen bioimager (Caliper Life Science), and the images were analyzed using Living Image (Caliper Life Science) version 4.7.3 software and Aura software (Spectral Instruments Imaging, LLC) version 3.2. For CGA (Sigma-Aldrich, St. Louis, MO, USA) treatment, the compound dissolved in deionized water was administered orally at doses of 200 mg/kg body weight per day. For GW4869 (Cayman Chemical, Ann Arbor, MI, USA) treatment, the drug was intraperitoneally (i.p.) injected at the dose of 2.5 µg/g every three days. For DMDP (Dichloromethylenediphosphonic acid disodium salt) treatment, the drug was intraperitoneally (i.p.) injected at the dose of 10 mg/kg twice a week. For in vivo exosome uptake assay, the mice were treated with 2 µg Vybrant DiD-labeled exosomes with or without 0.5 µg recombinant IBSP by injecting them into the tibias every two days. After two weeks, the bones were extracted and sectioned with a diamond knife. The sectioned bone was then stained with FITC-CTSK (Cathepsin K) and DAPI. The co-localization of OC and exosome was examined by Keyence All-in-one Fluorescence Microscope (BZ-X700). For measurement of the percentage of OC surface per bone surface (OC.S/BS%), bioluminescence and H&E staining were performed to identify the metastatic sites. For each of the mice, all the bone-metastatic sites were TRAP stained and cumulative osteoclast surface and bone surface were measured by ImageJ (FIJI, 1.52n)[78].

X-ray imaging. On days 28 before euthanization, X-ray images of the mice were captured with Faxitron Multifocus 10 × 15 Digital Radiography System. Mice were anesthetized and placed dorsal side up in the X-ray chamber with legs in the capture region. X-ray images of the tibias were analyzed using ImageJ (ImageJ 1.8.0_112; 64-bit; National Institute of Health) according to previous publications[79,80] and relative bone density was quantified. The image was calibrated to a standard aluminum wedge. The average mean grayscale value of the area of interest was recorded after the value of background soft-tissue was subtracted.

Human L1000 array. The cell culture supernatants were dialyzed and biotinylated according to the manual of L-Series Human Antibody Array 1000 (RayBiotech, Peachtree Corners, GA, USA). The glass slide arrays were then locked and incubated with biotin-labeled samples to allow the binding of target proteins to the pre-printed capture antibodies. Streptavidin-conjugated fluorescent dye is then used to interact with the bound proteins. Finally, when the slide is dried, laser fluorescence scanning was performed with GenePix® 4000B Microarray Scanner to visualize signals. To compare the expression of each protein target, Protein Array Analyzer was used to quantify the signals.

Gene knockout and overexpression. IBSP and miR-19a knockout was carried out with CRISPR/Cas9 system. lentiCRISPR v2 was a gift from Feng Zhang (Addgene plasmid # 52961; http://n2t.net/addgene:52961; RRID:Addgene_52961) Guide RNAs for IBSP (AGAACTTACTGAGAAAGCAC) and miR-19a (AATCTATG-CAAAACTGATGG) were cloned into vectors according to the provided protocol. Lentivirus was prepared by transfection of plasmids into HEK 293T cells. MCF7BoM2 was infected with lentivirus and screened with puromycin. The success of knockout was confirmed by the T7E1 assay (NEB). Single-cell clones were picked by limit dilution. Four miR-19a knockout clones and three IBSP knockout clones were selected. The knockout clones of each gene were mixed to generate the heterogeneous knockout cell lines and they were used for functional assays. The stabilities of the knockout were verified every five passages by PCR and western blot analysis. The plasmid for overexpression of IBSP (LV185867) was purchased from ABM (Applied Biological Materials, Richmond, BC, Canada) and the plasmid for overexpression of miR-19a (PCDH-miR-19a) was a kind gift from Dr. Yin-yuan Mo.

Osteoclastogenesis assay and tartrate-resistant acid phosphatase (TRAP) staining. Murine BMMs at a density of 1×10^6 cells/ml or RAW264.7 cells at a density of 1×10^5 cells/ml were plated in a chamber slide (Thermofisher, Waltham, MA, USA) and cultured in complete α-MEM supplemented with 50 ng/ml murine recombinant M-CSF, 25 ng/ml murine recombinant RANKL (Peprotech, Rocky Hill, NJ, USA) in the presence or absence of 20 µg/ml exosomes, a concentration used previously in multiple studies[27,66,81,82]. On day 4, TRAP staining was performed using a leukocyte acid phosphatase kit (Sigma-Aldrich, St. Louis, MO, USA) according to the manufacturer's instructions. The multinucleated TRAP-

positive cells from five biological replicates were considered mature OC cells and monitored by Zeiss Axioplan2 microscope. The size of OC cells was measured by ImageJ as reported[83].

Bone-resorption assay. To determine the role of exosomal miR-19a in the bone resorption activity of OC cells, pit assay was performed on bone slices (Immunodiagnostic Systems). 50,000 bone marrow-derived OC precursor BMMs were seeded on sterilized bone slices placed in a 96-well plate. The BMMs were cultured with complete α-MEM supplemented with 50 ng/ml murine recombinant M-CSF, 25 ng/ml murine recombinant RANKL (Peprotech, Rocky Hill, NJ, USA) in the presence or absence of 20 μg/ml exosomes. The media was changed every 2–3 days. After two weeks of cell culture, cells were washed, and resorption pits were stained with 1% toluidine blue. The resorption area was photographed under microscopy and the image was analyzed by ImageJ.

Extracellular vesicles purification and tracking analysis. Extracellular vesicles (EVs) from cells were isolated by ultracentrifugation. Cells were grown in EVs-depleted media for 48 h before CM was collected for EVs purification. To isolate total EVs, CM was centrifuged at 300 × *g* for 10 min to remove cells. EVs were collected by ultracentrifugation at 120,000 × *g* for 70 min. Apoptotic bodies (ABs), microvesicles (MVs), and exosomes were isolated by differential centrifugation as published before[84,85]. Briefly, the harvested CM was centrifuged at 300 × *g* for 10 min to remove cells. ABs were collected by centrifugation at 2000 × *g* for 20 min. The supernatant was centrifuged at 16,500 × *g* for 20 min to collect MVs. After that, the Supernatant was passed through a 0.2 μm filter (Sarstedt, Nümbrecht, GERMANY) to remove the particles larger than 200 nm. Exosomes were then pelleted by ultracentrifugation at 120,000 × *g* for 70 min. The isolated EVs were analyzed and quantified by nanoparticle tracking analysis (NTA) and electron microscope with negative staining.

Imaging of exosomes by transmission electron microscopy. For negative staining, Purified exosomes were incubated onto discharged 200 mesh copper EM grids and fixed with 2% Paraformaldehyde (PFA). 1% uranyl acetate (UA) solution was used to stain the exosomes on the surface of the EM grids. The exosomes were imaged by FEI Tecnai BioTwin Transmission Electron Microscope. For immunostaining of IBSP and CD63 on the surface of exosomes, Anti-CD63 (1:100) (Santa Cruz Biotechnology, Dallas, Texas, USA) and anti-IBSP (1:100) (Thermofisher, Waltham, MA, USA) were used to incubate the fixed exosomes on the grids. The 10 nm colloidal gold-labeled protein A (1:50)(BOSTER BIOLOGICAL TECHNOLOGY, Pleasanton, CA, USA) was then used to label the primary antibodies. After that, negative staining was performed with 2% uranyl acetate and the grid was imaged by transmission electron microscopy.

Exosome uptaking assay. Breast cancer cell lines were labeled with lentivirus expressing PalmGFP (a kind gift from Dr. Xandra O. Breakefield). Cells with intense fluorescence were selected by BD FACSAria Cell Sorter. Exosomes labeled with PalmGFP were isolated by differential ultracentrifuge. To monitor the uptake of exosomes in OC cells, RAW264.7 cells were seeded in chamber slides overnight and 20 μg/ml exosomes were added into the media. After 24 h of incubation, the cells were washed and fixed. Cell nuclei were stained with DAPI followed by sealing the slides with coverslips. The uptake of exosomes was confirmed by examining the GFP signal under Olympus FV1200 SPECTRAL laser scanning confocal microscope.

ExoELISA. To compare the exosome production from cells after ectopic expression of miR-19a and IBSP, exosome concentration in the cell culture media was determined using ExoElisa from System Biosciences (SBI, Mountain View, CA, USA). According to the manufacturer's instruction, exosomes from a comparable amount of different cell lines were purified by ExoQuick-TC precipitation solution (SBI, Mountain View, CA, USA). Diluted exosomes, together with protein standards, were incubated with a provided microtiter plate. The detection antibody was added to the wells, followed by a horseradish peroxidase enzyme-linked secondary antibody. Finally, TMB ELISA substrate was added to develop the signal, and a stop buffer was used to stop the reaction. OD value was recorded with a spectrophotometric plate reader at 450 nm. The data were normalized to the cell count.

Immunohistochemistry. Immunohistochemical analysis was carried out for paraffin-embedded, surgically resected specimens of breast cancer bone metastases. Briefly, the sections were de-paraffinized, rehydrated, and heated at 100 °C for 20 min in Tris-buffered saline (pH 9.0) for antigen exposure. They were treated with 3% H_2O_2 to block endogenous peroxidase activity, followed by treatment with 5% BSA solution for 30 min. The slides were then incubated with primary antibodies targeting IBSP (Invitrogen, PA5-50633, 1:100) and E-cadherin (Cell Signaling Technology, clone 24E10, #3195, 1:200) for 16 h at 4 °C. After washing in PBS/0.1% Tween-20, the sections were treated with the secondary antibody anti-rabbit (Bio-Rad, #1706515, 1:500). The sections were washed extensively, and DAB substrate chromogen solution was applied followed by counterstaining with hematoxylin. For negative control, we added the rabbit IgG isotype control (Invitrogen, 02-6102, 1:250) instead of primary antibodies during the primary antibody incubation. The expression of the protein of interest was evaluated by H scoring as the sum of the frequency and the intensity (0: none; 1: weak; 2: moderate; 3: strong). The final score = 1 × (% of 1 + cells) + 2 × (% of 2 + cells) + 3 × (% of 3 + cells). IHC scores were determined by concordance among the scores of two independent reviewers.

MTS assay. Viability of cell lines was quantified by using the CellTiter 96 Aqueous One solution cell proliferation assay kit (Promega, Madison, WI, USA). Cells were plated in 96-well tissue culture plates at a density of 5000 cells per well. At the time of measurement, 20 μl of CellTiter 96 AQueous One solution reagent was added into each well of the 96-well assay plate containing the samples in 100 μl of culture medium. The plate was incubated at 37 °C for 1 h in a humidified, 5% CO_2 atmosphere. The absorbance at 490 nm was measured and recorded.

Wound-healing migration assay. The cell migration was estimated by a wound-healing migration assay and monitored by the Olympus IX-70 microscope. Cells were seeded in 12 well cell culture dish and a scratch was made on the monolayer using a sterile tip when cells reach 100% confluence. The distance of migration by cancer cells was measured every 24 h.

Real-time PCR and western blotting. Total RNA was isolated by using Direct-zol RNA MiniPrep Plus (Zymo Research Corp, Irvine, CA, USA) and miRNeasy Mini Kit (Qiagen, Germantown, MD, USA) for mRNA and microRNA, respectively. We used iScript Reverse Transcription Supermix (Life Science Research, Hercules, CA, USA) and TaqMan MicroRNA Reverse Transcription kit (ThermoFisher Scientific, Waltham, MA, USA) for mRNA and miRNA reverse transcription, respectively. Quantitative PCR (qPCR) for miRNA was conducted by using TaqMan Universal Master Mix II and TaqMan microRNA assays (ThermoFisher Scientific, Waltham, MA, USA). All miRNA assays were purchased from ThermoFisher Scientific. U6 snRNA and RNU48 TaqMan probes were used as endogenous controls for human and mouse cells, respectively. For coding genes, qPCR was conducted by using iTaq Universal SYBR Green Supermix (Life Science Research, Hercules, CA, USA). Primers used in this study were listed in Supplementary Data 1. Western blotting was carried out using general methods. Briefly, the protein was extracted from the cells using RIPA buffer, quantified by Protein Assay (Bio-Rad, Hercules, California, USA), resolved by 10% SDS-polyacrylamide gel, and then electro-transferred to nitrocellulose membrane. Primary antibodies against IBSP (Invitrogen, PA5-50633, 1:500), Phospho-NF-κB p65 (Ser536) (Cell Signaling Technology, clone 93H1, #3033, 1:1000), NF-κB p65 (Cell Signaling Technology, #8242, 1:1000), Phospho-Akt (Ser473) (Cell Signaling Technology, clone D9E, #4060, 1:3000), Akt (Cell Signaling Technology, #9272, 1:2000), HSP70 (Invitrogen, Clone 5A5, #MA3-007, 1:1000), PTEN (Santa Cruz Biotechnology, clone A2B1, sc-7974, 1:1000), CD63 (Santa Cruz Biotechnology, clone MX-49.129.5, sc-5275, 1:500), TSG101 (Santa Cruz Biotechnology, clone C-2, sc-7964, 1:1000), GRP94 (Santa Cruz Biotechnology, clone H-10, sc-393402, 1:500), α-actinin-4 (Santa Cruz Biotechnology, clone G-4, sc-390205, 1:500), Calregulin (Santa Cruz Biotechnology, clone A-9, sc-166837, 1:500), GAPDH (Cell Signaling Technology, clone D16H11, #5174, 1:15,000), α-tubulin (Cell Signaling Technology, #2144, 1:2000) were used. HRP-conjugated anti-mouse IgG (Cell Signaling Technology, #7076) or anti-rabbit IgG (Bio-Rad, #1706515) and mouse IgG kappa binding protein m-IgGκ BP-HRP (Santa Cruz Biotechnology, sc-516102) were used as secondary antibodies. Immunoblotting images were captured by Amersham Imager 600 or the X-ray film processor. Images were quantified with ImageJ software.

Receptor–ligand in vitro binding assay. The receptor–ligand in vitro binding assay was developed according to previous publications[86,87]. Briefly, a high-binding 96-well plate was coated with integrin αVβ3 in the carbonate-bicarbonate buffer. The plate was sealed and incubated at 4 °C overnight. The plate was then washed and blocked with PBS (0.1% Tween and 1% BSA). IBSP with or without the natural compound library was incubated with coated integrin αVβ3 at room temperature for 2 h. The plate was then washed and further incubated with primary antibody Goat anti-IBSP (R&D SYSTEMS, AF4014, 1:100) or Goat IgG Control (R&D SYSTEMS, AB-108-C, 1:100). Anti-goat IgG tagged with either HRP (horseradish peroxidase) (Invitrogen, A15999, 1:5000) or AP (alkaline phosphatase) (Invitrogen, A16002, 1:2500) was used as the secondary antibody. After washing the plates, the substrate was added, and the plates were incubated for 30 min followed by adding the stop solution. The binding of integrin αVβ3 and IBSP was quantified by measuring the absorbance value with a plate reader.

μ-Slide chemotaxis assay. The μ-Slide chemotaxis assay was carried out according to the manufacturer's instructions. Briefly, OC precursors BMMs at 3×10^6 cells/ml were mixed with collagen type I gels and other ingredients before being seeded into the middle channel. Left and right chambers were filled with FBS media with or without IBSP. The movement of cells was tracked according to a previous publication[88]. Time-lapse video microscopy was performed using an inverted Nikon microscope. Cell tracking was performed using the ImageJ software (National Institutes of Health, Bethesda, USA) plugin "Manual Tracking" (Fabrice

Cordelières, Institut Curie, Orsay, France), then analyzed with Chemotaxis and Migration Tool (Version 2.0, IBIDI).

Clinical samples. Clinical samples from breast cancer patients and healthy individuals were obtained from Tumor Tissue and Pathology Shared Resource of Wake Forest Baptist Comprehensive Cancer Center and Cooperative Human Tissue Network. The serum samples from early-stage breast cancer patients were collected before surgery and the serum samples from advanced breast cancer patients were collected during the course of treatment. Population characteristics including patient age, race, diagnosis, metastasis, receptor status, and treatment history were retrieved from medical records, and summarized in Supplementary Data 2 and 3. The patient information of tumor tissue and healthy bone tissue was summarized in Supplementary Data 4.

MiRNA array, bioinformatics, statistical tests, and reproducibility. EVs from MCF7 and MCF7BoM2 were collected and miRNA was extracted using miRNeasy Micro Kit (Qiagen, Hilden, North Rhine-Westphalia, Germany). Expression profiling of miRNA was performed by using the Affymetrix GeneChip miRNA Array. For calculation of FDR and fold change in differential expression analyses, the ComparativeMarkerSelection module from GenePattern[89] (Broad Institute, Cambridge, MA, USA) was used. For clustering and visualization, the HierarchicalClustering and HierarchicalClusteringViewer modules from GenePattern were used. For metastasis-free survivals, Kaplan–Meier curves were plotted using the time to event as the outcome. Statistical differences in survival across groups were assessed using the log-rank test. For other analyses, student's *t*-tests (two-sided) were used unless otherwise noted. All other statistical analyses were performed using the GraphPad Prism 8 Program (GraphPad Software, San Diego, CA, USA). Asterisk: $^{*}p < 0.05$, $^{**}p < 0.01$, $^{***}p < 0.001$, $^{****}p < 0.001$, $^{ns}p \geq 0.05$. Representative experiments were repeated independently three times with similar results.

Reporting summary. Further information on research design is available in the Nature Research Reporting Summary linked to this article.

Data availability

CEL and expression files associated with the GeneChip miRNA array in this study are deposited at GEO (https://www.ncbi.nlm.nih.gov/geo/) with the accession number GSE176105. The GEO data set (GSE41922, GSE22220, GSE56493, GSE2034), TCGA referenced during the study are available in a public repository from https://www.ncbi.nlm.nih.gov/geo/ and https://portal.gdc.cancer.gov/ websites. The source data underlying Figs. 1–7 and Supplementary Figs. 1–8 are provided as a Source Data file. All the other data supporting the findings of this study are available within the article and its supplementary information files and from the corresponding author upon reasonable request. A reporting summary for this article is available as a Supplementary Information file. Source data are provided with this paper.

Received: 30 October 2019; Accepted: 10 August 2021;
Published online: 31 August 2021

References

1. Patanaphan, V., Salazar, O. M. & Risco, R. Breast cancer: metastatic patterns and their prognosis. *South. Med. J.* **81**, 1109–1112 (1988).
2. Manders, K. et al. Clinical management of women with metastatic breast cancer: a descriptive study according to age group. *BMC Cancer* **6**, 179 (2006).
3. Coleman, R. E. Clinical features of metastatic bone disease and risk of skeletal morbidity. *Clin. Cancer Res.* **12**, 6243s–6249s (2006).
4. Coleman, R. et al. Bone health in cancer patients: ESMO Clinical Practice Guidelines. *Ann. Oncol.* **25**, iii124–iii137 (2014).
5. Coleman, R. E. Metastatic bone disease: clinical features, pathophysiology and treatment strategies. *Cancer Treat. Rev.* **27**, 165–176 (2001).
6. Esposito, M., Guise, T. & Kang, Y. The biology of bone metastasis. *Cold Spring Harb. Perspect. Med.* **8**, a031252 (2018).
7. Roodman, G. D. Mechanisms of bone metastasis. *N. Engl. J. Med.* **350**, 1655–1664 (2004).
8. Kang, Y. et al. A multigenic program mediating breast cancer metastasis to bone. *Cancer Cell* **3**, 537–549 (2003).
9. Rucci, N., Sanita, P., Delle Monache, S., Alesse, E. & Angelucci, A. Molecular pathogenesis of bone metastases in breast cancer: proven and emerging therapeutic targets. *World J. Clin. Oncol.* **5**, 335–347 (2014).
10. Azim, H. A., Kamal, N. S. & Azim, H. A. Jr Bone metastasis in breast cancer: the story of RANK-ligand. *J. Egypt. Natl Cancer Inst.* **24**, 107–114 (2012).
11. Kang, Y. Dissecting tumor-stromal interactions in breast cancer bone metastasis. *Endocrinol. Metab.* **31**, 206–212 (2016).
12. Guise, T. A. The vicious cycle of bone metastases. *J. Musculoskelet. Neuronal Interact.* **2**, 570–572 (2002).
13. Coleman, R. et al. Adjuvant zoledronic acid in patients with early breast cancer: final efficacy analysis of the AZURE (BIG 01/04) randomised open-label phase 3 trial. *Lancet Oncol.* **15**, 997–1006 (2014).
14. Stopeck, A. T. et al. Denosumab compared with zoledronic acid for the treatment of bone metastases in patients with advanced breast cancer: a randomized, double-blind study. *J. Clin. Oncol.* **28**, 5132–5139 (2010).
15. Early Breast Cancer Trialists' Collaborative Group (EBCTCG). Adjuvant bisphosphonate treatment in early breast cancer: meta-analyses of individual patient data from randomised trials. *Lancet* **386**, 1353–1361 (2015).
16. Rodriguez-Lozano, F. & Oñate-Sanchez, R. Treatment of osteonecrosis of the jaw related to bisphosphonates and other antiresorptive agents. *Med. Oral Patol. Oral Cir. Bucal.* **21**, e595–600 (2016).
17. Ottewell, P. & Wilson, C. Bone-targeted agents in breast cancer: do we now have all the answers? *Breast Cancer* **13**, 117822341984350 (2019).
18. Coleman, R. et al. Safety of zoledronic acid and incidence of osteonecrosis of the jaw (ONJ) during adjuvant therapy in a randomised phase III trial (AZURE: BIG 01-04) for women with stage II/III breast cancer. *Breast Cancer Res. Treat.* **127**, 429–438 (2011).
19. Rosen, L. S. et al. Long-term efficacy and safety of zoledronic acid compared with pamidronate disodium in the treatment of skeletal complications in patients with advanced multiple myeloma or breast carcinoma: a randomized, double-blind, multicenter, comparative trial. *Cancer* **98**, 1735–1744 (2003).
20. Savci-Heijink, C. D. et al. Retrospective analysis of metastatic behaviour of breast cancer subtypes. *Breast Cancer Res. Treat.* **150**, 547–557 (2015).
21. Hess, K. R., Pusztai, L., Buzdar, A. U. & Hortobagyi, G. N. Estrogen receptors and distinct patterns of breast cancer relapse. *Breast Cancer Res. Treat.* **78**, 105–118 (2003).
22. Han, H. H. et al. Estrogen receptor status predicts late-onset skeletal recurrence in breast cancer patients. *Medicine* **95**, e2909 (2016).
23. Rueda, O. M. et al. Dynamics of breast-cancer relapse reveal late-recurring ER-positive genomic subgroups. *Nature* **567**, 399–404 (2019).
24. Mundy, G. R. Metastasis to bone: causes, consequences and therapeutic opportunities. *Nat. Rev. Cancer* **2**, 584–593 (2002).
25. Wu, K., Xing, F., Wu, S.-Y. & Watabe, K. Extracellular vesicles as emerging targets in cancer: Recent development from bench to bedside. *Biochim. Biophys. Acta* **1868**, 538–563 (2017).
26. Rossi, M., Battafarano, G., D'Agostini, M. & Del Fattore, A. The role of extracellular vesicles in bone metastasis. *Int. J. Mol. Sci.* **19**, 1136 (2018).
27. Peinado, H. et al. Melanoma exosomes educate bone marrow progenitor cells toward a pro-metastatic phenotype through MET. *Nat. Med.* **18**, 883–891 (2012).
28. Valencia, K. et al. miRNA cargo within exosome-like vesicle transfer influences metastatic bone colonization. *Mol. Oncol.* **8**, 689–703 (2014).
29. Tiedemann, K. et al. Exosomal release of L-plastin by breast cancer cells facilitates metastatic bone osteolysis. *Transl. Oncol.* **12**, 462–474 (2019).
30. Ouchida, M. et al. Novel direct targets of miR-19a identified in breast cancer cells by a quantitative proteomic approach. *PLoS ONE* **7**, e44095 (2012).
31. Peng, Y., Huang, D., Ma, K., Deng, X. & Shao, Z. MiR-19a as a prognostic indicator for cancer patients: a meta-analysis. *Biosci. Rep.* **39**, BSR20182370 (2019).
32. Bianco, P., Fisher, L. W., Young, M. F., Termine, J. D. & Robey, P. G. Expression of bone sialoprotein (BSP) in developing human tissues. *Calcif. Tissue Int.* **49**, 421–426 (1991).
33. Ferguson, S. W. & Nguyen, J. Exosomes as therapeutics: the implications of molecular composition and exosomal heterogeneity. *J. Control. Release* **228**, 179–190 (2016).
34. Goldie, B. J. et al. Activity-associated miRNA are packaged in Map1b-enriched exosomes released from depolarized neurons. *Nucleic Acids Res.* **42**, 9195–9208 (2014).
35. Kim, M. Y. et al. Tumor self-seeding by circulating cancer cells. *Cell* **139**, 1315–1326 (2009).
36. Zhang, X. H. et al. Latent bone metastasis in breast cancer tied to Src-dependent survival signals. *Cancer Cell* **16**, 67–78 (2009).
37. Gallo, A., Tandon, M., Alevizos, I. & Illei, G. G. The majority of microRNAs detectable in serum and saliva is concentrated in exosomes. *PLoS ONE* **7**, e30679 (2012).
38. Tanaka, Y. et al. Clinical impact of serum exosomal microRNA-21 as a clinical biomarker in human esophageal squamous cell carcinoma. *Cancer* **119**, 1159–1167 (2013).
39. Kawasaki, K., Suzuki, T. & Weiss, K. M. Genetic basis for the evolution of vertebrate mineralized tissue. *Proc. Natl Acad. Sci. USA* **101**, 11356–11361 (2004).
40. Malaval, L. et al. Bone sialoprotein plays a functional role in bone formation and osteoclastogenesis. *J. Exp. Med.* **205**, 1145–1153 (2008).

41. Ye, H. et al. MicroRNA and transcription factor co-regulatory network analysis reveals miR-19 inhibits CYLD in T-cell acute lymphoblastic leukemia. *Nucleic Acids Res.* **40**, 5201–5214 (2012).
42. Feng, Y. et al. miR-19a acts as an oncogenic microRNA and is up-regulated in bladder cancer. *J. Exp. Clin. Cancer Res.* **33**, 67 (2014).
43. Mogilyansky, E. & Rigoutsos, I. The miR-17/92 cluster: a comprehensive update on its genomics, genetics, functions and increasingly important and numerous roles in health and disease. *Cell Death Differ.* **20**, 1603–1614 (2013).
44. Zhang, X. et al. MicroRNA-19 (miR-19) regulates tissue factor expression in breast cancer cells. *J. Biol. Chem.* **286**, 1429–1435 (2011).
45. Wang, Y., Zhao, S., Zhu, L., Zhang, Q. & Ren, Y. MiR-19a negatively regulated the expression of PTEN and promoted the growth of ovarian cancer cells. *Gene* **670**, 166–173 (2018).
46. Boyce, B. F., Xiu, Y., Li, J., Xing, L. & Yao, Z. NF-κB-mediated regulation of osteoclastogenesis. *Endocrinol. Metab.* **30**, 35 (2015).
47. Moon, J. B. et al. Akt induces osteoclast differentiation through regulating the GSK3β/NFATc1 signaling cascade. *J. Immunol.* **188**, 163–169 (2012).
48. Georgescu, M. M. PTEN tumor suppressor network in PI3K-Akt pathway control. *Genes Cancer* **1**, 1170–1177 (2010).
49. Zhang, L.-L. et al. Phosphatase and Tensin Homolog (PTEN) represses colon cancer progression through inhibiting paxillin transcription via PI3K/AKT/NF-κB pathway. *J. Biol. Chem.* **290**, 15018–15029 (2015).
50. Kim, J.-M., Lee, K. & Jeong, D. Selective regulation of osteoclast adhesion and spreading by PLCγ/PKCα-PKCδ/RhoA-Rac1 signaling. *BMB Rep.* **51**, 230–235 (2018).
51. Nakamura, I. et al. Role of alpha(v)beta(3) integrin in osteoclast migration and formation of the sealing zone. *J. Cell Sci.* **112**, 3985–3993 (1999).
52. Hunter, G. K. & Goldberg, H. A. Nucleation of hydroxyapatite by bone sialoprotein. *Proc. Natl Acad. Sci. USA* **90**, 8562–8565 (1993).
53. Xiong, Z. et al. Bone metastasis pattern in initial metastatic breast cancer: a population-based study. *Cancer Manag. Res.* **10**, 287–295 (2018).
54. Lee, S. J. et al. Implications of bone-only metastases in breast cancer: favorable preference with excellent outcomes of hormone receptor positive breast cancer. *Cancer Res. Treat.* **43**, 89–95 (2011).
55. Kennecke, H. et al. Metastatic behavior of breast cancer subtypes. *J. Clin. Oncol.* **28**, 3271–3277 (2010).
56. Kort, E. J. et al. The E2F3-Oncomir-1 axis is activated in Wilms' tumor. *Cancer Res.* **68**, 4034–4038 (2008).
57. Liu, Y. et al. miR-19a promotes colorectal cancer proliferation and migration by targeting TIA1. *Mol. Cancer* **16**, 53 (2017).
58. Chen, Q., Guo, W., Zhang, Y., Wu, Y. & Xiang, J. MiR-19a promotes cell proliferation and invasion by targeting RhoB in human glioma cells. *Neurosci. Lett.* **628**, 161–166 (2016).
59. Ma, Q. et al. miR-19a correlates with poor prognosis of clear cell renal cell carcinoma patients via promoting cell proliferation and suppressing PTEN/SMAD4 expression. *Int. J. Oncol.* **49**, 2589–2599 (2016).
60. Wang, T. et al. miR-19a promotes colitis-associated colorectal cancer by regulating tumor necrosis factor alpha-induced protein 3-NF-kappaB feedback loops. *Oncogene* **36**, 3240–3251 (2016).
61. Hu, W., Jin, P., Ding, C. & Liu, W. miR-19a/b modulates lung cancer cells metastasis through suppression of MXD1 expression. *Oncol. Lett.* **12**, 1901–1905 (2016).
62. Pezzolesi, M. G., Platzer, P., Waite, K. A. & Eng, C. Differential expression of PTEN-targeting microRNAs miR-19a and miR-21 in Cowden syndrome. *Am. J. Hum. Genet.* **82**, 1141–1149 (2008).
63. Wang, F. et al. MicroRNA-19a/b regulates multidrug resistance in human gastric cancer cells by targeting PTEN. *Biochem. Biophys. Res. Commun.* **434**, 688–694 (2013).
64. Pandey, D. P. & Picard, D. miR-22 inhibits estrogen signaling by directly targeting the estrogen receptor mRNA. *Mol. Cell. Biol.* **29**, 3783–3790 (2009).
65. Kozlow, W. & Guise, T. A. Breast cancer metastasis to bone: mechanisms of osteolysis and implications for therapy. *J. Mammary Gland Biol. Neoplasia* **10**, 169–180 (2005).
66. Wang, H. et al. The osteogenic niche promotes early-stage bone colonization of disseminated breast cancer cells. *Cancer Cell* **27**, 193–210 (2015).
67. Sethi, N., Dai, X., Winter, C. G. & Kang, Y. Tumor-derived JAGGED1 promotes osteolytic bone metastasis of breast cancer by engaging notch signaling in bone cells. *Cancer Cell* **19**, 192–205 (2011).
68. Chen, Y. C., Sosnoski, D. M. & Mastro, A. M. Breast cancer metastasis to the bone: mechanisms of bone loss. *Breast Cancer Res.* **12**, 215 (2010).
69. Cortez, M. A., Welsh, J. W. & Calin, G. A. Circulating microRNAs as noninvasive biomarkers in breast cancer. *Recent Results Cancer Res.* **195**, 151–161 (2012).
70. Endzelins, E. et al. Diagnostic, prognostic and predictive value of cell-free miRNAs in prostate cancer: a systematic review. *Mol. Cancer* **15**, 41 (2016).
71. Izzotti, A. et al. Extracellular MicroRNA in liquid biopsy: applicability in cancer diagnosis and prevention. *Am. J. Cancer Res.* **6**, 1461–1493 (2016).
72. Kosaka, N., Iguchi, H. & Ochiya, T. Circulating microRNA in body fluid: a new potential biomarker for cancer diagnosis and prognosis. *Cancer Sci.* **101**, 2087–2092 (2010).
73. Fedarko, N. S., Jain, A., Karadag, A., Van Eman, M. R. & Fisher, L. W. Elevated serum bone sialoprotein and osteopontin in colon, breast, prostate, and lung cancer. *Clin. Cancer Res.* **7**, 4060–4066 (2001).
74. Sharp, J. A., Sung, V., Slavin, J., Thompson, E. W. & Henderson, M. A. Tumor cells are the source of osteopontin and bone sialoprotein expression in human breast cancer. *Lab. Investig.* **79**, 869–877 (1999).
75. Bellahcene, A., Menard, S., Bufalino, R., Moreau, L. & Castronovo, V. Expression of bone sialoprotein in primary human breast cancer is associated with poor survival. *Int. J. Cancer* **69**, 350–353 (1996).
76. Bos, P. D. et al. Genes that mediate breast cancer metastasis to the brain. *Nature* **459**, 1005–1009 (2009).
77. Yu, H. et al. FTY720 inhibited proinflammatory cytokine release and osteoclastogenesis induced by *Aggregatibacter actinomycetemcomitans*. *Lipids Health Dis.* **14**, 66 (2015).
78. Choi, S. W. et al. Osteoporotic bone of miR-150-deficient mice: Possibly due to low serum OPG-mediated osteoclast activation. *Bone Rep.* **3**, 5–10 (2015).
79. Falk, S., Al-Dihaissy, T., Mezzanotte, L. & Heegaard, A.-M. Sex-difference affects disease progression in the MRMT-1 model of cancer-induced bone pain. *F1000Res.* **4**, 445 (2015).
80. Sliepen, S. H. J. et al. Cancer-induced bone pain impairs burrowing behaviour in mouse and rat. *In Vivo* **33**, 1125–1132 (2019).
81. Nakase, I. & Futaki, S. Combined treatment with a pH-sensitive fusogenic peptide and cationic lipids achieves enhanced cytosolic delivery of exosomes. *Sci. Rep.* **5**, 10112 (2015).
82. Lv, L. H. et al. Anticancer drugs cause release of exosomes with heat shock proteins from human hepatocellular carcinoma cells that elicit effective natural killer cell antitumor responses in vitro. *J. Biol. Chem.* **287**, 15874–15885 (2012).
83. Geng, W. et al. Inhibition of osteoclast formation and function by bicarbonate: role of soluble adenylyl cyclase. *J. Cell. Physiol.* **220**, 332–340 (2009).
84. Crescitelli, R. et al. Distinct RNA profiles in subpopulations of extracellular vesicles: apoptotic bodies, microvesicles and exosomes. *J. Extracell. Vesicles* **2**, https://doi.org/10.3402/jev.v2i0.20677 (2013).
85. Thery, C., Amigorena, S., Raposo, G. & Clayton, A. Isolation and characterization of exosomes from cell culture supernatants and biological fluids. *Curr. Protoc. Cell Biol.* **Chapter 3**, Unit 3 22 (2006).
86. Li, C. W. et al. Eradication of triple-negative breast cancer cells by targeting glycosylated PD-L1. *Cancer Cell* **33**, 187–201.e110 (2018).
87. Biesiadecki, B. J. & Jin, J. P. A high-throughput solid-phase microplate protein-binding assay to investigate interactions between myofilament proteins. *J. Biomed. Biotechnol.* **2011**, 421701 (2011).
88. Zengel, P. et al. mu-Slide chemotaxis: a new chamber for long-term chemotaxis studies. *BMC Cell Biol.* **12**, 21 (2011).
89. Reich, M. et al. GenePattern 2.0. *Nat. Genet.* **38**, 500–501 (2006).

Acknowledgements

This work was supported by NIH grants RO1CA173499, R01CA185650, and R01CA205067 (to K.W.). This study used various Core Facilities and Departmental Shared Equipment resources including Cellular Imaging Shared Resource, Biostatistics Shared Resource, Tumor Tissue and Pathology Shared Resource Cell and Viral Vector Core Laboratory and Cancer Genomics Shared Resource that are supported by the Comprehensive Cancer Center of Wake Forest University NCI, National Institutes of Health Grant (P30CA012197). We also thank Dr. Xandra O. Breakefield, Ph.D. (Harvard Medical School), and Dr. Joan Massagué, Ph.D. (Memorial Sloan Kettering Cancer Center) for kindly providing the materials used in this work. The Figs. 4f, j and 8 were created from images provided by Servier Medical art (http://servier.com/Powerpoint-image-bank). Servier Medical Art by Servier is licensed under a Creative Commons Attribution 3.0 Unported License.

Author contributions

Conception and design: K. Wu and K. Watabe. Development of methodology: K. Wu, J.F., F.X., S.S., K. Watabe. Acquisition of data (provided animals, acquired and managed patient specimens, provided facilities, etc.): K. Wu, J.F., F.L., R.S., F.X., S.S., Y.L., S.-Y.W, D.Z, X.P., M.G.R., H.T., S.T., T.K., Y.-y.M., Y.S., A.T., R.P.D., K. Watabe. Analysis and interpretation of data (e.g., statistical analysis, biostatistics, computational analysis): K. Wu, D.Z., K. Watabe. Writing, review, and/or revision of the manuscript: K. Wu, S.S., K. Watabe. Administrative, technical, or material support: K. Wu, Y.L., R.S., K. Watabe. Study supervision: K. Watabe.

Competing interests

The authors declare no competing interests.

Additional information

Supplementary information The online version contains supplementary material available at https://doi.org/10.1038/s41467-021-25473-y.

Correspondence and requests for materials should be addressed to K.W.

Peer review information *Nature Communications* thanks Jacqueline F. Bromberg and the other, anonymous, reviewer(s) for their contribution to the peer review of this work. Peer reviewer reports are available.

Reprints and permission information is available at http://www.nature.com/reprints

Publisher's note Springer Nature remains neutral with regard to jurisdictional claims in published maps and institutional affiliations.

Open Access This article is licensed under a Creative Commons Attribution 4.0 International License, which permits use, sharing, adaptation, distribution and reproduction in any medium or format, as long as you give appropriate credit to the original author(s) and the source, provide a link to the Creative Commons license, and indicate if changes were made. The images or other third party material in this article are included in the article's Creative Commons license, unless indicated otherwise in a credit line to the material. If material is not included in the article's Creative Commons license and your intended use is not permitted by statutory regulation or exceeds the permitted use, you will need to obtain permission directly from the copyright holder. To view a copy of this license, visit http://creativecommons.org/licenses/by/4.0/.

© The Author(s) 2021

molecules

MDPI

Review

Progress in Targeted Alpha-Particle-Emitting Radiopharmaceuticals as Treatments for Prostate Cancer Patients with Bone Metastases

Chirayu M. Patel [1], Thaddeus J. Wadas [2] and Yusuke Shiozawa [1,*]

[1] Department of Cancer Biology and Comprehensive Cancer Center, Wake Forest University Health Sciences, Winston-Salem, NC 27157, USA; cpatel@wakehealth.edu
[2] Department of Radiology, University of Iowa, Iowa City, IA 52242, USA; thaddeus-wadas@uiowa.edu
* Correspondence: yshiozaw@wakehealth.edu; Tel.: +1-336-716-8743; Fax: +1-336-716-0255

Abstract: Bone metastasis remains a major cause of death in cancer patients, and current therapies for bone metastatic disease are mainly palliative. Bone metastases arise after cancer cells have colonized the bone and co-opted the normal bone remodeling process. In addition to bone-targeted therapies (e.g., bisphosphonate and denosumab), hormone therapy, chemotherapy, external beam radiation therapy, and surgical intervention, attempts have been made to use systemic radiotherapy as a means of delivering cytocidal radiation to every bone metastatic lesion. Initially, several bone-seeking beta-minus-particle-emitting radiopharmaceuticals were incorporated into the treatment for bone metastases, but they failed to extend the overall survival in patients. However, recent clinical trials indicate that radium-223 dichloride ($^{223}RaCl_2$), an alpha-particle-emitting radiopharmaceutical, improves the overall survival of prostate cancer patients with bone metastases. This success has renewed interest in targeted alpha-particle therapy development for visceral and bone metastasis. This review will discuss (i) the biology of bone metastasis, especially focusing on the vicious cycle of bone metastasis, (ii) how bone remodeling has been exploited to administer systemic radiotherapies, and (iii) targeted radiotherapy development and progress in the development of targeted alpha-particle therapy for the treatment of prostate cancer bone metastasis.

Keywords: bone metastases; radiopharmaceuticals; radium-223; actinium-225; targeted alpha-particle-emitting radiopharmaceuticals

check for updates

Citation: Patel, C.M.; Wadas, T.J.; Shiozawa, Y. Progress in Targeted Alpha-Particle-Emitting Radiopharmaceuticals as Treatments for Prostate Cancer Patients with Bone Metastases. *Molecules* **2021**, *26*, 2162. https://doi.org/10.3390/molecules26082162

Academic Editor: João D. G. Correia

Received: 18 March 2021
Accepted: 6 April 2021
Published: 9 April 2021

Publisher's Note: MDPI stays neutral with regard to jurisdictional claims in published maps and institutional affiliations.

Copyright: © 2021 by the authors. Licensee MDPI, Basel, Switzerland. This article is an open access article distributed under the terms and conditions of the Creative Commons Attribution (CC BY) license (https://creativecommons.org/licenses/by/4.0/).

1. Introduction

As a result of improvements in cancer research, prevention, early diagnosis, and treatment, the survival time of cancer patients with localized disease has increased. However, the prognosis for cancer patients with disseminated disease has decreased dramatically; distant metastases are responsible for 90% of all cancer-related deaths [1]. Although cancer cells may spread to any part of the body, different cancers have been observed to colonize different organs of the body at different rates and bone is a major metastatic site for several cancers. The relative incidence of bone metastasis is 65–75% in breast cancer, 65–75% in prostate cancer, 60% in thyroid cancer, 30–40% in lung cancer, 40% in bladder cancer, 20–25% in renal cell carcinoma, and 14–45% in melanoma [2]. Furthermore, the median survival time of patients with bone metastases is 19–25 months for breast cancer, 12–53 months for prostate cancer, 28 months for thyroid cancer, 6 months for lung cancer, 6 months for bladder cancer, 12 months for renal carcinoma, and 6 months for melanoma [3]. Importantly, the presence of metastatic bone disease alters the course of clinical care of patients, increases the immense physical and emotional burdens faced by patients, and augments the economic burden faced by patients and society [4–13]. For example, prostate cancer patients experiencing bone metastases incurred health care costs that were approximately $8000 more than those incurred by men without bone metastasis [14]. Interestingly, it has

been demonstrated that the total medical care costs for breast cancer patients with bone metastases who experienced skeletal-related events (SREs) are nearly $50,000 greater than for those without SREs [4,7].

Since bone metastasis is one of the major causes of death of cancer patients, eradicating cancer-induced bone diseases represents one of the greatest challenges of modern health care. Thus, there is a critical need to integrate our current understanding of cancer metastasis with emerging concepts in bone biology to advance our understanding of cancer-induced bone diseases, with the goal of improving treatment strategies and clinical outcomes, while reducing the financial difficulties experienced by patients. The treatment strategies for bone metastases are somewhat unique when compared to those for other metastases. Normally, the treatment strategies for both primary and metastatic tumors are similar—targeting the tumors themselves or inducing the immune system surrounding the tumors. However, for bone metastases, the treatments target the function of the metastatic organ, which is bone (an organ that continuously remodels throughout life by coupling osteoclast and osteoblast activity, which is called bone remodeling [15]). It has been suggested that the cells involved in bone remodeling (e.g., osteoclasts, osteoblasts, and osteocytes) and bone metastatic cancer cells interact with each other, and this crosstalk between bone-related cells and bone metastatic cancer cells stimulates further bone metastatic progression, known as "the vicious cycle of bone metastases" [16]. It is therefore natural to target bone remodeling to interfere with this cycle. Indeed, bisphosphonate and denosumab, a human monoclonal anti-receptor activator of nuclear factor κB ligand (RANKL) antibody, which decreases osteoclastic activity, have been used as treatments for bone metastases [17,18]. These treatments have been effective in reducing the painful complications of bone metastases but ultimately fail to improve the overall survival of cancer patients with bone metastases [17,18]. However, recent clinical trials indicate that an alpha-particle-emitting radiopharmaceutical radium-223 dichloride ($^{223}RaCl_2$), which targets hydroxyapatite or osteoblastic bone metastatic lesions, improves the overall survival of prostate cancer patients with bone metastases. Importantly, to date, this is the only bone-targeted treatment modality that can prolong the survival time of cancer patients with bone metastases, although several combinations of systemic treatments (e.g., hormone therapies and chemotherapies) are known to enhance the overall survival of metastatic castration-resistant prostate cancer patients, including patients with bone metastases [19]. Although $^{223}RaCl_2$'s success holds promise for alpha-particle-emitting radiopharmaceuticals for bone metastatic disease and has renewed interest in the development of these therapies [20–32], little is known as to the targeted treatment strategies for bone metastatic disease using alpha-particle-emitting radiopharmaceuticals.

While many excellent reviews relating to targeted radiotherapy have been published [22,33–35], this review will highlight (i) the biology of bone metastases by emphasizing the vicious cycle of bone metastasis, (ii) the treatment strategies for bone metastasis by mainly focusing on radiopharmaceuticals, and (iii) the future directions for targeted alpha-particle-emitting radiopharmaceutical treatment strategies in bone metastasis.

2. The Biology of the Vicious Cycle of Bone Metastases

Although personalized medicine strategies continue to be adopted in the clinic, the tumor phenotype at the primary site typically dictates the treatment regimen. However, these conventional treatment strategies usually fail to eradicate metastases. This leads to a more aggressive combination treatment, including chemotherapies, radiotherapies, immunotherapies, and/or targeted therapies, for cancer patients with metastases. Importantly, when considering the treatment of bone metastasis, the dynamics of bone turnover also needs to be considered during treatment planning.

Unlike other organs, bone is continuously renewed throughout life to maintain its structural integrity. Bone is composed of three parts: compact bone, trabecular bone, and bone marrow. Compact bone is a hard, solid bone tissue and forms the outside layer of bone. Trabecular bone (or spongy bone) and bone marrow are found in the inside of

bones. A part of trabecular bone eventually converts into compact bone. The bone marrow is composed of two distinct stem cell lineages, cells of hematopoietic origin and those of mesenchymal origin. Hematopoietic stem cells (HSCs) give rise to all blood cell types, including macrophages that differentiate into osteoclasts, while mesenchymal stem cells (MSCs) are responsible for the generation of stromal cells, osteoblasts, and osteocytes [36]. Additionally, these cells of mesenchymal origin are crucial for trabecular bone development. Interestingly, these two cell lineages interact with each other to maintain each other's functions. For example, osteoblasts serve as the microenvironment for HSCs, or the HSC niche [37–42], while HSCs support osteoblastic differentiation to establish the HSC niche [43]. Another example is that osteoblasts are responsible for the activation of osteoclasts [44], while these activated osteoclasts resorb the bone matrix to create the space for osteoblasts to form new bone [45]. As a result, compact bone, trabecular bone, and bone marrow crosstalk to maintain healthy bone development. This process, called bone remodeling, is a delicate balance that is often exploited by cancer cells that successfully colonize the bone [46].

Since Paget's seed and soil theory was proposed over a century ago [47], efforts have been made to understand why particular cancers prefer specific organs over others. Although blood flow and anatomical structure are considered as among the major contributing factors to the development of bone metastasis [48,49], proper physiological mechanisms of why particular types of cancers disseminate to the bone have not been fully uncovered. Additionally, recent evidence suggests that the establishment of organ-specific metastases is the result of not only the passive reception of circulating tumor cells through blood flow and anatomical structure but also the fact that the bone microenvironment selectively and actively recruits these circulating tumor cells [50]. This indicates that the interactions between the microenvironment of the bone marrow and bone metastatic cancer cells are crucial for the bone metastatic progression process.

Once these tumor cells have effectively seeded on the bone marrow, they begin to proliferate and interact with the cells involved in bone remodeling (e.g., osteoclasts, osteoblasts, and osteocytes) through paracrine and juxtacrine signaling events. This interaction creates an imbalance in the normal bone remodeling process in what has been termed the vicious cycle of bone metastases (Figure 1) [51]. Recent studies have revealed that bone metastatic prostate cancer cells hijack the interaction between the cells of hematopoietic and mesenchymal lineages, which is important for maintaining healthy bone remodeling, to establish metastatic growth within the marrow. For example, bone metastatic prostate cancer cells target the osteoblastic HSC niche during their dissemination to the bone and compete for occupancy of the HSC niche [52,53]. These observations are consistent with previous research that has demonstrated that metastatic colonization is frequently observed in bones that contain red marrow, where blood cell formation and bone formation are active (e.g., the axial skeleton, vertebrae, ribs, and the pelvis) [54].

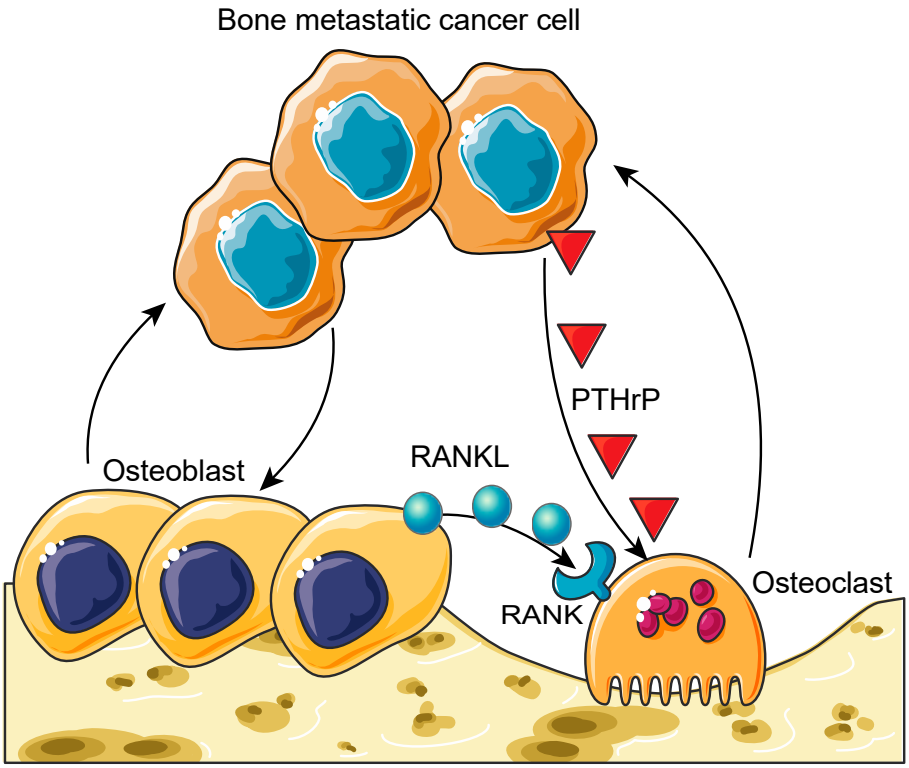

Figure 1. The vicious cycle of bone metastases. Bone metastatic cancer cells hijack the healthy bone remodeling process to create a suitable microenvironment for them to grow. Cancer cells induce hyper-osteoclastogenesis by activating osteoclasts through the secretion of parathyroid-hormone-related peptide (PTHrP). This process leads to osteolytic bone lesions and provides bone metastatic cancer cells more space to grow. On the other hand, cancer cells can over-activate osteoblasts, resulting in osteoblastic bone lesions. These hyper-activated osteoblasts also stimulate osteoclastogenesis through the receptor activator of the nuclear factor κB ligand (RANKL) (secreted from osteoblasts)/RANK (expressed on osteoclasts) axis. Furthermore, these hyper-activated osteoblasts and osteoclasts enhance the growth and survival of bone metastatic cancer cells. This process is called the vicious cycle of bone metastasis. Graphics adapted from Smart Servier Medical Art (https://smart.servier.com/, accessed on 18 March 2021).

Additionally, once the vicious cycle has been initiated, bone metastases may present as osteolytic (bone destructive), osteoblastic (bone forming), or mixed metastases, depending on how the infiltrating cancer cells have exploited the normal bone remodeling mechanisms. Although there are osteolytic- and osteoblastic-only bone metastases, most metastases arising from solid tumors have a heterogenous phenotype [55]. Osteolytic bone metastatic lesions are characterized by the destruction of normal bone formation, primarily mediated by the hyper-activation of osteoclasts (multinucleated cells that resorb the bone matrix and develop from a monocyte–macrophage lineage) [56]. In this destructive mechanism, bone metastatic cells induce the release of parathyroid-hormone-related peptide (PTHrP), which is known to activate osteoclasts and induce bone resorption [57,58]. Conversely, osteoblastic bone metastatic lesions are characterized by the deposition of new bone. Although the mechanisms of osteoblastic bone metastases are still poorly understood, they are believed to occur through the hyper-activation of osteoblasts [59]. However, the newly formed bone matrix is poorly organized, weak, and fragile [60,61]. This leads to a lack of mechanical strength and frequent fracture [60,61]. Moreover, as osteoblasts continue to proliferate, they can inadvertently cause increased bone resorption, since they release cytokines, such as RANKL, which stimulates osteoclast differentiation and activation [59,60,62].

Taken together, the bone marrow microenvironment, especially where active hematopoiesis and bone remodeling take place, may play a crucial role in the establishment and development of bone metastases, and therefore bone-marrow-microenvironment-targeting strategies have been used to treat bone metastatic disease.

3. Treatment of Bone Metastases

Current treatment options for bone metastasis include agents targeting bone remodeling (e.g., bisphosphonate and denosumab), hormone therapy, chemotherapy, external beam radiation therapy (EBRT), systemic radiotherapy, and surgical intervention [3,63,64]. Often, more than one intervention is used to suppress bone metastatic growth and maintain a patient's quality of life [65]. Although EBRT, bisphosphonate, and denosumab can reduce the onset of the painful complications of bone metastasis [17,18,66–71], delivering EBRT to every bone metastatic lesion is not practical and bisphosphonate and denosumab fail to improve the overall survival of bone metastatic patients (since these therapies mainly target bone remodeling but not cancer cells within the bone). Because of these limitations, bone metastasis is currently considered a hard-to-treat disease. Therefore, significant effort has been expended to develop ways to use the systemic delivery of therapeutic radionuclides to every bone metastatic lesion so that bone metastatic cancer cells can be exposed to the cytocidal effects of radiation.

3.1. Radiopharmaceuticals for Bone Metastases

Radionuclides derive their cytotoxicity from the particles they release during radioactive decay, which has been considered a systemic radiotherapy for bone metastasis. These particles include auger electrons (e^-), beta minus (β^-) particles, and alpha (α^{++}) particles (Table 1) [72].

Table 1. General characteristics of therapeutic radionuclides.

Decay	Particle	Maximum Particle Range (mm)	Maximum Particle Energy (MeV)	Linear Energy Transfer (kEV/μm)
Electron capture internal conversion	Non-energetic electrons	0.0005	0.001	26
Beta minus particle	Energetic electrons	12	2.3	0.2
Alpha particle	Helium nuclei	0.1	9	80

Auger electrons are released from an atom that undergoes electron capture or internal conversion. These particles have low energy, travel a maximum distance of a micron in tissue and have moderately high linear energy transfer (LET), which allows for many destructive ionization events along the path traveled by the particles [73]. These properties require that the emitting atom be localized in close proximity to the cancer cell's DNA to have a therapeutic effect [74,75].

Beta-minus-particle-emitting radionuclides decay by β^- emission. These negatively charged electrons have widely varying energies and path lengths, which may range from 0.05 keV to 2.3 MeV and from 0.05 mm to 12 mm, respectively. As these particles travel, they exhibit a lower LET than auger electrons. This results in few ionization events along the particles' path. Their cytocidal effect is believed to occur through the particles' ability to generate reactive oxygen species (ROS). In turn, these ROS generate single-stranded DNA breaks within the cancer cell. High concentrations of these β^--particles are required to create enough single-stranded DNA breaks to overwhelm DNA damage repair mechanisms and yield a therapeutic benefit.

Alpha-particle-emitting radionuclides are, by far, the most cytocidal radionuclides that have been used as systemic radiotherapy [76,77]. These particles have mass and charge equivalent to those of a helium nucleus. Alpha-particles are emitted with an energy range of 5–9 MeV, travel short distances (equivalent to no more than 10 cell diameters), and have an

LET that surpasses the LET of auger electrons to ensure a significant number of ionization events along the alpha-particle's path through tissue. These properties make the therapeutic efficacy of these radionuclides less dependent on chemo- and radio-resistance mechanisms or hypoxia. Although their cytotoxic properties have been recognized for decades, they are only now achieving clinical translation due to successful research initiatives that have explored how to efficiently attach these α^{++}-emitting radionuclides to targeting ligands such as antibodies and peptides for effective delivery to cancer cells.

Historically, the Food and Drug Administration (FDA) has approved beta-minus-particle-emitting radiopharmaceuticals as adjunct treatments for bone metastases because of their chemical properties that give them an affinity for the bone matrix [78–81]. These radiotherapies are either administered as an ionic salt solution or chelated to bone-seeking ligands, such as hydroxyethylidene diphosphonic acid (HEDP) or tetramethylene phosphonic acid (EDTMP) (Figure 2A); a brief review of each radionuclide is outlined below.

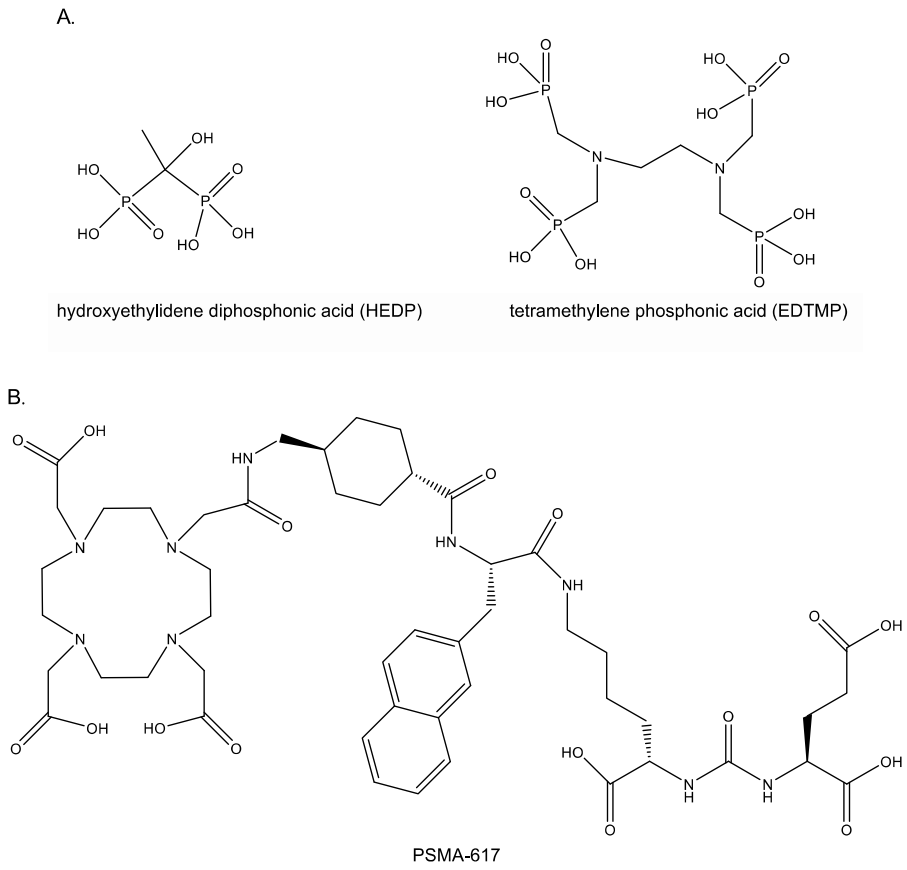

Figure 2. Several ligands used to deliver alpha-particle-emitting and beta-minus-particle-emitting radionuclides to bone metastasis. While ligands such as (**A**) hydroxyethylidene diphosphonic acid (HEDP) and tetramethylene phosphonic acid (EDTMP) target bone remodeling to deliver therapeutic radiation to bone metastases, ligands like (**B**) prostate-specific membrane antigen (PSMA)-617 target prostate cancer cell biomarkers.

Phosphorus-32 and strontium-89: Phosphorus-32 (^{32}P: $t_{1/2}$ = 14.3 d; $E_{\beta max}$ = 1.71 MeV; maximum penetration in tissue (average) = 8 mm (3 mm)) is produced by the irradiation of sulfur-32 (^{32}S) through neutron capture and is distributed as ^{32}P-orthophosphate. It has been investigated as a bone-pain-palliating radiopharmaceutical for more than 50 years [82]. After injection, approximately 90% of the injected dose is known to be incorporated at sites of bone remodeling due to the radiopharmaceutical's affinity for the hydroxyapatite within the bone matrix. In several studies, palliative response rates approached 80% [83–85] and were observed to last more than a year in patients who received multiple doses of the radiopharmaceutical. Unfortunately, due to the long particle path length and relatively high

energy of the β^--particle, pancytopenia was observed in most patients, resulting in disfavor of its clinical use [86,87]. Strontium-89 (^{89}Sr: $t_{1/2}$ = 50.5 d; $E_{\beta max}$ = 1.46 MeV; maximum penetration in tissue (average) = 6 mm (2.4 mm)) is produced by nuclear fission or through neutron capture and is distributed as $^{89}SrCl_2$. Since $^{89}Sr^{2+}$ ions exhibit similar chemical properties to Ca^{2+} ions, they are readily incorporated into the hydroxyapatite where active bone remodeling is occurring due to metastatic disease [78]. Typically, overall response rates, as defined by a reduction in bone pain, for patients receiving ^{89}Sr therapy approached 80%, with the palliative effects lasting approximately 15 months [87,88]. Although significant changes in red blood cell counts are not observed with this therapy, a decrease in white blood cell counts and platelets has been observed in 80% of patients [89–92], but these toxicities are resolved within 4 months of treatment cessation.

Rhenium-186 and Rhenium-188: Rhenium-186 (^{186}Re: $t_{1/2}$ = 3.8 d; $E_{\beta max}$ = 1.07 MeV; maximum penetration in tissue (average) = 4.5 mm (1.1 mm)) is routinely produced in nuclear reactors by direct neutron activation of metallic-enriched ^{185}Re. Rhenium-186 decays with a maximum beta energy of 1.07 MeV and a low abundance 137 keV gamma emission. It has a physical half-life of 89.3 h. Because of its maximum beta energy and particle path length, efforts have been made to determine its ability to treat bone metastasis, but since its chemical properties are not similar to those of calcium, it must be chelated to a bone-seeking ligand before injection. In the comparative study between the skeletal and soft-tissue uptake of ^{186}Re-HEDP (0.13 GBq) and ^{153}Sm-EDTMP (37 MBq/kg-body weight) in patients with confirmed bone metastasis, significantly less bone uptake was observed in patients receiving ^{186}Re-HEDP therapy, while soft-tissue retention was comparable for both radiopharmaceuticals [78]. Despite this fact, several studies have demonstrated that more than 80% of patients receiving ^{186}Re therapy reported an improvement in their bone pain [93–97]. Similar to other agents, thrombocytopenia was observed to be a major but reversible side effect of treatment [98,99]. Rhenium-188 (^{188}Re: $t_{1/2}$ = 0.7 d; $E_{\beta max}$ = 2.12 MeV; maximum penetration in tissue (average) = 10.4 mm (3.1 mm)), although not approved for clinical use, has also been investigated as an agent for bone pain management, since it can be produced and shipped to clinical sites as a $^{188}W/^{188}$Re generator [100]. When chelated to HEDP, it demonstrated therapeutic efficacy, and repeated administrations improved progression-free and overall survival [101]. Additionally, it was observed that only 63% of the patients receiving ^{188}Re-HEDP therapy reported grade I thrombocytopenia, 3% reported Grade II thrombocytopenia, and 3% of the patients reported grade I leukopenia, which were comparable for patients treated with ^{186}Re-HEDP or ^{153}Sm-EDTMP [101]. Furthermore, platelet and leukocyte counts returned to pretreatment levels within 3 months, suggesting that these toxicities are clinically manageable.

Samarium-153: Samarium-153 (^{153}Sm: $t_{1/2}$ = 1.9 d; $E_{\beta max}$ = 0.81 MeV; maximum penetration in tissue (average) = 2.5 mm (0.6 mm)), which is produced by the neutron irradiation of a samarium-152 target, has a half-life of 46.3 h and a range in bone of 1.7 mm [102]. To be effective, however, ^{153}Sm needs to be chelated to a ligand such as EDTMP, which like other phosphonic acid complexes has a high affinity for skeletal tissue while being rapidly cleared from the blood and local soft tissue. This radiopharmaceutical has shown clinical benefit in several clinical trials, with the majority of patients experiencing pain relief [103]. In one study involving 100 patients with confirmed metastatic disease, subjects received 18–37 MBq/kg of ^{153}Sm-EDTMP and were followed for several weeks after treatment [102]. Nearly 70% of the patients experienced symptomatic relief of their bone pain. Myelotoxicity was the main side effect of treatment, with nearly 90% of the subjects experiencing grade II thrombocytopenia or leukopenia, which resolved approximately 2 months after therapy. While several patients experienced grade III/IV myelotoxicity, these patients were observed to have a depleted hematopoietic reserve because of previous therapeutic interventions.

Lutetium-177: Lutetium-177 (^{177}Lu: $t_{1/2}$ = 6.7 d; $E_{\beta max}$ = 0.50 MeV; maximum penetration in tissue (average) = 2.2 mm (0.67 mm)) is produced by neutron irradiation of ^{176}Lu or ^{176}Yb targets. Although several cancer-targeting agents, such as Lutathera® and ^{117}Lu-PSMA-617, have been used to deliver targeted radiation therapy to cancer cells expressing

specific cancer cell antigens [104], additional studies have sought to use the radioactive decay properties of ^{177}Lu for treating bone metastasis. Several groups have investigated the utility of ^{177}Lu-EDTMP as a bone-seeking radiopharmaceutical since the energy of the emitted β^- is low enough to reduce bone marrow suppression, which has consistently been a major disadvantage of other β^--emitting bone-seeking agents [105,106]. Recently, the use of low- and high-dose ^{177}Lu-EDTMP was examined in a phase II study in patients with metastatic breast or prostate cancer [107]. In this study, subjects received either a low (0.13 GBq) or a high (0.26 GBq) dose of ^{177}Lu-EDTMP and were followed for 16 weeks post-treatment. Based upon pain assessment scores, the overall response rate was 86%. Additionally, treatment-related toxicity was evaluated in all patients. Grade I/II hematological toxicities were observed in 34% of the subjects, while grade III/IV toxicities were observed in 23% of the study participants. However, the observed toxicities were not significantly different in either the low- or the high-dose cohort, and this finding prompted the authors to conclude that ^{177}Lu-EDTMP is safe and effective as a treatment for bone pain palliation. More recently, several groups investigated whether using a bisphosphonate to deliver the cytocidal radiation released by ^{177}Lu to the metastatic deposit in bone would provide greater relief. While many bisphosphonates were studied, zoledronic acid was chosen for further study since it had significantly higher incorporation into hydroxyapatite [108,109]. Consequently, several groups studied ^{177}Lu-DOTA-zoledronic acid (^{177}Lu-DOTA-ZOL) and demonstrated that it has pharmacokinetics comparable to those of ^{177}Lu-EDTMP [110,111]. These studies also revealed higher absorption of the dose by the trabecular bone in patients who received ^{177}Lu-DOTA-ZOL vs. ^{177}Lu-EDTMP, but the dose absorbed by critical organs was much lower for the former radiopharmaceutical. Recently, the safety and efficacy of ^{177}Lu-DOTA-ZOL in 40 patients with metastatic bone disease was evaluated [112]. Eligible subjects received 0.13 GBq of ^{177}Lu-DOAT-ZOL at monthly intervals and then were monitored for a 12-week period after therapy. Based upon criteria such as pain palliation, an overall response rate of 90% was observed. However, unlike patients receiving ^{177}Lu-EDTMP, grade III/IV hematological toxicities were not observed, although several patients did experience grade II anemia. Moreover, renal toxicity and hyper-calcemia, which can be complications of bisphosphonate administration, were not observed in study participants. Interestingly, pain palliation was observed within 7 days of treatment, with relief lasting 10 months, which is more than twice that experienced by patients receiving ^{177}Lu-EDTMP.

Not only beta-minus-particle-emitting radiopharmaceuticals but also alpha-particle-emitting radiopharmaceuticals have been used as a treatment modality for bone metastatic disease. Radium-223 dichloride ($^{223}RaCl_2$: $T_{1/2}$ = 11.4 d; $E\alpha_{max}$ = 6–7 MeV) is a water-soluble salt that was approved nearly a decade ago by the FDA for the treatment of bone metastasis associated with metastatic prostate cancer. Similar to calcium ions, this alkaline earth ion accumulates in bone, where it decays through seven daughter radionuclides, while releasing four α^{++}-particles and two β^--particles, generating approximately 30 MeV of total kinetic energy, which is deposited in the surrounding bone cancer microenvironment [67–69,78,113]. This large energy deposition is believed to generate irreparable double-stranded DNA breaks within the DNA of tumor cells that have localized in the bone, causing cancer cell death [114–117]. This strategy has yielded clinical success. For example, in the ALSYMPCA trial (NCT00699751), which was a randomized, double-blind, placebo-controlled phase III trial that investigated the role of $^{223}RaCl_2$ in metastatic castration-resistant prostate cancer patients (n = 921), the median overall survival of patients treated with $^{223}RaCl_2$ (n = 614, 14.9 months) significantly improved compared with those treated with a placebo (n = 307, 11.3 months) (hazard ratio, 0.70; 95% confidence interval, 0.58 to 0.83; $p < 0.001$) [66]. Moreover, patients treated with $^{223}RaCl_2$ experienced decreased pain levels that correlated with increased overall survival [118]. Diarrhea, nausea, and vomiting were the most common side effects reported by patients. Additionally, pancytopenia was observed in many patients with grade III/IV thrombocytopenia, and neutropenia was observed in patients with compromised bone marrow function [119]. Since those initial trials, the use of $^{223}RaCl_2$ therapy in combination with other agents using a strategy that has

proven successful with non-radioactive therapeutics has been sought [120]. For example, a post hoc exploratory analysis of an international, early access, open-label, single-arm phase IIIb trial of the testing efficacy of $^{223}RaCl_2$ in metastatic castration-resistant prostate cancer patients following the ALSYMPCA trial revealed that a combination of $^{223}RaCl_2$ and androgen deprivation therapies (ADTs; abiraterone or enzalutamide) extended the patients' overall survival compared to therapy with $^{223}RaCl_2$ alone [118]. However, a recent multinational, multicenter, randomized, double-blind, placebo-controlled phase III trial of the combination of abiraterone and $^{223}RaCl_2$ in patients with metastatic castration-resistant prostate cancer (NCT02043678) not only failed to improve skeletal event-free survival but also increased the frequency of bone fractures compared to the placebo [121]. These contradictory results suggest that additional prospective studies are needed and caution is warranted when choosing an effective combination strategy that involves the use of ADTs and $^{223}RaCl_2$ therapy for treating prostate cancer patients with bone metastasis.

3.2. Targeted Radiopharmaceuticals for Bone Metastases

To date, the strategy for integrating systemic radiotherapies into the treatment plans of cancer patients with bone metastases has relied on bone metabolism to target bone metastatic disease. While successful, the results of this strategy have been primarily palliative, since the bone metastatic cancer cells are not specifically targeted by the radiopharmaceutical. As a result, efforts are being made to expand this strategy by developing agents that can selectively target biomarkers that are over-expressed on the cancer cells within the bone metastatic microenvironment, with the goal of improving therapeutic efficacy and patient outcomes. For example, one such strategy that has been successful in the treatment of metastatic prostate cancer has been the development of radiotherapies that specifically target prostate-specific membrane antigen (PSMA) [122]. PSMA is known to be highly expressed on prostate cancer cells at the primary tumor and within visceral and bone metastases [123]. PSMA-617, a small molecule that binds to PSMA with high affinity, was designed to target PSMA-expressing prostate cancer cells (Figure 2B) [124]. In a recent single-arm, single-center, phase II trial, ^{177}Lu-PSMA-617 was administered to men with metastatic castration-resistant prostate cancer (n =30) [125]. After four cycles of radiotherapy, 57% of these patients experienced minimal toxicity and achieved a greater-than-50% reduction in prostate-specific antigen (PSA) levels, which is one of the clinical surrogate markers for prostate cancer treatment response [125]. Based on these promising results, an international prospective open-label randomized phase III trial comparing the treatment efficacy between ^{177}Lu-PSMA-617 and the best standard of care in men with metastatic castration-resistant prostate cancer (VISION trial, NCT03511664) is currently underway [126], and as of 23 March 2021, the initial result that ^{177}Lu-PSMA-617 significantly improves the overall survival and radiographic progression-free survival of PSMA-positive metastatic castration-resistant prostate cancer patients was announced (https://www.novartis.com/news/media-releases/novartis-announces-positive-result-phase-iii-study-radioligand-therapy-177lu-psma-617-patients-advanced-prostate-cancer, (accessed on 1 April 2021)).

Despite the promise of ^{177}Lu-PSMA-617 therapy, approximately 30% of patients do not respond to this treatment [127]. These observations have led to the investigation of the use of ^{225}Ac-PSMA-617 as an alternative alpha-particle-emitting radiotherapy for refractory patients [127–129]. Actinium-225 (^{225}Ac: $t_{1/2}$ = 10 d; $E\alpha_{max}$ = 6–8 MeV) is a radioactive metal of the actinide series. Similar to $^{223}RaCl_2$, ^{225}Ac has a relatively long half-life and emits four α^{++}- and two β^--particles per nuclear decay. However, unlike $^{223}RaCl_2$, ^{225}Ac can be linked to a variety of targeting ligands [130–137]. In the early stage of the development of ^{225}Ac-PSMA-617, two patients received this therapy [127]. The first patient exhausted conventional chemotherapies, bone remodeling therapy, ADTs, and six cycles of $^{223}RaCl_2$ therapy. The patient received three cycles of approximately 10 MBq (100 kBq/kg body weight) of ^{225}Ac-PSMA-617. After 8 weeks, all visible visceral and bone metastases had decreased to a size that was below the limit of detection of clinical imaging scanners, while PSA levels had decreased from 3000 to 0.26 ng/mL. Similar to the first

patient, the second patient was refractory to conventional chemotherapies and ADTs and failed to respond to several cycles of ^{177}Lu-PSMA-617 therapy. This patient received three cycles of ^{225}Ac-PSMA-617 therapy (100 kBq/kg body weight) at bimonthly intervals. After completing the three cycles, the patient experienced complete remission, as indicated by the results of the restaging PSMA-PET/CT scans (Figure 3). Similar to the first patient, no relevant hematological toxicities were observed, although both subjects did experience moderate xerostomia.

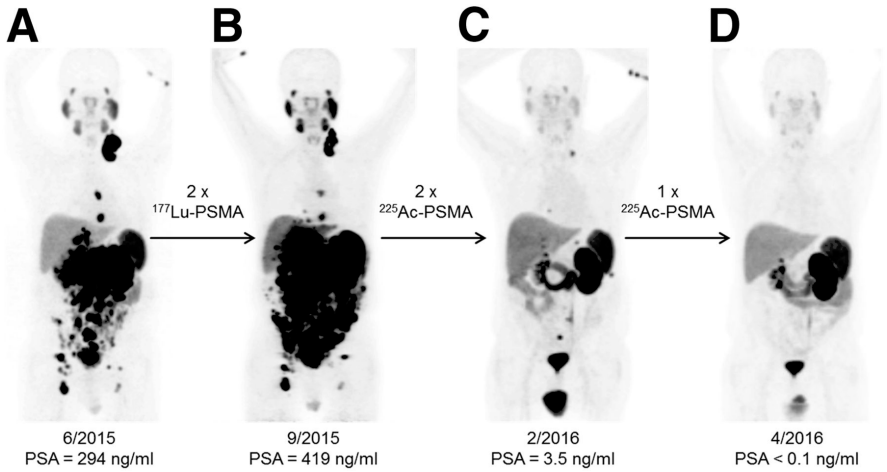

Figure 3. An example of the effective response of a prostate cancer patient to ^{225}Ac-PSMA-617 treatment. This research was originally published in the *Journal of Nuclear Medicine* [127]. Kratochwil C, Bruchertseifer F, Giesel FL, Weis M, Verburg FA, Mottaghy F, Kopka K, Apostolidis C, Haberkorn U, and Morgenstern A. 225Ac-PSMA-617 for PSMA-Targeted α-Radiation Therapy of Metastatic Castration-Resistant Prostate Cancer. J Nucl Med. 2016;57(12):1941-1944. © SNMMI. ^{68}Ga-PSMA-11 PET/CT scans of patient B in this manuscript (a prostate cancer patient who presented with peritoneal carcinomatosis and liver metastases that were progressive under ^{177}Lu-PSMA-617 therapy). In comparison to the initial tumor spread (**A**), restaging after 2 cycles of β-emitting ^{177}Lu-PSMA-617 presented progression (**B**). In contrast, restaging after second (**C**) and third (**D**) cycles of α-emitting ^{225}Ac-PSMA-617 presented an impressive response. Adapted from ref. [127].

In additional studies by this same group, chemotherapy-naive prostate cancer patients with extensive bone and lymph node metastases were selected to receive ^{225}Ac-PSMA-617 therapy [138]. All patients (n = 17) had failed prior treatments, which included radical prostatectomy, EBRT, ADT, brachytherapy, and ^{177}Lu-PSMA-617 therapy. Patients received between two and six cycles of ^{225}Ac-PSMA-617, with an average administered activity range between 4 and 13 MBq. Following treatment, 82% of the patients experienced a $\geq$90% reduction in PSA levels. Moreover, PSMA PET/CT revealed that 65% of the treated patients demonstrated a complete absence of metastatic lesions at the sites of metastases, previously identified on baseline imaging scans [138]. Similar to the initial two patients, no acute toxicities were experienced by any of the surviving patients, though all patients did experience xerostomia, which prompted additional investigations into the most efficient ways to salvage salivary gland function [139,140].

While a recent report of a patient achieving remission lasting longer than 5 years was published in the literature [141], these results should be tempered by recent observations that 17% of patients, many with bone metastasis, do not respond to ^{225}Ac-PSMA-617 therapy despite sufficient tumor uptake on PSMA-PET/CT. Investigations using CT-guided biopsy and targeted next-generation sequencing have revealed a total of 15 mutations in DNA-damage-repair-associated genes, which suggests that patients harboring these mutations may need a treatment strategy that combines ^{225}Ac-PSMA-617 with chemotherapies that target DNA damage repair pathways to achieve maximum clinical benefit [142].

Although ^{225}Ac-PSMA-617 is a promising treatment agent for metastatic castration-resistant prostate cancer, PSMA-targeted agents (e.g., antibody, nanobody, small molecule) labeled with other alpha-particle-emitting radiopharmaceuticals have also been explored

in both preclinical and clinical settings (Table 2). Since PSMA is expressed by not only bone metastatic prostate cancer cells but also those at the primary site and soft-tissue metastatic sites, this strategy is not specific for bone metastases. However, a majority of the patients with metastatic castration-resistant prostate cancer experience bone metastases during the course of disease progression. Therefore, the development of PSMA-targeted alpha-particle-emitting radiopharmaceuticals is crucial if eradicating bone metastatic prostate cancer is to be an achievable clinical goal. Further studies, including the assessments of their clinical efficacy and safety, are clearly warranted.

Table 2. The recent status of PSMA-targeted alpha-particle-emitting radiopharmaceuticals.

Agent	Conjugator	Development Phase	Refs.
^{213}Bi-J591	PSMA-targeting murine monoclonal antibody, J591	Preclinical study	[143–145]
^{213}Bi-PSMA I&T	PSMA-targeting (3*S*,7*S*)-29,32-dibenzyl-5,13,20,28,31,34-hexaoxo-37-(4,7,10-tris(carboxymethyl)-1,4,7,10-tetraazacyclododecan-1-yl)-4,6,12,21,27,30,33-heptaazaheptatriacontane-1,3,7,26,37-pentacarboxylic acid (DOTAGA-FFK(Sub-KuE)), PSMA I&T	Preclinical study	[146]
^{213}Bi-JVZ-008	PSMA-targeting nanobody, JVZ-008	Preclinical study	[146]
^{211}At-6	PSMA-targeting (2*S*)-2-(3-(1-carboxy-5-(4-^{211}At-astatobenzamido)pentyl)ureido)-pentanedioic acid, compound 6	Preclinical study	[147]
^{225}Ac-PSMA-617	PSMA-targeting small molecule, PSMA-617	Clinical study	[127,138,141,148]
^{227}Th-PSMA-TTC	PSMA-targeting fully human antibody, BAY 2315158	Clinical trial (phase I: NCT03724747)	[149]
^{225}Ac-J591	PSMA-targeting murine monoclonal antibody, J591	Clinical trial (phase I: NCT03276572)	

4. Conclusions

Bone metastasis creates enormous physical, emotional, and financial burdens for cancer patients and society; it is a significant contributor to cancer mortality rates. Systemically delivered radionuclides have been explored as potential therapies for bone metastasis. Initially, β^--emitting radionuclides were used because they could be delivered easily to sites of active bone remodeling. However, their efficacy has been limited to pain mitigation. Recently, systemically delivered $^{223}RaCl_2$, which decays through α^{++}-particle emission, has been observed to extend the overall survival of men with metastatic prostate cancer. These results have renewed interest in alpha-particle-emitting radiotherapies, and new molecularly targeted strategies to deliver this highly cytotoxic radiation directly to bone metastatic cancer cells within the bone marrow microenvironment are being investigated. Using this strategy, ^{225}Ac-PSMA-617, which has been an effective treatment for men with metastatic prostate cancer, which was previously believed to be refractory to conventional chemotherapies and standard of care radiotherapy, has been developed. While further clinical evaluation is warranted, current data suggest that targeted alpha-particle-emitting radiopharmaceuticals used alone or in concert with current standard treatments may lead to much-needed improvements in the clinical management of cancer bone metastasis.

Author Contributions: Conceptualization, T.J.W. and Y.S.; writing—original draft preparation, C.M.P., T.J.W., and Y.S.; writing—review and editing, T.J.W. and Y.S.; supervision, T.J.W. and Y.S.; and funding acquisition, T.J.W. and Y.S. All authors have read and agreed to the published version of the manuscript.

Funding: This research was funded by the National Cancer Institute, R01-CA238888; R44-CA203184; R21-CA227709; and P30-CA012197; the U.S. Department of Defense, W81XWH-17-1-0541; W81XWH-19-1-0045; and W81XWH-19-1-0046; and METAvivor, METAvivor Research Award. The APC was funded by W81XWH-19-1-0045.

Institutional Review Board Statement: Not applicable.

Informed Consent Statement: Not applicable.

Data Availability Statement: Not applicable.

Acknowledgments: This work is directly supported by the National Cancer Institute (R01-CA238888, Y.S.; R44-CA203184, Y.S.; and R21-CA227709, T.J.W.), the U.S. Department of Defense (W81XWH-17-1-0541, Y.S.; W81XWH-19-1-0045, Y.S.; and W81XWH-19-1-0046, T.J.W.), METAvivor (METAvivor Research Award, Y.S.), and the Wake Forest Baptist Comprehensive Cancer Center Internal Pilot Funding (Y.S.). This work is also supported by the National Cancer Institute's Cancer Center Support Grant award number P30-CA012197, issued to the Wake Forest Baptist Comprehensive Cancer Center. The content is solely the responsibility of the authors and does not necessarily represent the official views of the National Cancer Institute and Department of Defense.

Conflicts of Interest: Y.S. has received research funding from TEVA Pharmaceuticals, but not relevant to this study. No conflict of interest exists for the remaining authors.

References

1. Seyfried, T.N.; Huysentruyt, L.C. On the origin of cancer metastasis. *Crit. Rev. Oncog.* **2013**, *18*, 43–73. [CrossRef] [PubMed]
2. Macedo, F.; Ladeira, K.; Pinho, F.; Saraiva, N.; Bonito, N.; Pinto, L.; Goncalves, F. Bone Metastases: An Overview. *Oncol. Rev.* **2017**, *11*, 321. [PubMed]
3. Selvaggi, G.; Scagliotti, G.V. Management of bone metastases in cancer: A review. *Crit. Rev. Oncol. Hematol.* **2005**, *56*, 365–378. [CrossRef] [PubMed]
4. Hagiwara, M.; Delea, T.E.; Chung, K. Healthcare costs associated with skeletal-related events in breast cancer patients with bone metastases. *J. Med. Econ.* **2014**, *17*, 223–230. [CrossRef]
5. Barlev, A.; Song, X.; Ivanov, B.; Setty, V.; Chung, K. Payer costs for inpatient treatment of pathologic fracture, surgery to bone, and spinal cord compression among patients with multiple myeloma or bone metastasis secondary to prostate or breast cancer. *J. Manag. Care Pharm.* **2010**, *16*, 693–702. [CrossRef] [PubMed]
6. Delea, T.; Langer, C.; McKiernan, J.; Liss, M.; Edelsberg, J.; Brandman, J.; Sung, J.; Raut, M.; Oster, G. The cost of treatment of skeletal-related events in patients with bone metastases from lung cancer. *Oncology* **2004**, *67*, 390–396. [CrossRef]
7. Delea, T.; McKiernan, J.; Brandman, J.; Edelsberg, J.; Sung, J.; Raut, M.; Oster, G. Retrospective study of the effect of skeletal complications on total medical care costs in patients with bone metastases of breast cancer seen in typical clinical practice. *J. Support. Oncol.* **2006**, *4*, 341–347.
8. Delea, T.E.; McKiernan, J.; Brandman, J.; Edelsberg, J.; Sung, J.; Raut, M.; Oster, G. Impact of skeletal complications on total medical care costs among patients with bone metastases of lung cancer. *J. Thorac. Oncol.* **2006**, *1*, 571–576. [CrossRef]
9. Lage, M.J.; Barber, B.L.; Harrison, D.J.; Jun, S. The cost of treating skeletal-related events in patients with prostate cancer. *Am. J. Manag. Care* **2008**, *14*, 317–322.
10. Krupski, T.L.; Foley, K.A.; Baser, O.; Long, S.; Macarios, D.; Litwin, M.S. Health care cost associated with prostate cancer, androgen deprivation therapy and bone complications. *J. Urol.* **2007**, *178*, 1423–1428. [CrossRef]
11. Groot, M.T.; Boeken Kruger, C.G.; Pelger, R.C.; Uyl-de Groot, C.A. Costs of prostate cancer, metastatic to the bone, in the Netherlands. *Eur. Urol.* **2003**, *43*, 226–232. [CrossRef]
12. Duran, I.; Garzon, C.; Sanchez, A.; Garcia-Carbonero, I.; Perez-Gracia, J.L.; Segui-Palmer, M.A.; Wei, R.; Restovic, G.; Gasquet, J.A.; Gutierrez, L. Cost analysis of skeletal-related events in Spanish patients with bone metastases from solid tumours. *Clin. Transl. Oncol.* **2014**, *16*, 322–329. [CrossRef]
13. Hechmati, G.; Cure, S.; Gouepo, A.; Hoefeler, H.; Lorusso, V.; Luftner, D.; Duran, I.; Garzon-Rodriguez, C.; Ashcroft, J.; Wei, R.; et al. Cost of skeletal-related events in European patients with solid tumours and bone metastases: Data from a prospective multinational observational study. *J. Med. Econ.* **2013**, *16*, 691–700. [CrossRef] [PubMed]
14. Tangirala, K.; Appukkuttan, S.; Simmons, S. Costs and Healthcare Resource Utilization Associated with Hospital Admissions of Patients with Metastatic or Nonmetastatic Prostate Cancer. *Am. Health Drug Benef.* **2019**, *12*, 306–312.
15. Hadjidakis, D.J.; Androulakis, I.I. Bone remodeling. *Ann. N. Y. Acad. Sci.* **2006**, *1092*, 385–396. [CrossRef] [PubMed]
16. Guise, T.A. The vicious cycle of bone metastases. *J. Musculoskelet. Neuronal. Interact.* **2002**, *2*, 570–572. [PubMed]
17. Stopeck, A.T.; Lipton, A.; Body, J.J.; Steger, G.G.; Tonkin, K.; de Boer, R.H.; Lichinitser, M.; Fujiwara, Y.; Yardley, D.A.; Viniegra, M.; et al. Denosumab compared with zoledronic acid for the treatment of bone metastases in patients with advanced breast cancer: A randomized, double-blind study. *J. Clin. Oncol.* **2010**, *28*, 5132–5139. [CrossRef]

18. Fizazi, K.; Carducci, M.; Smith, M.; Damiao, R.; Brown, J.; Karsh, L.; Milecki, P.; Shore, N.; Rader, M.; Wang, H.; et al. Denosumab versus zoledronic acid for treatment of bone metastases in men with castration-resistant prostate cancer: A randomised, double-blind study. *Lancet* **2011**, *377*, 813–822. [CrossRef]
19. McCain, J. Drugs that offer a survival advantage for men with bone metastases resulting from castration-resistant prostate cancer: New and emerging treatment options. *Pharm. Ther.* **2014**, *39*, 130–143.
20. Nguyen, N.C.; Shah, M.; Appleman, L.J.; Parikh, R.; Mountz, J.M. Radium-223 Therapy for Patients with Metastatic Castrate-Resistant Prostate Cancer: An Update on Literature with Case Presentation. *Int. J. Mol. Imaging* **2016**, *2016*, 2568031. [CrossRef] [PubMed]
21. Vogelzang, N.J.; Coleman, R.E.; Michalski, J.M.; Nilsson, S.; O'Sullivan, J.M.; Parker, C.; Widmark, A.; Thuresson, M.; Xu, L.; Germino, J.; et al. Hematologic Safety of Radium-223 Dichloride: Baseline Prognostic Factors Associated with Myelosuppression in the ALSYMPCA Trial. *Clin. Genitourin Cancer* **2017**, *15*, 42–52. [CrossRef]
22. Wadas, T.J.; Pandya, D.N.; Solingapuram Sai, K.K.; Mintz, A. Molecular targeted alpha-particle therapy for oncologic applications. *AJR Am. J. Roentgenol.* **2014**, *203*, 253–260. [CrossRef] [PubMed]
23. Scheinberg, D.A.; McDevitt, M.R. Actinium-225 in targeted alpha-particle therapeutic applications. *Curr. RadioPharm.* **2011**, *4*, 306–320. [CrossRef] [PubMed]
24. Yamazaki, H.; Nakamura, S.; Suzuki, G.; Yoshida, K.; Yoshioka, Y.; Koizumi, M.; Ogawa, K. Hypofractionated Radiotherapy for Localized Prostate Cancer: A Challenging Accelerated Hypofractionated Radiotherapy. *Anticancer Res.* **2015**, *35*, 5167–5177. [PubMed]
25. Lewis, B.; Chalhoub, E.; Chalouhy, C.; Sartor, O. Radium-223 in Bone-Metastatic Prostate Cancer: Current Data and Future Prospects. *Oncology (Williston Park)* **2015**, *29*, 483–488. [PubMed]
26. de Kruijff, R.M.; Wolterbeek, H.T.; Denkova, A.G. A Critical Review of Alpha Radionuclide Therapy-How to Deal with Recoiling Daughters? *Pharmaceuticals (Basel)* **2015**, *8*, 321–336. [CrossRef]
27. Guerard, F.; Barbet, J.; Chatal, J.F.; Kraeber-Bodere, F.; Cherel, M.; Haddad, F. Which radionuclide, carrier molecule and clinical indication for alpha-immunotherapy? *Q. J. Nucl. Med. Mol. Imaging* **2015**, *59*, 161–167.
28. McGann, S.; Horton, E.R. Radium-223 dichloride: A novel treatment option for castration-resistant prostate cancer patients with symptomatic bone metastases. *Ann. Pharmacother.* **2015**, *49*, 469–476. [CrossRef]
29. Qi, W.X.; Fu, S.; Zhang, Q.; Guo, X.M. Charged particle therapy versus photon therapy for patients with hepatocellular carcinoma: A systematic review and meta-analysis. *Radiother. Oncol.* **2015**, *114*, 289–295. [CrossRef] [PubMed]
30. Buroni, F.E.; Persico, M.G.; Pasi, F.; Lodola, L.; Nano, R.; Aprile, C. Radium-223: Insight and Perspectives in Bone-metastatic Castration-resistant Prostate Cancer. *Anticancer Res.* **2016**, *36*, 5719–5730. [CrossRef]
31. Cordier, D.; Krolicki, L.; Morgenstern, A.; Merlo, A. Targeted Radiolabeled Compounds in Glioma Therapy. *Semin. Nucl. Med.* **2016**, *46*, 243–249. [CrossRef]
32. Ettari, R.; Previti, S.; Bitto, A.; Grasso, S.; Zappala, M. Immunoproteasome-Selective Inhibitors: A Promising Strategy to Treat Hematologic Malignancies, Autoimmune and Inflammatory Diseases. *Curr. Med. Chem.* **2016**, *23*, 1217–1238. [CrossRef]
33. Sgouros, G.; Bodei, L.; McDevitt, M.R.; Nedrow, J.R. Radiopharmaceutical therapy in cancer: Clinical advances and challenges. *Nat. Rev. Drug Discov.* **2020**, *19*, 589–608. [CrossRef]
34. Tafreshi, N.K.; Doligalski, M.L.; Tichacek, C.J.; Pandya, D.N.; Budzevich, M.M.; El-Haddad, G.; Khushalani, N.I.; Moros, E.G.; McLaughlin, M.L.; Wadas, T.J.; et al. Development of Targeted Alpha Particle Therapy for Solid Tumors. *Molecules* **2019**, *24*, 4314. [CrossRef]
35. Schaue, D.; McBride, W.H. Opportunities and challenges of radiotherapy for treating cancer. *Nat. Rev. Clin. Oncol.* **2015**, *12*, 527–540. [CrossRef]
36. Laurenti, E.; Gottgens, B. From haematopoietic stem cells to complex differentiation landscapes. *Nature* **2018**, *553*, 418–426. [CrossRef]
37. Shiozawa, Y.; Taichman, R.S. Getting blood from bone: An emerging understanding of the role that osteoblasts play in regulating hematopoietic stem cells within their niche. *Exp. Hematol.* **2012**, *40*, 685–694. [CrossRef]
38. Galan-Diez, M.; Kousteni, S. The osteoblastic niche in hematopoiesis and hematological myeloid malignancies. *Curr. Mol. Biol. Rep.* **2017**, *3*, 53–62. [CrossRef] [PubMed]
39. Yin, T.; Li, L. The stem cell niches in bone. *J. Clin. Investig.* **2006**, *116*, 1195–1201. [CrossRef]
40. Askmyr, M.; Sims, N.A.; Martin, T.J.; Purton, L.E. What is the true nature of the osteoblastic hematopoietic stem cell niche? *Trends Endocrinol. Metab.* **2009**, *20*, 303–309. [CrossRef]
41. Szade, K.; Gulati, G.S.; Chan, C.K.F.; Kao, K.S.; Miyanishi, M.; Marjon, K.D.; Sinha, R.; George, B.M.; Chen, J.Y.; Weissman, I.L. Where Hematopoietic Stem Cells Live: The Bone Marrow Niche. *Antioxid. Redox Signal.* **2018**, *29*, 191–204. [CrossRef]
42. Pinho, S.; Frenette, P.S. Haematopoietic stem cell activity and interactions with the niche. *Nat. Rev. Mol. Cell Biol.* **2019**, *20*, 303–320. [CrossRef]
43. Jung, Y.; Song, J.; Shiozawa, Y.; Wang, J.; Wang, Z.; Williams, B.; Havens, A.; Schneider, A.; Ge, C.; Franceschi, R.T.; et al. Hematopoietic stem cells regulate mesenchymal stromal cell induction into osteoblasts thereby participating in the formation of the stem cell niche. *Stem Cells* **2008**, *26*, 2042–2051. [CrossRef] [PubMed]
44. Chen, X.; Wang, Z.; Duan, N.; Zhu, G.; Schwarz, E.M.; Xie, C. Osteoblast-osteoclast interactions. *Connect. Tissue Res.* **2018**, *59*, 99–107. [CrossRef]

45. Sims, N.A.; Martin, T.J. Coupling the activities of bone formation and resorption: A multitude of signals within the basic multicellular unit. *Bonekey Rep.* **2014**, *3*, 481. [CrossRef] [PubMed]
46. Vessella, R.L.; Corey, E. Targeting factors involved in bone remodeling as treatment strategies in prostate cancer bone metastasis. *Clin. Cancer Res.* **2006**, *12*, 6285s–6290s. [CrossRef]
47. Paget, S. The distribution of secondary growths in cancer of the breast. 1889. *Cancer Metastasis Rev.* **1989**, *8*, 98–101.
48. Raubenheimer, E.J.; Noffke, C.E. Pathogenesis of bone metastasis: A review. *J. Oral. Pathol. Med.* **2006**, *35*, 129–135. [CrossRef]
49. Guise, T.A.; Mundy, G.R. Cancer and bone. *Endocr. Rev.* **1998**, *19*, 18–54.
50. Chantrain, C.F.; Feron, O.; Marbaix, E.; DeClerck, Y.A. Bone marrow microenvironment and tumor progression. *Cancer Microenviron.* **2008**, *1*, 23–35. [CrossRef]
51. Cook, L.M.; Shay, G.; Araujo, A.; Lynch, C.C. Integrating new discoveries into the "vicious cycle" paradigm of prostate to bone metastases. *Cancer Metastasis Rev.* **2014**, *33*, 511–525. [CrossRef] [PubMed]
52. Shiozawa, Y.; Pedersen, E.A.; Havens, A.M.; Jung, Y.; Mishra, A.; Joseph, J.; Kim, J.K.; Patel, L.R.; Ying, C.; Ziegler, A.M.; et al. Human prostate cancer metastases target the hematopoietic stem cell niche to establish footholds in mouse bone marrow. *J. Clin. Investig.* **2011**, *121*, 1298–1312. [CrossRef]
53. Shiozawa, Y.; Berry, J.E.; Eber, M.R.; Jung, Y.; Yumoto, K.; Cackowski, F.C.; Yoon, H.J.; Parsana, P.; Mehra, R.; Wang, J.; et al. The marrow niche controls the cancer stem cell phenotype of disseminated prostate cancer. *Oncotarget* **2016**, *7*, 41217–41232. [CrossRef]
54. Hage, W.D.; Aboulafia, A.J.; Aboulafia, D.M. Incidence, location, and diagnostic evaluation of metastatic bone disease. *Orthop. Clin. N. Am.* **2000**, *31*, 515–528. [CrossRef]
55. Mundy, G.R. Metastasis to bone: Causes, consequences and therapeutic opportunities. *Nat. Rev. Cancer* **2002**, *2*, 584–593. [CrossRef]
56. Taube, T.; Elomaa, I.; Blomqvist, C.; Beneton, M.N.; Kanis, J.A. Histomorphometric evidence for osteoclast-mediated bone resorption in metastatic breast cancer. *Bone* **1994**, *15*, 161–166. [CrossRef]
57. Martin, T.J. Osteoblast-derived PTHrP is a physiological regulator of bone formation. *J. Clin. Investig.* **2005**, *115*, 2322–2324. [CrossRef]
58. Iwamura, M.; di Sant'Agnese, P.A.; Wu, G.; Benning, C.M.; Cockett, A.T.; Deftos, L.J.; Abrahamsson, P.A. Immunohistochemical localization of parathyroid hormone-related protein in human prostate cancer. *Cancer Res.* **1993**, *53*, 1724–1726. [PubMed]
59. Weilbaecher, K.N.; Guise, T.A.; McCauley, L.K. Cancer to bone: A fatal attraction. *Nat. Rev. Cancer* **2011**, *11*, 411–425. [CrossRef]
60. Keller, E.T.; Brown, J. Prostate cancer bone metastases promote both osteolytic and osteoblastic activity. *J. Cell Biochem.* **2004**, *91*, 718–729. [CrossRef]
61. Ganguly, S.S.; Li, X.; Miranti, C.K. The host microenvironment influences prostate cancer invasion, systemic spread, bone colonization, and osteoblastic metastasis. *Front. Oncol.* **2014**, *4*, 364. [CrossRef] [PubMed]
62. Kohli, S.S.; Kohli, V.S. Role of RANKL-RANK/osteoprotegerin molecular complex in bone remodeling and its immunopathologic implications. *Indian J. Endocrinol. Metab.* **2011**, *15*, 175–181. [CrossRef]
63. Pinski, J.; Dorff, T.B. Prostate cancer metastases to bone: Pathophysiology, pain management, and the promise of targeted therapy. *Eur. J. Cancer* **2005**, *41*, 932–940. [CrossRef]
64. Lipton, A. Management of bone metastases in breast cancer. *Curr. Treat. Options Oncol.* **2005**, *6*, 161–171. [CrossRef]
65. Woolf, D.K.; Padhani, A.R.; Makris, A. Assessing response to treatment of bone metastases from breast cancer: What should be the standard of care? *Ann. Oncol.* **2015**, *26*, 1048–1057. [CrossRef]
66. Parker, C.; Nilsson, S.; Heinrich, D.; Helle, S.I.; O'Sullivan, J.M.; Fossa, S.D.; Chodacki, A.; Wiechno, P.; Logue, J.; Seke, M.; et al. Alpha emitter radium-223 and survival in metastatic prostate cancer. *N. Engl. J. Med.* **2013**, *369*, 213–223. [CrossRef]
67. Badrising, S.K.; van der Noort, V.; Hamberg, P.; Coenen, J.L.; Aarts, M.J.; van Oort, I.M.; van den Eertwegh, A.J.; Los, M.; van den Berg, H.P.; Gelderblom, H.; et al. Enzalutamide as a Fourth- or Fifth-Line Treatment Option for Metastatic Castration-Resistant Prostate Cancer. *Oncology* **2016**, *91*, 267–273. [CrossRef]
68. Vignani, F.; Bertaglia, V.; Buttigliero, C.; Tucci, M.; Scagliotti, G.V.; Di Maio, M. Skeletal metastases and impact of anticancer and bone-targeted agents in patients with castration-resistant prostate cancer. *Cancer Treat. Rev.* **2016**, *44*, 61–73. [CrossRef]
69. Abou, D.S.; Ulmert, D.; Doucet, M.; Hobbs, R.F.; Riddle, R.C.; Thorek, D.L. Whole-Body and Microenvironmental Localization of Radium-223 in Naive and Mouse Models of Prostate Cancer Metastasis. *J. Natl Cancer Inst.* **2016**, *108*, djv380. [CrossRef]
70. Laird, B.J.; Walley, J.; Murray, G.D.; Clausen, E.; Colvin, L.A.; Fallon, M.T. Characterization of cancer-induced bone pain: An exploratory study. *Support. Care Cancer* **2011**, *19*, 1393–1401. [CrossRef]
71. De Felice, F.; Piccioli, A.; Musio, D.; Tombolini, V. The role of radiation therapy in bone metastases management. *Oncotarget* **2017**, *8*, 25691–25699. [CrossRef]
72. Kassis, A.I.; Adelstein, S.J. Radiobiologic principles in radionuclide therapy. *J. Nucl. Med.* **2005**, *46* (Suppl. 1), 4S–12S. [PubMed]
73. Cole, A. Absorption of 20-eV to 50,000-eV electron beams in air and plastic. *Radiat. Res.* **1969**, *38*, 7–33. [CrossRef] [PubMed]
74. Kassis, A.I.; Adelstein, S.J.; Haydock, C.; Sastry, K.S.; McElvany, K.D.; Welch, M.J. Lethality of Auger electrons from the decay of bromine-77 in the DNA of mammalian cells. *Radiat. Res.* **1982**, *90*, 362–373. [CrossRef]
75. Kassis, A.I.; Sastry, K.S.; Adelstein, S.J. Kinetics of uptake, retention, and radiotoxicity of 125IUdR in mammalian cells: Implications of localized energy deposition by Auger processes. *Radiat. Res.* **1987**, *109*, 78–89. [CrossRef]

76. Walicka, M.A.; Vaidyanathan, G.; Zalutsky, M.R.; Adelstein, S.J.; Kassis, A.I. Survival and DNA damage in Chinese hamster V79 cells exposed to alpha particles emitted by DNA-incorporated astatine-211. *Radiat. Res.* **1998**, *150*, 263–268. [CrossRef]
77. Goddu, S.M.; Howell, R.W.; Rao, D.V. Cellular dosimetry: Absorbed fractions for monoenergetic electron and alpha particle sources and S-values for radionuclides uniformly distributed in different cell compartments. *J. Nucl. Med.* **1994**, *35*, 303–316. [PubMed]
78. Choi, J.Y. Treatment of Bone Metastasis with Bone-Targeting Radiopharmaceuticals. *Nucl. Med. Mol. Imaging* **2018**, *52*, 200–207. [CrossRef]
79. Paes, F.M.; Serafini, A.N. Systemic metabolic radiopharmaceutical therapy in the treatment of metastatic bone pain. *Semin Nucl. Med.* **2010**, *40*, 89–104. [CrossRef]
80. Lepareur, N.; Lacoeuille, F.; Bouvry, C.; Hindre, F.; Garcion, E.; Cherel, M.; Noiret, N.; Garin, E.; Knapp, F.F.R., Jr. Rhenium-188 Labeled Radiopharmaceuticals: Current Clinical Applications in Oncology and Promising Perspectives. *Front. Med. (Lausanne)* **2019**, *6*, 132. [CrossRef]
81. Alavi, M.; Omidvari, S.; Mehdizadeh, A.; Jalilian, A.R.; Bahrami-Samani, A. Metastatic Bone Pain Palliation using (177)Lu-Ethylenediaminetetramethylene Phosphonic Acid. *World J. Nucl. Med.* **2015**, *14*, 109–115. [CrossRef] [PubMed]
82. Friedell, H.L.; Storaasli, J.P. The use of radioactive phosphorus in the treatment of carcinoma of the breast with widespread metastases to bone. *Am. J. Roentgenol. Radium Ther.* **1950**, *64*, 559–575. [PubMed]
83. Maxfield, J.R., Jr.; Maxfield, J.G.; Maxfield, W.S. The use of radioactive phosphorus and testosterone in metastatic bone lesions from breast and prostate. *South. Med. J.* **1958**, *51*, 320–327. [CrossRef]
84. Miller, A.D. Radiophosphorous (P32) treatment in carcinoma of the breast and prostate: Report of 39 cases. *J. Am. Osteopath Assoc.* **1974**, *74*, 217–222. [PubMed]
85. Cheung, A.; Driedger, A.A. Evaluation of radioactive phosphorus in the palliation of metastatic bone lesions from carcinoma of the breast and prostate. *Radiology* **1980**, *134*, 209–212. [CrossRef]
86. Silberstein, E.B. The treatment of painful osseous metastases with phosphorus-32-labeled phosphates. *Semin. Oncol.* **1993**, *20* (Suppl. 2), 10–21.
87. Nair, N. Relative efficacy of 32P and 89Sr in palliation in skeletal metastases. *J. Nucl. Med.* **1999**, *40*, 256–261.
88. Blake, G.M.; Zivanovic, M.A.; McEwan, A.J.; Ackery, D.M. Sr-89 therapy: Strontium kinetics in disseminated carcinoma of the prostate. *Eur. J. Nucl. Med.* **1986**, *12*, 447–454. [CrossRef]
89. Finlay, I.G.; Mason, M.D.; Shelley, M. Radioisotopes for the palliation of metastatic bone cancer: A systematic review. *Lancet Oncol.* **2005**, *6*, 392–400. [CrossRef]
90. Silberstein, E.B.; Williams, C. Strontium-89 therapy for the pain of osseous metastases. *J. Nucl. Med.* **1985**, *26*, 345–348. [PubMed]
91. Robinson, R.G.; Preston, D.F.; Spicer, J.A.; Baxter, K.G. Radionuclide therapy of intractable bone pain: Emphasis on strontium-89. *Semin. Nucl. Med.* **1992**, *22*, 28–32. [CrossRef]
92. Mertens, W.C.; Stitt, L.; Porter, A.T. Strontium 89 therapy and relief of pain in patients with prostatic carcinoma metastatic to bone: A dose response relationship? *Am. J. Clin. Oncol.* **1993**, *16*, 238–242. [CrossRef]
93. Maxon, H.R., 3rd; Schroder, L.E.; Thomas, S.R.; Hertzberg, V.S.; Deutsch, E.A.; Scher, H.I.; Samaratunga, R.C.; Libson, K.F.; Williams, C.C.; Moulton, J.S.; et al. Re-186(Sn) HEDP for treatment of painful osseous metastases: Initial clinical experience in 20 patients with hormone-resistant prostate cancer. *Radiology* **1990**, *176*, 155–159. [CrossRef]
94. Giannakenas, C.; Kalofonos, H.P.; Apostolopoulos, D.J.; Zarakovitis, J.; Kosmas, C.; Vassilakos, P.J. Preliminary results of the use of Re-186-HEDP for palliation of pain in patients with metastatic bone disease. *Am. J. Clin. Oncol.* **2000**, *23*, 83–88. [CrossRef]
95. Kolesnikov-Gauthier, H.; Carpentier, P.; Depreux, P.; Vennin, P.; Caty, A.; Sulman, C. Evaluation of toxicity and efficacy of 186Re-hydroxyethylidene diphosphonate in patients with painful bone metastases of prostate or breast cancer. *J. Nucl. Med.* **2000**, *41*, 1689–1694.
96. Sciuto, R.; Tofani, A.; Festa, A.; Giannarelli, D.; Pasqualoni, R.; Maini, C.L. Short- and long-term effects of 186Re-1,1-hydroxyethylidene diphosphonate in the treatment of painful bone metastases. *J. Nucl. Med.* **2000**, *41*, 647–654.
97. Quirijnen, J.M.; Han, S.H.; Zonnenberg, B.A.; de Klerk, J.M.; van het Schip, A.D.; van Dijk, A.; ten Kroode, H.F.; Blijham, G.H.; van Rijk, P.P. Efficacy of rhenium-186-etidronate in prostate cancer patients with metastatic bone pain. *J. Nucl. Med.* **1996**, *37*, 1511–1515.
98. Maxon, H.R., 3rd; Schroder, L.E.; Hertzberg, V.S.; Thomas, S.R.; Englaro, E.E.; Samaratunga, R.; Smith, H.; Moulton, J.S.; Williams, C.C.; Ehrhardt, G.J.; et al. Rhenium-186(Sn)HEDP for treatment of painful osseous metastases: Results of a double-blind crossover comparison with placebo. *J. Nucl. Med.* **1991**, *32*, 1877–1881.
99. Han, S.H.; de Klerk, J.M.; Tan, S.; van het Schip, A.D.; Derksen, B.H.; van Dijk, A.; Kruitwagen, C.L.; Blijham, G.H.; van Rijk, P.P.; Zonnenberg, B.A. The PLACORHEN study: A double-blind, placebo-controlled, randomized radionuclide study with (186)Re-etidronate in hormone-resistant prostate cancer patients with painful bone metastases. Placebo Controlled Rhenium Study. *J. Nucl. Med.* **2002**, *43*, 1150–1156.
100. Liepe, K. (188)Re-HEDP therapy in the therapy of painful bone metastases. *World J. Nucl. Med.* **2018**, *17*, 133–138. [CrossRef]
101. Liepe, K.; Kotzerke, J. A comparative study of 188Re-HEDP, 186Re-HEDP, 153Sm-EDTMP and 89Sr in the treatment of painful skeletal metastases. *Nucl. Med. Commun.* **2007**, *28*, 623–630. [CrossRef]

102. Resche, I.; Chatal, J.F.; Pecking, A.; Ell, P.; Duchesne, G.; Rubens, R.; Fogelman, I.; Houston, S.; Fauser, A.; Fischer, M.; et al. A dose-controlled study of 153Sm-ethylenediaminetetramethylenephosphonate (EDTMP) in the treatment of patients with painful bone metastases. *Eur. J. Cancer* **1997**, *33*, 1583–1591. [CrossRef]
103. Tian, J.H.; Zhang, J.M.; Hou, Q.T.; Oyang, Q.H.; Wang, J.M.; Luan, Z.S.; Chuan, L.; He, Y.J. Multicentre trial on the efficacy and toxicity of single-dose samarium-153-ethylene diamine tetramethylene phosphonate as a palliative treatment for painful skeletal metastases in China. *Eur. J. Nucl. Med.* **1999**, *26*, 2–7. [CrossRef] [PubMed]
104. Yadav, M.P.; Ballal, S.; Sahoo, R.K.; Dwivedi, S.N.; Bal, C. Radioligand Therapy With (177)Lu-PSMA for Metastatic Castration-Resistant Prostate Cancer: A Systematic Review and Meta-Analysis. *AJR Am. J. Roentgenol.* **2019**, *213*, 275–285. [CrossRef] [PubMed]
105. Chakraborty, S.; Das, T.; Banerjee, S.; Balogh, L.; Chaudhari, P.R.; Sarma, H.D.; Polyak, A.; Mathe, D.; Venkatesh, M.; Janoki, G.; et al. 177Lu-EDTMP: A viable bone pain palliative in skeletal metastasis. *Cancer Biother. Radio Pharm.* **2008**, *23*, 202–213. [CrossRef] [PubMed]
106. Mathe, D.; Balogh, L.; Polyak, A.; Kiraly, R.; Marian, T.; Pawlak, D.; Zaknun, J.J.; Pillai, M.R.; Janoki, G.A. Multispecies animal investigation on biodistribution, pharmacokinetics and toxicity of 177Lu-EDTMP, a potential bone pain palliation agent. *Nucl. Med. Biol.* **2010**, *37*, 215–226. [CrossRef]
107. Agarwal, K.K.; Singla, S.; Arora, G.; Bal, C. (177)Lu-EDTMP for palliation of pain from bone metastases in patients with prostate and breast cancer: A phase II study. *Eur. J. Nucl. Med. Mol. Imaging* **2015**, *42*, 79–88. [CrossRef] [PubMed]
108. Chakraborty, S.; Das, T.; Sarma, H.D.; Venkatesh, M.; Banerjee, S. Comparative studies of 177Lu-EDTMP and 177Lu-DOTMP as potential agents for palliative radiotherapy of bone metastasis. *Appl. Radiat. Isot.* **2008**, *66*, 1196–1205. [CrossRef]
109. Das, T.; Shinto, A.; Karuppuswamy Kamaleshwaran, K.; Banerjee, S. Theranostic Treatment of Metastatic Bone Pain with 177Lu-DOTMP. *Clin. Nucl. Med.* **2016**, *41*, 966–967. [CrossRef]
110. Bahrami-Samani, A.; Anvari, A.; Jalilian, A.R.; Shirvani-Arani, S.; Yousefnia, H.; Aghamiri, M.R.; Ghannadi-Maragheh, M. Production, Quality Control and Pharmacokinetic Studies of (177)Lu-EDTMP for Human Bone Pain Palliation Therapy Trials. *Iran. J. Pharm. Res.* **2012**, *11*, 137–144.
111. Yousefnia, H.; Zolghadri, S.; Jalilian, A.R. Absorbed dose assessment of (177)Lu-zoledronate and (177)Lu-EDTMP for human based on biodistribution data in rats. *J. Med. Phys.* **2015**, *40*, 102–108. [PubMed]
112. Yadav, M.P.; Ballal, S.; Meckel, M.; Roesch, F.; Bal, C. [(177)Lu]Lu-DOTA-ZOL bone pain palliation in patients with skeletal metastases from various cancers: Efficacy and safety results. *EJNMMI Res.* **2020**, *10*, 130. [CrossRef] [PubMed]
113. Wissing, M.D.; van Leeuwen, F.W.; van der Pluijm, G.; Gelderblom, H. Radium-223 chloride: Extending life in prostate cancer patients by treating bone metastases. *Clin. Cancer Res.* **2013**, *19*, 5822–5827. [CrossRef] [PubMed]
114. Kassis, A.I. Therapeutic radionuclides: Biophysical and radiobiologic principles. *Semin Nucl. Med.* **2008**, *38*, 358–366. [CrossRef] [PubMed]
115. Baidoo, K.E.; Yong, K.; Brechbiel, M.W. Molecular pathways: Targeted alpha-particle radiation therapy. *Clin. Cancer Res.* **2013**, *19*, 530–537. [CrossRef] [PubMed]
116. Sgouros, G.; Hobbs, R.F.; Song, H. Modelling and dosimetry for alpha-particle therapy. *Curr. Radio Pharm.* **2011**, *4*, 261–265. [CrossRef] [PubMed]
117. Song, H.; Hobbs, R.F.; Vajravelu, R.; Huso, D.L.; Esaias, C.; Apostolidis, C.; Morgenstern, A.; Sgouros, G. Radioimmunotherapy of breast cancer metastases with alpha-particle emitter 225Ac: Comparing efficacy with 213Bi and 90Y. *Cancer Res.* **2009**, *69*, 8941–8948. [CrossRef]
118. Saad, F.; Carles, J.; Gillessen, S.; Heidenreich, A.; Heinrich, D.; Gratt, J.; Levy, J.; Miller, K.; Nilsson, S.; Petrenciuc, O.; et al. Radium-223 and concomitant therapies in patients with metastatic castration-resistant prostate cancer: An international, early access, open-label, single-arm phase 3b trial. *Lancet Oncol.* **2016**, *17*, 1306–1316. [CrossRef]
119. Delgado Bolton, R.C.; Giammarile, F. Bone radionuclide therapy and increased survival with radium-223 is the way to go for nuclear medicine: The offer that oncologists cannot refuse. *Eur. J. Nucl. Med. Mol. Imaging* **2018**, *45*, 822–823. [CrossRef] [PubMed]
120. Gravis, G. Systemic treatment for metastatic prostate cancer. *Asian J. Urol.* **2019**, *6*, 162–168. [CrossRef]
121. Smith, M.; Parker, C.; Saad, F.; Miller, K.; Tombal, B.; Ng, Q.S.; Boegemann, M.; Matveev, V.; Piulats, J.M.; Zucca, L.E.; et al. Addition of radium-223 to abiraterone acetate and prednisone or prednisolone in patients with castration-resistant prostate cancer and bone metastases (ERA 223): A randomised, double-blind, placebo-controlled, phase 3 trial. *Lancet Oncol.* **2019**, *20*, 408–419. [CrossRef]
122. Chang, S.S. Overview of prostate-specific membrane antigen. *Rev. Urol.* **2004**, *6* (Suppl. 10), S13–S18. [PubMed]
123. Hupe, M.C.; Philippi, C.; Roth, D.; Kumpers, C.; Ribbat-Idel, J.; Becker, F.; Joerg, V.; Duensing, S.; Lubczyk, V.H.; Kirfel, J.; et al. Expression of Prostate-Specific Membrane Antigen (PSMA) on Biopsies Is an Independent Risk Stratifier of Prostate Cancer Patients at Time of Initial Diagnosis. *Front. Oncol.* **2018**, *8*, 623. [CrossRef]
124. Sun, M.; Niaz, M.O.; Nelson, A.; Skafida, M.; Niaz, M.J. Review of 177Lu-PSMA-617 in Patients with Metastatic Castration-Resistant Prostate Cancer. *Cureus* **2020**, *12*, e8921. [CrossRef]
125. Hofman, M.S.; Violet, J.; Hicks, R.J.; Ferdinandus, J.; Thang, S.P.; Akhurst, T.; Iravani, A.; Kong, G.; Ravi Kumar, A.; Murphy, D.G.; et al. [(177)Lu]-PSMA-617 radionuclide treatment in patients with metastatic castration-resistant prostate cancer (LuPSMA trial): A single-centre, single-arm, phase 2 study. *Lancet Oncol.* **2018**, *19*, 825–833. [CrossRef]

126. Rahbar, K.; Bodei, L.; Morris, M.J. Is the Vision of Radioligand Therapy for Prostate Cancer Becoming a Reality? An Overview of the Phase III VISION Trial and Its Importance for the Future of Theranostics. *J. Nucl. Med.* **2019**, *60*, 1504–1506. [CrossRef]
127. Kratochwil, C.; Bruchertseifer, F.; Giesel, F.L.; Weis, M.; Verburg, F.A.; Mottaghy, F.; Kopka, K.; Apostolidis, C.; Haberkorn, U.; Morgenstern, A. 225Ac-PSMA-617 for PSMA-Targeted alpha-Radiation Therapy of Metastatic Castration-Resistant Prostate Cancer. *J. Nucl. Med.* **2016**, *57*, 1941–1944. [CrossRef] [PubMed]
128. Yadav, M.P.; Ballal, S.; Sahoo, R.K.; Tripathi, M.; Seth, A.; Bal, C. Efficacy and safety of (225)Ac-PSMA-617 targeted alpha therapy in metastatic castration-resistant Prostate Cancer patients. *Theranostics* **2020**, *10*, 9364–9377. [CrossRef] [PubMed]
129. Kratochwil, C.; Haberkorn, U.; Giesel, F.L. (225)Ac-PSMA-617 for Therapy of Prostate Cancer. *Semin. Nucl. Med.* **2020**, *50*, 133–140. [CrossRef]
130. Deblonde, G.J.; Abergel, R.J. Active actinium. *Nat. Chem.* **2016**, *8*, 1084. [CrossRef] [PubMed]
131. Vasiliev, A.; Severin, A.; Lapshina, E.; Chernykh, E.; Ermolaev, S.; Kalmykov, S. Hydroxylapatite particles as carriers for ^{223}Ra. *J. Radioanal. Nuclear Chem.* **2016**, *311*, 1503–1509. [CrossRef]
132. McDevitt, M.R.; Ma, D.; Simon, J.; Frank, R.K.; Scheinberg, D.A. Design and synthesis of 225Ac radioimmunopharmaceuticals. *Appl. Radiat. Isot.* **2002**, *57*, 841–847. [CrossRef]
133. Sofou, S.; Kappel, B.J.; Jaggi, J.S.; McDevitt, M.R.; Scheinberg, D.A.; Sgouros, G. Enhanced retention of the alpha-particle-emitting daughters of Actinium-225 by liposome carriers. *Bioconjug. Chem.* **2007**, *18*, 2061–2067. [CrossRef] [PubMed]
134. Antczak, C.; Jaggi, J.S.; LeFave, C.V.; Curcio, M.J.; McDevitt, M.R.; Scheinberg, D.A. Influence of the linker on the biodistribution and catabolism of actinium-225 self-immolative tumor-targeted isotope generators. *Bioconjug. Chem.* **2006**, *17*, 1551–1560. [CrossRef] [PubMed]
135. Borchardt, P.E.; Yuan, R.R.; Miederer, M.; McDevitt, M.R.; Scheinberg, D.A. Targeted actinium-225 in vivo generators for therapy of ovarian cancer. *Cancer Res.* **2003**, *63*, 5084–5090.
136. Davis, I.A.; Glowienka, K.A.; Boll, R.A.; Deal, K.A.; Brechbiel, M.W.; Stabin, M.; Bochsler, P.N.; Mirzadeh, S.; Kennel, S.J. Comparison of 225actinium chelates: Tissue distribution and radiotoxicity. *Nucl. Med. Biol.* **1999**, *26*, 581–589. [CrossRef]
137. Deal, K.A.; Davis, I.A.; Mirzadeh, S.; Kennel, S.J.; Brechbiel, M.W. Improved in vivo stability of actinium-225 macrocyclic complexes. *J. Med. Chem.* **1999**, *42*, 2988–2992. [CrossRef] [PubMed]
138. Sathekge, M.; Bruchertseifer, F.; Knoesen, O.; Reyneke, F.; Lawal, I.; Lengana, T.; Davis, C.; Mahapane, J.; Corbett, C.; Vorster, M.; et al. (225)Ac-PSMA-617 in chemotherapy-naive patients with advanced prostate cancer: A pilot study. *Eur. J. Nucl. Med. Mol. Imaging* **2019**, *46*, 129–138. [CrossRef]
139. Paganelli, G.; Sarnelli, A.; Severi, S.; Sansovini, M.; Belli, M.L.; Monti, M.; Foca, F.; Celli, M.; Nicolini, S.; Tardelli, E.; et al. Dosimetry and safety of (177)Lu PSMA-617 along with polyglutamate parotid gland protector: Preliminary results in metastatic castration-resistant prostate cancer patients. *Eur. J. Nucl. Med. Mol. Imaging* **2020**, *47*, 3008–3017. [CrossRef]
140. Langbein, T.; Chausse, G.; Baum, R.P. Salivary Gland Toxicity of PSMA Radioligand Therapy: Relevance and Preventive Strategies. *J. Nucl. Med.* **2018**, *59*, 1172–1173. [CrossRef] [PubMed]
141. Rathke, H.; Bruchertseifer, F.; Kratochwil, C.; Keller, H.; Giesel, F.L.; Apostolidis, C.; Haberkorn, U.; Morgenstern, A. First patient exceeding 5-year complete remission after (225)Ac-PSMA-TAT. *Eur. J. Nucl. Med. Mol. Imaging* **2021**, *48*, 311–312. [CrossRef] [PubMed]
142. Kratochwil, C.; Giesel, F.L.; Heussel, C.P.; Kazdal, D.; Endris, V.; Nientiedt, C.; Bruchertseifer, F.; Kippenberger, M.; Rathke, H.; Leichsenring, J.; et al. Patients Resistant Against PSMA-Targeting alpha-Radiation Therapy Often Harbor Mutations in DNA Damage-Repair-Associated Genes. *J. Nucl. Med.* **2020**, *61*, 683–688. [CrossRef]
143. McDevitt, M.R.; Barendswaard, E.; Ma, D.; Lai, L.; Curcio, M.J.; Sgouros, G.; Ballangrud, A.M.; Yang, W.H.; Finn, R.D.; Pellegrini, V.; et al. An alpha-particle emitting antibody ([213Bi]J591) for radioimmunotherapy of prostate cancer. *Cancer Res.* **2000**, *60*, 6095–6100.
144. Ballangrud, A.M.; Yang, W.H.; Charlton, D.E.; McDevitt, M.R.; Hamacher, K.A.; Panageas, K.S.; Ma, D.; Bander, N.H.; Scheinberg, D.A.; Sgouros, G. Response of LNCaP spheroids after treatment with an alpha-particle emitter (213Bi)-labeled anti-prostate-specific membrane antigen antibody (J591). *Cancer Res.* **2001**, *61*, 2008–2014. [PubMed]
145. Li, Y.; Tian, Z.; Rizvi, S.M.; Bander, N.H.; Allen, B.J. In vitro and preclinical targeted alpha therapy of human prostate cancer with Bi-213 labeled J591 antibody against the prostate specific membrane antigen. *Prostate Cancer Prostatic Dis.* **2002**, *5*, 36–46. [CrossRef] [PubMed]
146. Nonnekens, J.; Chatalic, K.L.; Molkenboer-Kuenen, J.D.; Beerens, C.E.; Bruchertseifer, F.; Morgenstern, A.; Veldhoven-Zweistra, J.; Schottelius, M.; Wester, H.J.; van Gent, D.C.; et al. (213)Bi-Labeled Prostate-Specific Membrane Antigen-Targeting Agents Induce DNA Double-Strand Breaks in Prostate Cancer Xenografts. *Cancer Biother. Radio Pharm.* **2017**, *32*, 67–73.
147. Kiess, A.P.; Minn, I.; Vaidyanathan, G.; Hobbs, R.F.; Josefsson, A.; Shen, C.; Brummet, M.; Chen, Y.; Choi, J.; Koumarianou, E.; et al. (2S)-2-(3-(1-Carboxy-5-(4-211At-Astatobenzamido)Pentyl)Ureido)-Pentanedioic Acid for PSMA-Targeted alpha-Particle Radiopharmaceutical Therapy. *J. Nucl. Med.* **2016**, *57*, 1569–1575. [CrossRef] [PubMed]
148. Khreish, F.; Ebert, N.; Ries, M.; Maus, S.; Rosar, F.; Bohnenberger, H.; Stemler, T.; Saar, M.; Bartholoma, M.; Ezziddin, S. (225)Ac-PSMA-617/(177)Lu-PSMA-617 tandem therapy of metastatic castration-resistant prostate cancer: Pilot experience. *Eur. J. Nucl. Med. Mol. Imaging* **2020**, *47*, 721–728. [CrossRef] [PubMed]

149. Hammer, S.; Hagemann, U.B.; Zitzmann-Kolbe, S.; Larsen, A.; Ellingsen, C.; Geraudie, S.; Grant, D.; Indrevoll, B.; Smeets, R.; von Ahsen, O.; et al. Preclinical Efficacy of a PSMA-Targeted Thorium-227 Conjugate (PSMA-TTC), a Targeted Alpha Therapy for Prostate Cancer. *Clin. Cancer Res.* **2020**, *26*, 1985–1996. [CrossRef]